NASA Contract NAS9-15423
Report No. CASD-NAS-78-011

NASA CR-
151831

FINAL REPORT

ACHIEVABLE FLATNESS IN A LARGE MICROWAVE POWER ANTENNA STUDY

(DRL Item No. 2)

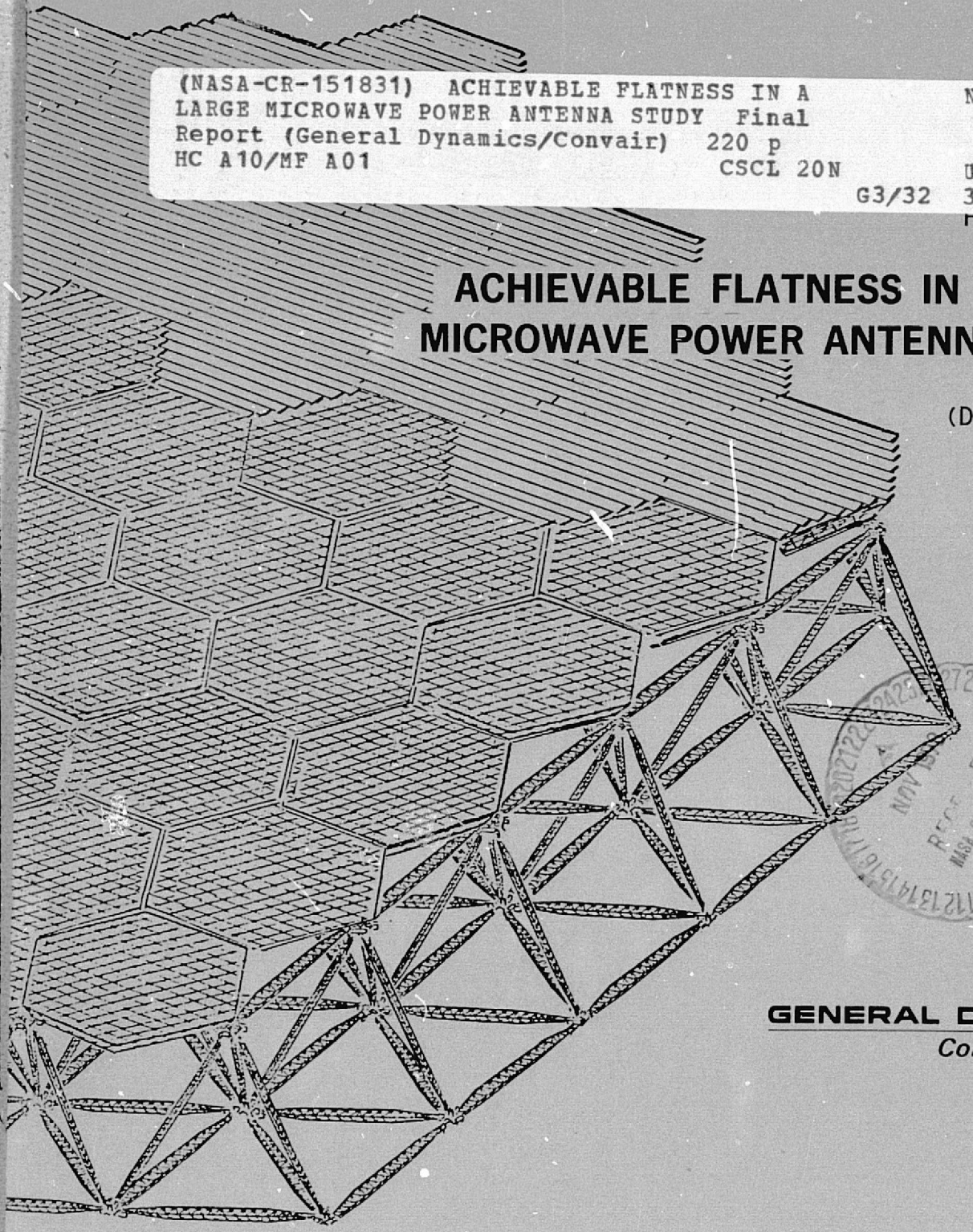

GENERAL DYNAMICS
Convair Division

Report No. CASD-NAS-78-011

FINAL REPORT

ACHIEVABLE FLATNESS IN A LARGE MICROWAVE POWER ANTENNA STUDY

(DRL Item No. 2)

18 August 1978

Prepared under
Contract No. NAS9-15423
for
National Aeronautics and Space Administration
LYNDON B. JOHNSON SPACE CENTER
Houston, Texas 77058

Prepared by
GENERAL DYNAMICS CONVAIR DIVISION
P.O. Box 80847
San Diego, California 92138

NASA Technical Monitor
F.J. STEBBINS
NASA/JSC
Houston, Texas 77058

Convair Project Manager
J.A. FAGER
GD/Convair
San Diego, California 92138

CONTENTS

Illustrations

Tables

SUMMARY

The Solar Power Satellite (SPS) is a viable alternative energy source to replace fossile fuel dependent systems. Its large solar energy collector is a source of electrical power which is converted to microwave energy and relayed from the collection site in geosynchronous orbit to the ground receiving system. The feasibility of the relay link depends on the capability of keeping each transmitting planar array antenna with its beam center pointed at the ground receiving antenna (rectenna), and the phase error over the aperture small enough so that efficiency is high. Pointing error and phase error should also be small to minimize incidence of stray energy peaks outside of the rectenna aperture. This study was performed to evaluate the tolerance variations in the structure of the MPTS, and their contribution to slope error of the antenna array. Each SPS has two power transmitting antennas. The general characteristics of each antenna are shown in Table 1. On the basis of most parameters except frequency, the MPTS represents a major advancement in the state of the art for large microwave antennas. For comparison purposes, the gains of several large existing antennas are shown in Figure 1. The MPTS has over 10 times the aperture area of the largest (Arecibo), and approximately 20 times the gain at 2.45 GHz.

Figure 2 shows the elements of the MPTS that function to achieve performance of this magnitude. Pure mechanical pointing and surface figure control over the 1-km aperture cannot be expected to achieve the necessary beam characteristics. The antenna system is a hybrid design of a coarse mechanical pointing and surface control system and an electronic phasing system for fine wavefront adjustment.

A tower is used to attach the antenna primary structure to the SPS solar collector. A 360-degree pivot allows the antenna to rotate once per day to track the rectenna. In the baseline approach for this study, a constant angular rate pivot is used, with the fine pointing accomplished at the antenna interface. This simplifies the 360-degree pivot design where rotating contacts are needed to transfer power from the solar collector to the tower. A $\pm$ 10 degree pivot on two axes is used at the antenna. Flexlines carry power around this junction. There are a number of viable approaches for attitude control. Because of the inherent rigidity of the primary structure, distributed control actuators do not appear necessary.

The antenna system operates in an environment which causes structural deformations and beam pointing error (see Figure 3). These must be minimized so that the distorted wavefront can be corrected electronically. The antenna points at a rectenna which is probably not located on the equator. The resulting elevation pointing angle causes gravity gradient and dynamic unbalance torques on the antenna. The acceleration of the antenna toward the cg of the SPS is appreciable because of the large separation. Transient forces and torques are also transmitted through the support tower. The effects of these acceleration loads have been found to be very small.

Table 1. MPTS parameters.

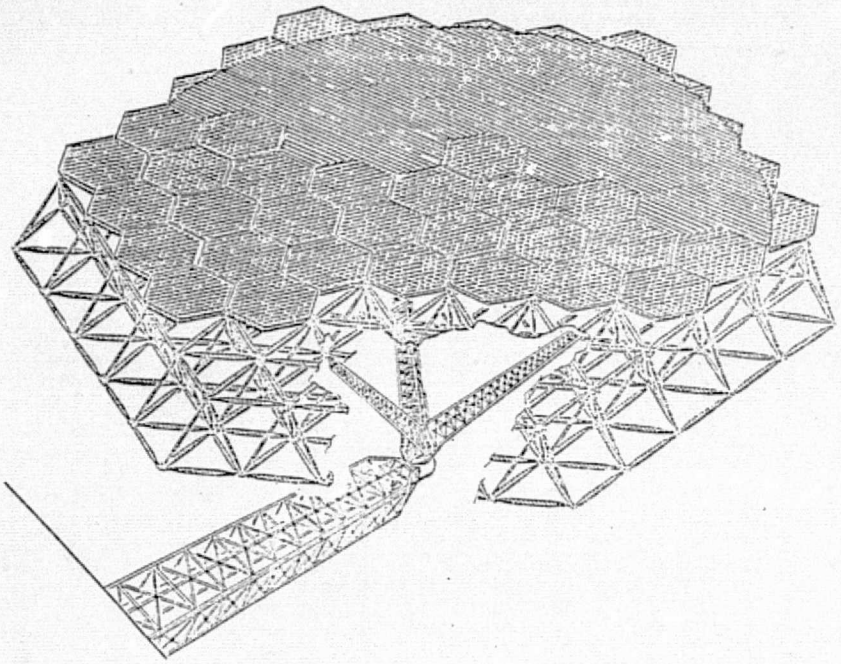

Type of antenna	Planar array
Diameter of aperture	1000 m (3281 ft)
Antenna mass	3.58 Mkg (18.92 x 10^6 lb)
Power transmitted (CW)	5 GW (67 dBW)
Frequency	2.45 GHz
Directivity	86 dB
Beamwidth (3-dB)	31.4 arc sec
Mount — Azimuth range	360 degrees
Elevation range	$\pm$ 10 degrees
Slewing rates (maximum)	1 arc sec/sec
Mechanical pointing accuracy	2 arc minutes
Electronic pointing accuracy	6 arc sec
Illumination taper	10 dB
Bandwidth — modulation	Not applicable

Thermal distortions, primarily caused by the waste heat rejection of the rf system, are controlled by the use of low thermal expansion composites in the primary and secondary structures.

The basic alignment requirement for the structure of the subarray surface is 3 arc min. maximum slope error in the operating environment. This encompasses all manufacturing errors, thermal distortions, static structural loads, and dynamic movement resulting from transient loads. Slope error (tilt errors of the subarrays with respect to the line of sight to the rectenna) has two effects on performance. It results in loss of directivity, and in pointing error. The rms slope error over the aperture is a

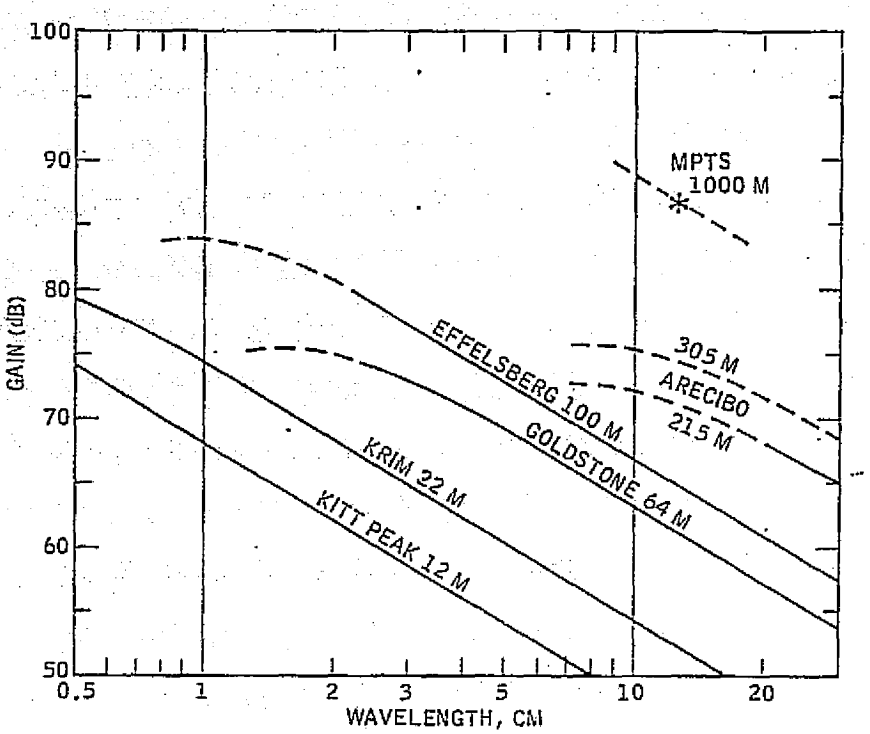

Figure 1. The MPTS will exceed the gain of the largest existing microwave antennas.

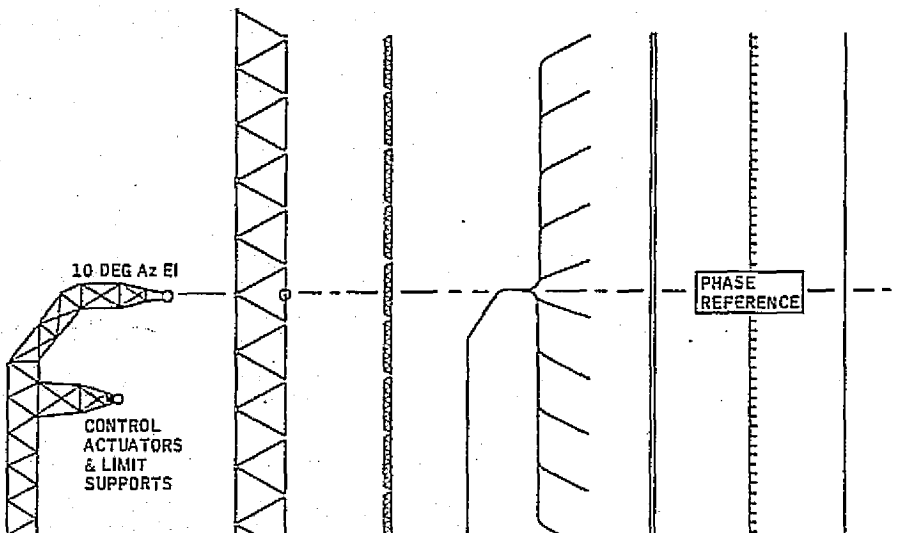

Figure 2. Functional elements of the MPTS.

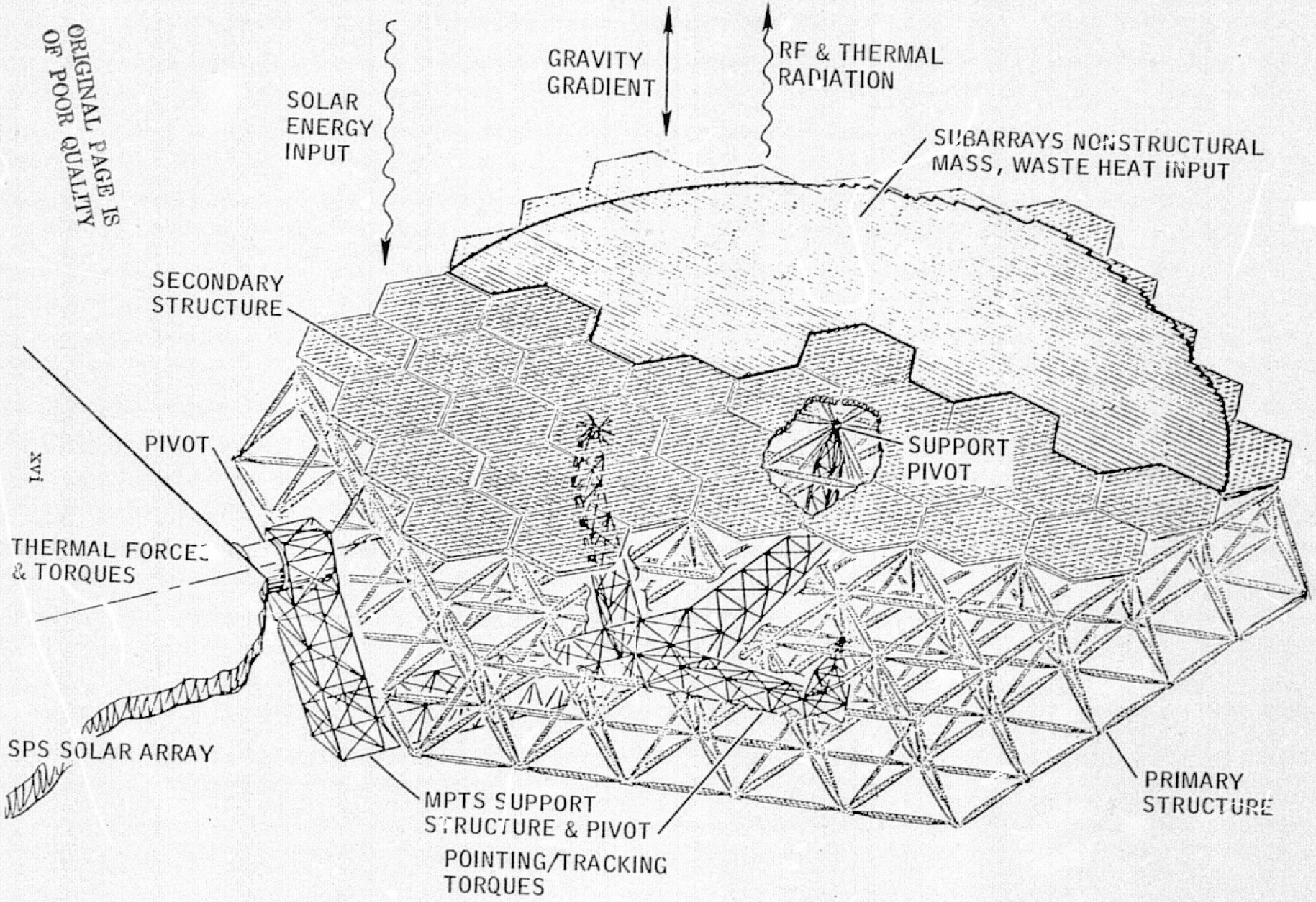

Figure 3. Environmental interface considerations.

measure of directivity and related energy transfer efficiency. The line-of-sight (LOS) pointing accuracy is the second major performance criterion.

Slope accuracy and pointing LOS accuracy budgets were established early in the study to provide guidance in selection of materials and loading conditions, and development of control concepts. The design goal for slope accuracy is 2 arc minutes rms. This is apportioned to manufacturing, thermal, and maneuvering error sources. The design goal for LOS pointing accuracy is 2 arc minutes maximum (3σ). This is apportioned to thermal distortion, maneuvering distortion, and the control system accuracy. Manufacturing tolerance does not contribute to pointing accuracy because it is a static misalignment which is correctable by bias pointing.

The rms slope accuracy and pointing accuracy budgets are listed in Table 2.

The overall slope accuracy goals can be met even if all individual goals are not met. If necessary, the budget could be revised to accommodate a critical error source or to take advantage of the elimination of error sources, for example, by active control.

Table 2. Accuracy error budgets.

Total Budget	Slope Error rms arc min 2.00*	LOS Error max arc min 2.00*
Manufacturing Tolerance	1.50	0.00
Primary Structure	0.64	0.00
Primary/Secondary Interface	0.06	0.00
Secondary Structure	1.32	0.00
Subarray Interface	0.32	0.00
Maneuvering Allowance	1.10	1.00
Primary Distortions	0.46	1.00
Secondary Distortions	1.00	0.00
Thermal Allowance	0.70	1.00
Primary Distortions	0.31	1.00
Secondary Distortions	0.63	0.00
Attitude Control System	0.00	1.41

*Totals by root-sum-square combination of uncorrelated contributions.

The following paragraphs list some of the more significant study results and conclusions.

- Slope error is a dimensionless parameter, not directly related to size of the antenna. Distortions can be expected to grow with size, but not the ratio of distortion to size, i.e. slope error.

- Existing materials measurement, manufacturing, assembly and alignment techniques can be used to build the MPTS antenna structure, orders of magnitude larger than current space systems.

- Manufacturing tolerance can be critical to rms slope error. Study results show that the slope error budget can be met with a passive system. As a backup approach, initial active alignment can be used to correct the interface between the structures. Tolerance then is limited by measurement accuracy and actuator resolution.

- Because of the inherent long term dimensional stability of graphite/epoxy structure under light loading conditions, the structures are expected to remain in alignment if adjusted accurately initially. The 30-year service life does lower confidence in long term creep predictions. Test data is needed for candidate fiber/matrix systems.

- Manufacturing tolerance does not contribute appreciably to pointing accuracy. A pointing bias caused by manufacturing error can be corrected by the attitude control system.

- Joints without free play are preferable in the assembly of the large truss structures. Joint "slop," as contrasted to joint tolerance, can be eliminated by bonding or welding. Joint tolerance is a small part of overall strut length, and makes a minor contribution to slope error.

- The material properties of GY-70/X-30 pseudoisotropic graphite/epoxy composite were used as representative of strength, modulus and coefficient of thermal expansion (see Table 3). Variation in material properties, particularly for CTE, from part to part is more significant than the actual value. The design can accommodate predictable length changes and still achieve the required flatness. The uncertainty in CTE leads to the thermal distortion that degrades performance. However, thermal distortion is small over the range of operating temperatures, and material properties not as well regulated as those of GY-70/X-30 will meet requirements.

- Two configurations of the secondary structure were considered. The first has 61 separate hexagonal structural elements. The second has the same elements joined to form a continuous secondary structure over the entire aperture. There is not a significant difference in parts count or performance. The continuous secondary behaves as a homogeneous plate attached at 75 nodes of the primary interface. Since it carries bending stress, it can distort the primary or conversely smooth out primary distortions. It tends to transfer distortions to the outer edge where slope error has less effect on performance. The 61 separate secondary structures are easier to simulate and analyze.

- Active control during operation is not warranted. Initial alignment of the primary structure, and secondary structural elements is considered as an alternative to "tinker toy" assembly of accurately "trimmed" truss elements. The initial

Table 3. Pseudoisotropic GY-70/X-30 is a representative dimensionally stable composite.

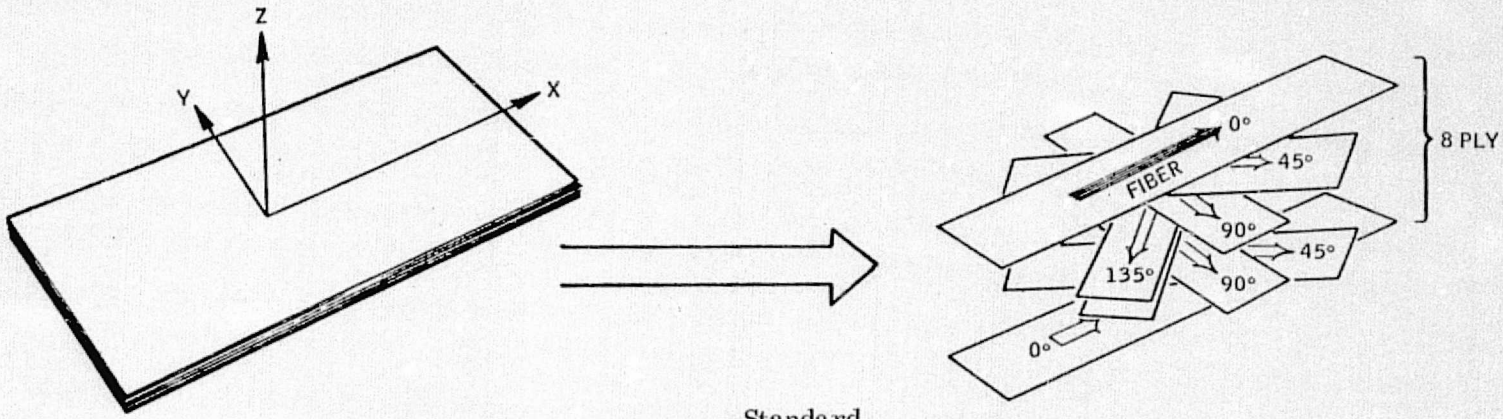

Characteristic	Mean	Standard Deviation	Units
Fiber volume	62	0.7	percent
Density	1.80 (0.065)		g/cc (lb/cu in.)
Tensile strength, F_{TU}	2.61E8 (37.8)	4.03E7 (5.85)	N/m^2 (ksi)
Elastic modulus, E_T	1.08E11 (15.7)	6.76E9 (0.98)	N/m^2 (msi)
Poisson's ratio, μ_T	0.32		
Compressive strength, F_{CU}	2.43E8 (35.2)	1.61E7 (2.34)	N/m^2 (ksi)
Elastic modulus, E_C	9.65E10 (14.0)	6.14E9 (0.89)	N/m^2 (msi)
Poisson's ratio, μ_C	0.30		
Ultimate shear stress, F_{SU}	1.5E8 (22.3)		N/m^2 (ksi)
Rigidity, G	3.5E10 (5.04)		N/m^2 (msi)
Thermal coefficient, CTE	-0.038 (-0.021)	0.072 (0.040)	ϵ/C (ϵ/F)
Specific heat	0.20 (31.9)	0.004 (0.004)	Cal/gm-C (Btu/lb-F)
Thermal conductivity	0.132 (31.9)		Cal/cm-sec-C (Btu/ft-hr-F)
Resistivity	2.8E-5 (1.1E-3)		ohm-m (ohm-in.)
Solar absorptance, α	0.91		
Thermal emittance, ϵ	0.81		

alignment system could be used periodically if necessary to realign during the service life, but active figure control to compensate for dynamic and thermal distortion is not necessary.

- The improvement in efficiency with active control is small compared to the potential improvement of a slight increase in system size at the same approximate cost.

- Distributed attitude control is not necessary for the MPTS. The truss structures are stiff enough so that even with the large nonstructural weights supported, the antenna behaves essentially as a rigid body. An alternative combined use of CMG packages to sense and damp oscillations within the structure as well as to provide steering torques can be used if larger than anticipated disturbances are generated by the SPS solar collector, e.g. those resulting from an aluminum SPS structure.

- The preferred attitude control approach is direct drive, i.e., steering the antenna by applying torques at the interface to the solar collector. System weight and complexity increases for momentum exchange devices, and jet systems are impractical for the 30-year operational life because of fuel requirements.

- An increase in secondary subarray size reduces the strut count in the structure, increases depth and stiffness, and improves the structural accuracy. A suggested reduction in subarray count from 7854 to 6932 can be accommodated by a 10-bay primary (with the secondary supported on the larger face), and a 12-bay secondary structure.

The basic objective of this study has been to determine the achievable flatness for the MPTS structure. The study shows feasibility, even for a passive structure. The real objective of the study then becomes the identification of new technology areas requiring effort to ensure the success of the MPTS antenna concept.

Attitude control of the MPTS requires definition. The effectiveness of a "direct drive" control system is not certain until the entire SPS is modeled and the interaction of the solar collector and MPTS structures have been examined. A study is proposed for preliminary design of direct drive variations and analysis of the control system performance.

Material properties are areas of uncertainty. Although the required MPTS performance can be achieved with existing composites, considerable improvement is anticipated before actual construction of the SPS begins. Materials and processes are interrelated. A new technology area of considerable scope is represented by the optimization of materials and processes for MPTS fabrication. Two study areas are suggested for continuing work. The first has as its objective, to develop an ideal graphite/resin system for MPTS application, considering the necessary processes for in-space fabrication. The second is a comprehensive materials test program for a representative pitch fiber/polyimide composite system. The latter program's

objective is to provide a materials properties data base with emphasis on statistical distribution for continuing analysis of MPTS performance.

Other areas are suggested for investigation, including laser measurement systems and reliable, space-qualified linear actuators for the active control and attitude control options. Zero tolerance joints, that can be made reliably in space are needed. Much of the new technology required for the MPTS, e.g., beam builders for large space structures, is already in development.

In short, the MPTS structure represents a reasonable extension of the present state of the art. Furthermore, the probability is high that the accuracy requirements can be achieved with a passive system.

Report No. CASD-NAS-78-011

FINAL REPORT

ACHIEVABLE FLATNESS IN A LARGE MICROWAVE POWER ANTENNA STUDY

(DRL Item No. 2)

1. INTRODUCTION

Prepared under
Contract No. NAS9-15423
for
National Aeronautics and Space Administration
LYNDON B. JOHNSON SPACE CENTER
Houston, Texas 77058

Prepared by
GENERAL DYNAMICS CONVAIR DIVISION
P.O. Box 80847
San Diego, California 92138

1

INTRODUCTION

1.1 OBJECTIVES AND SCOPE

The study objective was to determine achievable flatness for the microwave power transmission system (MPTS) antenna array. The support structure of the array achieves this flatness while interacting with the larger solar array structure, its own attitude control system, its payload of rf transmitting subsystems and antenna arrays, and the space environment.

The scope of the study is depicted in Figure 1-1, which shows the five basic tasks and their interactions:

- Task 1: Preliminary Design and Analysis of the Passive Configurations. Two configurations, A and B, were analyzed in detail and evaluated as to their net potential misalignment. Manufacturing, joint slack, assembly, alignment and environmental effects were considered. Approaches to each aspect were analyzed to minimize their contributions to distortion.

- Task 2: Environmental Effects. Orbital effects, including thermal, solar pressure and gravity gradient perturbations, were evaluated. Heating effects of the operational element, were also evaluated. Distortions were derived using finite element computer modeling techniques.

- Task 3: Figure and Pointing Control Methods. The effects of the control system, and its design integration into the structure, on structures' distortion were evaluated. Combined effects from Tasks 1, 2 and 3 provided the basis for making a baseline system recommendation.

- Task 4: Technology Plan. In the course of each study element new development requirements were identified. They were collected in Task 4 in an overall Technology Plan.

- Task 5: Material Properties. Basic material properties (such as E and CTE) were evaluated to determine their contributions to distortion.

Results of the individual tasks, and overall study activities, are presented in Chapters 2, 3, 4, 5 and 6.

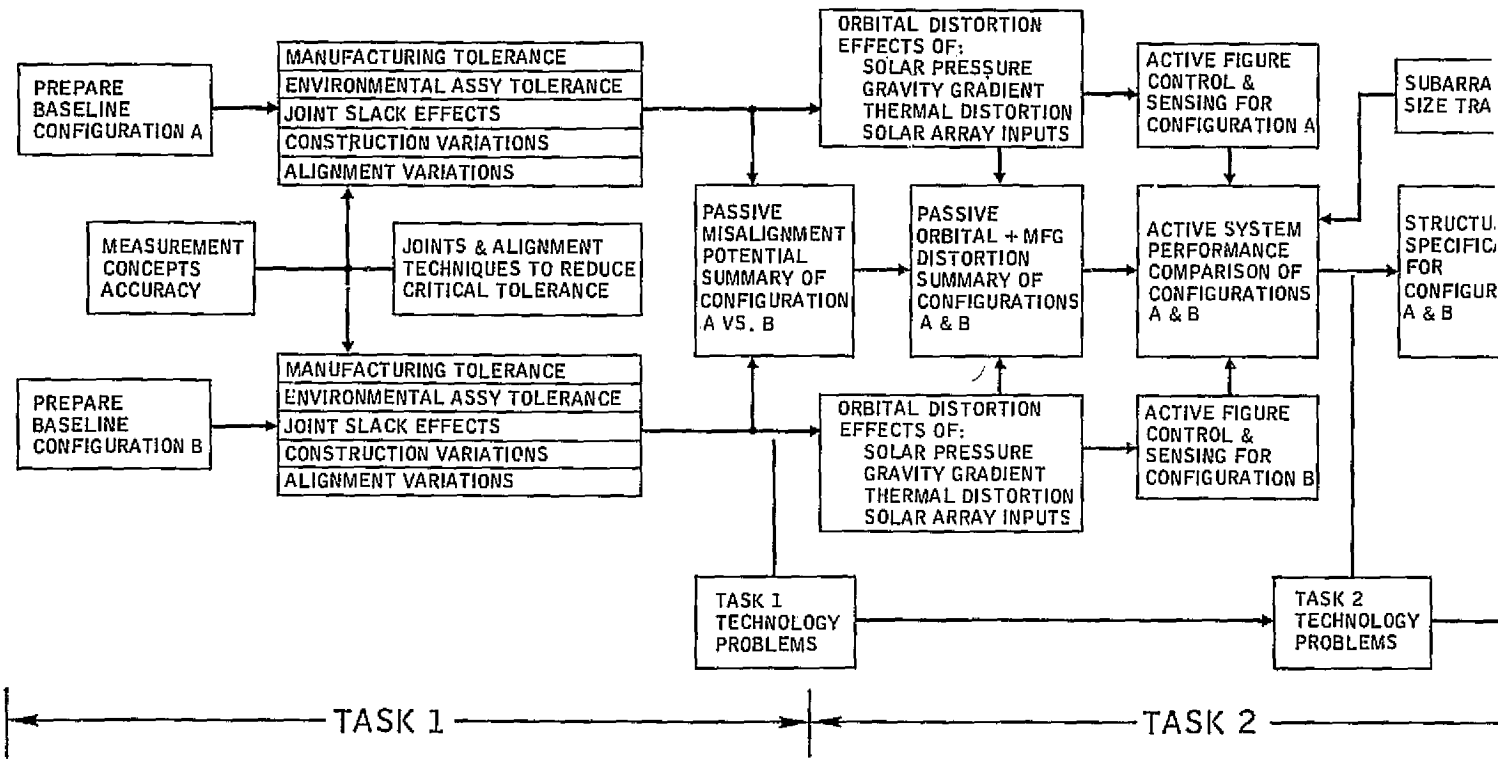

Figure 1-1. MPTS flatness study task flow.

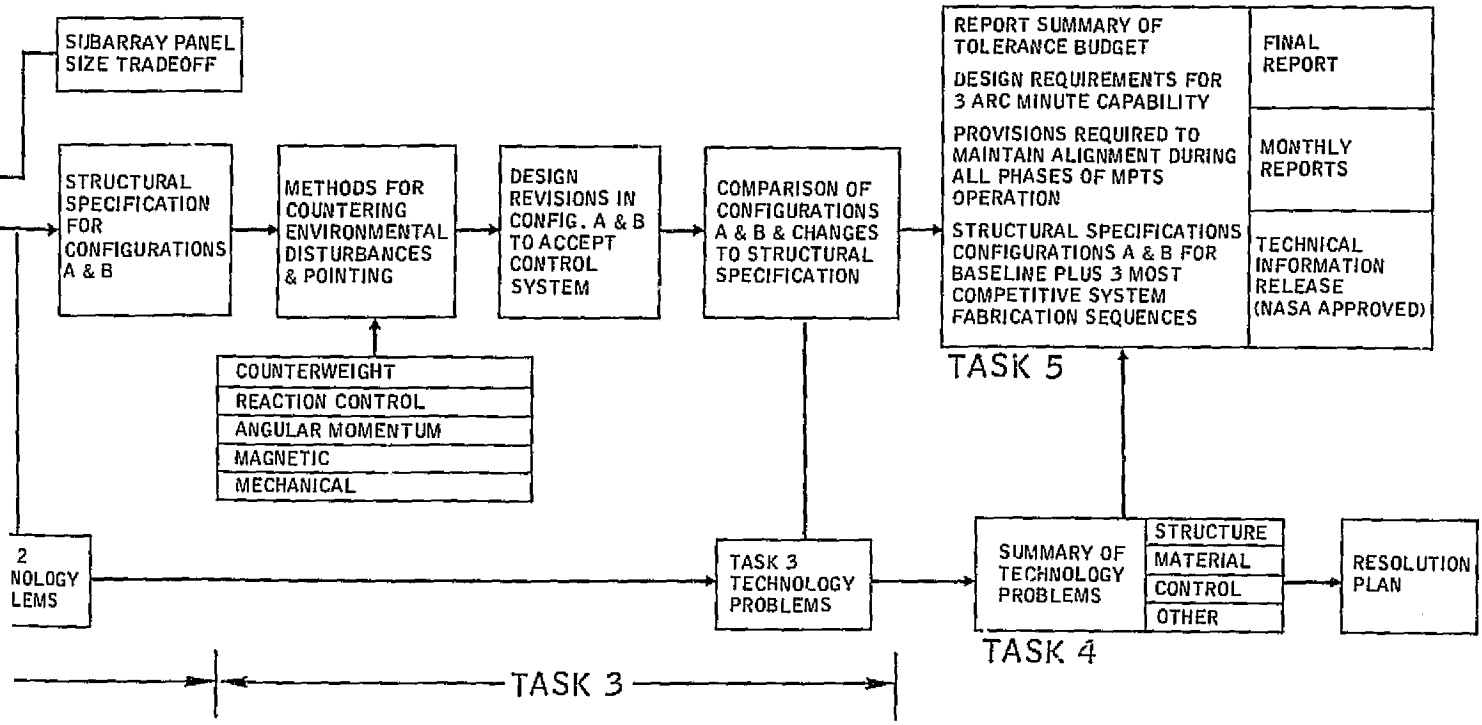

1.2 REQUIREMENTS

The basic requirement specified in the Statement of Work is 3 arc minutes of slope accuracy during all phases of operation.

Operational and environmental loadings must be accommodated within this array surface limitation. Other system requirements include:

- Operating Frequency — 2.45 GHz
- Allowable Waveguide Temperature — 485K (maximum)
- Microwave Transmission Beam Taper — 10 dB (Gaussian)
- Antenna Aperture Diameter — 1 Km
- Nonstructural Mass Distribution — Per SOW Table II
- Subarray Size (for evaluation in this study) — 10 m x 10 m
- Grid Power — 5 gigawatt
- Retrodirective/Electronic Control System Accuracy (signal originates at center of rectenna complex) — 2 arc sec

1.3 STUDY GUIDELINES

The structural configuration has evolved in previous studies conducted by JSC. The structure is based on regular tetrahedral truss elements joined to form a primary space frame. A similar structure, but using smaller truss elements forms a secondary surface which spans the primary structure, and forms a surface for support of the individual transmitting antenna subarrays.

The basic configuration is shown in Figure 1-2. Each tetrahedral element is considered a "bay" in the structure. The primary structure has 10 bays on a major diagonal. The hexagonal elements of the secondary structure are 14-bay structures. Alternatively these are designated as 5 and 7 ring structures respectively. The study did not deviate from this basic geometry except to investigate the impact of variation in subarray size.

The environment for operation is a synchronous equatorial orbit with small allowable inclination and eccentricity. The preferred orientation of the major satellite axis is perpendicular to the orbital plane. This leaves the MPTS in a relatively static position and orientation with respect to the ground receiving antenna in the earth-fixed rotating reference system.

Two configurations are considered for the secondary structure. In the first, there are 61 separate hexagonal "flats." Each can be oriented independently on its three primary structure supports. In the second approach, a continuous secondary structure is used. Throughout the study, both configurations are considered to see if either has an inherent advantage.

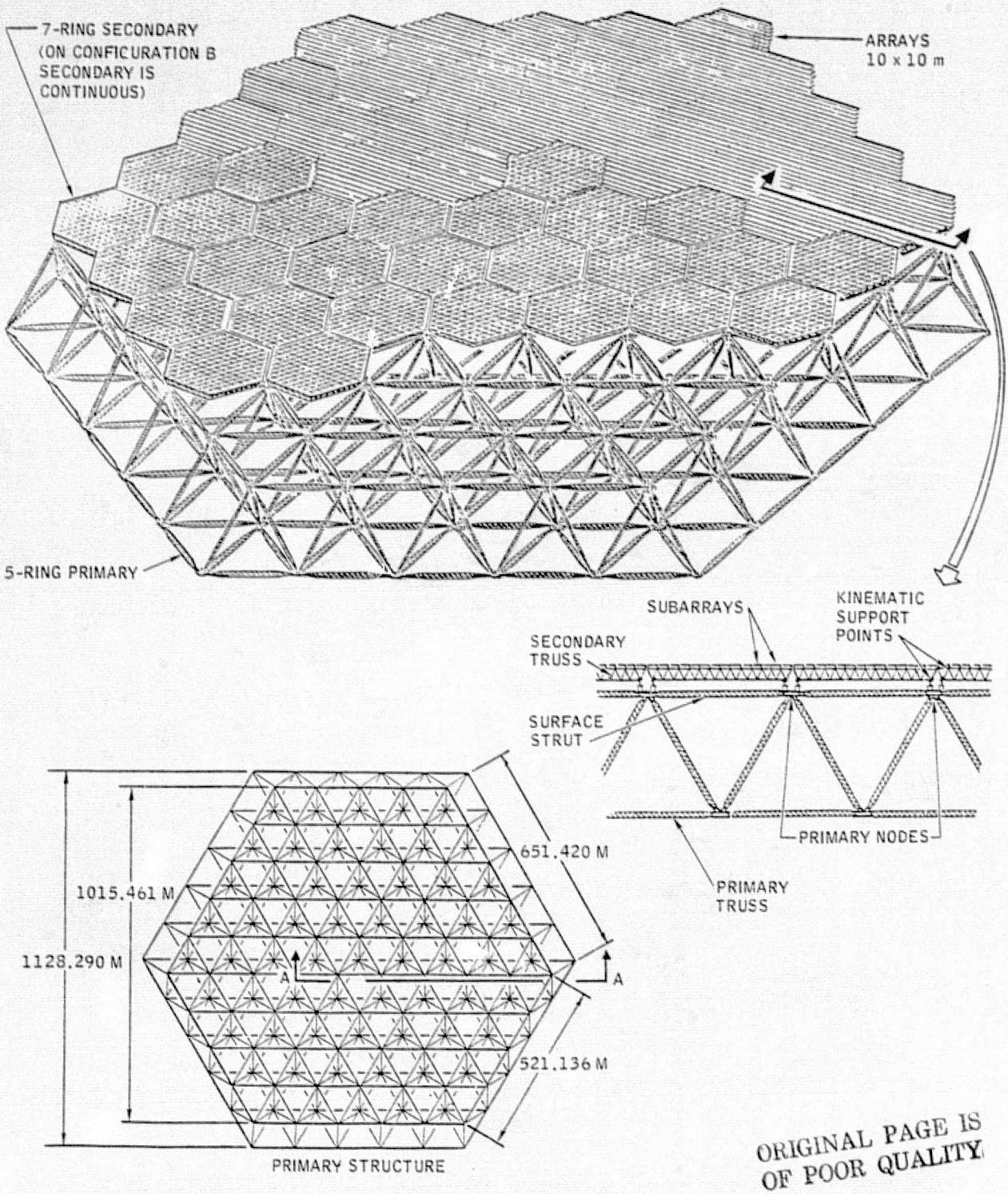

Figure 1-2. Basic configuration.

The material properties of graphite fiber reinforced epoxy composites are used in the structural analysis. A specific fiber/resin system to meet stiffness, stability and the operating temperature requirements can only be selected after considerations of availability, cost, energy balance and other factors beyond the scope of this study. The properties of GY-70/X-30 pseudoisotropic laminate have been used as representative of thermally stable composite materials.

A contributing factor in the dimensional accuracy of complex structures like 3-dimensional trusses is fit tolerance in joints. The effect, joint slop, is difficult to simulate using linear analysis techniques. The approach agreed upon in the study has been to eliminate or minimize the problem in joint design rather than try to simulate and analyze loose connections in the indeterminate truss structure. The zero slop joint implies welding, bonding, or mechanical force fit that precludes looseness.

Report No. CASD-NAS-78-011

FINAL REPORT

ACHIEVABLE FLATNESS IN A LARGE MICROWAVE POWER ANTENNA STUDY

(DRL Item No. 2)

2. TASK 1 – BASELINE CONFIGURATIONS PRELIMINARY DESIGN & ANALYSIS

Prepared under
Contract No. NAS9-15423
for
National Aeronautics and Space Administration
LYNDON B. JOHNSON SPACE CENTER
Houston, Texas 77058

Prepared by
GENERAL DYNAMICS CONVAIR DIVISION
P.O. Box 80847
San Diego, California 92138

2

TASK 1

BASELINE CONFIGURATIONS
PRELIMINARY DESIGN AND ANALYSIS

The major steps of Task 1 (Figure 2-1) were:

1. Preliminary design of the antenna structure.
2. Modeling of the primary and secondary structures.
3. Computer structural analysis of the models.
4. Postprocessing to determine slope errors, maximum deflections, maximum internal loads, and provide graphic displays of outputs.
5. Analysis and interpretation of results.

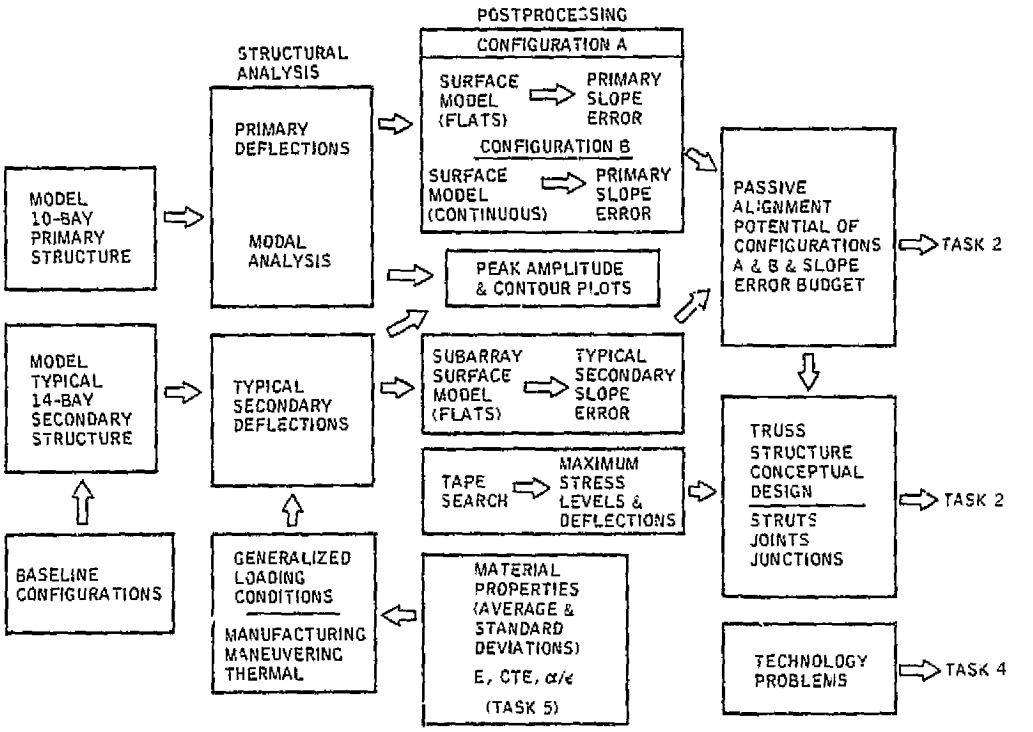

Figure 2-1. Task 1 — study task flow.

A single 10-bay primary structure was modeled for use with configurations A and B secondary structure. Its geometry was based on regular tetrahedron structural elements. In similar manner, a single 14-bay secondary structure was modeled. It represents a typical configuration A secondary structure and an equivalent area within the larger configuration B secondary structure. It is not practical to model the 80,000-strut complete configuration B on a strut-by-strut basis.

In the computer analysis, 20 loading conditions were used to simulate manufacturing tolerance and variations in temperature, coefficient of thermal expansion, and modulus of elasticity. With the secondary and nonstructural weight added, the lowest modal frequencies were determined in the primary structure. A variety of postprocessing programs were then used to translate structural deflections into slope error. Contour plots were generated of deflections and slope errors for configurations A and B. Maximum stress levels were found for input into the strut design activity and maximum deflections established requirements for actuator control range.

2.1 BASELINE CONFIGURATIONS

The baseline configurations were established by Reference 2-1 and baseline development was not included in the study tasks. There were two configurations, denoted by "A" and "B". Both A and B consisted of a two-tier construction comprised of a primary structure which provides the basic structural strength and stiffness, and a secondary structure which bridges the relatively coarse spaced primary structural joints so as to provide for mounting of the subarrays. Configuration A is characterized by a secondary structure made up of 61 individual truss sections whereas configuration B has a continuous tetrahedral structure for the secondary. Figure 2-2 shows the general arrangement for configuration A and the dimensions of the primary structure. The differences between the two configurations are depicted in Figure 2-3. Table 2-1 presents the quantity and typical lengths for the primary and secondary members. Since the secondary structure is used for providing a place to mount the subarrays rather than contribute overall strength, it has been included in the nonstructural weight baseline as shown in Table 2-2. References 2-2 and 2-3 (the Green Book and the Red Book) were used for additional interface and baseline data such as power dissipation and orbital characteristics.

For purposes of determining flatness a subarray support plane was established. The support plane is defined by the three subarray support points as indicated in Figure 2-4. As shown in the figure, each subarray is 10,746 m by 9.306 m which gives a transmission area of 100 square meters.

Reference 2-1. NAS/JSC Request for Proposal No. 9-BC73-37-7-113P.

Reference 2-2. Initial Technical, Environmental and Economic Evaluation of Space Solar Power Concepts, Volume II — Detailed Report, JSC 11568, 8-31-76.

Reference 2-3. Solar Power Satellite Concept Evaluation, Activities Report, July 1976 to June 1977, Vol. 1 — Detailed Report. JSC-12973, July 1977.

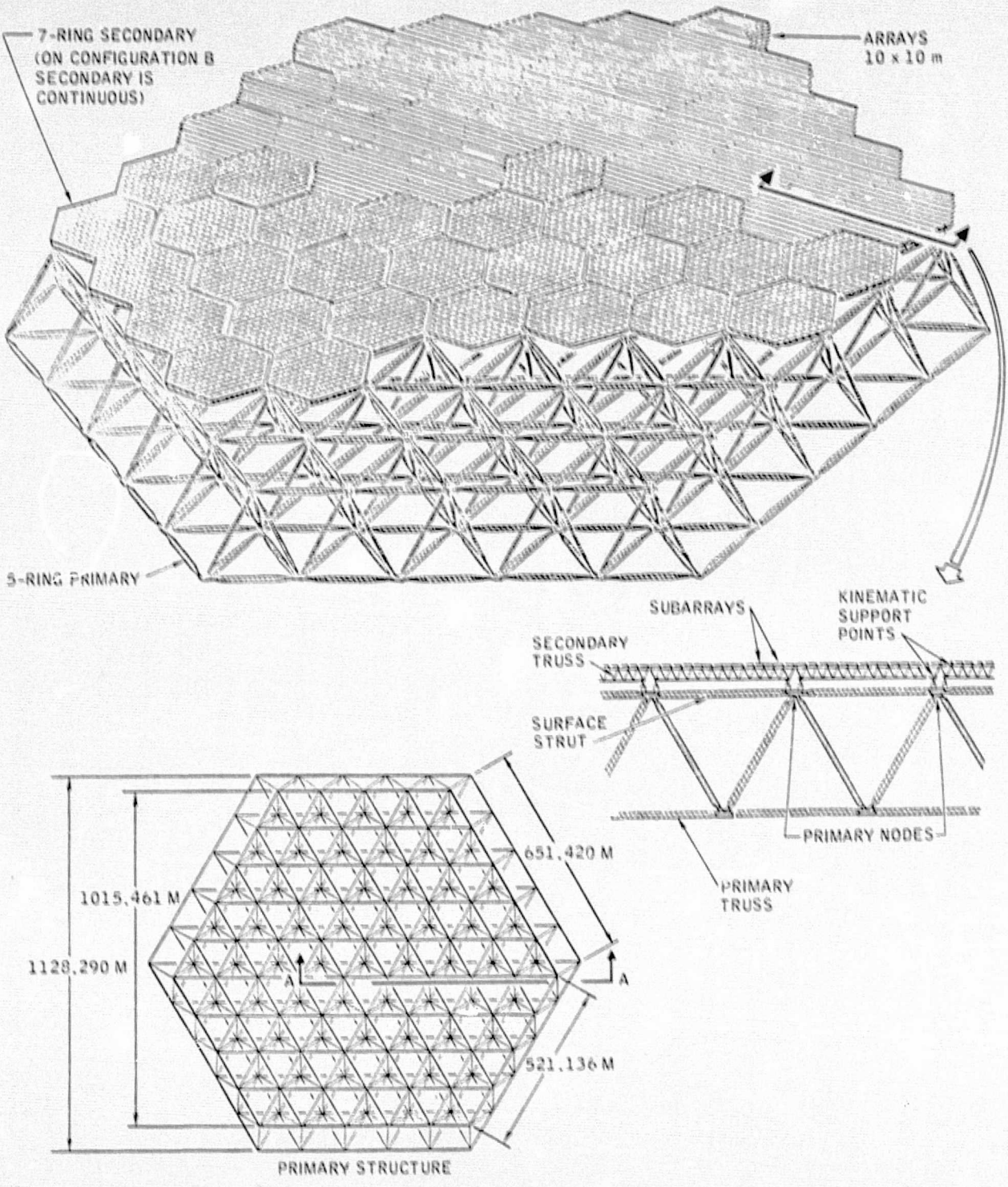

Figure 2-2. General arrangement for configuration A.

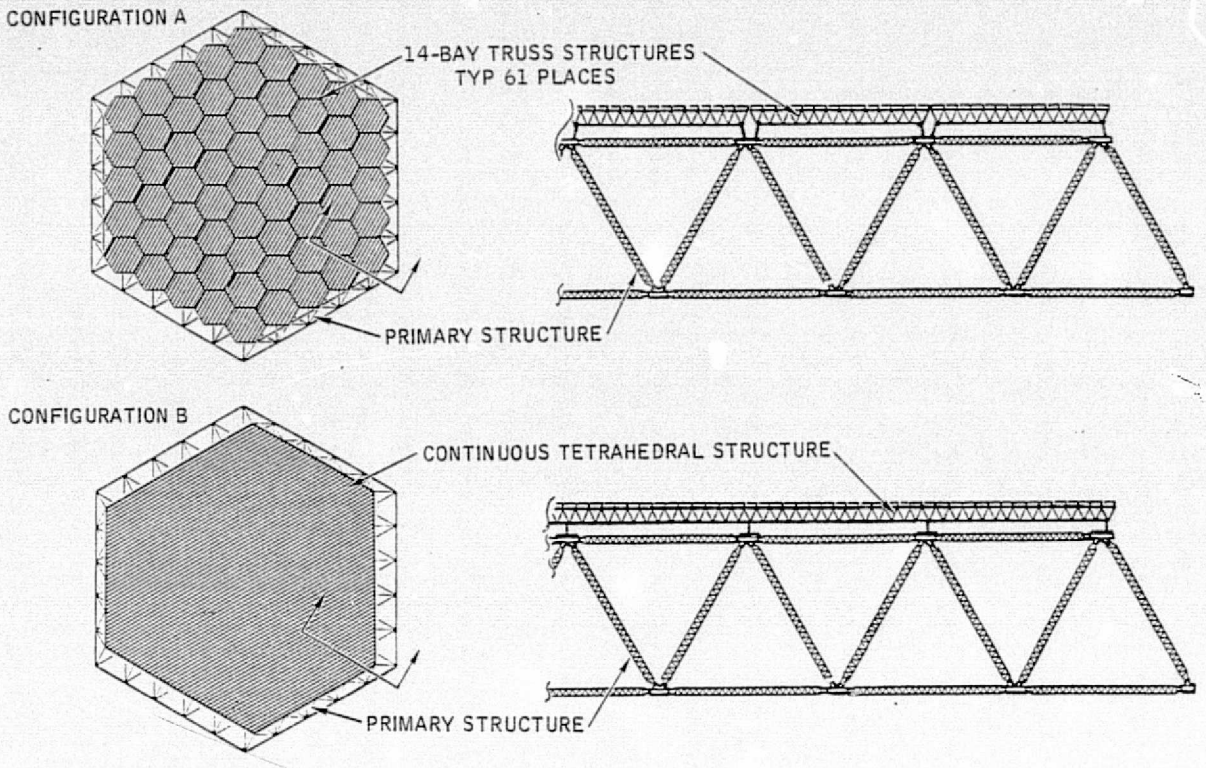

Figure 2-3. Configurations A and B.

Table 2-1. Baseline planar truss data (reproduced from Reference 2-1).

STRUCTURE	n	NUMBER OF NODES	NUMBER OF MEMBERS	TYP MEMBER LENGTH (M)	NUMBER REQUIRED
PRIMARY	5	166	660	130.284	1
CONFIGURATION A SECONDARY	7	316	1,302	10.7456	61
CONFIGURATION B SECONDARY	63	24,004	106,974	10.7456	1

n = number of hexagonal rings

number of nodes

symmetrical side = $3n(n+1)+1$

asymmetrical side = $3n^2$

total = $3n(2n+1)+1$

number of members = $3n(9n-1)$

Table 2-2. MPTS nonstructural mass distribution (reproduced from Reference 2-1).

RING NO.	MASS POINTS/ RING	RING RADIUS (METERS)	MASS (kg)	MASS/RING
1	6	60.	256,714	1,540,284
2	6	130.526	214,357	1,286,142
3	12	252.157	150,177	1,802,124
4	18	375.835	100,119	1,802,142
5	24	500.	70,596	1,694,304

*Includes secondary structure. Σ 8,124,996 kg

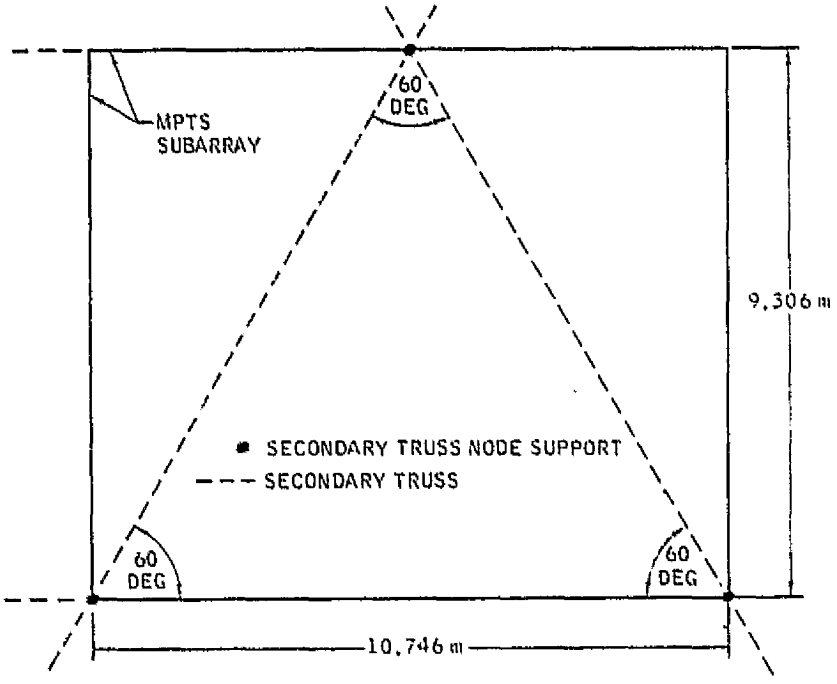

Figure 2-4. Subarray support geometry (reproduced from Reference 2-1).

2.2 BASELINE DESIGN

Our study examined the multiplicity of elements that contribute to distorting the operational flatness of the microwave power transmission system (MPTS) antenna. In determining the magnitude and relationship of the critical tolerance components in the antenna, and avoiding nontolerance related details of the system, we made some simplifying assumptions:

1. We assumed availability of elements to be assembled into the truss in GEO without concern for the packaging and boost phase problems.

2. We assume that the power system has been built and initiated our flatness study assuming a stable hub. Pogo-type motion of the hub was not considered, at this time, though there may be a problem when the entire system is evaluated.

The structural configurations used in this study are evolved from previous studies by JSC based on regular tetrahedral truss elements that are joined to form a space-frame.

In the baseline design the entire MPTS is supported at three nodes of the primary structure (see Figure 2-5). There are variations in the design depending on the location and type of pivots used, but all use the 3-point support.

2.2.1 BASELINE CONFIGURATIONS — Two baseline configurations "A" and "B" were evaluated to determine their relative merits in meeting the various structural requirements. Of primary concern was the structure's ability to maintain the slope of the subarrays within the accuracy budget.

A brief description of each structural candidate follows.

2.2.1.1 Baseline Configuration "A" — Configuration A of the RFP is shown in Figure 2-3. It is a two-tier structure consisting of one large (10-bay) primary and 61 smaller (14-bay) secondary tetrahedral trusses. The primary truss structure is made from equal length truss struts joined at 60-degree surface angles at each node to form a flat structure. The secondary truss structures are attached to the primary structure at three points as shown in Figure 2-6. The construction of the secondary structure is similar to the primary except smaller.

2.2.1.2 Baseline Configuration "B" — As requested, in configuration B the primary structure is exactly the same as described for configuration A, but the secondary structure is continuous, forming a 126-bay tetrahedral truss structure (see Figure 2-8).

The secondary structure is attached to the primary structure at only one attach point at each primary node. An advantage of this configuration is to lower the relative motion between subarrays versus the motion of the intersection of the two separate 14-bay structures in configuration A. While configuration A is a deflection oriented approach, configuration B is a load oriented system. The construction of the configuration B secondary structure would be similar to configuration A except that the outer interconnecting truss members would not be installed — instead the partially complete 14-bay hexagons would be assembled into a continuous structure.

2.2.2 DETAIL DESIGN TRADE STUDIES — During this phase of the study, a single 10-bay primary structure was modeled for use with configurations A and B secondary structure. Its geometry was based on regular tetrahedron structural elements. In a similar manner, a single 14-bay secondary structure was modeled. It represents a typical configuration A secondary structure and an equivalent area within the larger configuration B secondary structure.

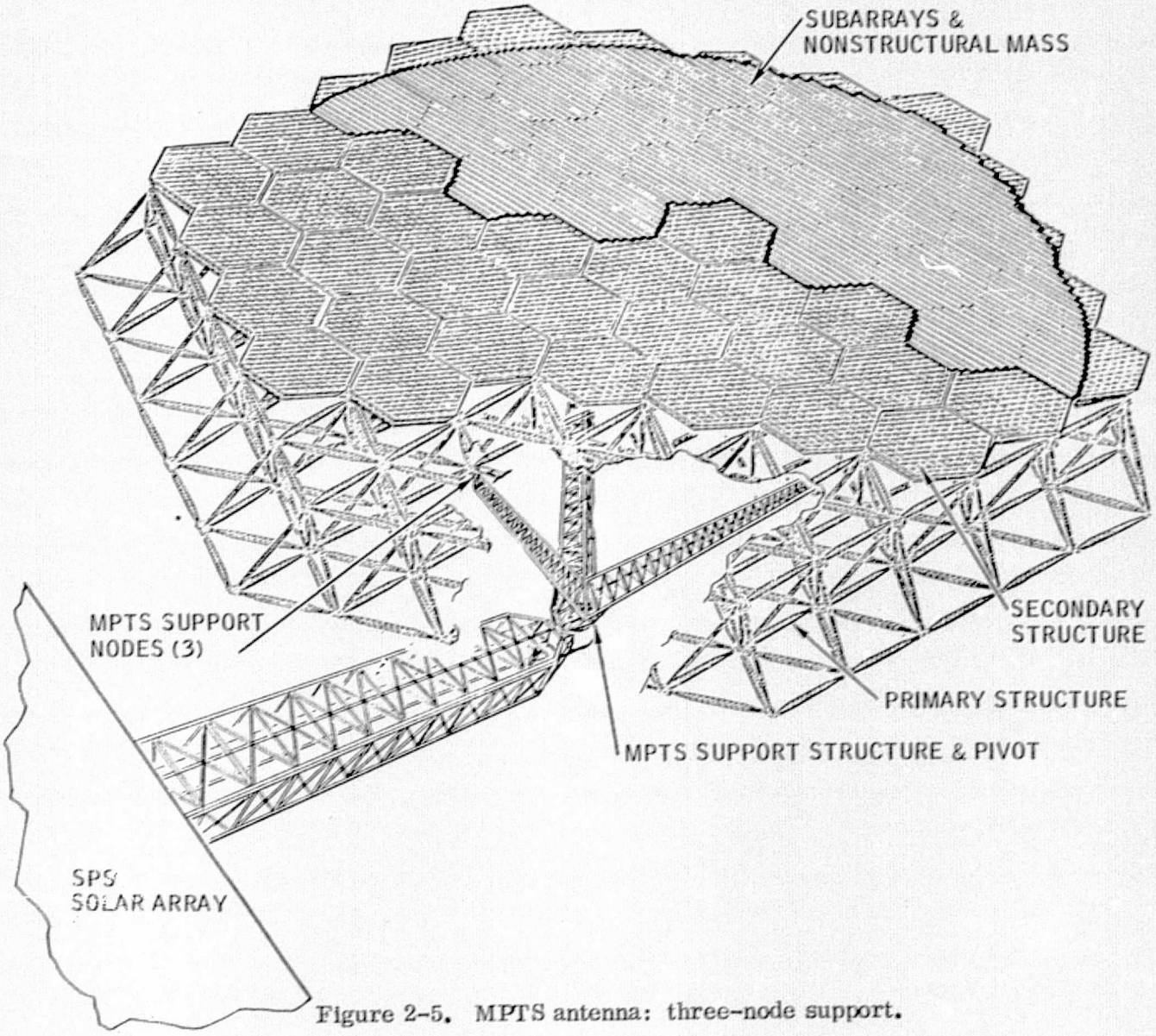

Figure 2-5. MPTS antenna: three-node support.

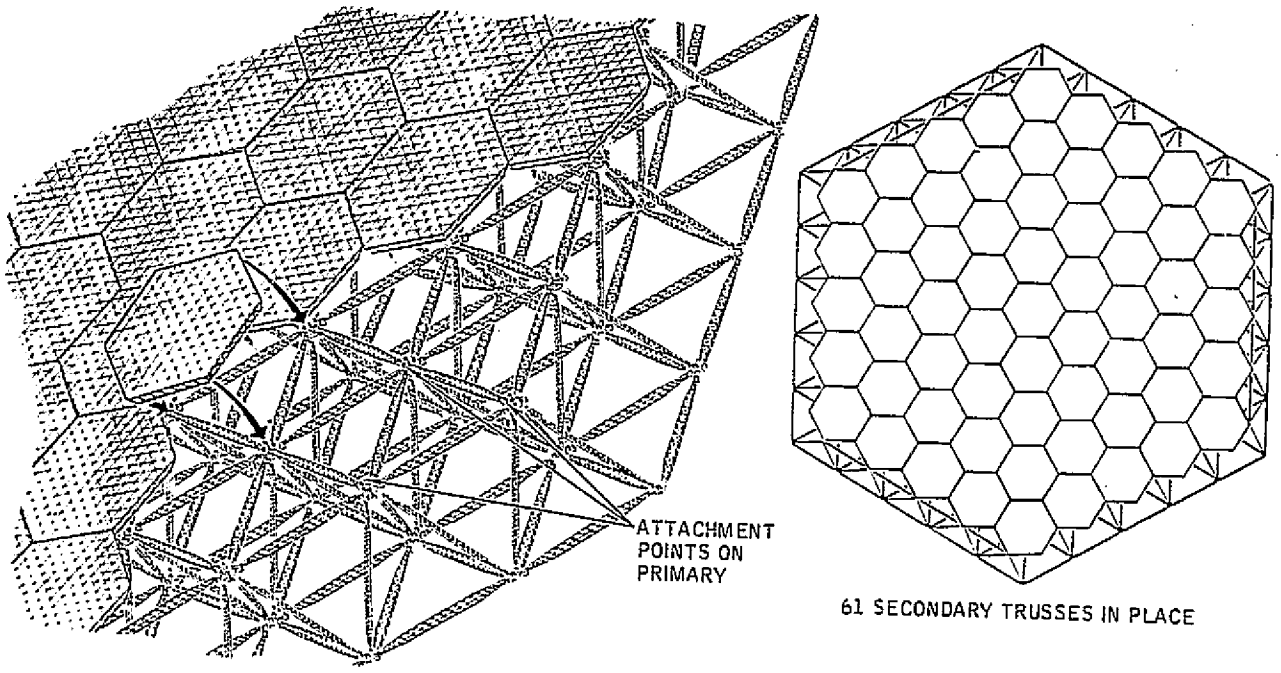

Figure 2-6. Assembly of configuration A secondary to primary.

In the computer analysis of Task 1, 20 loading conditions were used to simulate manufacturing tolerance and variations in temperature, coefficient of thermal expansion, and modulus of elasticity. In Task 2, 31 additional thermal conditions were simulated representing the synchronous orbit environment. Maximum stress levels and maximum deflections were found by postprocessing routines.

The strut and joint design activity produced information relative to quantitative data on manufacturing tolerance buildup, and joint and actuator tolerances.

These studies are covered more fully in the following sections.

2.2.2.1 Mechanical Loads — For the geo-truss in the assembled configuration the principal loading conditions will be thermal and inertia loads due to rigid body acceleration and rotations. The SOLID SAP finite element model of the geo-truss was used for the analysis. The load conditions are based on a geo-synchronous equatorial orbit. The acceleration loading conditions are shown in Table 2-3.

Six unit rigid body accelerations and rotations were analyzed for resulting surface distortions and internal loads. The actual accelerations due to rigid body torques and forces were computed showing that only the rotation about the x-x axis was significant. To find the resulting maximum strut loads the actual acceleration α_{xx} was multiplied by the unit conditions shown below. Again the actual strut loads are very small. The general conclusion that can be reached is that the loads in the struts of the geo-truss in the assembly configuration are very small.

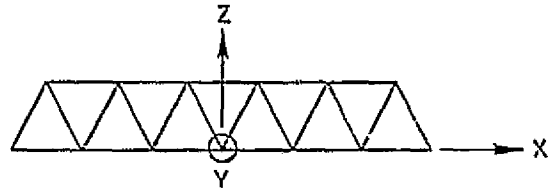

RESULTS OF MAX-MIN SEARCH OF 660 STRUTS

LOAD CONDITION	TENSION	COMPRESSION
1.0-G – X	14.02×10^6 N	-14.02×10^6 N
1.0-G – Y	8.57×10^6 N	-16.19×10^6 N
1.0-G – Z	9.41×10^6 N	-13.25×10^6 N
1.0 RAD/SEC^2 – XX	56.76×10^6 N	-113.51×10^6 N
1.0 RAD/SEC^2 – YY	98.30×10^6 N	-98.30×10^6 N
1.0 RAD/SEC^2 – ZZ	65.83×10^6 N	-65.83×10^6 N

Table 2-3. Primary structure acceleration loads.

LOADING	α_{XX} (RAD/SEC^2)	α_{YY} (RAD/SEC^2)	α_{ZZ} (RAD/SEC^2)
DYNAMIC UNBALANCE	-1.333×10^{-9}	0.0	0.0
GRAVITY GRADIENT	-3.999×10^{-9}	0.0	0.0
TRACKING	$-0.187 \times 10^{-9} \sin\omega t$	$0.2647 \times 10^{-9} \cos\omega t$	0.0
TOTAL	-5.519×10^{-9}	0.2647×10^{-9}	0.0

The worst case loading condition of -5.519×10^{-9} rad/sec^2 on the x axis, leads to an insignificant compression load in a strut of:

$$P_{C_{max}} = (-113.51 \times 10^6 \text{ N/rad/sec}^2) \times (-5.519 \times 10^{-9} \text{ rad/sec}^2)$$
$$= 6.3 \text{ N } (1.4 \text{ lb})$$

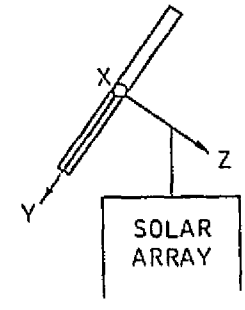

The 31 thermal cases analyzed in Task 2 gave temperature histories for each strut of the primary structure. We computed a temperature dependent random CTE for each strut based on the measured CTE distribution for GY-70/X-30. The temperatures and CTE values were input for each of 660 struts, and the structural deformations calculated. A postprocessing routine was used to find the worst case stress levels. Table 2-4 shows the results.

Table 2-4. Primary structure thermal stress levels.

Strut	38	172	568
Type	Back	Back	Front
Connects	1014	1061	2037
Nodes	1022	1070	2046
Load Condition (End of Shadow)	17	17	17
Temperature (F)	-287.5	-290.0	-262.7
CTE ($\mu\epsilon$/F)	0.036	-0.298	0.153
CTE x T ($\mu\epsilon$)	-12.9	107.3	-51.0
Length (in.)	5130.9	5130.9	51.30.9
Area (sq.in.)	0.88	0.88	0.88
E (msi)	15.7	15.7	15.7
Force (lb)	-722.7	839.6	625.6
Strain (in.)	-0.384	0.428	-0.019

Strut number 38 had the largest force — 3215N (-722.7 lb). The strut itself has a low thermal coefficient, and the worst case load is the result of distortion in adjacent structure more than the result of thermal contraction of strut.

Strut number 172 is unique in that it has the largest magnitude for CTE. It is relatively unconstrained in the randomly modeled structure and displays a large change in length, but a relatively low stress level.

The third case is strut 568. It is unique in that it has a relatively large CTE and is almost fully constrained in the model. It has high force applied and almost no elongation.

These represent conditions that were computed for one random arrangement of CTE. Other arrangements would lead to larger thermal loads. One other consideration is that E can be correlated with CTE. This could further increase the loads.

During the assembly of the struts into the geo-truss, a configuration is reached that becomes rigid before all the struts are in place. At this point in the assembly, if the additional struts are not of perfect length or there is not a length adjustment mechanism, or thermal distortion has occurred, (see Figure 2-7), the remaining struts must be either stretched or shortened to fit, thus inducing loads into the structure. This analysis was done by a computer finite element solution as described earlier by introducing random length errors into the 660 struts of the primary.

$$\text{Load } P = \frac{AE\delta}{\ell} = \frac{\text{Area x Modulus x Axial Distortion}}{\text{Length}}$$

$$\text{For Primary Baseline: } P = \frac{(2.277 \times 10^{-4})\ (107.5 \times 10^{9})\delta}{103.3} = 1.88 \times 10^{5}\delta \text{ N}(1080\delta \text{ Lb})$$

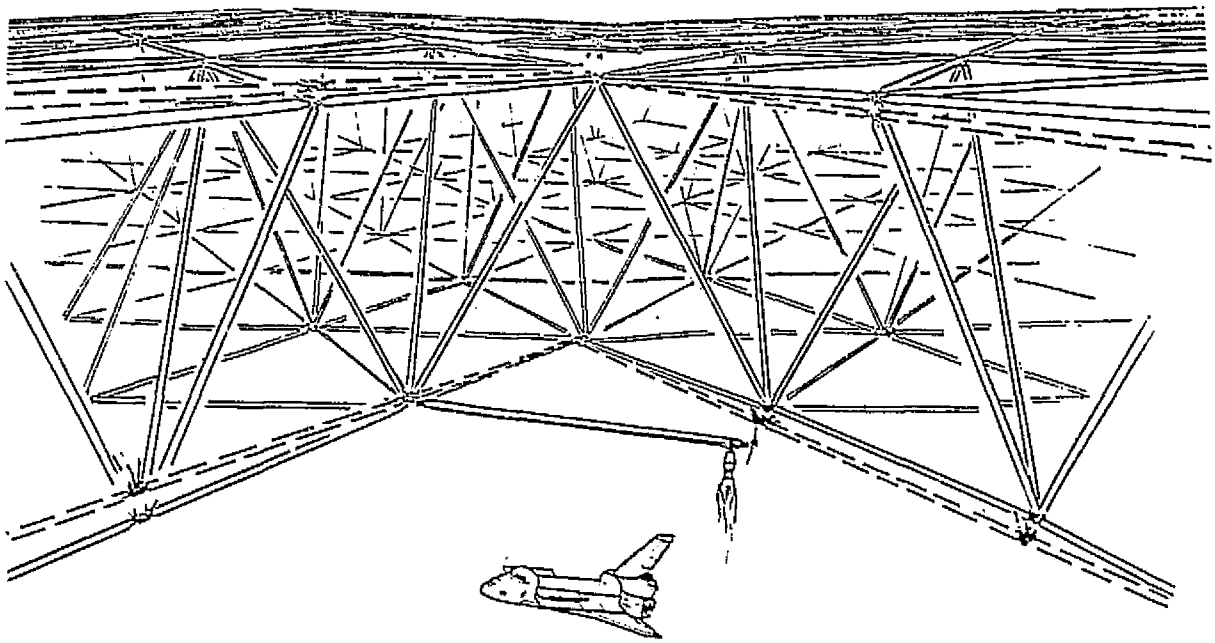

Figure 2-7. Thermal distortion of partially assembled structure.

Another approach is to consider only an individual strut. The load versus deflection curve for the baseline primary strut is plotted (see Figure 2-8), to show the maximum allowable axial shortening using linear theory and the induced strut load due to the anticipated length error in a strut. The actual loads in the fully assembled geotruss would be lower due to the elasticity of the adjoining struts which were determined in the finite element solution.

2.2.2.2 Structural Material — The selection of the proper materials of construction for the MPTS is dependent upon specified design criteria. For an orbital structure this, in general, requires a thermally stable structure of low weight and mass moment of inertia, coupled with high stiffness, strength and natural frequency. The interaction of these factors and their influence on spacecraft performance are shown in Figure 2-9.

Key factors in the selection of the MPTS material of construction are a low coefficient of expansion (α) and specific weight (ρ), and high Youngs modulus (E) and ultimate tensile strength F_{tu}. These factors vary from material to material and typical values, of candidate materials, are presented in Table 2-5. The structural efficiency of a material is commonly measured by means of a merit function number obtained by dividing the material's modulus by the product of its specific weight and expansion coefficient. Thus, a high merit function characterizes a material with high stiffness and low weight, that is thermally stable. The merit functions of various materials have been computed and are compared in Figure 2-10. An examination of this chart will show that, for our application, graphite/epoxy is far superior to the other materials (by a factor of ten when in a unidirectional configuration; and, by a factor of eight in an isotropic form).

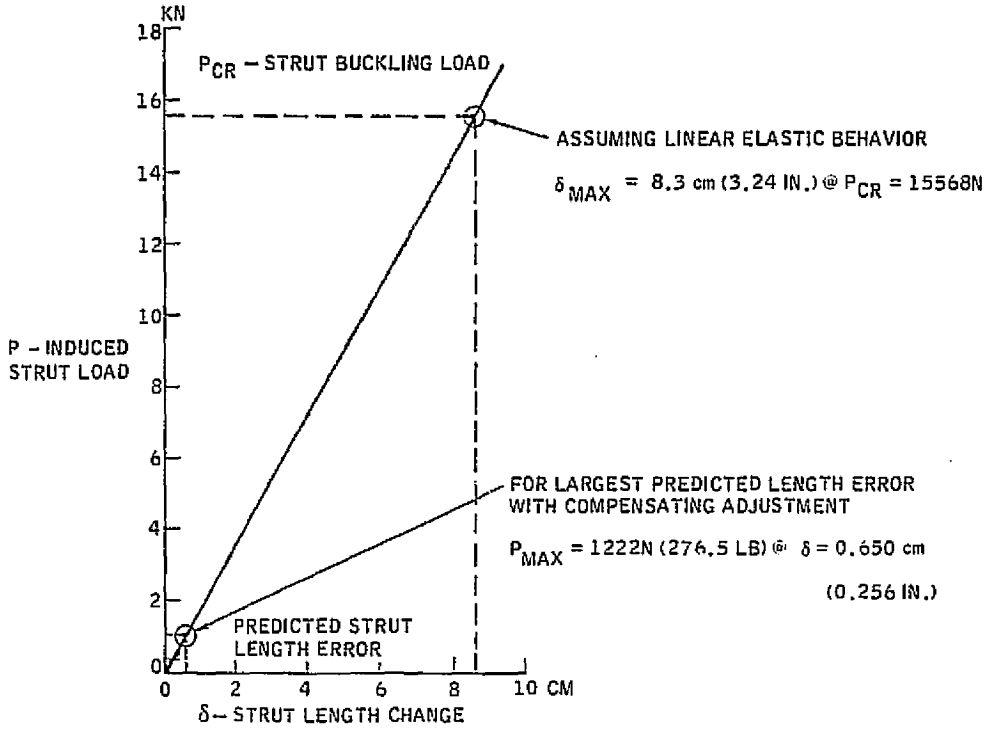

Figure 2-8. Built-in loads in primary.

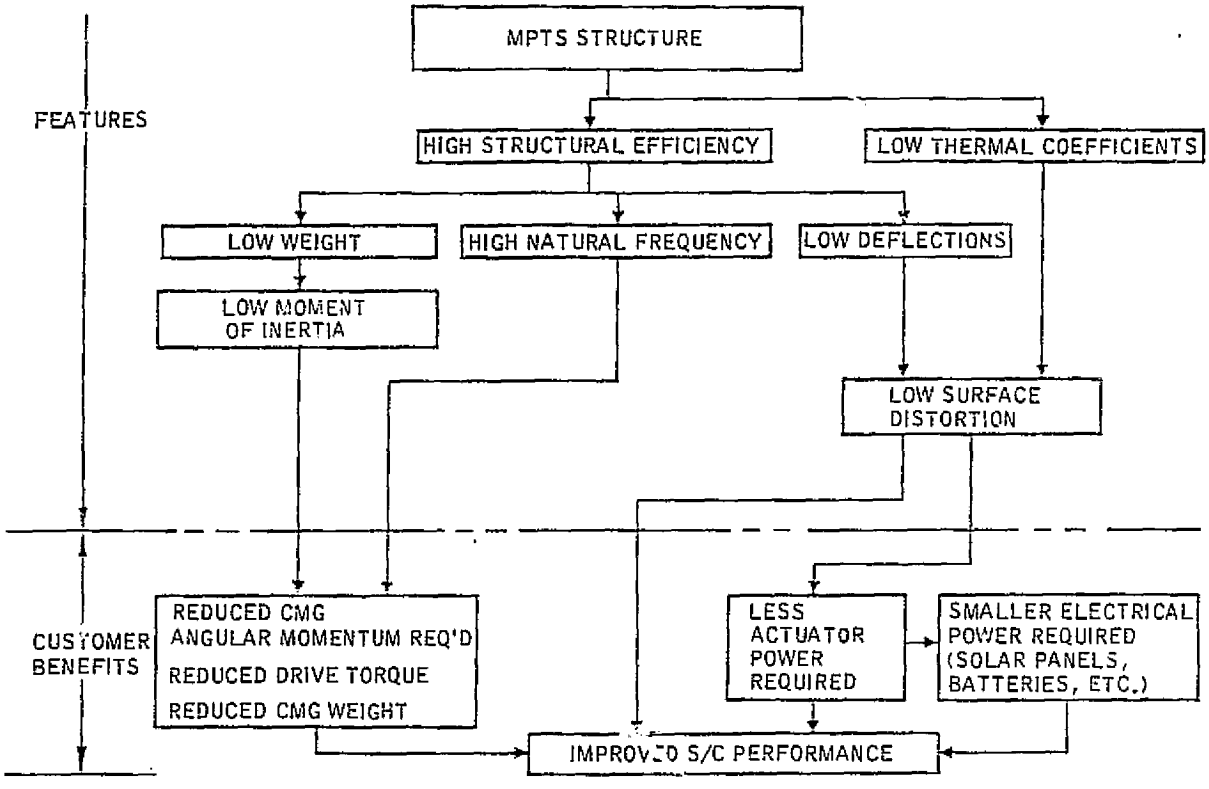

Figure 2-9. MPTS design optimization.

Table 2-5. Material comparison.

MATERIAL	$\rho \frac{LB}{IN.^3}$	$E \frac{LB}{IN.^2} \times 10^6$	$F_{t_u} \frac{LB}{IN.^2} \times 10^3$	$\alpha \frac{IN.}{IN.^\circ F} \times 10^{-6}$
G/E (UNI)	0.064	40.0	80	-0.51
G/E (ISO)	0.064	15.0	28	-0.03
MAGNESIUM	0.064	6.5	15	14.00
BERYLLIUM	0.066	43.5	69	6.00
BORON AL.	0.096	18.0	76	3.20
ALUMINUM	0.100	10.0	77	13.00
TITANIUM	0.160	16.0	134	5.30
CRES. STEEL	0.286	29.0	30	8.80
INVAR	0.295	21.0	32	0.70

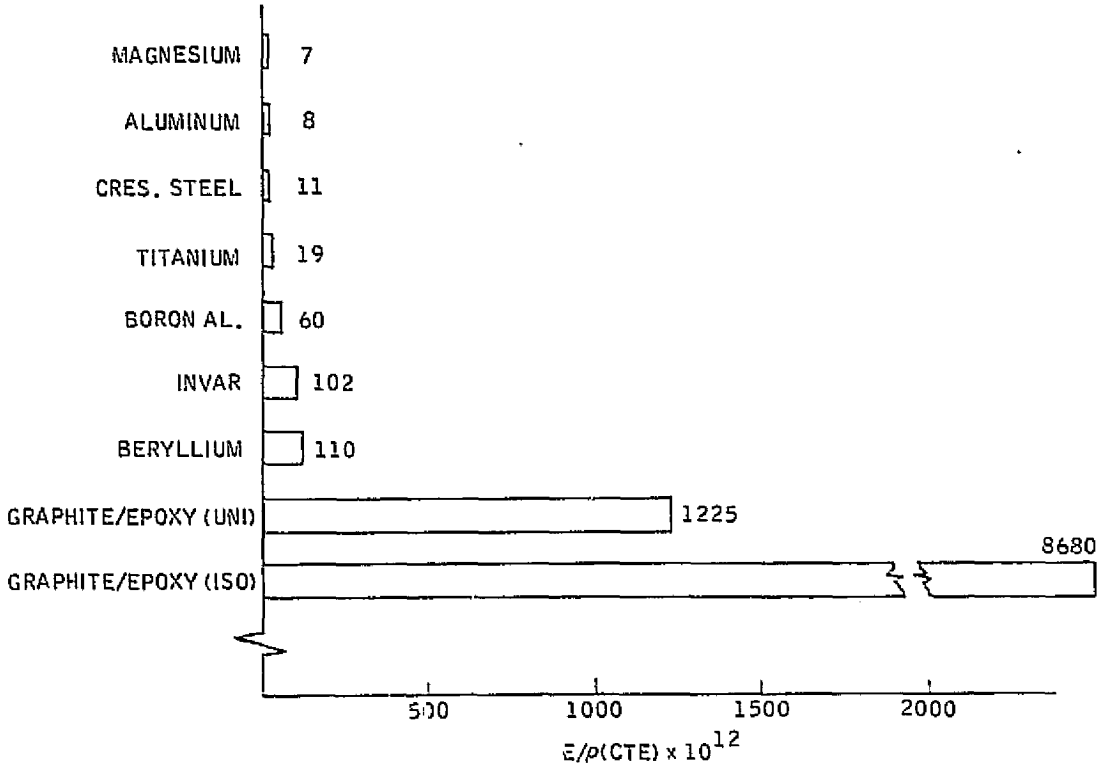

Figure 2-10. Merit function comparison.

The strength to weight ratio of the candidate materials has also been computed. This data is illustrated in Figure 2-11 and unidirectional graphite/epoxy again is shown to be the better material. The strength to weight ratio of isotropic graphite/epoxy is about twice that of magnesium and about half that of aluminum. The MPTS structure is stiffness, not strength, critical. In those areas where high loading is encountered, such as support points, adequate strength may be achieved by adding unidirectional material as required.

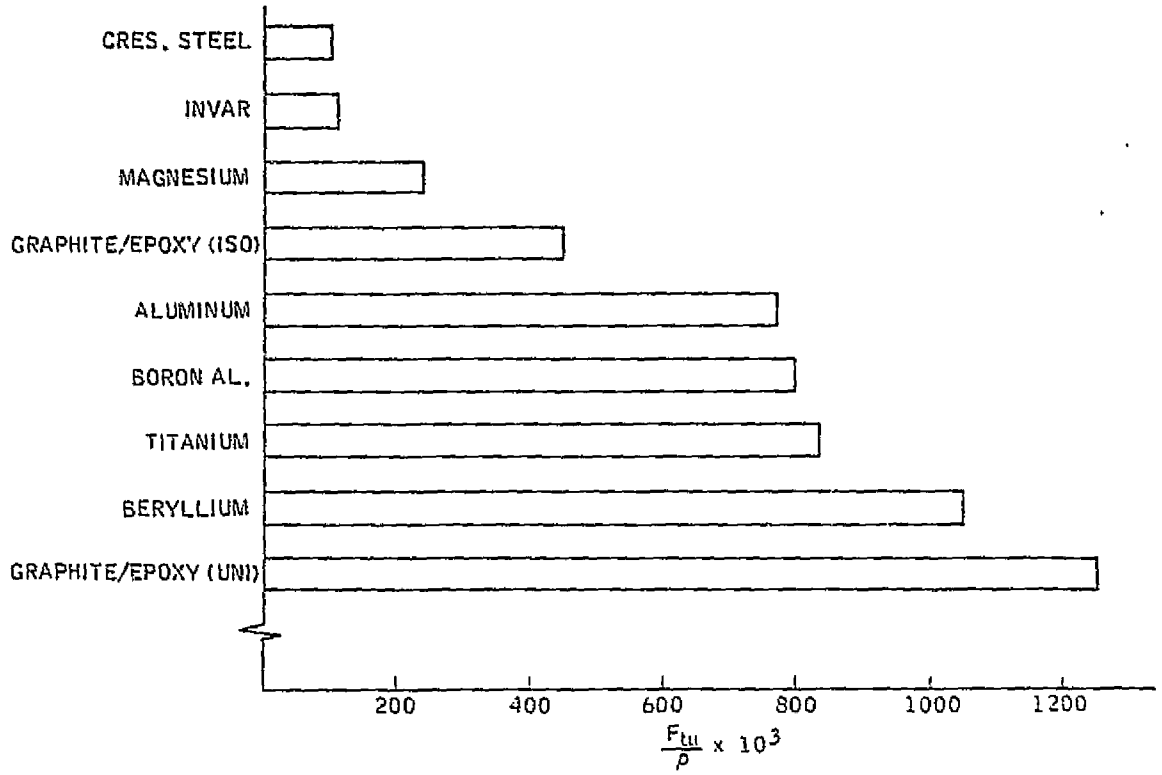

Figure 2-11. Strength to weight comparison.

The performance characteristics of the structure under consideration in this study are such that the use of graphite/resin composite materials is essential. The above merit function comparisons, shown in Figures 2-10 and 2-11, substantiate its selection over conventional aerospace materials.

Convair selected Fiberite's GY-70/X-30 from the available graphite composites as a representative composite system for structural applications in this study. GY-70/X-30 provides extremely high stiffness properties and exhibits excellent thermal dimensional stability when arranged in a cross-plied laminate. A merit function comparison of candidate fiber systems is shown in Figure 2-12, and substantiates the selection of GY-70 over the other fiber materials.

2.2.2.3 Strut Configuration Trades — The primary consideration in the beams of the antenna geo-truss structure are stiffness and light weight. For these reasons a tubular, triangular beam was selected as a baseline configuration. Various configurations of diagonal struts were considered — two of these are shown in Figure 2-13. The single stiffened diagonal or barber pole configuration showed promise because of fewer diagonal struts and fewer joints. Internally the beam has balanced forces, but it was found that at each end there was an unbalanced torque. Since the torque on each end was in opposite directions, the result was a twisting moment on the beam. This was discovered by deflecting a computer model.

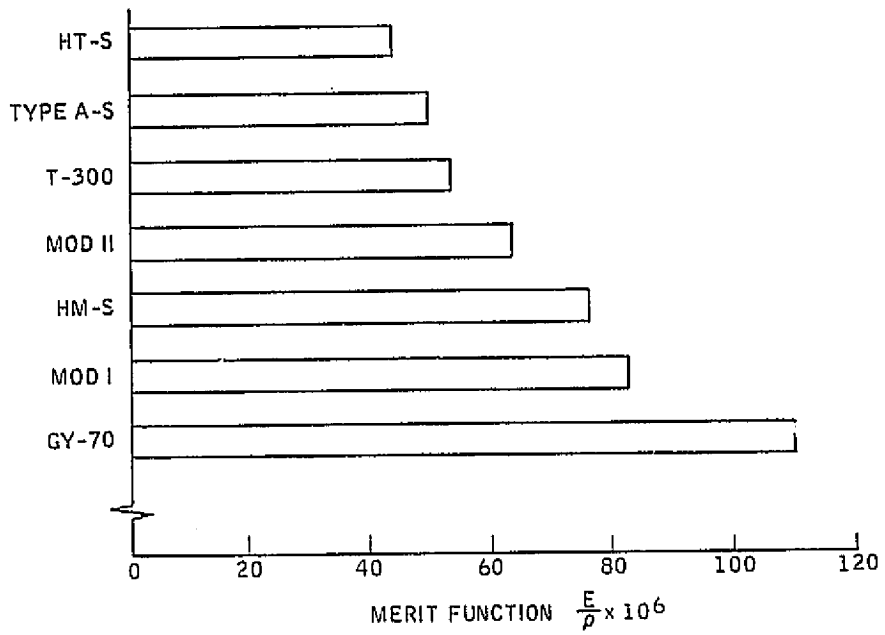

Figure 2-12. Fiber system merit function.

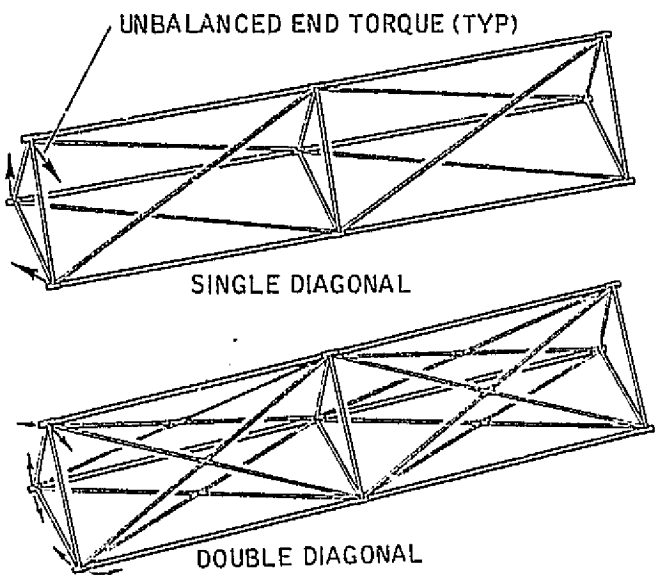

Figure 2-13. Basic beam configuration.

The double stiffened diagonal configuration (also see Figure 2-13) was more complicated since it required the second diagonal plus a joint at the intersection of the two diagonals. The diagonals were sized using only one diagonal and then adding the other redundantly. This resulted in a heavier structure than actually needed. We are presently working on a redundant solution to size these diagonals. This configuration does not require pretensioning.

A double cord diagonal configuration is less complicated in that the diagonal to apex tube intersection is less difficult and there is no joint required at the cord diagonal intersections. The beam configuration is totally balanced and readily analyzed. Some pretensioning of the cords would be required since the coefficient of thermal expansion of the cords would not match that of the apex tubes.

In sizing the beams of the tetra-truss, it was noted that the basic geometry varied little regardless of the beam configuration chosen. The light loading on the beam usually resulted in minimum gages and cap tube diameters ranging from about 2 to 3 inches. The post diameters were smaller and the diagonal diameters larger, but they still held to minimum gages and varied little in diameter. Bay lengths and beam heights also showed reasonable consistency. This indicates that general size, configuration and weight are reasonably predictable even without a completely defined design. The largest unknown would be in the inefficient structure such as joints and connections.

The sizing shown in Table 2-6 is for a double-cord diagonal beam configuration.

Table 2-6. Basic beam geometry (double cord diagonal).

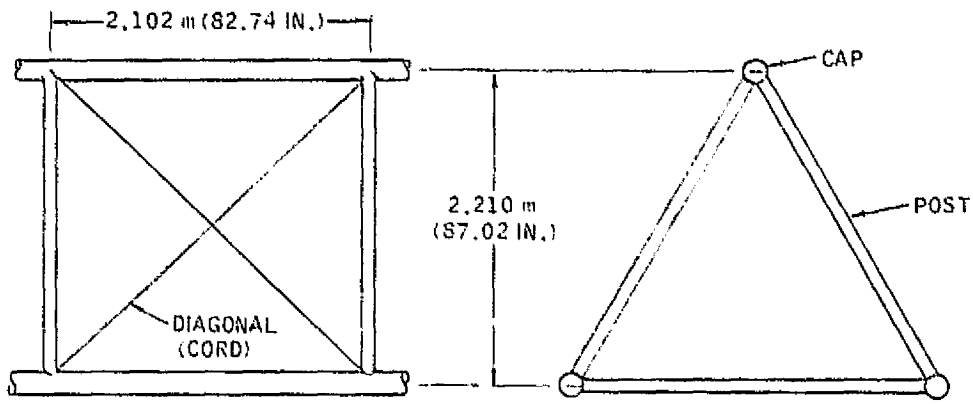

ITEM	LENGTH		DIAMETER		AREA	
	METERS	INCHES	METERS	INCHES	SQ.METERS	SQ.INCHES
CAP	2.102	(82.74)	0.0476	(1.874)	7.590×10^{-5}	(0.1177)
POST	2.552	(100.48)	0.0286	(1.124)	4.555×10^{-5}	(0.0706)
DIAGONAL	2.722	(107.20)	0.0036	(0.142)	1.0238×10^{-5}	(0.01587)

2.2.2.3.1 Tetra-Truss Beam Intersections — In considering methods of connecting the beams of the tetra-truss, various methods were considered. Some tapered the beams down to a single point and others left the beam constant and allowed the individual members of the beam to intersect. The resulting figure in this second method was named a space polygon (see Figure 2-14). This space polygon proved to be a very interesting and promising design concept.

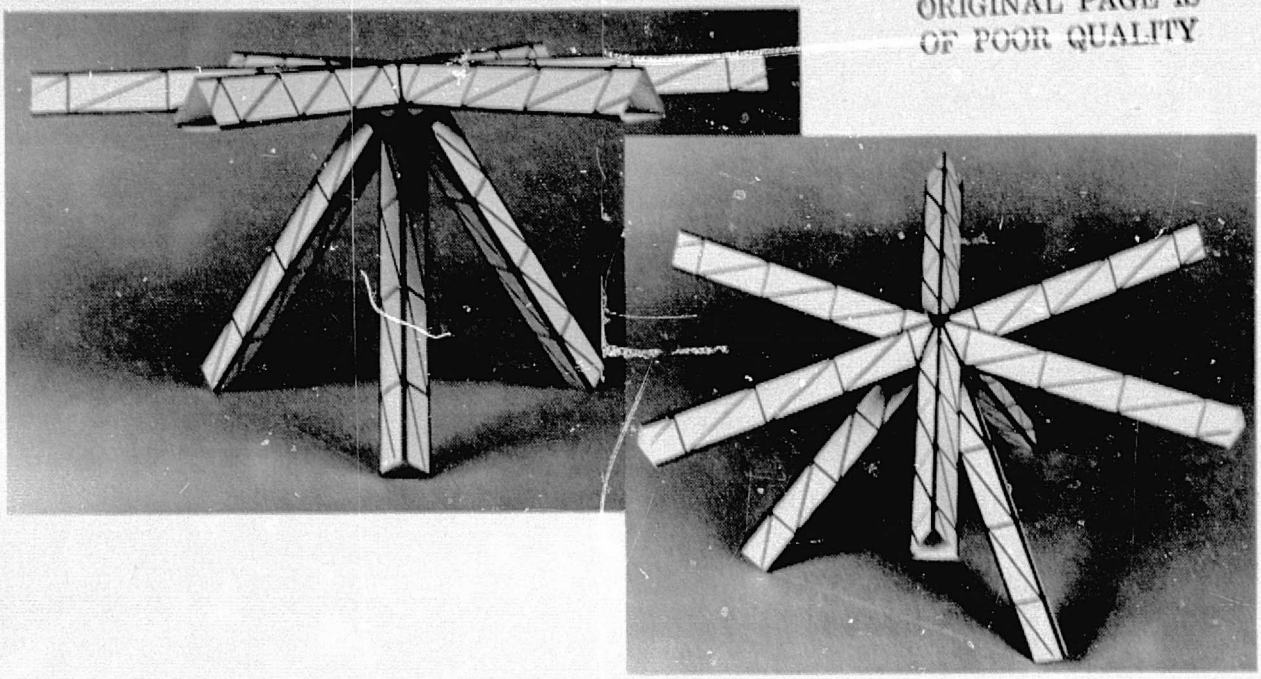

Figure 2-14. Tetra-truss beam intersections.

The space polygon allowed the space beam, the basic building block of the tetrahedral primary structure, to be standardized.

This standardization took on two very important aspects: 1) the beam could be made the same throughout its length without tapering, thus standardizing the individual members, joints, etc. in each bay of the beam; and 2) the beam length was also standardized by using a common length and method of joining to the space polygon at the intersections in a square beam end. All beams in the upper and lower decks of the tetrahedral structure are identical in this manner. This also standardized the major assembly of the beams to the central hub or spider.

An attempt was also made to standardize the diagonal beams joining the upper and lower decks of the tetrahedral structure and also make them common in size, length and connections to those in the upper and lower decks. The designs presented hereafter achieved these design goals, making it possible to completely standardize the beams throughout the structure.

2.2.2.3.2 Space Polygons — The design of the tetra-truss beam intersection was found to divide into two parts: 1) the intersection of the six beams of the upper and lower decks, and 2) the attachment of the three diagonal beams to this intersection to form a complete polygon.

The intersection of the six beams was achieved by placing all beams with one apex up and two down and then allowing these beams to come together to form a natural geometric shape much like that of a roof on a house. As the upper single six apexes come together they form a single point and as the lower two flat side apexes come together

they form a hexagon with each side of the hexagon equal in length to one side of the triangular beam (see Figure 2-15).

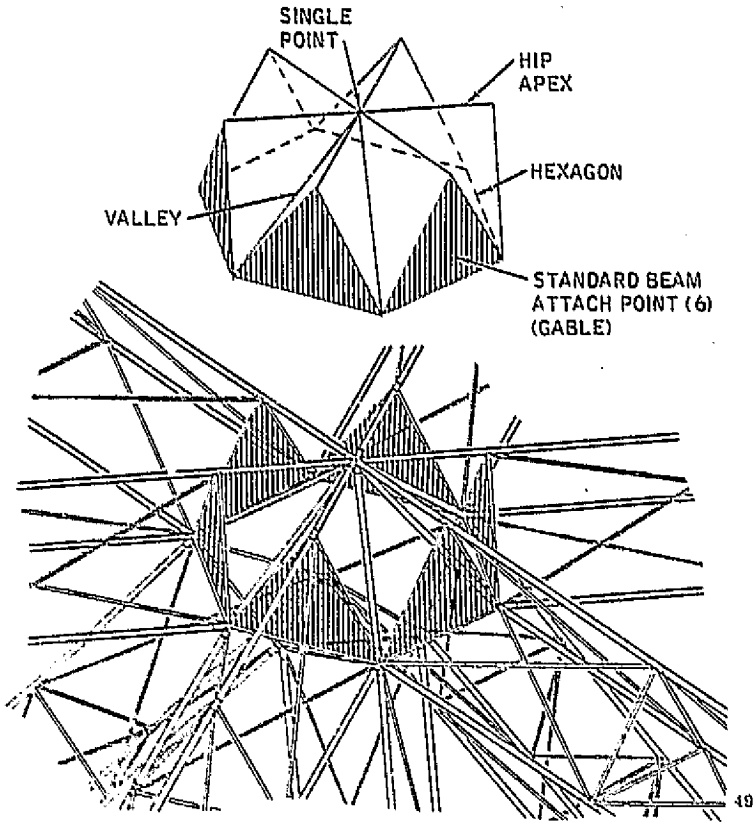

- STANDARD INTERSECTION USED ON BOTH UPPER & LOWER DECKS
- BEAMS INTERSECT WITHOUT CHANGING CROSS SECTION
- RESULTING INTERSECTION RESEMBLES ROOF WITH SIX GABLES
- STANDARD LENGTH & SQUARE END BEAMS USED THROUGHOUT

Figure 2-15. Standard deck beam intersection (upper portion of space polygon).

Struts were placed in the resulting shape to define the hips, valleys and square attaching places (gables) for each beam, thus making a figure to resemble a roof with six gables.

This shape was used as the upper portion of the space polygon design.

The lower portion of the space polygon presented a design challenge in that when one apex of the beam was placed up one polygon resulted at the upper deck and a different one at the lower deck. If the centroids of the beams all coincided, the ends of the beam did not attach at natural intersections of the upper portion of the polygon at either deck. Allowing a slight shift in centroid intersection resulted in a very natural and simplified lower portion of the polygon at the upper deck.

This concept allowed the utilization of existing intersection points on the hexagon to connect to the upper apexes of the diagonal beams. As the lower two flat side apexes come together they form an equilateral triangle. With the addition of three struts to connect each corner of the equilateral triangle to the three remaining corners of the

hexagon a very sturdy and simple lower portion of the upper polygon resulted (see Figure 2-16).

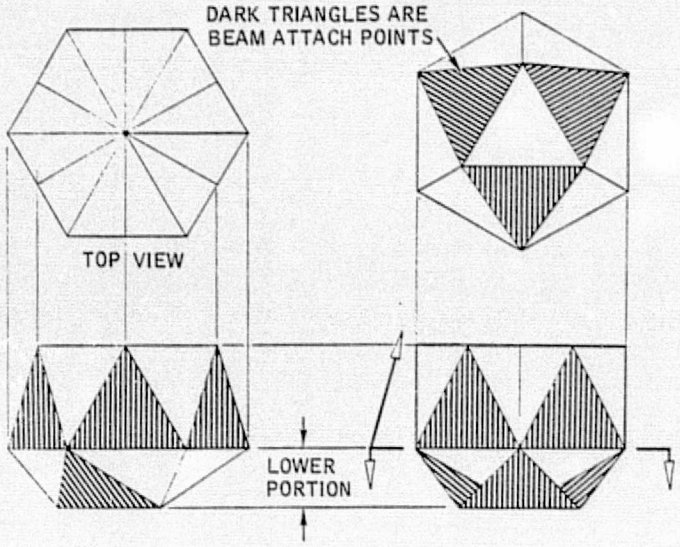

Figure 2-16. Upper spider space polygon.

Using the standardized length beams from the upper and loser deck, the three upper apexes of the diagonal beams are brought together at the lower deck to form the completed tetrahedron.

With the apexes still up on the three diagonal struts and utilizing the standardized beam length, the three apexes come together at a point above the intersection of the six lower deck beams (see Figure 2-17). The lower two flat side apexes form an unequal sided hexagon when these struts are added to connect their outer corners together. Three sides are equal in length to the length of the side of the beam and the

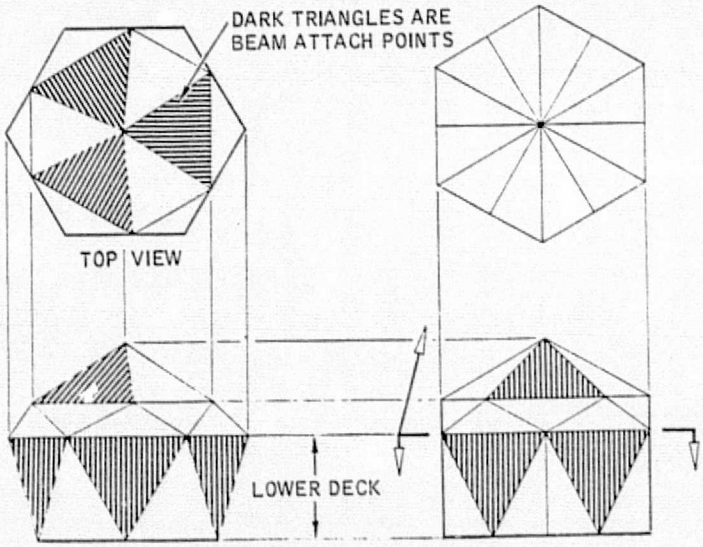

Figure 2-17. Lower spider space polygon.

other three are shorter. The corners of this unbalanced hexagon fall on the sides of the hexagon of the upper portion of the polygon (turned upside down here but unchanged).

If these corners connected directly to the regular hexagon there would be no vertical support and an additional six vertical struts would need to be added for support of these points. Also the centroids of the diagonal beams greatly miss that of the deck beams. This concept was not used or shown.

The lower deck was then lowered to a point where the centroids of the diagonals nearly coincided with those of the deck beams. This separated the regular hexagon and the unbalanced hexagon enough for struts to be added to connect the apexes of the two hexagons.

The addition of these 12 struts completed the lower space polygon, making it a rigid structure but different from the upper.

The three additional struts in the upper and 15 additional struts in the lower polygon resulted in a total of 18 additional struts for this design.

2.2.2.3.3 Common Space Polygon — In this design it was assumed that the diagonal beams could be rotated to a position where the ends of all three of the apexes of each diagonal would fall on the surface of a sphere. This was found to be true.

The standard length of beam from the upper and lower decks was used and the centroids of the diagonals passed exactly through the intersection of the deck beam centroids. This then made a theoretically perfect tetrahedral and used the standard beams.

None of the diagonal beam apex ends however fell on existing intersection points of the upper part of the space polygon. It was therefore necessary to add 18 struts per polygon to support the ends of these beams.

Both the upper and lower space polygons would be the same configuration for this design (see Figure 2-18).

The common spider design concept was modeled on the computer. This allowed us to check the structure for continuity and also rotate it to better visualize it (see Figure 2-19).

The six upper deck beams were held fixed and loads applied to the diagonal beams to test the stability of the space polygon spider. It was found to be stable.

2.2.2.3.4 Comparison of Candidate Strut Configurations — There are several potential configurations for the strut members of the MPTS geo-truss structure. Three representative configurations were compared: the triangular cross section with tubular caps, the cylindrical cross section with geodetic arrangement of solid rods, and the triangular cross section with open caps based on the SCAFEDS concept developed by Convair for JSC under Contract No. NAS9-15310 (see Figure 2-20).

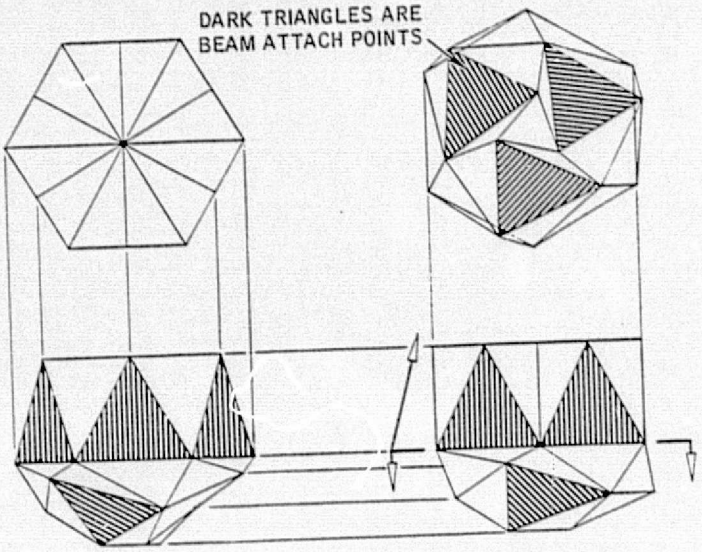

Figure 2-18. Common space polygon.

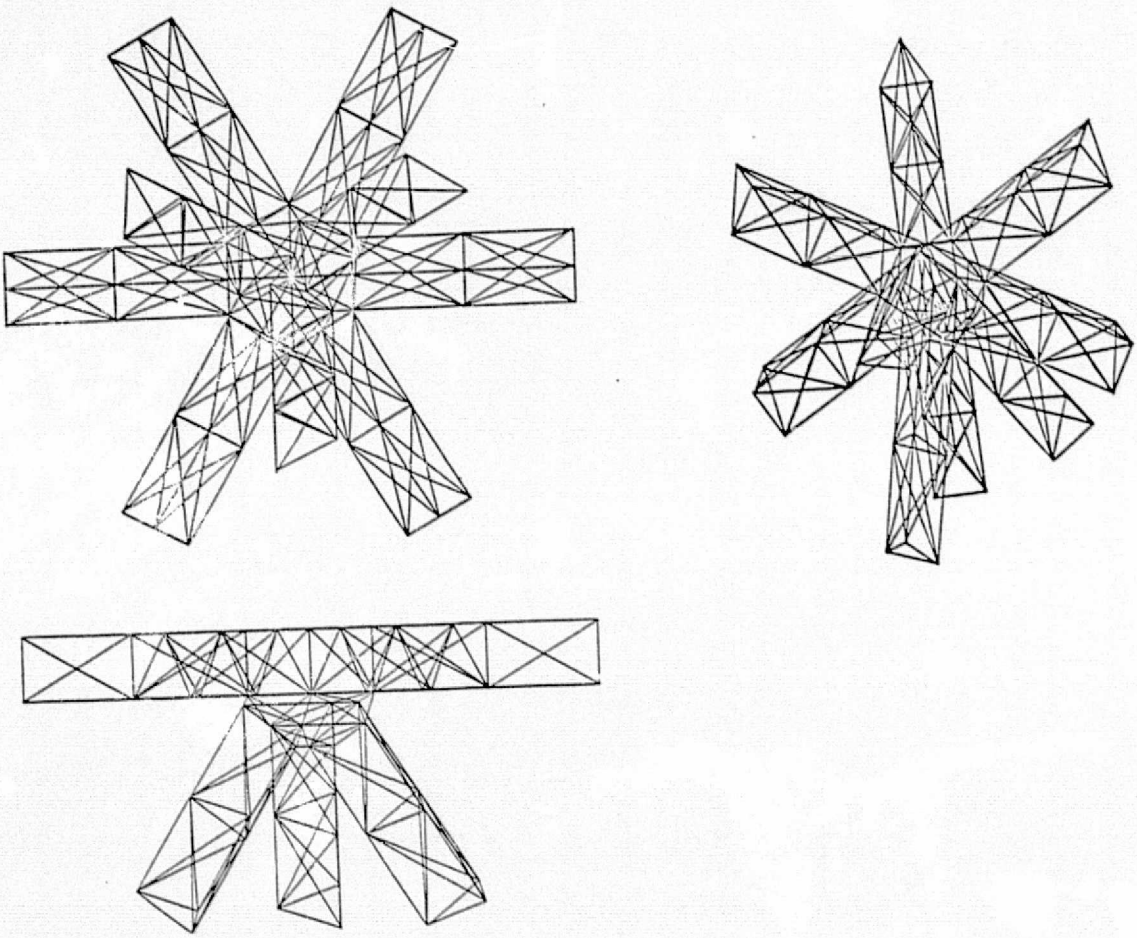

Figure 2-19. Computer model of common spider polygon.

TRIANGULAR CROSS SECTION
TUBULAR CAPS

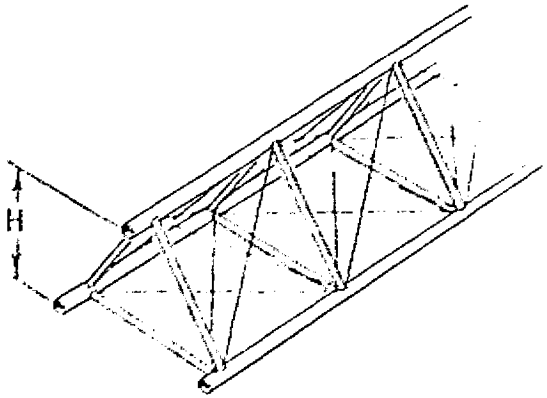

P_{CR} = 15568N (3500 LB)
L = 130.3 m (5129.92 IN.)
E = 107.5 GN/m^2 (15.7 MSI)
H = 2.210 m (87.02 IN.)
$\overline{W}$ = 0.843 KG/m (0.566 LB/FT)
α_{AVG} = -0.0378 μ/m/C (-0.021 μIN./IN./F)

CYLINDRICAL CROSS SECTION
GEODETIC SOLID RODS

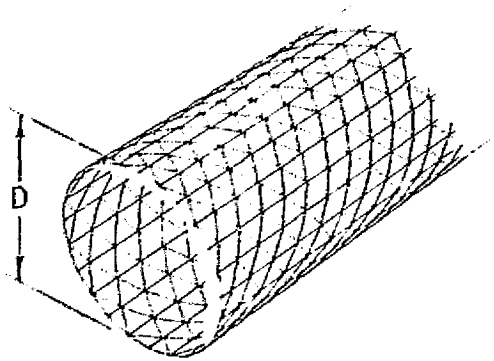

P_{CR} = 15568N (3500 LB)
L = 130.3 m (5129.92 IN.)
E = 296.5 GN/m^2 (43.3 MSI)
D = 2.023 m (79.64 IN.)
$\overline{W}$ = 0.938 KG/m (0.648 LB/FT)
α_{AVG} = 0.0

TRIANGULAR CROSS SECTION
OPEN CAPS (SCAFE)

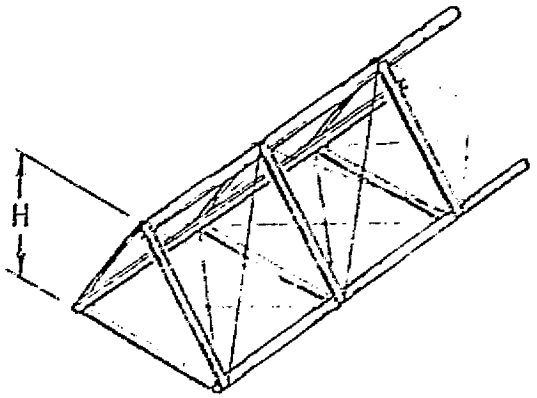

P_{CR} = 15568N (3500 LB)
L = 130.3 m (5129.92 IN.)
E = 141.75 GN/m^2 (20.7 MSI)
H = 1.860 m (73.20 IN.)
$\overline{W}$ = 1.104 KG/m (0.742 LB/FT)
α_{AVG} = -0.380 μ/m/C (-0.211 μIN./IN./F)

Figure 2-20. Comparison of candidate strut configurations.

The column critical load of 15568N (3500 lb) was used as the comparison load for convenience and was not intended to be the design final load. The 3500-lb load is the critical column load for the open cap triangular cross section strut. This load was derived by using the SCAFE cap cross section torsional buckling allowable and optimizing the overall geometry of the strut as a column rather than as a beam in bending which was the case for the SCAFE concept. The other two concepts were then sized for the same load. The geodetic strut was sized using the code developed by NASA personnel.

Even though the 3500-lb load was used for sizing, the weight of the struts of the primary structure does not change the results and conclusions of the flatness study. The structural weight of the antenna is small compared to the nonstructural weight. Therefore sizing a strut to an exact design load is not critical.

The factors that do affect flatness are variations of strut properties, particularly cross section area, and the material properties of elastic modulus and coefficient of thermal expansion. These factors led to the choice of the triangular cross section with tubular caps as the baseline because it can be analyzed using the properties of the well characterized GY-70/X-30 material and can be programmed for optimization easily.

At the time of actual design of the strut, one factor will be the practical limit on how small the members of the strut can be. The loads in the struts in the assembled geotruss are very low — on the order of 1000 or 2000N. But if these loads were used to size the strut as a column, the struts would be very fragile and may be difficult to build and assemble. So there might be other factors that will ultimately design the strut size other than actual operating loads.

To substantiate the argument that the results of the flatness are independent of the absolute values of a strut design, a series of weight calculations using struts with varying axial load capabilities were made using the General Dynamics/Convair Tetrahedral Truss Structure Synthesis (GDTTSS) program. The program has several strut configurations available as options, but for this study the triangular cross section with tubular caps was used.

Figure 2-21 is a plot of total strut weight which includes an estimate for end fitting weight versus column critical load. This curve shows that there is a significant effect on strut weight for changes in design load. Although this curve was generated using the triangular cross section with tubular caps, the curve is representative of other strut configurations.

The effect of varying the strut weight as a function of critical column load on the overall mass of the antenna is shown in Figure 2-22. For this curve the mass of the secondary structure and nonstructural mass are held constant.

These two curves show that the total antenna weight varies from 8.549×10^6 KG (18.85×10^6 lb) to 8.618×10^6 KG (19.00×10^6 lb) or a 0.81% increase for a change in design strut column load from 1000N (225 lb) to 17928N (4000 lb). The conclusion

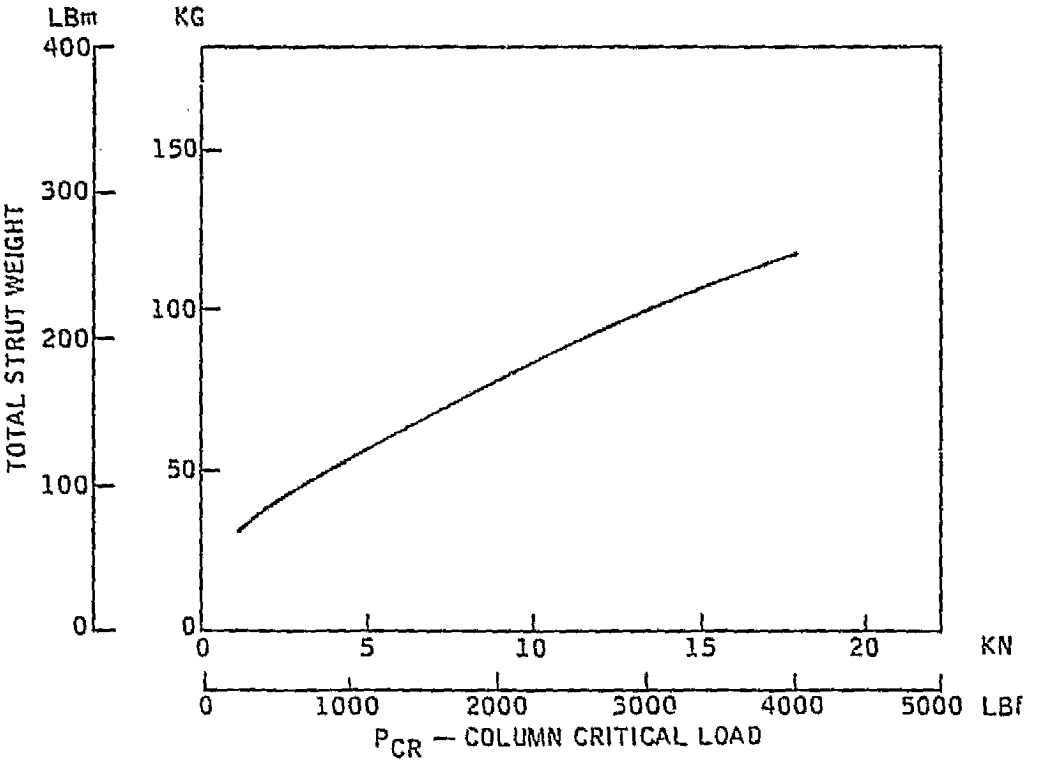

Figure 2-21. Primary strut weight versus column critical load.

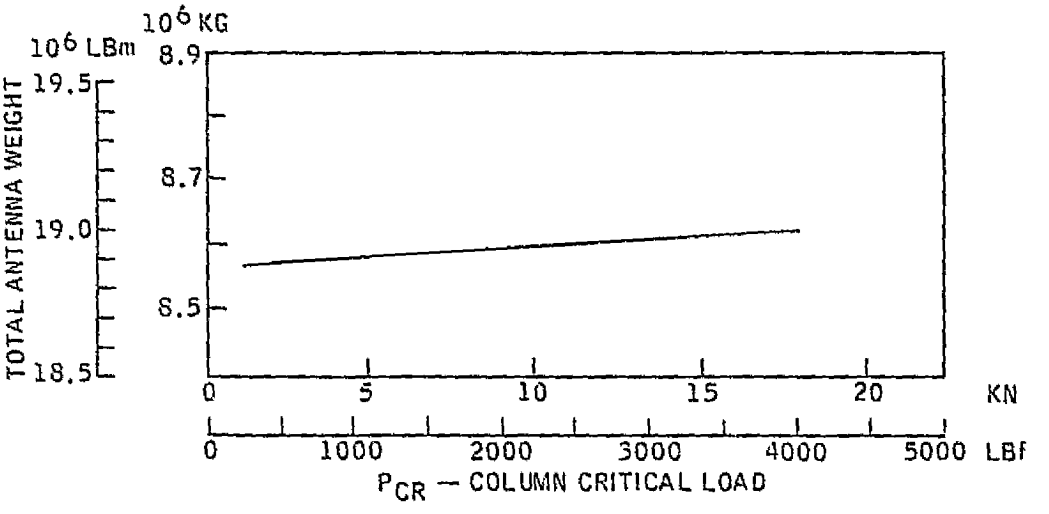

Figure 2-22. Total antenna weight versus strut column critical load.

is that for the flatness study the actual critical column design load for the struts of the primary structure do not significantly affect the total mass and mass moments of inertia and further these values are used only for load conditions involving accelerations.

As can be seen by reviewing the results of the comparison in Figure 2-20, there isn't a significant difference in the results that effect the flatness study. The overall height or diameter of the three are very similar. The weight variation between the three does vary but when considering that the structure of the antenna is only 13% of the total weight and the total weight does not directly affect the flatness of the antenna, the variation is not critical in the choice of strut configuration.

The material used is a function of the configuration. The triangular cross section with tubular caps uses pseudoisotropic GY-70/X-30, the cylindrical geodetic strut used a hybrid of GY-70 and boron fibers to achieve an average CTE of zero, and the SCAFE strut used a hybrid of pitch/glass fabric and glass fabric. Only the GY-70 is well characterized statistically, in terms of variations of properties, at this time and is the main reason for choosing the triangular cross section with tubular caps. For the flatness study it is the variation of the properties that is important rather than the absolute average values.

One of the considerations in choosing a strut size or P_{cr} that sizes the strut is the practicality of the configuration, such as the tube size or height of the strut. For example, the resulting diameter of tubular cap for P_{cr} = 15568N is 4.76 cm (1.874 inches) with a wall thickness of 0.0508 cm (0.020 inch). This size is a reasonable one when considering the overall geometry of a strut that is 130 m long and possible astronaut handling requirements.

To support the flatness study, baseline strut configurations for the primary and secondary structures were needed. The goal of the selection process was to pick configurations that were representative of possible choices but not necessarily the final design of the strut.

The trade study of three potential strut configurations showed a triangular strut with tubular caps with cords as diagonals to be the lighest and to use a material best characterized at this time. A computer code was written to optimize this configuration for minimum weight. The sizing of the diagonals is based on Timoshenko's (Theory of Elastic Stability) analysis of latticed struts which accounts for the effects of shear deflection on the critical buckling load (see Figure 2-23).

For the secondary structure the geodetic cylinder is baselined (see Figure 2-24). Due to the much shorter length of the secondary struts and lower anticipated loads, the triangular configuration used in the primary would not be practical. The geodetic strut was sized using the computer optimization code developed by NASA-JSC personnel. The minimum weight configuration is not necessarily practical from a manufacturing standpoint. A more practical design would use fewer longitudinals and as a result be slightly heavier for the same strength.

PRIMARY — TUBULAR CAPS/CORD DIAGONALS

P_{CR} = 15568N (3500 LB)
L = 130.284 m (5129.29 IN.)
H = 2.210 m (87.02 IN.)
A_{CAP} = 7.59×10^{-5} m^2 (0.1177 $IN.^2$)
R_{CAP} = 0.0238 m (0.937 IN.)
E_{CAP} = 107.5 GN/m^2 (15.7 MSI)
$A_{DIAG.}$ = 1.026×10^{-5} m^2 (0.0159 $IN.^2$)
$E_{DIAG.}$ = 68.95 GN/m^2 (10.0 MSI)
$\overline{W}$ = 0.843 KG/m (0.566 LB/FT)
α_{AVG} = -0.0378 μ/m/C (-0.021 μIN./IN./F) (GY-70/X-30)

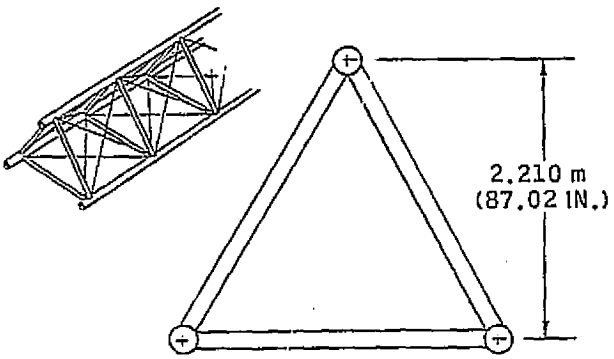

Figure 2-23. Baseline strut configuration for the primary structure.

SECONDARY — CYLINDRICAL GEODETIC

P_{CR} = 1334.4N (300 LB)
L = 10.746 m (423.07 IN.)
D = 0.248 m (9.78 IN.)
N = 54 (NO. OF LONGITUDINALS)
E = 298.54 GN/m^2 (43.3 MSI)
$\overline{W}$ = 0.036 KG/m (0.024 LB/FT)
α_{AVG} = 0.0 (USED GY-70/X-30 VALUES FOR ANALYSIS)

Figure 2-24. Baseline strut configuration for the secondary structure.

Each of the three concepts uses for its material a graphite fiber composite, either exclusively or in a hybrid of boron or glass (see Table 2-7). Graphite composites are best suited for large space structures such as the microwave antenna under study because they offer high stiffness, near zero coefficient of thermal expansion, and low density.

Table 2-7. Average material properties for candidate configurations.

TUBULAR MEMBERS	GEODETIC	SCAFE
PSEUDOISOTROPIC GY-70 ($\pm$45°, 90°/0°)	GY-70/BORON HYBRID UNIDIRECTIONAL	GRAPHITE PITCH/GLASS HYBRID (120/W-704$_3$/120)
t = 0.0508 cm (0.020 IN.)	b = 0.168 cm (0.066 IN.) (b x b SQUARE)	t = 0.0775 cm (0.0305 IN.)
E_x = 108.2 GN/m^2 (15.7 MSI)	E_x = 298.5 BN/m^2 (43.4 MSI)	E_x = 143.1 GN/m^2 (20.76 MSI)
α_x = -0.0378 μ/m/C (-0.021 μIN./IN./F)	α_x = 0.0	α_x = -0.380 μ/m/C (-0.211 μIN./IN./F)

The baseline configuration for the flatness study utilizes pseudoisotropic GY-70 laid up to form tubes. The GY-70 in the pseudoisotropic configuration (± 45, 90-deg, 0-deg) results in the lowest achievable CTE in the graphite fiber family and thus is used when thermally stable structures are required such as optical benches, microwave antennas, etc. Considerable test data exists for pseudoisotropic GY-70 allowing for a statistical analysis of a variation of material properties. These variations are input randomly into the finite element model to determine their effects on the surface slope error.

For the cylindrical geodetic strut, the basic structural element is a rod of either a circular or square cross section made of unidirectional fibers. In order to achieve a zero coefficient of thermal expansion a theoretical combination of GY-70 and boron fibers was devised. This approach looks very attractive with the zero CTE and high stiffness but must be verified by tests.

The SCAFE material is a hybrid of pitch woven cloth W-704 and 120 glass fabric. The rationale for this configuration in the SCAFE program was that the laminate exhibited relatively high modulus, low CTE, low energy required during forming and is low in cost.

2.2.2.4 Joints at Strut Junctions — Multijointed structures, similar to the tetrahedral trusses considered in the MPTS antenna study, are subject to potential surface misalignments caused by joint slack and manufacturing tolerance buildups. Structures with joint free-play or slack do not respond to typical thermal, static or dynamic load conditions in a linear manner. The joints contribute to exaggerated deflections which do not agree with those predicted based on linear elastic theory. In some cases joint free-play may completely alter load paths and hence structural response. This requires that some form of "zero tolerance" (no slop) joint be used to attach the struts at their intersections.

Various attachment methods could fit this category; for instance: welding, explosive joining, and various mechanical attachments.

Each of the joining methods has its merits, but for this study it was decided to concentrate on explosive joints as they require the least complex machinery to operate in space and can be accomplished quickly. A representative explosive joint method is shown in Figures 2-25 through 2-27. This method would be easy to do in space and require very little power or equipment to perform. By using an overcenter spring operating latching mechanism the struts can be semipermanently assembled to the spider. Later, after all the other struts are assembled, the explosive can be ignited to form a permanent tight joint.

Figures 2-25 through 2-27 show typical secondary structure struts and spiders but the same attachment method is applicable to the primary struts by putting an end fitting with explosive shear pins on each of the three tubes used for caps on the primary triangular beam.

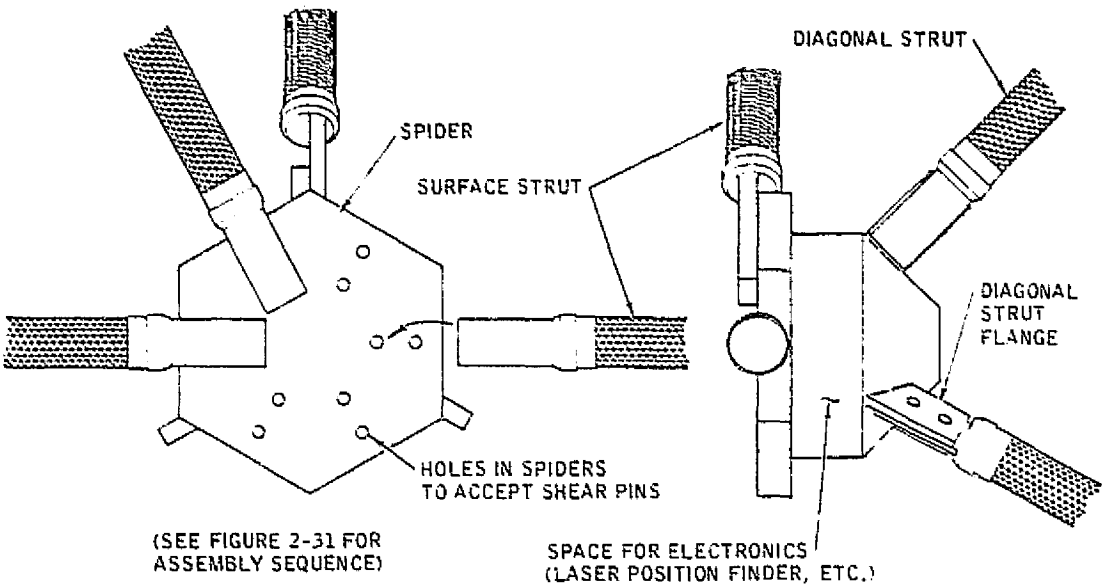

Figure 2-25. Typical secondary node joint.

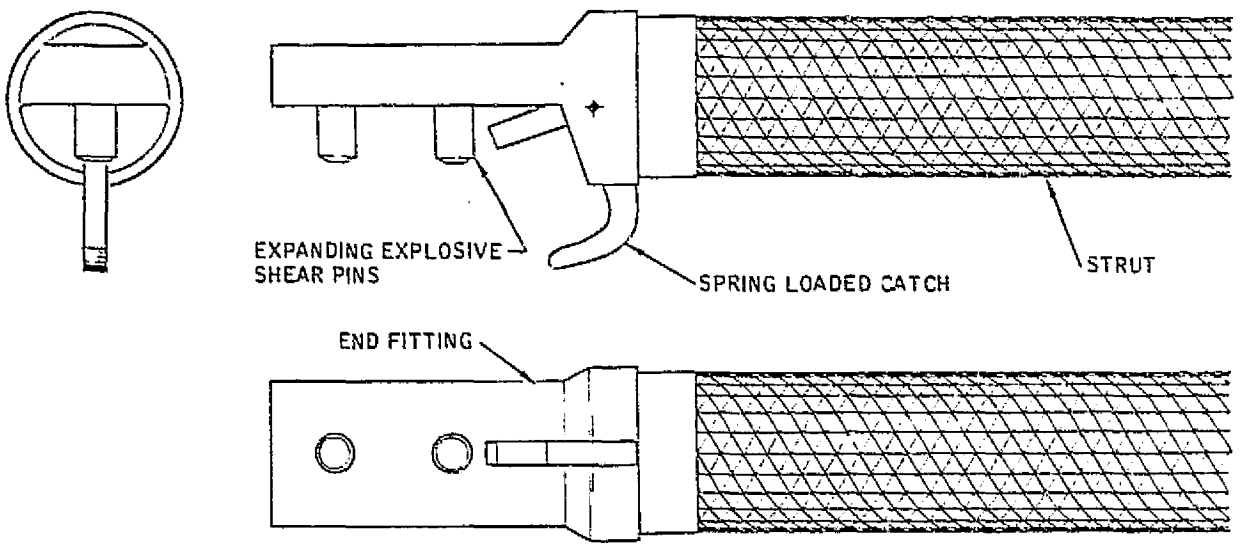

Figure 2-26. Typical secondary structure strut.

The explosive joint design was not developed into a working concept since it was not within the scope of this study to do so. Rather it is only to demonstrate that a zero tolerance (no slop) joint can be assumed for the baseline design and be used when calculating the tolerance buildup.

The attachment of the secondary structure to the primary structure and the subarrays to the secondary structure may best be accomplished with a joint that would allow some adjustment. A mechanism similar to a screw jack (see Figure 2-28), could be used to perform this adjustment.

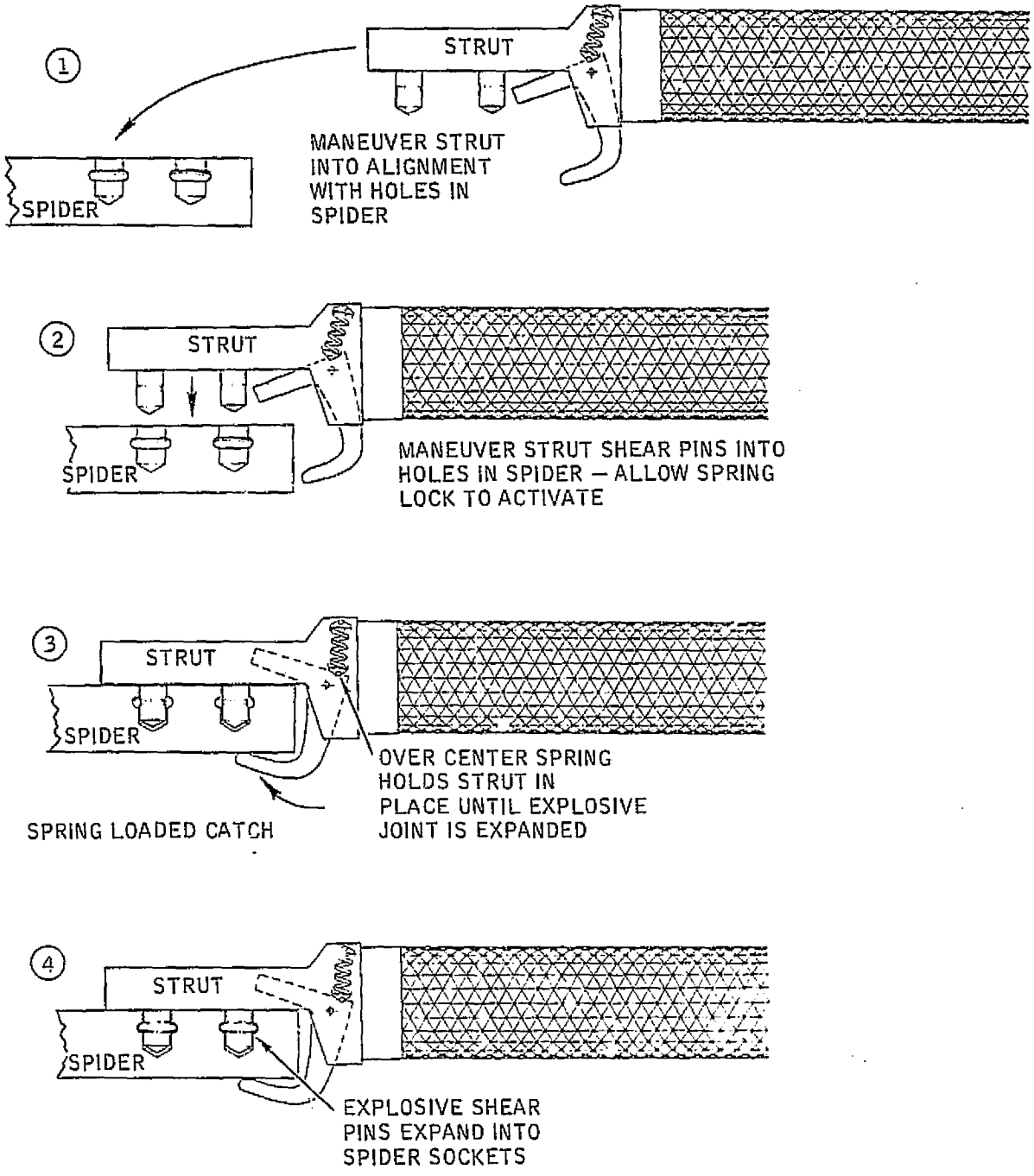

Figure 2-27. Explosive joint assembly structure.

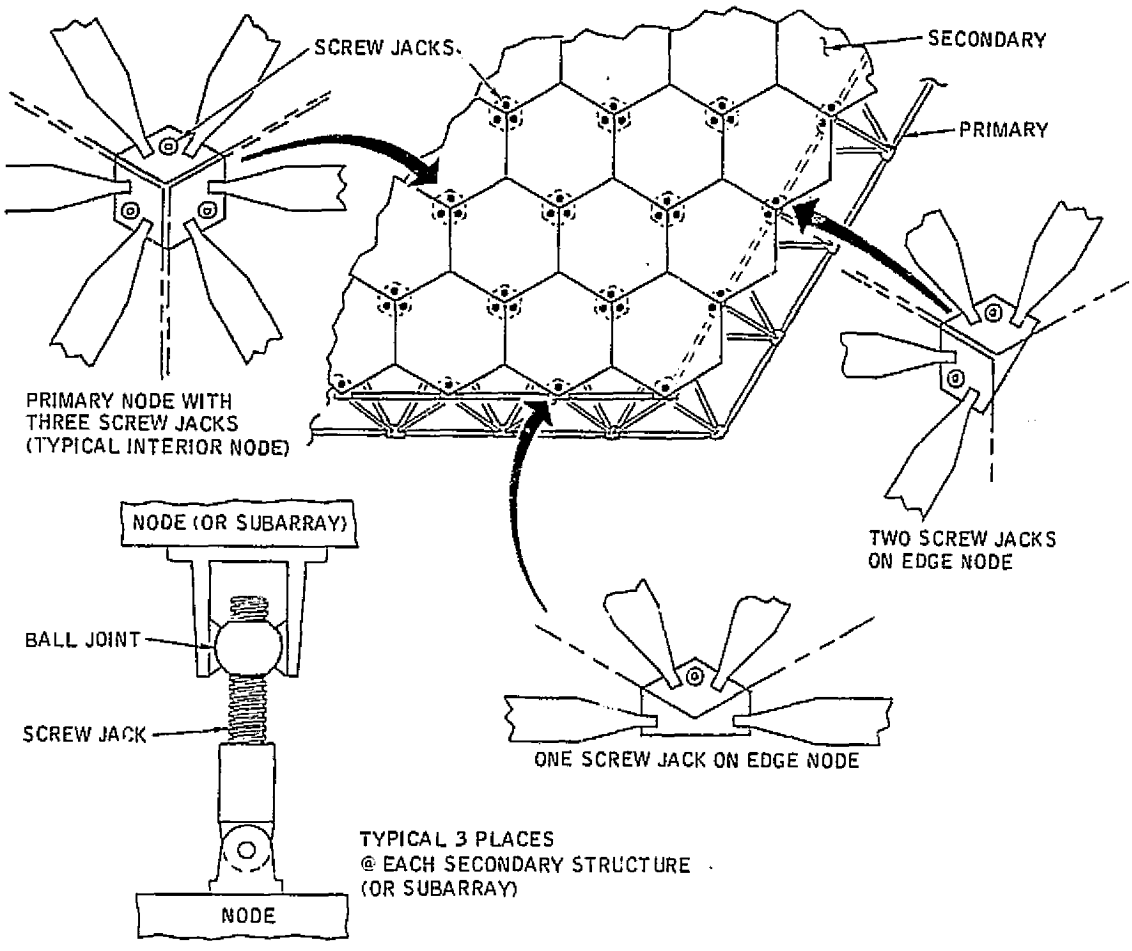

Figure 2-28. Assembly adjustment points.

Variations in both the secondary and primary structure can be compensated for by this adjustment mechanism. As shown in Figure 2-29, the basic requirements are relative alignment and phase of the rf elements.

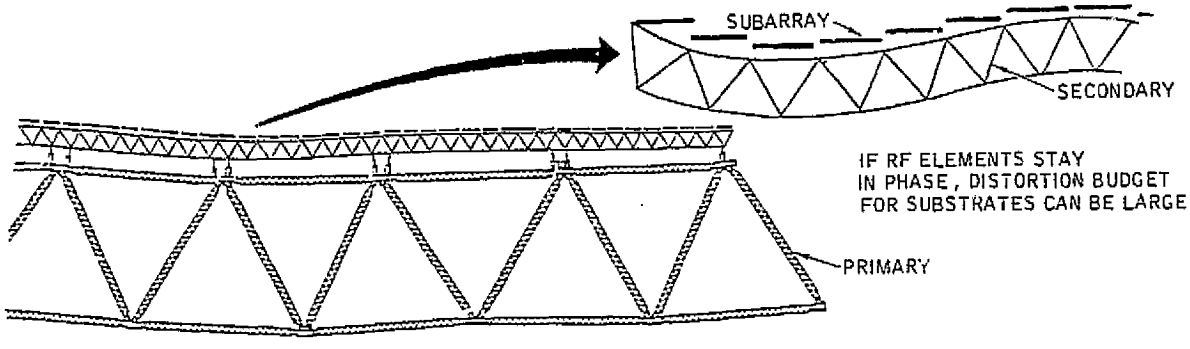

Figure 2-29. Distortion of primary and secondary can be allowed if sufficient adjustment capability is available.

A small amount of joint slop could occur in an adjustment mechanism and therefore will be carried as part of our tolerance budget and is shown in Table 2-8.

Table 2-8. Flatness study baseline manufacturing tolerance budget (all tolerances are ±).

FUNCTION	(A) PRIMARY STRUCTURE TOLERANCE	(B) SECONDARY STRUCTURE TOLERANCE	(C) SUBARRAY TOLERANCE	REMARKS
SPIDER (NODE) FABRICATION	0.076 CM (0.030 IN.)	0.025 (0.010)	N/A	MFG./TOOLING ERROR
STRUT LENGTH	0.381 (0.150)	0.051 (0.020)	N/A	MFG./TOOLING ERROR
ALIGNMENT (STRAIGHTNESS)	0.076 (0.030)	0.025 (0.010)	0.025 (0.010)	
STRUT TO SPIDER JOINT SLOP	ZERO	ZERO	ZERO	ZERO TOL. JOINT
ACTUATOR JOINT SLOP	0.003 (0.001)	0.003 (0.001)	N/A	AT BALL JOINT AND OR SCREW THREADS
MEASUREMENT EQUIPMENT	NEGL	NEGL	NEGL	VERY SMALL IF KEPT CALIBRATED
MISCELLANEOUS (ASSEMBLY TOL.)	0.127 (0.050)	0.025 (0.010)	0.025 (0.010)	
RSS SUBTOTAL	0.417 (0.164)	0.071 (0.028)	0.036 (0.014)	
RSS TOTAL (A, B, & C)				0.422 CM (0.166 IN.)
EQUIVALENT FLATNESS AT SUBARRAY (WITHOUT SCREWJACK ADJUSTERS)				0.149 ARC MIN.
EQUIVALENT FLATNESS AT SUBARRAY (WITH PASSIVE SCREWJACKS)				0.77 ARC MIN.

2.2.3 BASELINE DESIGN — This section summarizes the results of the trade studies of the previous section into one baseline design. This is not necessarily the final optimal design. However, it is a structure that is characteristic of a typical structure to fulfill the requirements of the MPTS antenna.

2.2.3.1 Baseline Configuration — Configuration A (61 separate 14-bay secondary structures) was picked for the baseline design, not because of an inherent slope accuracy advantage, but rather for its simplicity of analysis (see Figure 2-30).

The baseline primary structure is composed of the double cord diagonal strut beams joined at common spider polygons using zero tolerance explosive joints (Figure 2-31).

The baseline secondary structure would be attached to the primary structure using passive adjustment screw jacks at three corners (see Figure 2-32). A kinematic mounting system would be used to allow differential expansion between the structures (see Figure 2-33).

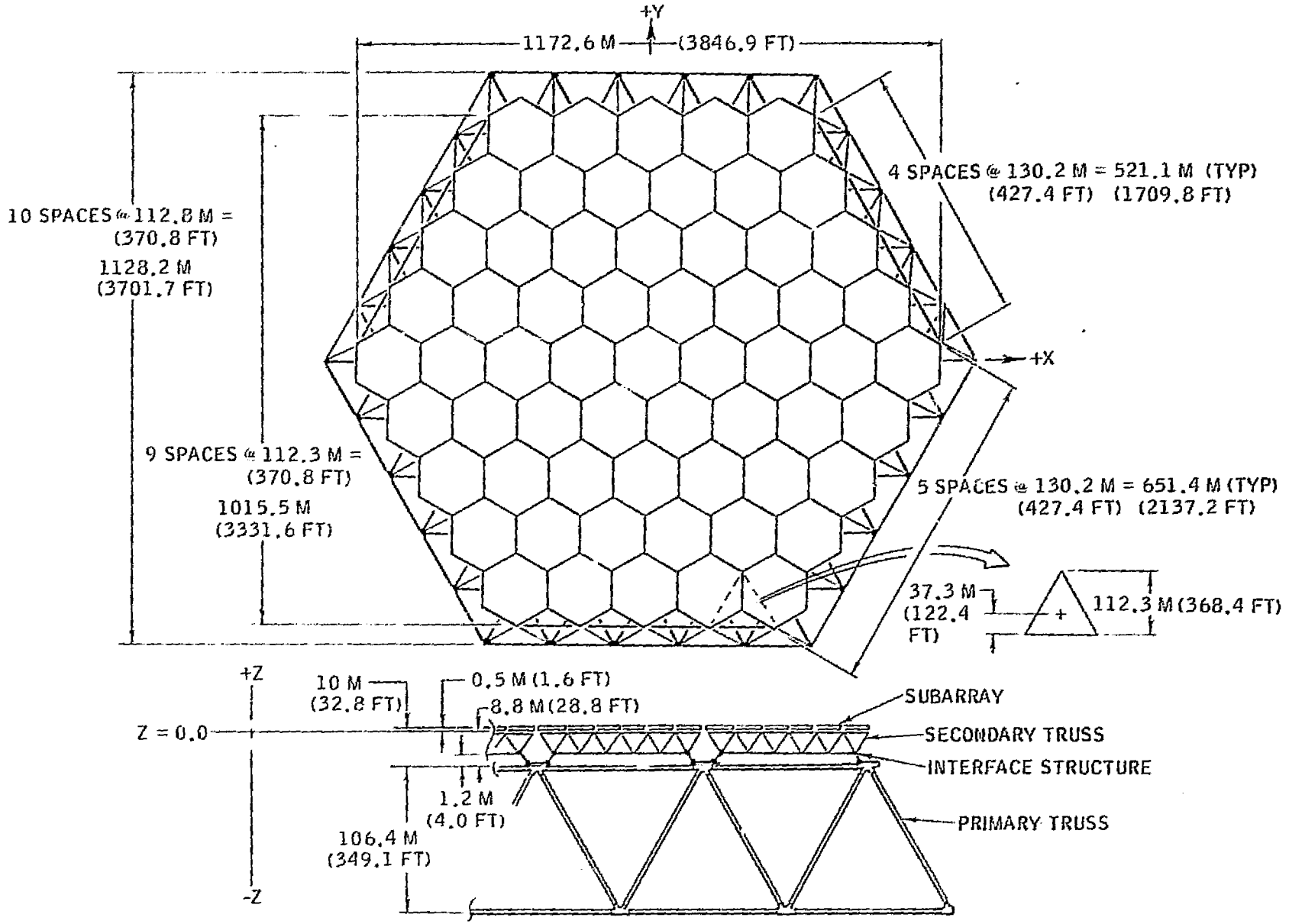

Figure 2-30. Baseline structural geometry (configuration A).

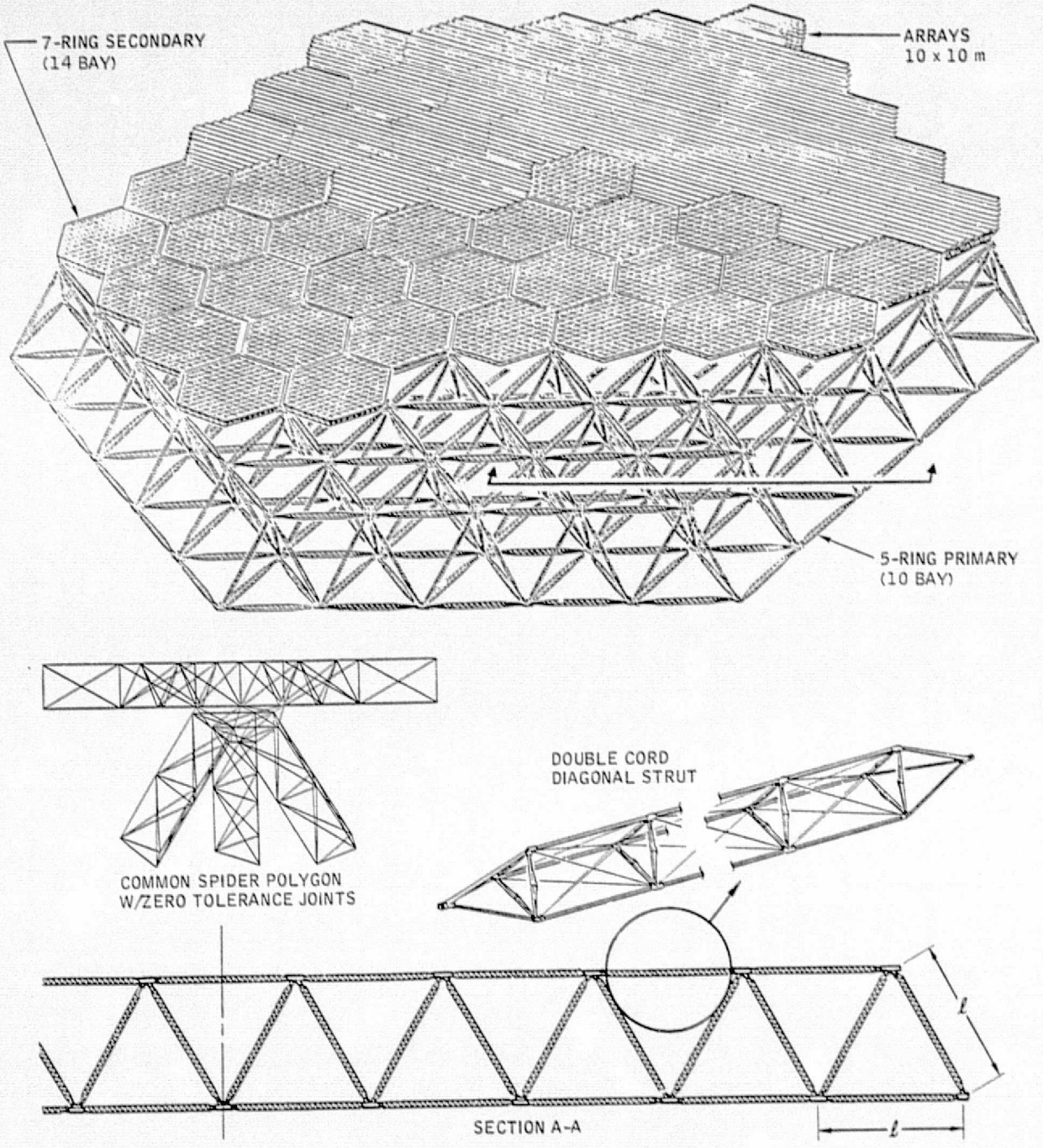

Figure 2-31. Baseline primary structure.

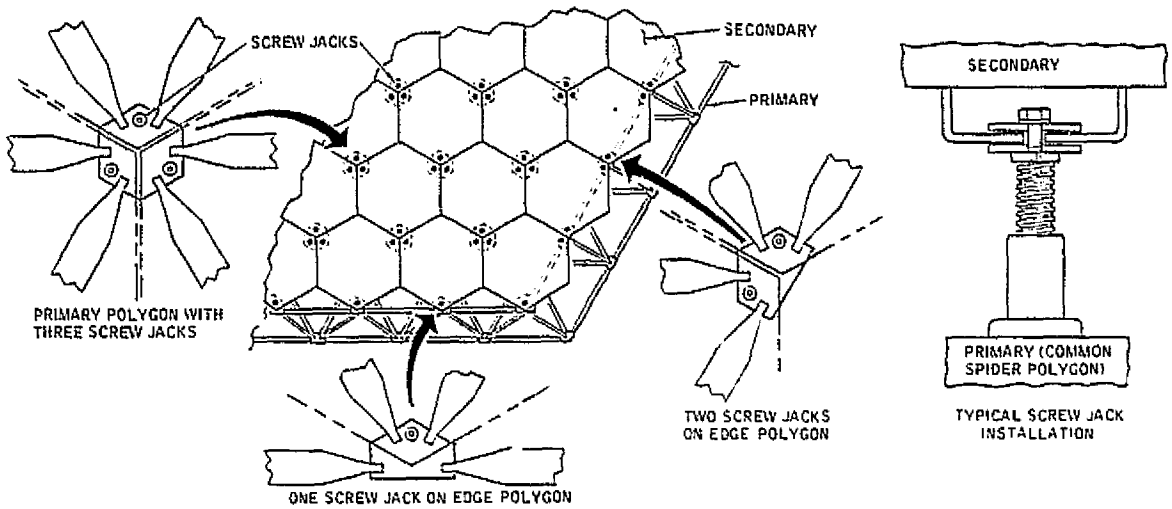

Figure 2-32. Assembly adjustment points.

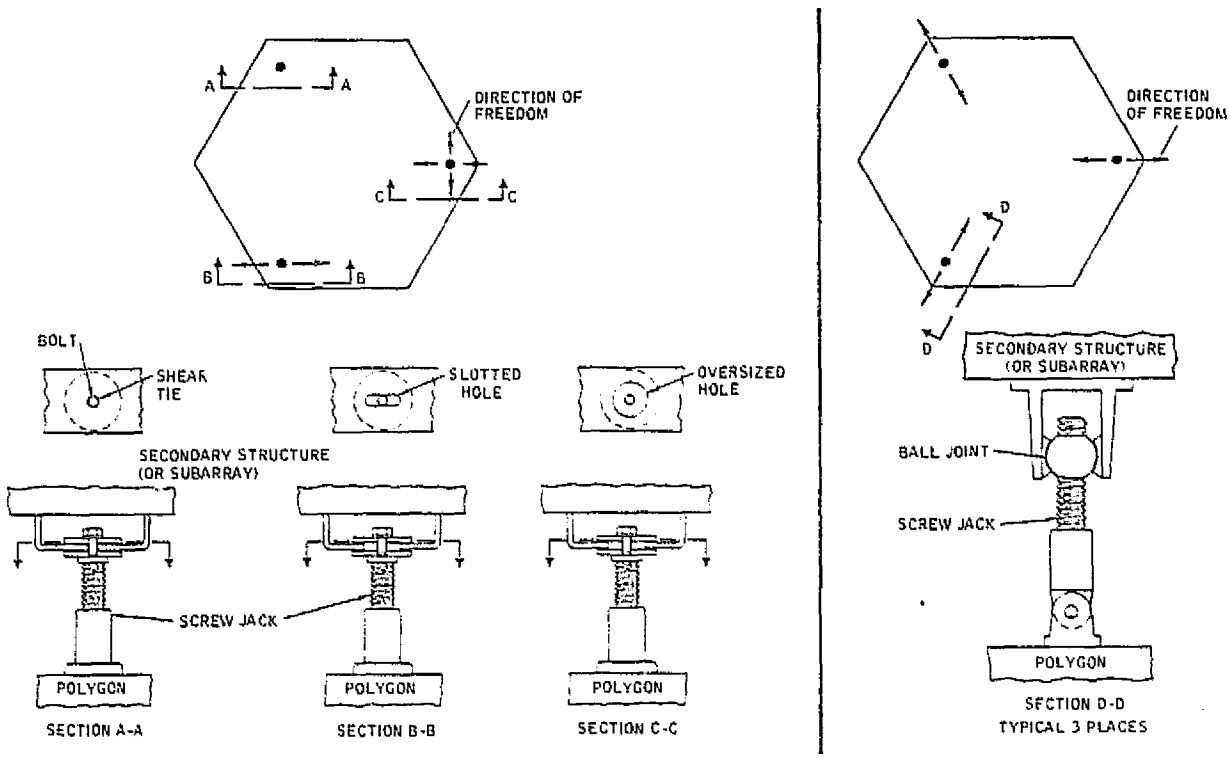

Figure 2-33. Kinematic mount options.

The secondary structure would be made up of cylindrical cross section geodetic struts ending at spiders with zero tolerance explosive joints (see Figure 2-34).

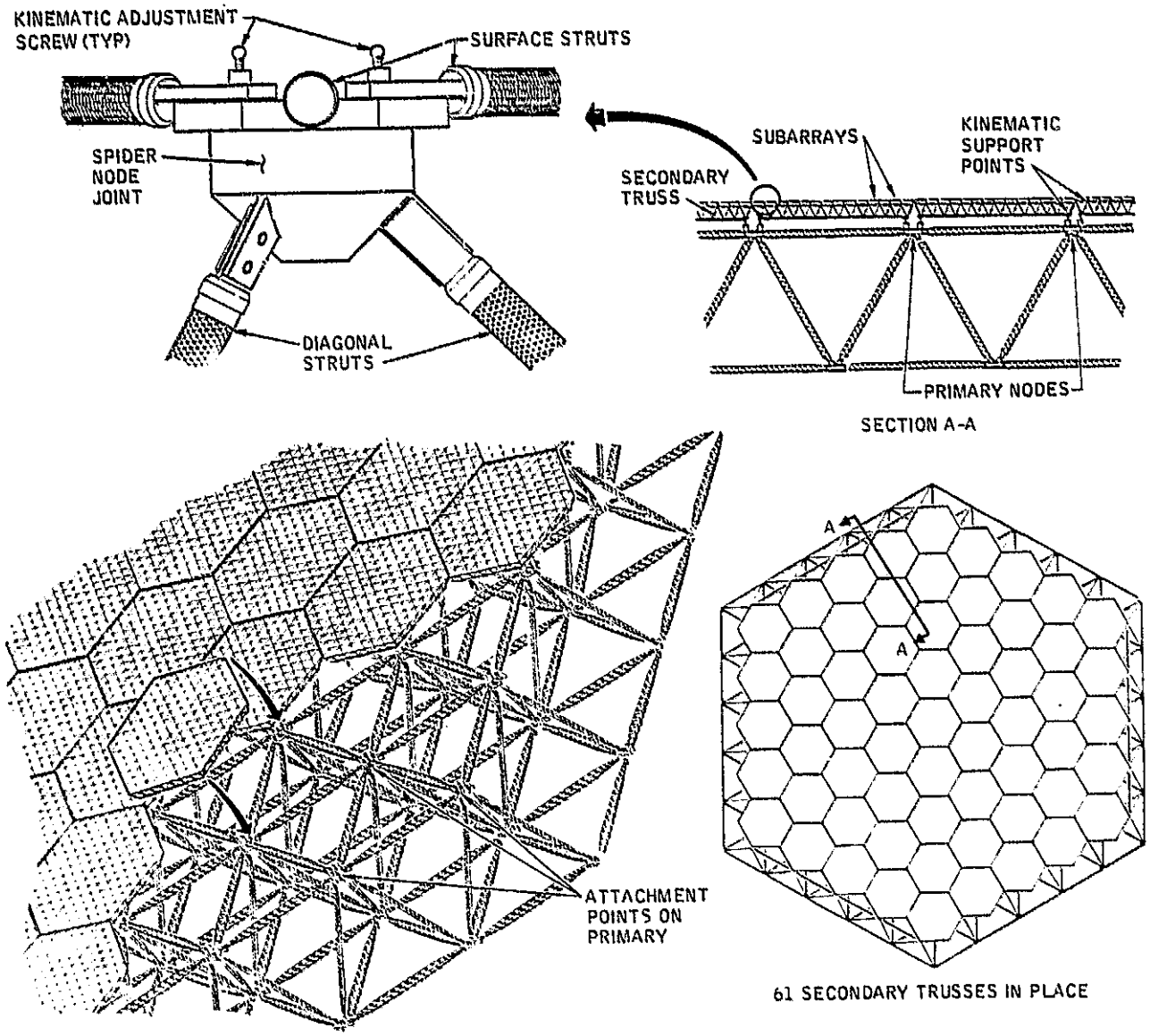

Figure 2-34. Assembly of baseline secondary structure.

The subarrays themselves are not a part of this tolerance study but the mechanism (or structure) to attach them is included in the baseline tolerance budget. The method anticipated is another passive adjustable screw jack similar to that used between the primary and secondary structures.

As explained earlier, the purpose of projecting a representative baseline design was to aid us in establishing reasonable tolerance budget amounts to be used in establishing the total structure distortion and thus determining the surface flatness that could be expected.

Table 2-8 summarizes the budget amount allocations making up the total budget for manufacturing tolerance flatness error category. The total that can be allotted to this category and still meet the three arc minute flatness requirement was 1.5 arc minutes. The individual tolerance amounts are all plus and minus and unrelated, therefore, it is logical to combine them using the root sum of squares (rss) method.

If no passive adjustment screw jack is used between the primary and secondary structures, the tolerances combine to give an rss total deflection at an individual subarray of 0.442 cm (0.166 inch). This amount is approximately equivalent to a 1.49 arc minute flatness error (goal 1.5 arc minute).

Assuming that passive (i.e., no active control during operation) screw jack adjusters are used between the primary and secondary structures and the secondary structure to the subarrays, the primary and secondary tolerances are replaced by one tolerance amount covering the accuracy to which the actuators can be adjusted and measured. Each actuator tolerance is estimated to be $\pm$ 0.152 cm (0.060 inch), and combining this with the subarray budget gives an equivalent flatness of 0.77 arc minutes.

2.2.3.2 Mass Properties Summary — The General Dynamics/Convair Tetrahedral Truss Structure Synthesis (GDTTSS) program was used to support the study effort. The program computes the nodal geometry, member connectivity, tube thickness, member diameter from input length over radius of gyration of tube, and member thickness from diameter over thickness input. The mass properties of each member are computed and summed from input tube density and point design fitting weights. The nodal mass distributions are derived by distributing tube and fitting weight to the two connecting nodes. The program develops a complete math model input deck for the General Dynamics Structural Analysis Program (Solid SAP) and Dynamics Mode Analysis. The mass properties as used in the finite element models for the trade study were derived by the use of the GDTTSS program for the primary and secondary truss, a weight allocation for the interface mechanism, and for the nonstructural mass. Results are summarized in Table 2-9.

2.2.4 MANUFACTURING AND ASSEMBLY TECHNIQUES — In both configuration A and B designs, the secondary structure is used to support individual transmitting antenna subarrays. In planform (see Figure 2-30) these structures are characterized by a hexagonal shape measuring 1,128 meters across the corners. Their overall depth, from subarray to the back of the primary structure, is 116.4 meters. Typical member lengths are 130 meters for the primary structure and 10.75 meters for the secondary structure. The selected material of construction, for both the primary and secondary, is GY-70 graphite/epoxy arranged in a four-ply pseudoisotropic layup. In order to estimate the magnitude of the fabrication task, a parts count of the major structural components was undertaken. The results of this study are presented in Table 2-10. Alternative methods of manufacture of these structural elements were considered.

Table 2-9. Mass properties summary.

	NONSTRUCTURAL MASS (SUBARRAYS, ETC)	SECONDARY TRUSS	INTERFACE MECHANISM & STRUCTURE	PRIMARY TRUSS	TOTAL
WEIGHT KILOGRAMS (LB)	7.32×10^6 (16.1×10^6)	0.804×10^6 (1.77×10^6)	0.137×10^6 (0.302×10^6)	0.316×10^6 (0.698×10^6)	8.58×10^6 (18.92×10^6)
CENTER OF GRAVITY					
X METERS (FT)	0.0 (0.0)	0.0 (0.0)	0.0 (0.0)	0.0 (0.0)	0.0 (0.0)
Y METERS (FT)	0.0 (0.0)	0.0 (0.0)	0.0 (0.0)	0.0 (0.0)	0.0 (0.0)
Z METERS (FT)	1.0 (3.3)	-4.1 (-13.4)	-9.4 (-30.8)	-67.9 (-219.6)	-2.15 (-7.1)
MOMENTS OF INERTIA					
I_{XX} KgM^2 (SLUG-FT^2)	369×10^9 (272×10^9)	58×10^9 (43×10^9)	0.505×10^9 (0.372×10^9)	28×10^9 (20.8×10^9)	458×10^9 (337×10^9)
I_{YY} KgM^2 (SLUG-FT^2)	369×10^9 (272×10^9)	58×10^9 (43×10^9)	0.505×10^9 (0.372×10^9)	28×10^9 (20.8×10^9)	458×10^9 (337×10^9)
I_{ZZ} KgM^2 (SLUG-FT^2)	739×10^9 (545×10^9)	116×10^9 85×10^9)	1.012×10^9 (0.746×10^9)	55×10^9 (40.8×10^9)	912×10^9 (672×10^9)

Table 2-10. Structural parts count.

	Primary Structure	Secondary Structure	
		Config. A	Config. B
Number Bays	10	14	126
No. Structural Elements	1	61	1
Spider Assemblies	166	19,276	24,004
Upper Surface Struts	240	28,182	35,910
Lower Surface Struts	195	24,339	35,343
Diagonals	225	26,901	35,721

2.2.4.1 Triangular Beam Builder — The ultra-large size of the structural members and the number of parts required preclude detail fabrication on earth and transportation to orbit for assembly. A machine capable of rapidly building extremely long truss members has recently been developed by Convair for Johnson Space Center, Houston. The automatic beam-builder, shown in Figure 2-35, was designed for use with the Space Shuttle. The device operates as a cyclic feed fabricator, i.e. the machine is programmed to extend the beam one bay, then pause to permit assembly and joining of the beam component members before proceeding. The beam caps are continuously

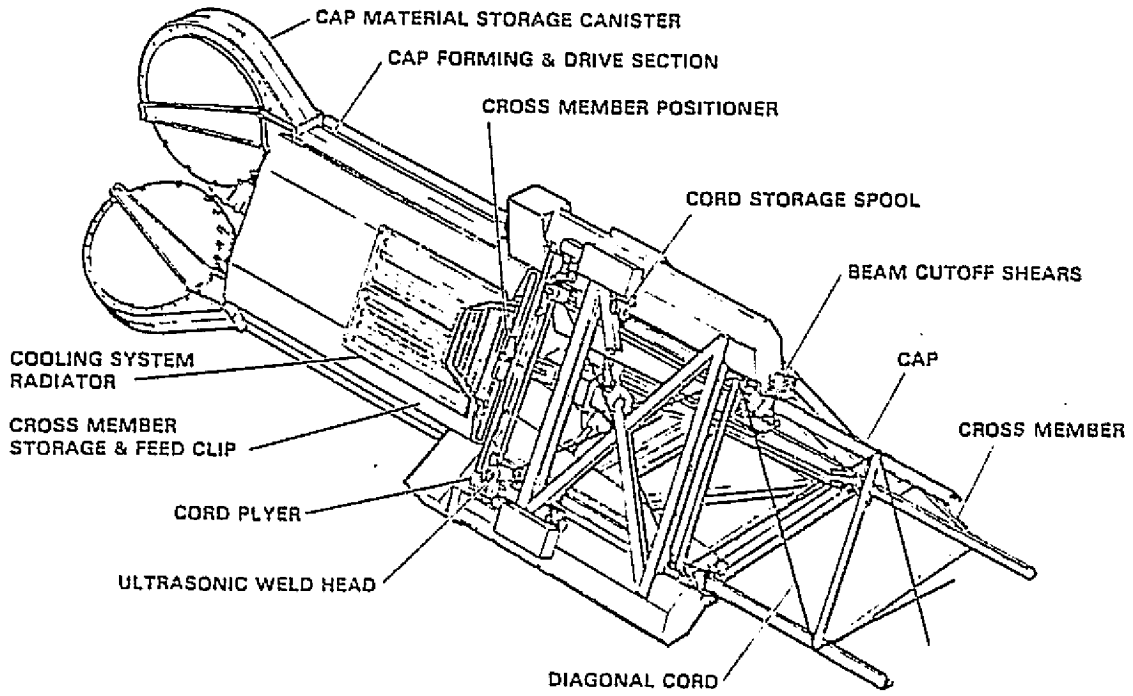

Figure 2-35. Convair beam-builder.

processed from GY-70 graphite/epoxy flat strip stock. Approximately 1,050 meters of material is coiled in the storage canister. The material passes from the canister through a heating area and into a forming section. The material then passes into a cooling section where it is contact-cooled by aluminum platens. The cooling platens cool one bay length of cap during the pause period. A drive system is incorporated in the beam-builder to provide the necessary force to each cap to drive the material from the storage canisters through the various processing sections and also to provide the force required to advance the beam out of the beam-builder. A beam cutoff mechanism is provided to shear each cap and thus separate the completed beam from the beam-builder.

A subsystem for deploying and tensioning the diagonal chord members, has also been developed. A chord tension force is applied to each chord during assembly. This preloads the chords sufficiently to preclude any slackening or over-tensioning due to thermal and dynamic deflection effects.

The cross-member strut is constructed from preformed graphite/epoxy material cut to size and stored in bins on each side of the beam-builder exterior surface. A positioner/handler mechanism transports the cross members, one at a time, from their respective storage bins to their proper position along the beam where they are ultrasonically welded.

The beam welding mechanism has six ultrasonic weld head assemblies, which are driven in pairs by a redundant motor drive for each pair. The three weld head positions are: 1) fully retracted to allow the cross members to be positioned by the

cross member positioners; 2) pierce position, where the piercing pin on each weld horn has penetrated the cross member and cap; and 3) the weld position, where the weld horn is engaged and properly loaded to enable the welds to be accomplished. Each weld horn is equipped to perform two dimple spot welds and one special cord capturing weld simultaneously.

2.2.4.2 Geodetic Beam Builder — An alternative "geodetic" beam concept for large space structures has been developed. This beam is characterized by a circular cross section formed by an open grid system of continuous elements arranged longitudinally and in counterwound spirals.

This grid is similar to the 0-deg/± 60-deg pattern, shown in Figure 2-36, which illustrates three metallic mesh tube specimens produced and evaluated in a 1968 Convair lightweight structures program. The 0-deg/± 60-deg pattern was adopted in the current assessment since elements in all three "directions" are continuous and can, therefore, be fed from either rolled or coiled compact-storage equipment into an automated fabrication machine capable of producing a continuous member of great length.

The baseline graphite/epoxy geodetic beam configuration, shown in Figure 2-37, consists of twelve axial members sandwiched between twelve (6 right and 6 left hand) helical members. The axial members are equally spaced about the beam circumference and joined at their intersection points with the helical member by ultrasonic welds.

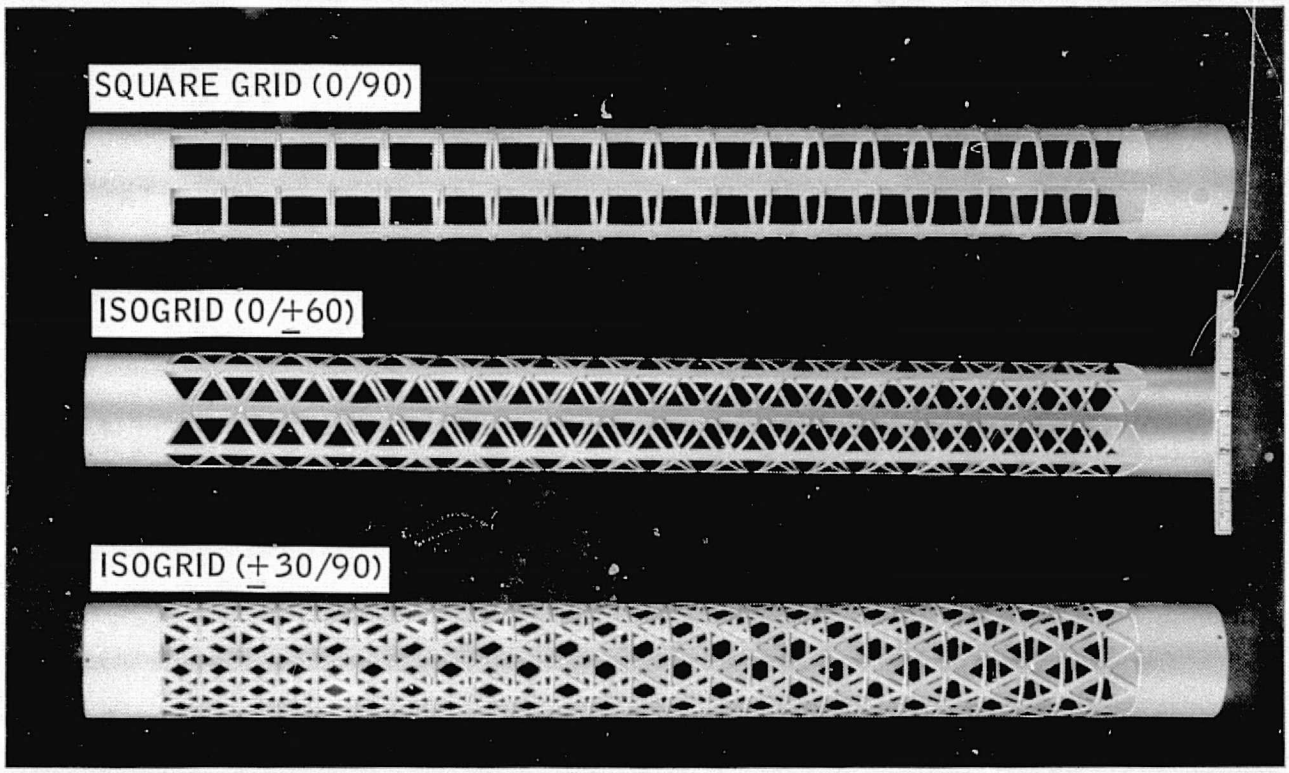

Figure 2-36. Mesh tube concepts.

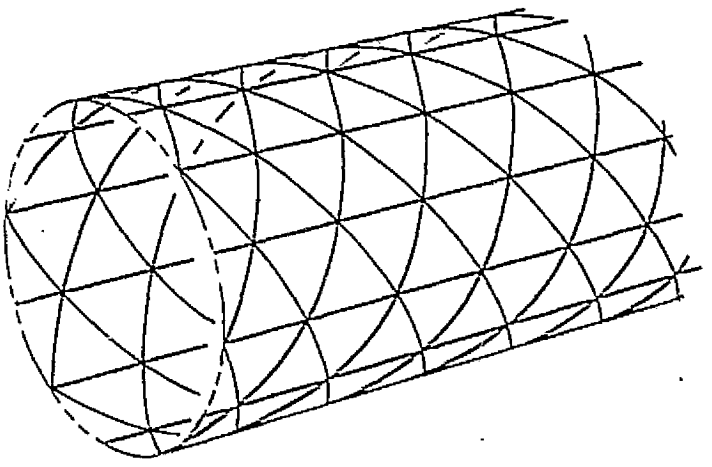

Figure 2-37. Cylindrical geodetic beam.

The geodetic beam fabrication machine, shown in Figure 2-38, is a nonoptimized, feasible, point design concept in which heat forming was avoided to eliminate fiber breakage and buckling associated with forming bends in graphite/epoxy material.

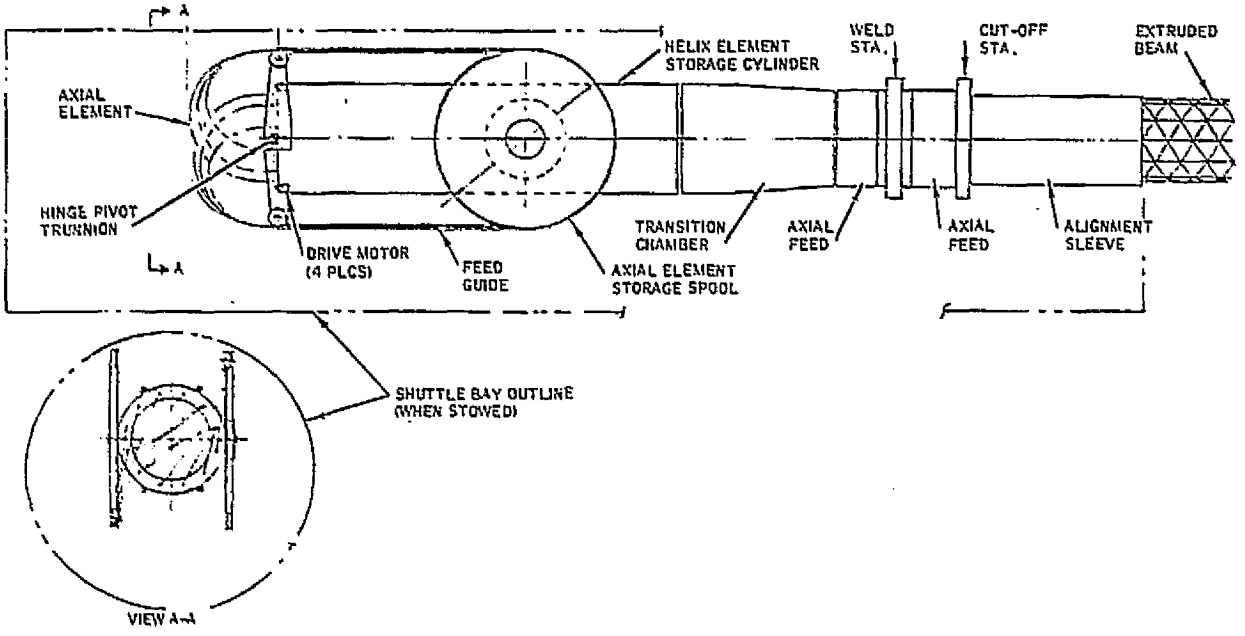

Figure 2-38. Beam fabricator concept.

The precured, axial members are stored in two canisters, each of which can accommodate six, 1,050 meter long, coils of material. The counter spiraling helical members require a different storage approach because of their greater length and the necessity of achieving a stress-free form when integrated into the beam. The helical elements are preformed and cured to their deployed configuration and then compressed solid in coil-spring fashion, for storage. This compression incurs very little stress within the members since the uniaxial material is torsionally flexible.

However, due to the total quantity of material involved (six helical elements in each direction), it is necessary to concentrically stack these compressed coils in radial disposition (i.e., two layers of three parallel right-hand wound elements over two layers of three parallel left-hand wound elements), with suitable support sleeves for layer separation.

The following paragraphs describe, sequentially, the various operations necessary to fabricate the geodetic beam.

Material Feed. Motor-driven spools containing axial material are activated by microswitch sensors positioned at the member loop area. Helical material is peel ring fed when activated by microswitch sensors within the transition chamber.

Prefeed Orientation. Helical material enters the transition chamber from the peel rings and contracts into respective internal and external contact with axial members preparatory to entering the preweld feed unit.

Beam Feed. Two powered beam feed units (one each side of the weld station) initiate linear extension of beam. Because uniformity of the beam is dependent upon close repetitive tolerance between intersectional nodes, a simple friction drive of elements is not practical. Therefore, the feed system is composed of a series of axially reciprocating intersection-grasping jaws. Element intersections are grasped prior to, during, and after joining. Jaw feed prior to welding aligns only the intersection of the helical elements along the path of the axial elements. Jaw alignment hold at the welding head is positioned relative to the postweld feed jaws to maintain correct node pitch sequencing. Postweld feed jaws provide linear expulsion of beam by driving the now rigidly fixed intersections.

Welding. Six ultrasonic weld heads, supported on a ring, reciprocating through 30-deg about the beam axis to cover all twelve axial members, grasp the node intersections for alignment during weld. A segmented weld anvil is internally expanded by a spreader sleeve in sequence with the weld operation.

Ultrasonic welding was selected for element joining since it does not degrade the element interfaces, require contour deviation for added cross section, nor require additional components or complicated manipulation. The element fibers, both axial and helical, remain continuous with joining accomplished by fusion of the resin matrix without the production of debris, nor fiber displacement or breakage.

Beam Straightness. An external alignment sleeve is provided for beam stabilization beyond the postweld feed unit.

Beam Cutoff. Six ultrasonic guillotines, oriented similar to weld units, perform cutoff of beam members midway between the circumferentially staggered nodal intersections. Cutoff in this manner provides element material beyond each welded intersection for attachment to a closure ring and does not produce waste or debris.

2.2.4.3 Spider Fabrication — Two spider designs are required; one for the primary, the other for the secondary. The secondary spider is a hexagonal structure spanning approximately five feet across its corners. This component will comfortably fit within the Space Shuttle cargo bay and may therefore be fabricated on earth and transported into orbit for assembly. The primary spiders, however, are trussed, hexagonal, space frames, illustrated in Figure 2-16, which measure approximately 17 feet across their corners. The individual truss elements, making up the spider are identical to the primary surface and diagonal beams, differing only in their lengths. The overall size of the primary spider's structure will necessitate assembly in orbit.

2.2.4.4 Orbital Construction Base — The Convair-developed system of space construction, using automatic fabrication methods, is shown in Figure 2-39, and was used as the basic concept in developing an orbital construction base. In this design, a beam builder, similar to that described in Section 2.2.4.1 above, moves to successive positions along a Shuttle-attached assembly jig and automatically fabricates triangular beams, each 130 meters long. The retention of the completed beams is provided by the assembly jig. The beam-builder then moves to the position shown and fabricates the first of a series of shorter, but otherwise identical, cross beams. After the first cross beam is mated to the longitudinal beams, the assembly is automatically transported across the jig face to the next cross beam location, where the second cross beam is fabricated and installed. This process is repeated until a raft-like platform is complete. The cross beams will later be assembled to form a primary spider truss structure and are only temporarily attached to the longitudinal beams.

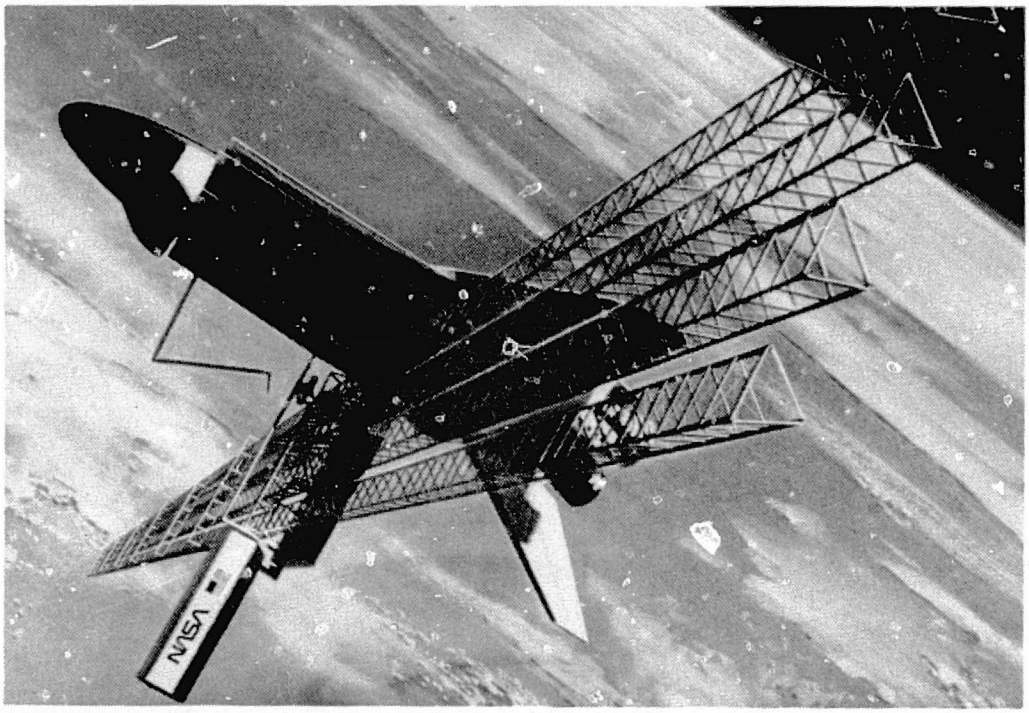

Figure 2-39. Space construction system concept.

In this way, a stock pile of component parts could be manufactured and conveniently stored in orbit until such time as assembly of the primary structure required their use.

Realization that the use of an orbiter to support a long-term construction project is expensive and that several shuttle loads of hardware and raw materials may be required to complete the task, led to the concept of a construction capsule. In essence, the capsule shown in Figure 2-40 is a cargo bay within a cargo bay, removable cylindrical structure in which are mounted a beam fabricator and all fixtures and equipment necessary for structures fabrication. A construction system designed along these lines has an initial ability to operate out of the orbiter cargo bay. It can subsequently be parked in orbit and attached to a power module. It can be closed up for servicing in a shirtsleeve environment or be returned to earth for servicing and updating of equipment.

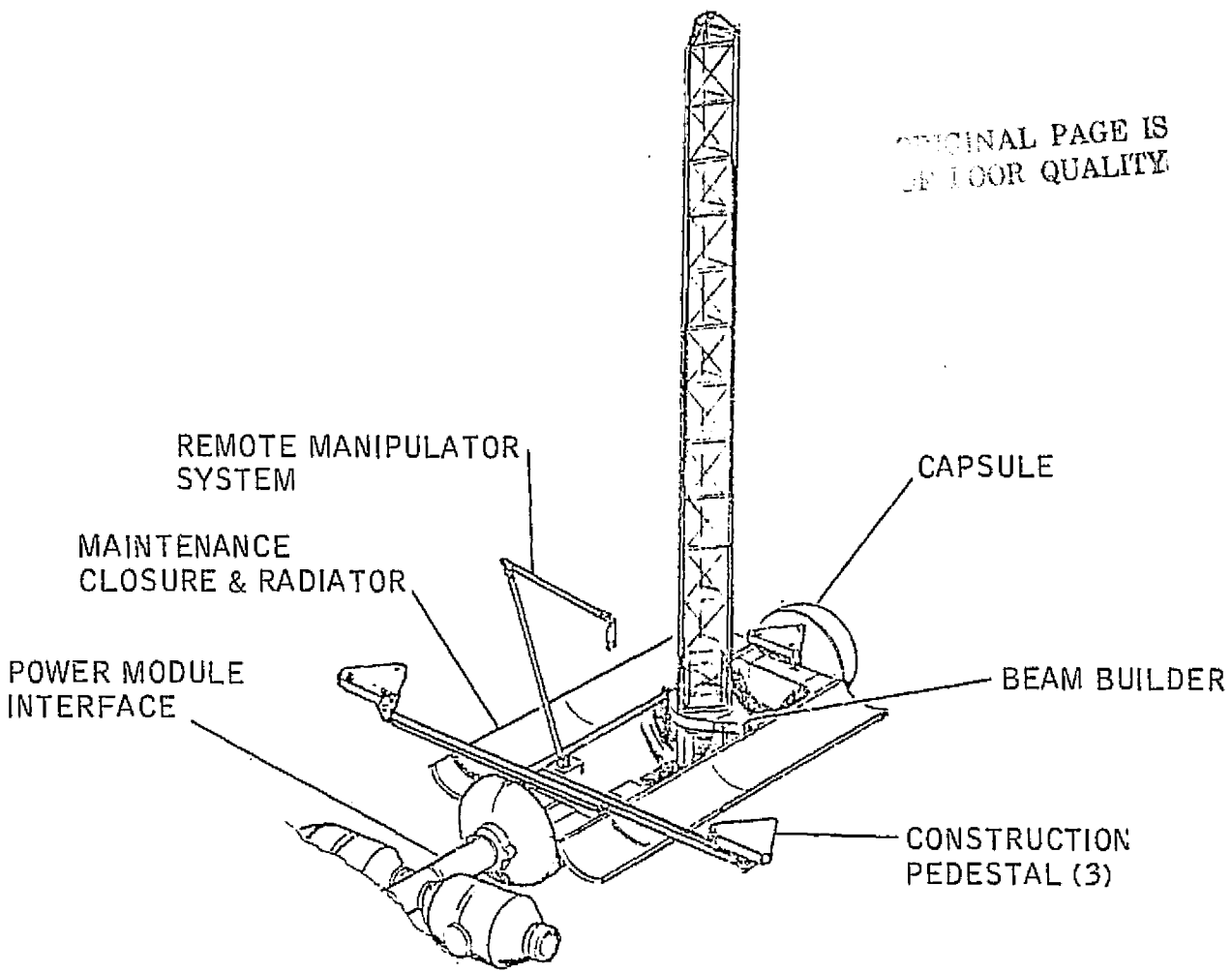

Figure 2-40. Space construction capsule.

The beam fabricator within the construction capsule is capable of building single beams which are sequentially joined to form a large subassembly. Such a structure consisting of two primary spiders and six surface beams is illustrated in Figure 2-41. During assembly with its mating geo-truss structure, small thrusters will be required to maneuver this structure into its proper position. Dynamic stability is achieved by installing a removable gyro pack. Should the subassembly be fabricated in low earth orbit, a removable rocket engine may be installed to propel the structure to geosynchronous earth orbit.

2.2.4.5 Structural Assembly — A primary program objective is to fabricate a structure which, while in orbit, will exhibit a maximum slope error of three arc seconds for each subarray. Of this allowable error, one and a half arc seconds is budgeted for manufacturing distortion, the balance being reserved for thermal and dynamic deformation. This stringent requirement led to the identification of possible sources of manufacturing error and to the realization of the necessity of maintaining tight dimensional control during detail fabrication and final assembly. Specific error sources and manufacturing tolerances are treated in Section 2.3 below while structural member alignment and measuring systems are discussed in Section 2.4.

Early in the assembly of the geo-truss, a stable configuration is reached. After this point, if additional struts are not of perfect length they must be stretched or shortened to fit the available space and thus induce fabrication loads into the structure. Preliminary analysis indicates that the greatest load due to strut length error is in the neighborhood of 1222N (277 pounds). The magnitude of this load greatly exceeds the capability of a EVA crew member and will require the use of a jack-like tool to apply the installation force.

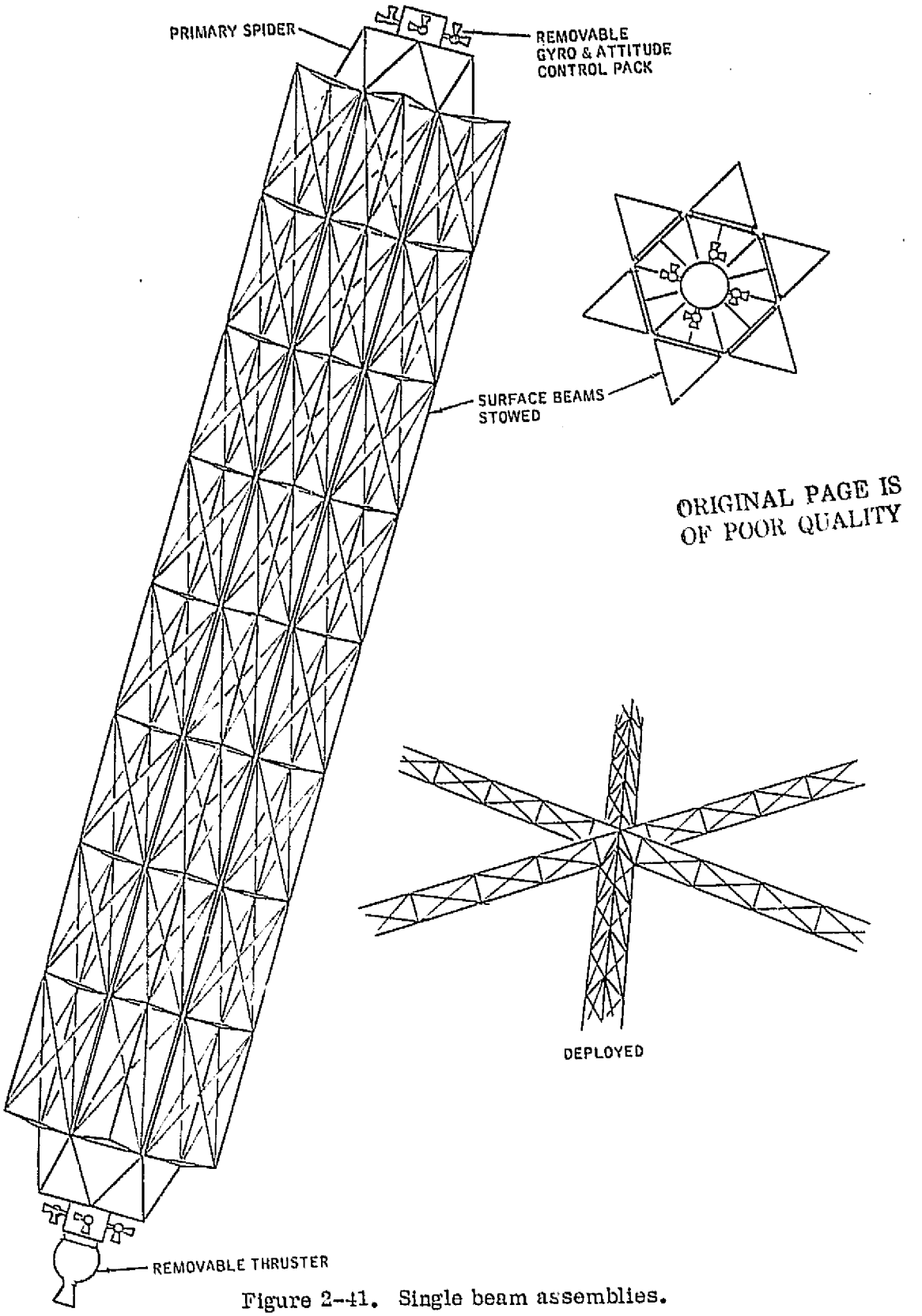

Figure 2-41. Single beam assemblies.

2.3 PERFORMANCE ERROR ANALYSIS

Two performance parameters of the MPTS system are critical to this study. These ar the linear phase errors over the antenna subarray panels, and the mechanical line-of-sight error of the array beam. Both errors result from slope error in the orientation of the individual planar subarrays with respect to the aperture plane. The former places an upper bound on antenna efficiency since subarrays with slope error deliver less than peak energy to the rectenna. The latter also causes a loss of efficiency, if the beam moves out of alignment with the rectenna. Line-of-sight (LOS) error is correctable electronically by generating a phase correction for each subarray, or group of subarrays depending on the LOS error magnitude. Generally, the linear phase errors resulting from tilt of the subarray cannot be corrected practically by electronic means.

Slope error of the subarray panels, then, contributes to two mechanisms that cause loss of power transmission efficiency. Random tilt of individual subarrays causes beam broadening with loss of efficiency, and general tilting of the whole structure causes the beam to be displaced with resulting loss of efficiency unless corrected electronically. In the first case, it is the rms slope error (after systematic tilt of the structure has been accounted for) that must be minimized. We use a 2 arc min. rms slope error as the performance goal of the random contribution. The second case is the systematic tilt, which should be minimized to keep electronic phasing requirements within practical limits. We use 2 arc min. maximum as the performance goal for mechanical LOS accuracy.

2.3.1 RMS SLOPE ERROR RELATIONSHIP TO BEAM EFFICIENCY — The potential field of a single subarray, normalized to unity on axis, is approximated by:

$$g(u) = \frac{\sin(u)}{u}, \quad u = \frac{\pi D}{\lambda} \sin\Theta$$

D is the effective diameter, 11.28 m (444.1 inches)

λ is the wavelength, 12.24 cm (4.82 inches)

Θ is the slope error of the subarray

The power density of angle θ is $(g(u))^2$ relative to unity at the beam center axis. A requirement is that power density should not fall below 0.98 of maximum as a result of slope error of the subarray. Solving for θ, the 3 arc minute slope error is generated. The 98 percent efficiency can be met for the entire MPTS with some subarrays tilted more than 3 arc minute slope if others are less than 3 arc minute.

Many contributing factors lead to displacement of the support points of the subarrays. These factors tend to give a normally distributed displacement error. This error leads to a bivariate normal distribution of slope on two orthogonal axes in the subarray surface. Total slope error can then be expected to have a Rayleigh distribution. This distribution gives an indication of the probability of different values of slope error, s, for a root-mean-square slope error, rms. The relationship of rms slope error and beam efficiency is shown in Figure 2-42.

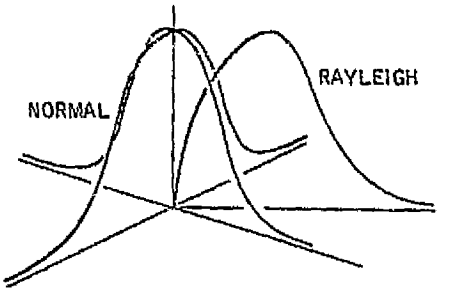

$$s^2 = x^2 + y^2$$

$$p(s) = \frac{2s}{(rms)^2}\, e^{-\left(\frac{s^2}{rms}\right)}$$

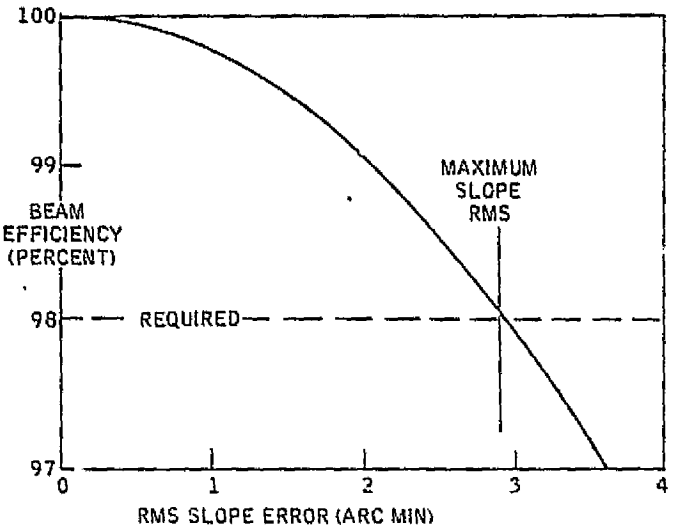

$$\text{EFFICIENCY} = \int_0^{\infty} \frac{2s}{(rms)^2}\, e^{-\left(\frac{s^2}{rms^2}\right)} \left(\frac{\sin\left(\frac{\pi D}{\lambda} \sin s\right)}{\frac{\pi D}{\lambda} \sin s} \right)^2 ds$$

Figure 2-42. RMS slope error relationship to efficiency.

Combining the power density, and its probability of occurring, the efficiency is then computed for any rms slope error. An rms slope error of 2.9 arc min. can be expected to give a 98 percent beam efficiency. For one design goal we have used 2 arc minutes, equivalent to 99 percent beam efficiency.

This is a conservative estimate because the largest distortions usually occur at the edge of the structures. For the primary structure, the major errors will occur where illumination is reduced and the overall efficiency of the MPTS antenna should be higher than that predicted above.

2.3.2 COMBINATION OF RMS SLOPE ERRORS — Slope over the subarray surface is a random variable. Each subarray panel has a slope with respect to the principal axis of the antenna. The efficiency of the antenna is relatable to the root mean square (RMS) slope of all the panels.

The rms slope of a surface A is the square root of the expectation of A^2:

$$\text{RMS}(A) = \left[E(A^2)\right]^{\frac{1}{2}} = \left[\frac{1}{n} \sum_{i=1}^{n} A^2\right]^{\frac{1}{2}}$$

RMS slope error is one figure of merit for rating structural performance in this study. We compute the slope error for surface A by combining the tilt of the surface on two axes. These are also random variables: C and D (Figure 2-43). Using the small angle

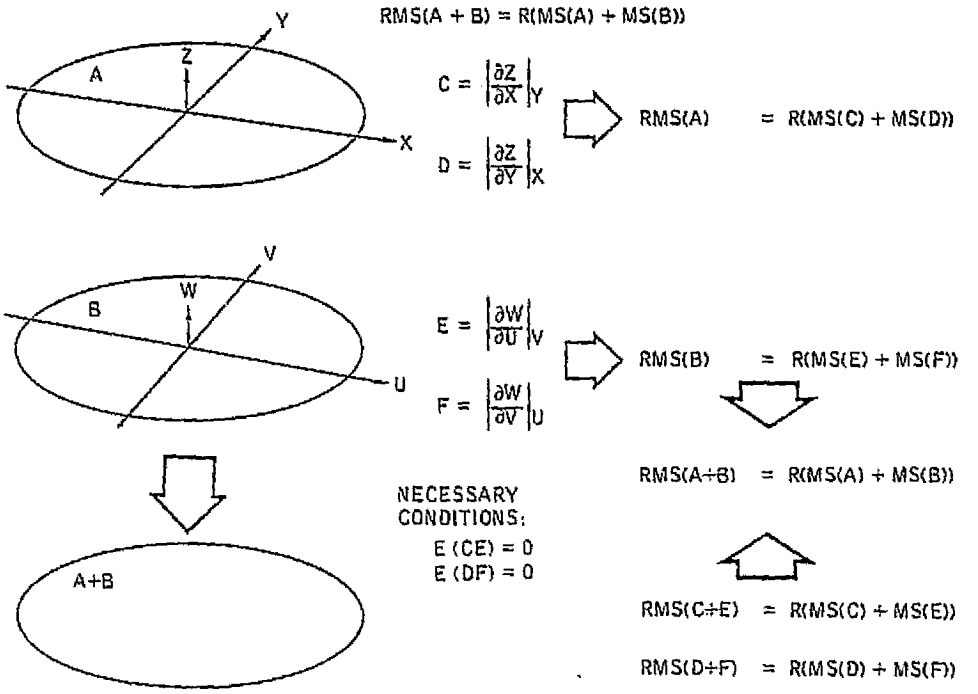

Figure 2-43. Combination of rms slope errors.

approximation rms (A) is equal to the root sum square (RSS) of rms (C) and rms (D) = R (MS (C) + MS (D)). We wish to be able to combine the slope error of surfaces A & B by the same process rms (A+B) = R (MS (A) + MS (B)), where A and B are two error sources that contribute to total slope error (e.g., manufacturing tolerance and thermal distortion).

We know that the individual tilt errors on the same axis are additive (e.g., C and E). We could combine n values of C and E and then calculate rms (E+E). Fortunately if error sources A and B are independent then the expectation of CE is zero and we can get the same result by combining the squares of rms (C) and (E). Now rms (C+E) and rms (D+F) are combined (RSS) to get rms (A+B). Rearranging the right hand terms, the final result is obtained:

$$\text{RMS (A+B)} = \text{R (MS (A)} + \text{MS (B))}$$

This equation permits the direct combination of overall rms slope errors from various sources and from the primary and secondary structures.

2.3.3 LINE-OF-SIGHT (LOS) AND RMS SLOPE ERROR CALCULATION FROM SURFACE DEFLECTIONS — The second figure of merit for evaluating structural performance is LOS accuracy. If all subarrays of the transmitting system are driven in phase, the beam will deviate from the line-of-sight to the rectenna because of the combined effects of attitude control error and array surface distortion. This structural

LOS error is corrected electronically by differential phasing of the subarrays, since the difficulty of making the electronic correction increases with structural pointing error magnitude. The general requirement for 3 arc min. maximum slope error for the entire antenna limits pointing error to 3 arc min. With a number of statistically distributed error sources causing slope error, it is not possible to guarantee that some individual subarrays will not exceed 3 arc min. slope error. The distribution of slope error has little effect on pointing accuracy. Rather, it is the systematic slope error over the surface which causes the beam to be displaced. We have used 2 arc min. maximum as our study goal for the beam displacement resulting from the various distributions of slope error encountered.

LOS accuracy is the angle through which the antenna structure would be rotated to maximize the received energy at the rectenna. Rigorous calculation of this angle would require an approach equivalent to calculation of the far field pattern of the aperture represented by the distorted array surface. This pattern would be projected on the rectenna using the geometry of the earth/orbit model. A linear phase distribution over the aperture would then be calculated to center the beam on the rectenna in a way to maximize energy transfer. The equivalent angle of the linear phase distribution is the theoretical LOS error.

Practically, with many distortion cases being considered in this parametric analysis, a few assumptions must be made to simplify LOS accuracy calculations. We assume that the beam is symmetric, maximum energy is received when the beam is centered on the rectenna, and the beam center is deflected by the average slope of the surface. Slope on an axis was defined in Figure 2-43. LOS accuracy is the rms of the average slope error on the x and y axes. The equivalent in optics is tilt about 2 axes which determines beam displacement of a planar reflector.

Slope error is computed from the surface displacements parallel to the LOS. The distribution of these surface errors is a random variable z. The Variance of z is:

$$\text{Var}(z) = E(z - \mu - ax - by)^2 \qquad (1)$$

where: μ is the expectation of z, E(z)
a and b are tilt of the surface on two axes
x and y are the coordinates of error z

Expanding (1):

$$\text{Var}(z) = E(z^2) - \mu^2 + a^2 E(x^2) + b^2 E(y^2) - 2a E(xz) - 2b E(yz) \qquad (2)$$

The remaining terms are zero because E (x) = E (y) = E (xy) = 0 for the symmetrical structures considered.

For Var (z) to be a minimum: $\frac{\partial \text{Var}(z)}{\partial a} = \frac{\partial \text{Var}(z)}{\partial b} = 0$ (3)

Differentiating (2) and solving for a and b yields:

$$a = \frac{E\,(xz)}{E\,(x^2)} \qquad b = \frac{E\,(yz)}{E\,(y^2)} \tag{4}$$

Finally:

$$\text{Var}\,(z) = E\,(z^2) - \mu^2 - \frac{(E(xz))^2}{E\,(x^2)} - \frac{(E(yz))^2}{E\,(y^2)} \tag{5}$$

Interpreting (5), Var (z) is a measure of surface distortion after corrections have been made for average displacement (μ) which contributes only group phase error and is not significant to this study, and for tip and tilt. The new variable

$$z' = z - \mu - ax - by \tag{6}$$

is used to compute rms slope error which influences beam efficiency but not LOS accuracy. For these values of z', u, v, and w, tilt of a single panel is:

$$\begin{matrix}\text{panel tilt} \\ \text{(arc min.)}\end{matrix} = 60 \tan^{-1} \left\{ \frac{(u^2 - uv + v^2 - vw + w^2 - wu)^{\frac{1}{2}}}{930.6} \right\} \tag{7}$$

RMS slope error is the root mean square of all panel slope errors.

Equations (4) gives average slope on the x and y axes. Since these slopes are small, the absolute value of LOS angular accuracy is:

$$\text{LOS (arc min.)} = \frac{10800}{\pi} (a^2 + b^2)^{\frac{1}{2}} \tag{8}$$

2.3.4 ERROR SOURCES

Slope error is a function of deflections of the MPTS supporting truss structures. Specifically, deflections normal to the flat subarray surface at the interface nodes between the primary and secondary structures, and at the support nodes of the subarrays on the secondary structure determine the slope error contribution of the truss structures.

There are three basic categories of error sources (Figure 2-44). They are: manufacturing, maneuvering and thermal. In the first, we have included all error sources that contribute to variation in assembled node-to-node strut length evaluated in an arbitrary standard environment. Maneuvering error sources result from external forces and moments applied to the support structure by attitude control maneuvers, stationkeeping and other environmental perturbing forces. Thermal expansion encompasses all error sources that influence slope error as a result of temperature change from the standard environment to the operational environment.

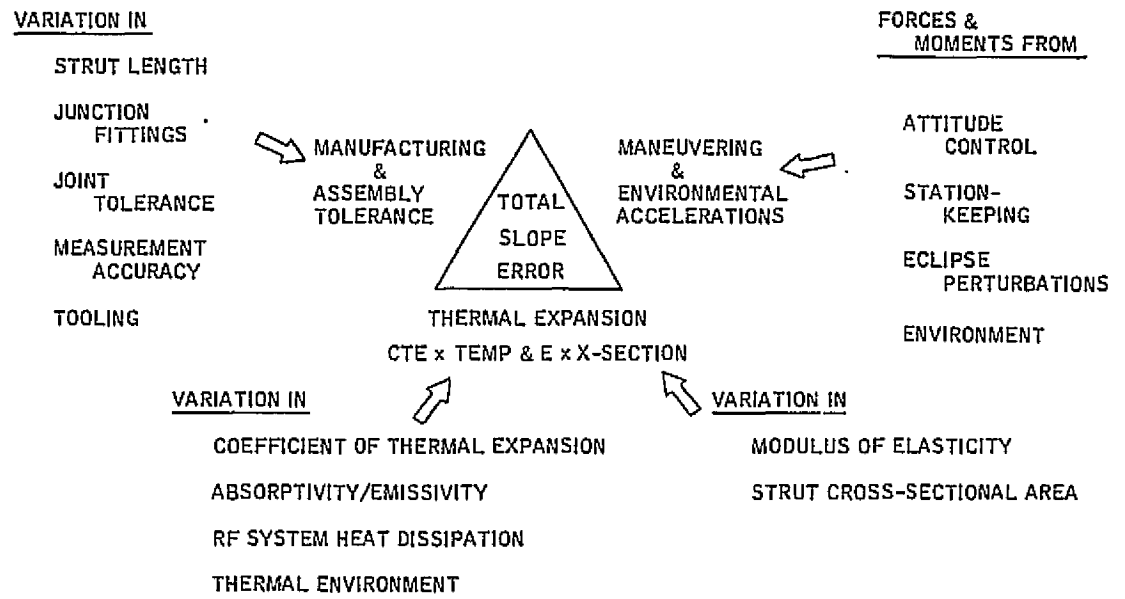

Figure 2-44. Slope error sources.

Maneuvering accelerations are error sources that exist regardless of the design parameters. Slope error can be minimized by distributing control forces, increasing structural stiffness, and designing the structure so that slope error is less sensitive to the anticipated accelerations.

Manufacturing and thermal error sources are primarily the result of uncertainties in measurement, material properties and the environment. We can design to generate a flat structure in the operational environment if CTE, temperature, E, and strut dimensions are known. It is the uncertainties in these values that lead to the operational slope error in the passive system.

2.3.5 CALCULATION OF DISTORTION FROM KNOWN ERROR SOURCES — We have identified the error sources, and discussed the relationship of the resulting surface distortions to slope error and to beam efficiency and LOS accuracy. A process of finite element modeling and analysis is used to complete the sequence from error source to structural figure of merit.

Two major programs are used in the modeling and analysis. The first is the truss structure synthesizer, and the second is the structural analysis program. The synthesizer generates the arrays of nodes representing the structure, and the connectivity. A variety of algorithms are available to establish the strut weight depending on type, ℓ/ρ, minimum gage material, and design load. The model generated is compatible with the Convair Structural Analysis Program, and NASTRAN.

2.4 MODAL SURVEY/NATURAL FREQUENCIES

Investigations of natural frequency characteristics were carried out for the baseline design considering the five ring primary structure as the only flexible portion of the system. The secondary structure and rf systems were carried as nonstructural weight on the forward surface of the primary array.

The structure is treated as a pin-ended truss system, free in space and thus will exhibit six rigid body modes as well as elastic dynamic characteristics. A mathematical simulation of the structure was developed and analyzed by finite element methods with NASTRAN.

Due to the topological similarity of this structure with Convair's geo-truss antenna structures, it was possible to use automated methods developed for those systems in the formulation of the MPTS modal study. The GDC tetrahedral truss structure synthesizer program (GDTTSS) formulated the necessary geometric data for the MPTS using an infinite focal length and the proper diameter. This program establishes truss joint locations in space and defines the appropriate connectivity for a tetrahedral truss system. Member stiffness and mass properties are also defined, along with contribution of nonstructural mass to front surface model grid points. All mass items were represented by lumped mass simulation.

Frequencies and modal characteristics for the baseline primary structure are summarized in Table 2-11. Mode shapes for modes 7 - 10 are illustrated in Figures 2-45 through 2-48. These are the first elastic body modes, whereas modes 1 through 6 are rigid body, zero frequency modes. Modes 7 and 8 display astigmatic bending; mode 9 is a basic defocus mode; and mode 10 is a trefoil bending distortion.

Table 2-11. Natural frequencies, baseline primary structure.

Mode No.	Frequency Hz	Description
1	0.	Rigid Body
2	0.	Rigid Body
3	0.	Rigid Body
4	0.	Rigid Body
5	0.	Rigid Body
6	0.	Rigid Body
7	0.084776	Astigmatism
8	0.084776	Astigmatism
9	0.141367	Defocus
10	0.148123	Trefoil Bending

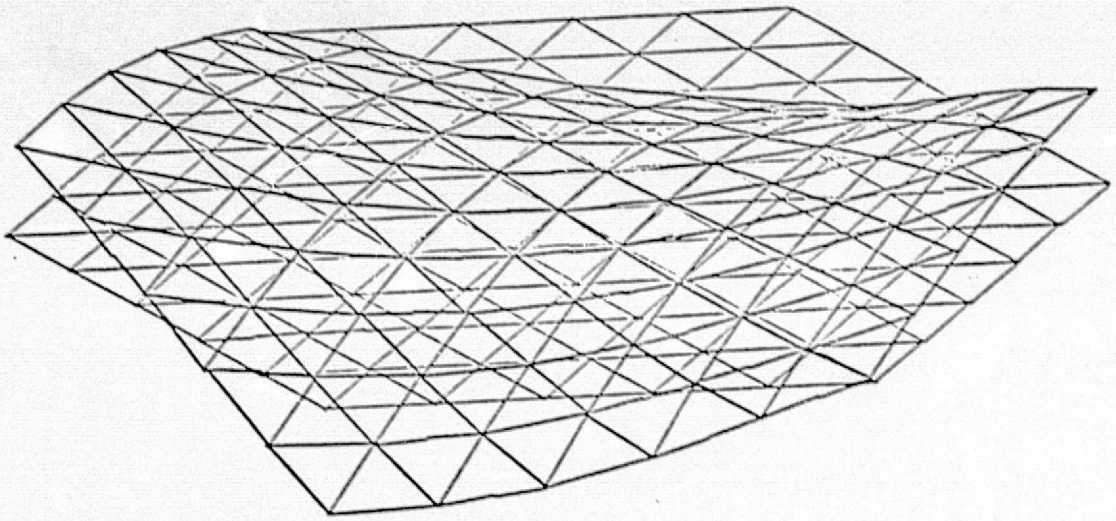

Figure 2-45. Baseline design, Mode 7, f = 0.0848 Hz.

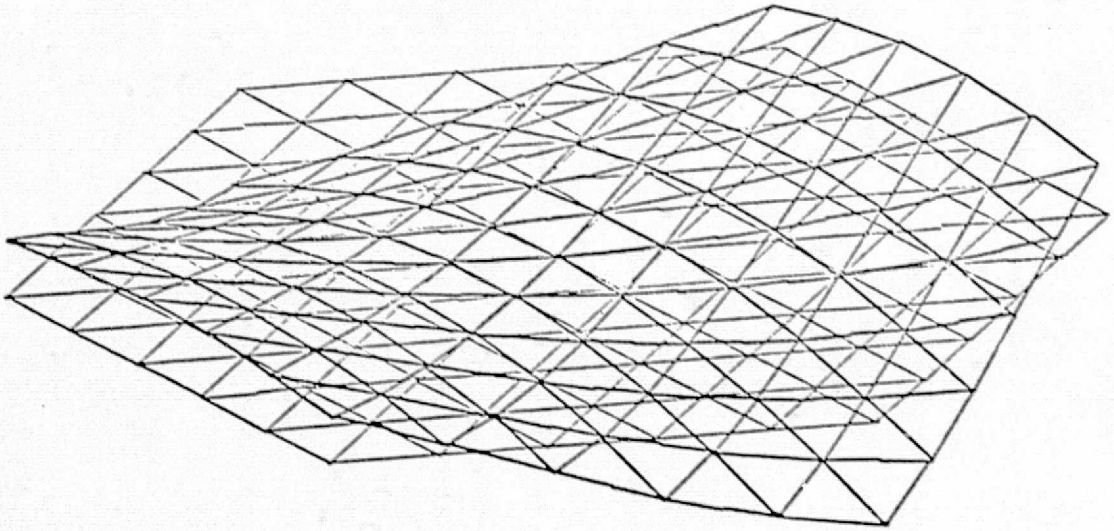

Figure 2-46. Baseline design, Mode 8, f = 0.0848 Hz.

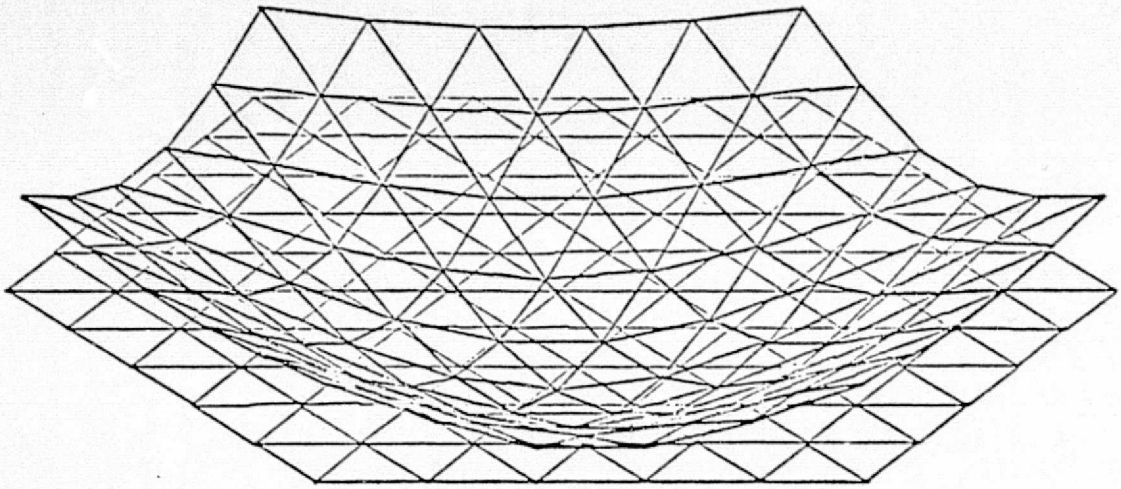

Figure 2-47. Baseline design, Mode 9, f = 0.1414 Hz.

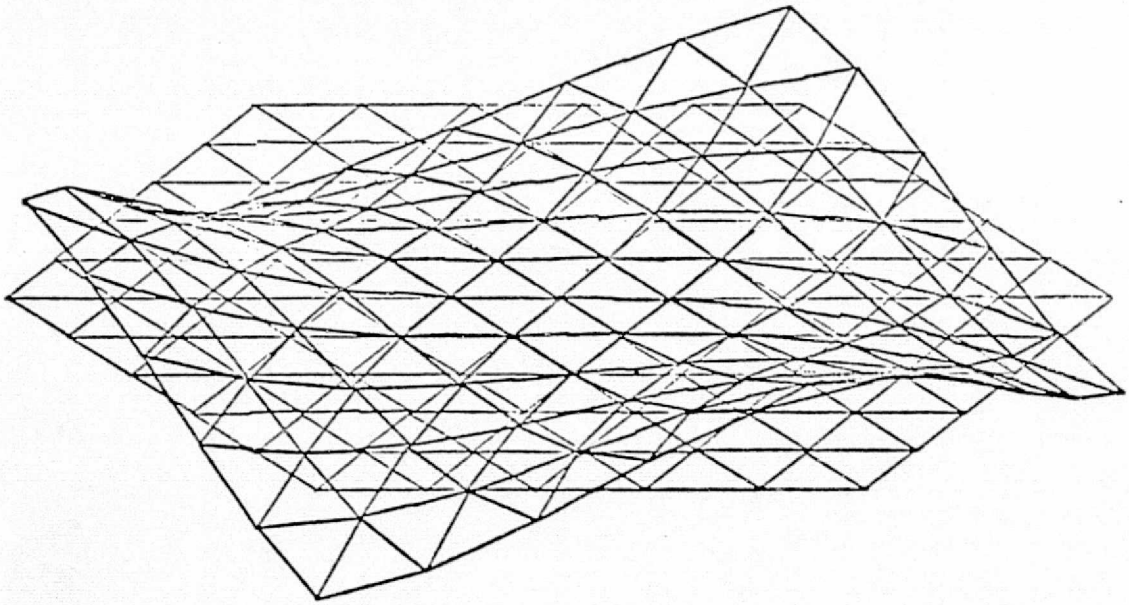

Figure 2-48. Baseline design, Mode 10, f = 0.1481 Hz.

Of the various material properties, only the modulus of elasticity, E, has an influence on structural frequency. As this parameter is varied, the natural frequencies will change as the square root ($f \sim \sqrt{E}$). Geometric changes can produce significant changes in frequency: changing the array depth results in directly proportional frequency changes. Increasing the number of rings of the truss structure for a given diameter decreases the depth and reduces the frequency. It is not anticipated, however, that structural frequencies will control such fundamental design parameters as number of rings or depth, since the frequency range is so low that the usual frequency sensitivities, e.g., control system considerations, are not present.

2.5 GENERALIZED FLATNESS STUDY

In Task 1, a generalized slope error study was performed. This approach is a convenient starting point as it provides a means of calculating representative slope errors associated with probable values of error sources. It makes use of unit material parameters and loading conditions. With derivation of scaling laws, the slope errors corresponding to unit disturbances can be scaled to examine the effects of the various error sources. This analysis can be accomplished before the detailed thermal environment (Task 2), and the actual acceleration environment (Tasks 2 and 3) have been established.

A common figure of merit, in this case rms slope error, is used to get combined slope error from uncorrelated error sources, e.g. manufacturing tolerance and thermal. Line-of-sight error is also computed for unit accelerations.

This process minimizes computer time expended. As an example, random temperatures are introduced in each strut in the primary structure. Processing the resulting distortions for unit CTE yields data that can be interpreted as the effects of:

1. Random temperature resulting from variation in the absorptivity/emissivity ratio.
2. Random distribution of CTE.
3. Manufacturing tolerance in strut length.

Generalized results were obtained for:

1. Linear and angular accelerations.
2. Manufacturing tolerance buildup.
3. Variation in CTE.
4. Uniform and Gaussian temperature distribution.
5. Variation in modulus and strut cross section.

2.5.1 RMS SLOPE ERROR RESULTING FROM MANEUVERING ACCELERATIONS — Six standard loading conditions corresponding to linear acceleration on three orthogonal axes, and angular accelerations about the axes are incorporated in the typical

finite-element structural deflection analysis. Postprocessing of the deflections then yields rms slope error for the MPTS flat surfaces represented by the structure.

The resulting slope error has been scaled to correspond to one thousandth of a "g" linear, and to 1 arc sec/sec^2 angular accelerations. While these accelerations are small, they are relatively large compared to those anticipated for the MPTS structure in its operational environment. For example, the MPTS rotates once per day to remain pointed at the ground receiver antenna. An angular deceleration of 1 arc sec/sec^2 would stop this rotational rate in 15 seconds elapsed time. Typical maneuvering will not approach these acceleration levels.

The primary structure is supported at three back surface nodes at the corners of an equilateral triangle of sides 391 m (1,283 feet). These nodes are grounded in the structural analysis. This represents a typical mounting condition. For thermal distortion minimization, a kinematic mount would be better. It would allow uniform growth without distortion and make the antenna structure insensitive to dimensional changes in the supports. It would, however, increase distortion resulting from forces transmitted through the support interface. If either thermal distortion or acceleration distortions is critical the situation could probably be improved by redesign of the support system.

The rms slope error in arc minutes in given in Table 2-12 for the six standard loading conditions. Distortion and resulting slope error is not as severe in the primary

Table 2-12. Generalized rms slope error (arc min) resulting from maneuvering accelerations.

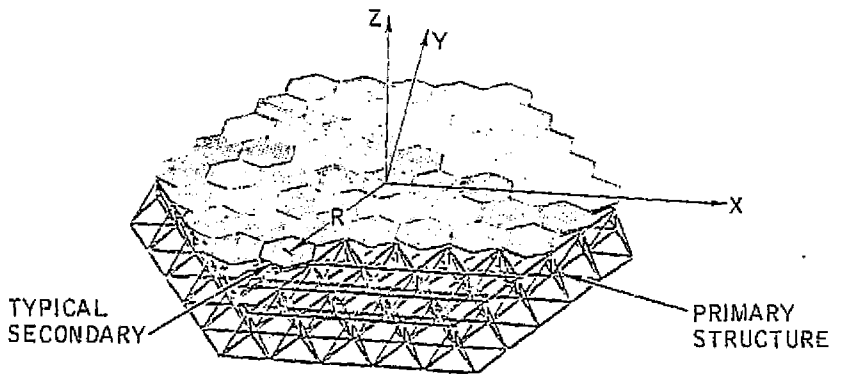

ACCELERATION	PRIMARY STRUCTURE CONFIG. A	PRIMARY STRUCTURE CONFIG. B	SECONDARY STRUCTURE	OFFSET CG ALLOWANCE	TOTAL RMS SLOPE ERROR
10^{-3} G X	0.668	0.653	0.349		0.754
10^{-3} G Y	0.668	0.653	0.349		0.754
10^{-3} G Z	0.576	0.574	1.697		1.792
1 ARC SEC/SEC^2 X	0.302	0.295	0.055	0.409	0.511
1 ARC SEC/SEC^2 Y	0.302	0.295	0.055	0.409	0.511
1 ARC SEC/SEC^2 Z	0.019	0.017	0.003	0.059	0.062

structure for disturbances on the Z axis as for the in-plane axes. The secondary structure is supported at three added back surface nodes at corners of the hexagonal planform. It is particularly sensitive to Z axis acceleration because of the large span, heavy nonstructural mass loading, and relatively small depth.

A slightly different rms slope error is given for the primary structures of configurations A and B. The primary deflections are essentially the same, but the slope error distributed over the secondary is somewhat different for the individual flat plates of configuration A, and the continuous secondary surface of configuration B. The larger value is used in the estimation of total rms slope error. The differences will be discussed in the Section 2.8 comparison of the inherent flatness of A and B configurations.

The slope errors shown for the secondary structure are small for angular rotations about the center of the structure. If the secondary structure segment is located at some radius, R, from the center of the primary, an additional linear acceleration is computed. The radius of gyration is used as the representative radius of the secondary structures. The resulting distortions are listed as the offset allowance.

The final total rms slope error is estimated to be the RSS of the contributing slope errors of the primary and secondary structures.

2.5.2 TOLERANCE BUILDUP EFFECTS ON RMS SLOPE ERROR — Manufacturing tolerance in strut length results in internal loads in the assembled structure, and initial deformation of the flat surfaces. The easiest way to simulate strut length variation is to enter varying temperatures for each strut in the structure. These temperatures, in conjunction with a constant nonzero CTE, simulate a dimensional distribution. The finite-element analysis then computes the induced loads as a result of the strut length variation. Finally, with the stiffness matrix, the equilibrium deflections and residual stresses are computed.

For this analysis, a temperature distribution with a standard deviation of 16.7C (30F) and a CTE of 1.8 μ/m/C (1 μin./in./F) were used. For the primary structure, the normally distributed temperatures were computed for each of 660 struts. For the secondary structure (one representative hexagonal element) temperatures were computed for 1302 regular struts and 9 supporting tripod struts. Six separate cases were constructed for both the primary and typical secondary structure for a minimum size Monte Carlo-type analysis. The worst case results are reported in Figure 2-49.

The reference error size is 1 part in 10,000 (1σ). This is equivalent to a $\pm$ 3.9 cm (1.5 inch) tolerance on primary struts. This allowance covers the node-to-node path so must include strut length variation, joint tolerances and junction fitting tolerances. Secondary strut tolerance is essentially $\pm$ 3.2 mm (0.13 inch).

The dominant error source is the secondary strut distortion. This appears to result from the somewhat greater diameter to thickness ratio of the secondary. The final numerical value of rms slope error would be unacceptably large, however, the actual

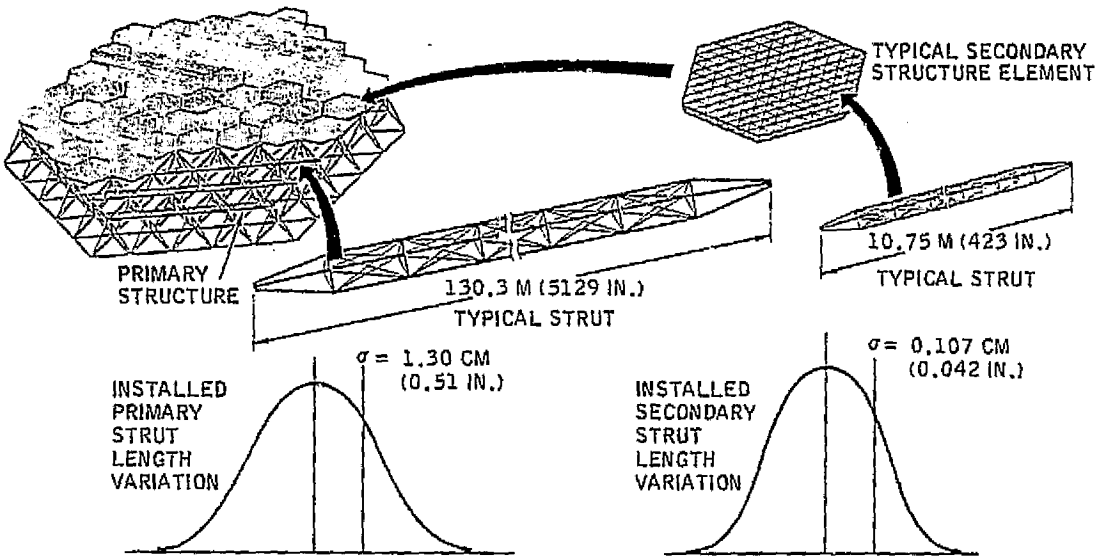

EFFECT OF 1 PART IN 10,000 (1σ) ACCURACY IN NODE-TO-NODE LENGTH OF INSTALLED STRUT

PRIMARY STRUCTURE		SECONDARY	TOTAL RMS
CONFIG. A	CONFIG. B	STRUCTURE	SLOPE ERROR
1.215	1.091	2.275	2.579

Figure 2-49. Generalized tolerance buildup effects rms slope error (arc min).

manufacturing and assembly tolerances should be less than 1 part in 10,000. At any rate, tolerance buildup is a critical area, suggesting that initial alignment and adjustment may be necessary at time of assembly.

2.5.3 EFFECT OF CTE AND TEMPERATURE CHANGE — The properties of GY-70/X-30 pseudoisotropic material were used to represent the anticipated CTE. A normal distribution of CTE is used with a mean value of -0.038 μ/m/C (-0.021 μin./in./F), and a standard deviation of 0.072 (0.040). For a temperature environment, a uniform temperature rise of 100C (180F) and an additional gaussian distributed 100C (180F) gradient across the entire structure are used.

A constant nonzero CTE coupled with a uniform rise in temperature results in uniform growth (or shrinkage) for the structure except for the distortion introduced by the constraints imposed at the mounting points. Variation in CTE or temperature over the structure results in distortion which causes slope error. The total estimated slope error for a 100C (180F) temperature rise is 0.186 arc min rms. The distortion of the secondary structure predominates, probably because it has a larger diameter to depth ratio. The effects of σ_{CTE} were simulated by generation of random CTE x T products for each element of the structure. The results are shown in Figure 2-50.

In calculation of the effects of the gaussian temperature distribution, both μ_{CTE} and σ_{CTE} are significant. To calculate the distortion resulting from μ_{CTE}, one simulation was conducted with a CTE of -0.038 (-0.021) for all elements and temperatures

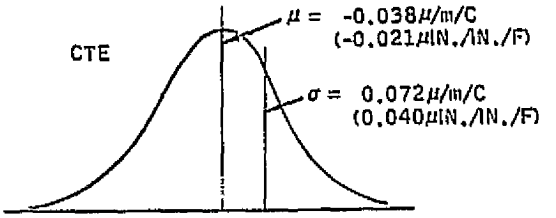

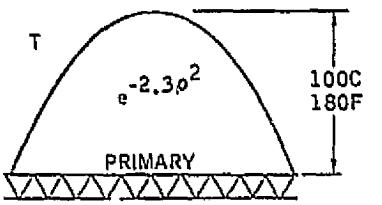

100C (180F) UNIFORM RISE IN TEMPERATURE

	PRIMARY STRUCTURE CONFIG. A	PRIMARY STRUCTURE CONFIG. B	SECONDARY STRUCTURE	TOTAL RMS SLOPE ERROR
σ_{CTE}	0.087	0.079	0.164	0.186

100C (180F) EXPONENTIAL TEMPERATURE GRADIENT

	PRIMARY STRUCTURE CONFIG. A	PRIMARY STRUCTURE CONFIG. B	SECONDARY STRUCTURE	TOTAL RMS SLOPE ERROR
μ_{CTE}	0.009	0.009	0.000	0.130
σ_{CTE}	0.034	0.034	0.125	
			OVERALL TOTAL	0.316

Figure 2-50. Generalized rms slope error (arc min) resulting from temperature change.

computed for each element based on its radial position in the primary structure. The secondary structure does not have a significant gradient over each hexagonal element, and therefore has no contributing slope error. The CTE x T product for each structural element of the primary was computed for the random normally distributed CTE, $\sigma = 0.072$ (0.040) and the gaussian temperature. The response of the secondary structure is computed by rms calculation of the individual secondary structures each with a uniform temperature rise corresponding to its position on the primary. The combined effects result in a predicted 0.130 arc min rms slope error.

The overall total is taken as the sum of the uniform and gaussian slope errors because the two would be expected to be correlated since the type of distortion is similar for both. The overall total rms slope error is 0.316 arc min. In Task 2 (refer to Section 3.2), the actual temperature distributions are computed for different positions in orbit, and the slope errors examined in detail.

2.5.4 RMS SLOPE ERROR RESULTING FROM VARIATION IN Et — In the manufacture of graphite/epoxy tubes, the diameter is determined by tooling and is relatively constant from part to part. The thickness, t, of the laminate (tube wall) varies with material thickness and variation in cure. The properties of the laminate are measured for specimens that vary in thickness. Frequently, the variation in E measured will be greater than for the product Et because the thicker specimens result from a surplus of resin matrix which does not contribute significantly to elastic modulus. The E x area product for the truss strut is proportional to Et. Deflections of the flat

surface depend on the variation in E x area from strut to strut. This analysis was conducted to establish the magnitude of slope error resulting from a nominal variation in Et.

The Et product can be varied by distributing either E or t. Variation in t is easier to implement, so inputs were prepared for each of the 660 struts. The area used for the primary strut had a normal distribution with μ = 5,692 sq. cm (0.8823 sq. in.) and σ = 0.3555 sq. cm (0.0551 sq. in.). These numbers were selected to correspond to a measured variation in E for GY-70/X-30 of 6.24 percent of the mean value standard deviation. To complete the model, E was set at 108 GN/M^2 (15.7 MSI), and the CTE at -0.028 μ/m/C (-0.021 μin./in./F).

Distortion results from variation in Et and an applied load. The loading was provided by a uniform temperature rise of 100C (180F) above the stress-free reference 22.2C (70F), and a gaussian 10 dB tapered gradient of 100C (180F).

Because the magnitude of the errors is small, the simulation was not extended to the secondary structure. The secondary distortion was estimated from the ratio of secondary slope error to primary slope error for the effect of CTE variation. The results are shown in Figure 2-51. Variation in elastic modulus is not a significant error source.

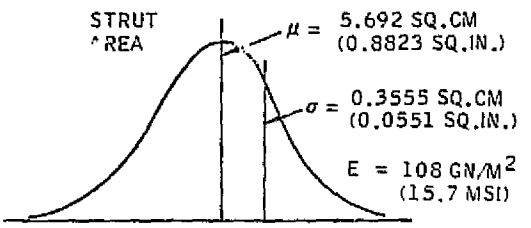

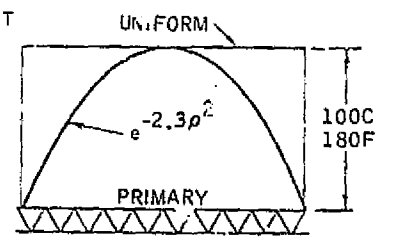

100C (180F) UNIFORM RISE IN TEMPERATURE

PRIMARY STRUCTURE CONFIG. A	PRIMARY STRUCTURE CONFIG. B	SECONDARY STRUCTURE	TOTAL RMS SLOPE ERROR
0.0082	0.0083	0.0156*	0.0176

100C (180F) EXPONENTIAL TEMPERATURE GRADIENT

PRIMARY STRUCTURE CONFIG. A	PRIMARY STRUCTURE CONFIG. B	SECONDARY STRUCTURE	TOTAL RMS SLOPE ERROR
0.0055	0.0056	0.0106*	0.0120

* ESTIMATED FROM EFFECT OF CTE SECONDARY-TO-PRIMARY RATIO

OVERALL TOTAL 0.030

Figure 2-51. Generalized rms slope error (arc min) resulting from variation in Et (modulus x laminate thickness).

2.5.5 POINTING ACCURACY ANALYSIS — Three points at the rear of the primary truss have been used throughout the analysis to establish a reference coordinate system. These are nodes 1034, 1037, and 1066, located at 120-degree intervals on a circle of radius 225.7 meters (8887 inches) around the geometric center of the rear surface. All six degrees of freedom are constrained for these three points. All slope errors computed in this study are with respect to a plane through these points.

Pointing accuracy can be separated into two parts. The first relates to the accuracy of the attitude control system in maintaining this plane normal to the optical axis from the transmitting antenna to the rectenna. This is the pointing accuracy for a rigid body antenna structure. The second relates to the nonrigid body behavior of the antenna under acceleration and as a result of thermal distortion. This deformation causes the beam center to be displaced from the axis normal to the reference plane.

The generalized beam displacements for unit linear and angular accelerations are shown in Table 2-13. The linear accelerations at 1 cm/sec^2 are larger than predicted for worst case expansion of the solar collector. The 0.55×10^{-3} acceleration reported at midterm has been used as the step function excitation for dynamic analysis. This linear acceleration generates a beam displacement of less than 0.2 arc minute from the principal axis. The angular acceleration effect is even less significant. This magnitude of angular acceleration also results in beam displacement from the optical axis of less than 0.2 arc minute.

Table 2-13. Beam displacements for linear and angular accelerations.

LINEAR ACCELERATION (-1 CM/SEC^2)	BEAM POINTING ERROR (ARC MIN)		
AXIS	X AXIS ROTATION	Y AXIS ROTATION	TOTAL ANGLE
X	0.000	-0.319	0.319
Y	0.319	0.000	0.319
Z	0.000	0.000	0.000

ANGULAR ACCELERATION (-1 ARC SEC/SEC^2)	BEAM POINTING ERROR (ARC MIN)		
ROTATION ABOUT	X AXIS ROTATION	Y AXIS ROTATION	TOTAL ANGLE
X	0.141	0.000	0.141
Y	0.000	0.141	0.141
Z	0.000	0.000	0.000

2.6 TECHNIQUES AND PROCESSES FOR PREDICTING (AND MINIMIZING) MISALIGNMENT

Misalignment in the structures is the result of all manufacturing, assembly and adjustment tolerances. It causes the subarray surface in the nominal operational environment to deviate from an ideal flat. It results in LOS error and a loss in power transmission efficiency.

Fortunately, the LOS error is a fixed boresight error which can be corrected by a small bias in the attitude control pointing commands. The rms slope error remaining after the correction for LOS error is relatively random over the surface. It represents a loss of efficiency in power transmission which will exist for the life of the satellite. It is necessary then to predict the magnitude of the misalignment, and take steps to ensure that it is within tolerable limits. Because of the long term stability of graphite/epoxy structures (i.e. creep and microstrain less than a few parts per million length), control of misalignment is an initial manufacturing, assembly and alignment problem. If active control of the surface figure were required to accommodate thermal and acceleration loads from the nominal operational condition, then correction for initial misalignment would be automatic. Since active figure control is not warranted, minimization of misalignment is important.

In Section 2.6, the generalized distortions and resulting rms slope error were computed for a random strut length variation of 1 part (1σ) in 10,000. The result is 2.6 arc min. rms. The budget for the contribution of manufacturing tolerance is 1.5 arc min. rms, or nominally 39 ppm (1σ) variation in node-to-node distance in the primary and secondary structure. The largest part of the slope error budget is allocated to misalignment, and study results have shown that it is the most difficult error source to control within budget.

Table 2-14 lists the potential error sources and their orders of magnitude in ppm of the node-to-node distance. In the following subsections we describe the manufacturing process, and the steps taken to minimize the misalignment loss. The RSS total is equivalent to 0.5 arc min. rms total manufacturing error. This should be acceptable without further improvement.

Table 2-14. Manufacturing and alignment error sources.

Error	Primary, ppm (1σ)	Secondary, ppm (1σ)
Length Determination in Strut	10	10
Joint Tolerance	1	2
Junction Fitting Tolerance	1	1
Thermal Distortion	13	13
Elastic Modulus Effect	2	2
RSS Total	16.6	16.7

2.1.1 MANUFACTURING ENVIRONMENT — The most probable site for manufacture of the structural elements of the primary and secondary structure is in low earth orbit. The feasibility of the MPTS antenna does not depend on the site however, and most of the fabrication may occur on earth, and final assembly of major components may most effectively be done in synchronous orbit. The environment in each case will have a bearing on the accuracy of the assembled structure. The major environmental considerations are:

1. Zero-g or one-g
2. Vacuum or atmosphere
3. Temperature
4. Humidity

The fundamental step in the manufacturing process that most affects structural alignment is measurement of the critical dimensions of each structural element. Whether the manufacturing process for an individual strut makes use of a beam builder, or consists of assembly of finished detail parts, or relies on a single-cure integral beam, at some point the beam must be "trimmed" to its finished length. Trimming can be equivalent to drilling a tooling hole or bonding an end fitting — whatever establishes the final effective length of the part.

Gravity Effects — Handling and measurement of ultra-lightweight struts would be facilitated in the zero or low-g environment of an orbital manufacturing site. At one-g, it would be difficult to support a strut so that its stress-free length could be determined. Supported vertically, from one end, the 130-m (5118-in.) primary strut would stretch 2.5 mm (0.1 in.) or 20 ppm. Using zero-g simulating supports along the length, this elongation could probably be reduced to 2 ppm with high confidence. In a zero-g environment, the true length could be measured.

Pressure Environment — There are no major effects of atmospheric pressure in the manufacturing environment on the achievable structural accuracy. If a shirtsleeve environment is provided for crew, there are important considerations related to maintaining a suitable environment in an enclosed space where graphite fibers and various resin systems and adhesives are being used.

One possible effect on measurement in air atmosphere relates to use of velocity of light in the length determination. If a laser interferometer is used to generate a standard length for coordinating the length of struts, the measurement will fluctuate with the velocity of light in the path. A ranging system such as the Kern Mekometer (Section 3.4) uses an internal cavity as the length reference. It is also sensitive to the velocity of light. For this application, the variation in measurement due to atmospheric density is negligible.

Temperature Environment — The temperature at which the length of a structural element is fixed is very important. If a primary strut is fabricated and trimmed at room temperature and then brought to operating temperature, the stress-free length can change considerably. Using typical values for CTE and operational temperature, a structural element (graphite/epoxy) at the center of the primary structure will shorten

an average of 7 ppm in length. More significantly, because of the distribution in CTE, the actual length change could vary from -47 to +34 ppm. This variation at 13 ppm (1σ) is 26 percent of the overall budget for node-to-node distance variation. It suggests that temperature control is advisable at the time of dimensioning of structural elements.

Humidity — The effect of humidity on isotropic GY-70/X-30 is a microstrain at equilibrium approximately equal to the relative humidity in percent. The process is reversible, and for the thin gages considered for the MPTS, the structures would dry to a stable length within a few weeks at operational temperatures in space. If the structural element is fabricated on earth or in a space facility that has a shirtsleeve environment, a minimum of 20 percent RH is acceptable for operator comfort. Thin wall tubes, panels and other G/E detail parts would be expected to grow to a maximum of 20 ppm in length after about 6 months exposure at normal temperature. The estimated distribution in this growth is 5 ppm (1σ).

This effect is minimized or eliminated by:

1. Fabrication and trimming in a dry or vacuum environment.
2. Manufacturing in a 20% RH environment. Trimming after equilibrium growth has been reached, with allowance made for mean hygroscopic expansion.
3. Using accelerated drying (and thermal cycling) to stabilize structure and then trimming.

Mechanical Stress — Generally the strut or fitting should be stress free at time of trimming. There may be exceptions. A strut with nominal E and F values would have a microstrain of 1000 at ultimate loading conditions. If we know that it will be loaded because of gravity gradient or rotational accelerations in the operational environment, we can predict the nominal length change. The options are:

1. Trim under nominal operational stress level.
2. Bias trim to compensate for known load.
3. Trim to standard length.

The third option is probably valid. Although the deflections under load may be hundreds of ppm, this only occurs at a few struts near the hub, and the result is a rigid body rotation of the antenna. This leads to mechanical pointing error which is corrected by attitude control.

2.6.2 MATERIAL PROPERTIES — Thermal distortion results from variations in the coefficient of thermal expansion, and the elastic modulus. The latter causes thermal distorting because of the redundant load paths in the three dimensional structures. If the structure is aligned at one temperature, and operated at another, variation in E will cause misalignment even though uniform growth would be expected for a constant CTE. Since the misalignments from these sources are the result of manufacturing and initial alignment, they are correctable or can be minimized in the manufacturing process.

If uncorrected, the maximum random strut length variation for CTE effects and E effects are 13 and 2 ppm respectively for the structures. This assumes that the properties of GY-70/X-30 are achieved by the selected G/E composite. We can eliminate E as an error source. It may be advantageous to use materials with greater variation in E as a cost saving or logistics benefit. Unfortunately, CTE for graphite fiber is correlated with E so that close tolerance on CTE which is necessary will probably automatically keep E within limits to make its effect negligible.

Control of CTE will be facilitated by automated processes which will increase the uniformity of fibers, matrix composition, fiber volume, lamina thickness, ply angles, and cure and postcure processes.

2.6.3 ASSEMBLY PROCESSES — In the node-to-node structural path, there are two major joints in either the primary or secondary configurations. These are at the junctions of the struts and the junction fitting. The designs considered are based on a "zero slop" joint. This means that once joined, length through the joint does not vary because of looseness in the joint. In the initial assembly, there is tolerance, however, and this contributes to misalignment. With the low loads involved, the joint can be made with a small pin in coordinated tooling holes. Joint tolerance can be made arbitrarily small. If we include the drilling of the holes, after the correct length has been established as part of the joint tolerance, the result is a conservative $\pm 250\mu$ ($\pm$ 10 mils) tolerance for the primary joint and $\pm 50\mu$ ($\pm$ 2 mils) for the secondary. This is equivalent to a standard deviation of 118μ (4.64 mils) for two joints in the primary strut, and 23.5μ (0.93 mils) in the secondary. These are equivalent to 1 ppm, and 2ppm for the respective strut lengths.

Joint tolerance, if minimized by good engineering practice, does not contribute significantly to misalignment of the assembled structure.

2.6.4 MEASUREMENT OF LENGTH — Final assembly of the truss junction fittings can take place in accurate jigs and fixtures. Trimming, spot facing, drilling, etc. at interface points, if accomplished using typical engineering practices will lead to negligible contribution to misalignment.

The strut itself, because of its length contributes most to uncertainty in node-to-node distance. In Section 3.4, the sensor options are discussed. The present state-of-the-art is 0.5 ppm for optical ranging. This means that master tooling for trimming struts could be held to at least a few ppm if necessary by an active system. Conservatively, an allowance of 10 ppm is made. Actually a small bias error in the master tool for trimming the primary struts would not lead to misalignment of the total structure, but only to uniform growth or shrinkage from the design point. This growth would have no measureable effect on system performance.

If a single stable fixture was used for trimming of all primary struts, and one of a number of fixtures was used for all secondary struts in a single hexagonal secondary structure panel there would be little if any measureable effect. Some adjustment would be required in joining the configuration B secondary panels to account for size variation.

2.7 CONFIGURATION A AND B PASSIVE ALIGNMENT POTENTIAL

In configuration A, the secondary structure is divided into 61 separate, hexagonal, 3-dimensional, truss elements. In our model, 9 additional struts form tripods at three corners for attachment of the secondary element to the supports on the primary nodes. Configuration B has a continuous 3-dimensional truss secondary structure. Three struts are used at each interface location to connect back nodes of the secondary to the support point on the primary. Structurally, there is little difference between the configurations. But, because of the discontinuities in configuration A secondary structure and the continuous nature of configuration B, the two will respond differently to the disturbing conditions that influence flatness.

An objective of this study has been to determine whether either configuration has an inherent advantage in providing a stable, flat, platform for support of the antenna array components. The study conclusion is that:

1. On the basis of slope error, neither approach has a clearcut advantage.
2. Configuration A is the least complicated for simulation and analysis.

In Task 2, deflections were computed for orbital thermal conditions. In this more detailed analysis, a 10 dB illumination taper was used to establish a weighting function in the determination of rms slope error. This equivalent field strength distribution weights the outer edge at only 1/3 the value of the antenna center. Since configuration B tends to transfer distortions out to the edge, it showed a consistently lower rms slope error than configuration A.

Configuration B is difficult to analyze because the secondary structure is a homogeneous plate attached at 75 nodes of the primary. Since it carries bending stress it can cause distortion in the primary. The secondary structure was approximated by a 28-term polynomial surface. It is equivalent to a continuous plate supported on stiff springs at 75 primary nodes. It tends to smooth out primary distortions.

2.7.1 MODELS OF THE SECONDARY STRUCTURE SURFACE — The secondary structure is supported on 75 interface nodes on the primary structure. The surface represented by 10.309 front surface nodes of the secondary structure has different characteristics for configurations A and B. In particular, the continuous surface of configuration B responds differently than the separate flat hexagonal plates of contiguration A when distortion exists in the primary structure (see Figure 2-52).

The procedure of computing rms slope error resulting from primary structure deflection was as follows:

1. Use finite element analysis to determine the displacement of interface surface nodes of the primary structure.
2. Model the two secondary surface configurations as functions of primary node displacements.

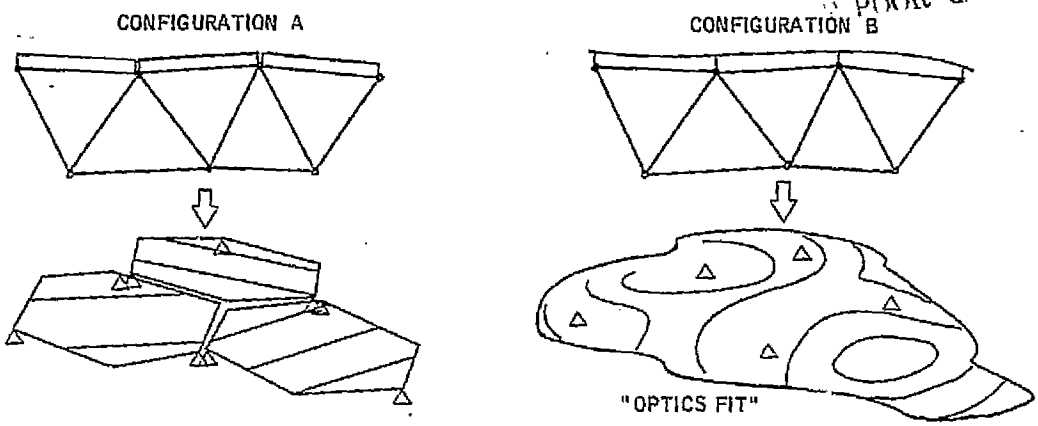

FLAT PLATES

$a_1x + b_1y + c_1z = 1$

$a_2x + b_2y + c_2z = 1$

$\vdots$

$a_{61}x + b_{61}y + c_{61}z = 1$

183 COEFFICIENTS

POLYNOMIAL SURFACE

28 TERMS OF:

$\rho^n \cos m\theta$ & $\rho^n \sin m\theta$

$n \geq m \quad m = n, n-2, n-4 \ldots, n = 0,1,2\ldots$

$a_0 + a_1 \rho\cos\theta + \cdots + a_{27} \rho^6 \sin 6\theta$

28 COEFFICIENTS

Figure 2-52. Surface models for configurations A and B.

3. Compute slope error over the two surfaces.
4. Compute rms slope error for each configuration.

To model configuration A, each hexagonal element of secondary structure is a flat plate. The three coefficients of each plane surface are computed from the three points supporting the surface. A total of 183 coefficients are required. The slope for small angles is $(a^2 + b^2)^{\frac{1}{2}}/(a^2 + b^2 + c^2)^{\frac{1}{2}}$.

Configuration B has a continuous surface. A continuous function with 75 coefficients can be defined that passes through all primary nodes exactly. As in any curve fitting operation, the resulting surface can be erratic between nodes. Use of less coefficients gives a smoother curve, with some compromise in the fit to the support nodes. In this analysis, 28 terms are used in the polynomial fit. In the cylindrical coordinates, all terms to ρ^6 and 6θ are included. To find the coefficients, each set of 75 nodal deflections gives 75 equations in 28 unknowns. These are reduced to 28 equations for a "best fit" solution, and then the coefficients are determined. Once the coefficients are determined, the slope at any point can be computed. The rms slope over the entire surface is computed by numerical integration.

2.7.2 INHERENT SLOPE ACCURACIES OF CONFIGURATIONS A AND B — A primary objective of Task 1 was to determine whether configuration A or B has an inherent advantage in minimizing slope error. There are other considerations such as ease of

assembly analysis, complexity of supports, etc. which are also important. Purely from a slope error standpoint, neither configuration demonstrates a conclusive advantage.

The approach taken has been to compute the distortion of the secondary surface as a result of primary structure deflections. In each case, the simulation was designed to answer some other question about the relationship of slope error to structural or environmental factors but slope error was computed with the two alternative secondary surface models.

There are 52 loading conditions considered of which 32 are orbital temperature conditions. In most of these cases the distortions are low order and the continuous surface of configuration B complies readily. It then gives a slightly higher slope error for the same primary distortions. Results are listed in Table 2-15.

For 6 acceleration cases, configuration B gives slightly lower slope errors and for the 12 random temperature cases, B is considerably lower. These loading conditions, particularly the random cases, result in an irregular higher order surface. The continuous surface of B in the model tends to smooth the small irregularities and indicate lower slope error.

While B shows an advantage, it does so by sharing primary structure loads. Practically, if the B secondary surface is rigid enough to begin to smooth primary deflections, it can also introduce deflections into the primary, and any advantage is probably lost.

Table 2-15. Comparison of slope error for configurations A and B.

NUMBER OF CASES	LOADING CONDITION	SIMULATION	RMS (B) / RMS (A)
3	LINEAR ACCELERATIONS	ENVIRONMENTAL & CONTROL FORCES	0.9842
3	ROTATIONAL ACCELERATIONS	ENVIRONMENTAL & CONTROL MOMENTS	0.9548
6	RANDOM TEMPERATURE DISTRIBUTIONS	MANUFACTURING TOLERANCE RANDOM CTE x TEMPERATURE	0.8930
1	GAUSSIAN 10-DB TEMPERATURE GRADIENT	AVERAGE CTE EFFECT	1.0203
6	RANDOM & 10-DB TAPER TEMPERATURE DISTRIBUTION	RANDOM CTE & TEMPERATURE TAPER	0.8253
23	STEADY-STATE TEMPERATURES	NONECLIPSE ORBITAL CONDITIONS	1.0112
9	TRANSIENT TEMPERATURES	ECLIPSE ORBITAL CONDITIONS	1.0063
1	UNIFORM TEMPERATURE	RANDOM E x X-SECTION	1.0142
TOTAL 52		AVERAGE	0.9701

The conclusion is that B does not show a clearout advantage and A remains the least complicated approach for simulation and analysis.

Configuration A secondary structure hexagonal elements deflect with primary support motion. There is no residual stress after the structure reaches equilibrium. Configuration B, however, exhibits both internal stress and deflections under deflection loading by the primary structure. Configuration B tends to have larger residual stress levels toward the center of the antenna, and larger deflections toward the edge in response to primary structure deflections. The calculated rms slope error over the surface is reduced for configuration B if an illumination taper weighting function is used.

In Task 2, the orbital temperature cases were rerun using a 4-coefficient CTE. Distortions were converted to slope error and a tapered weighting function was used to compute rms slope error. The 23 steady state temperatures gave a ratio of rms of the B configuration to rms of the A of 0.745 (comparable to 1.011 in Table 2-15). The 9 transient cases gave a ratio of 0.886 (compared to 1.007 before).

2.7.3 CONTOUR PLOTS — The difference in behavior of configurations A and B can be seen from the distortion contour plots and slope error plots. In the following figures distortion of the secondary surface, as the result of deflections in the primary, are illustrated. This sequence of contour plots is prepared for each loading condition as part of the postprocessing slope error computation.

In the first plot, Figure 2-53, the edge of each hexagon flat element is not necessarily continuous with the adjacent segments. Each flat segment is supported on three primary structure nodes. In each hexagon, the supporting nodes are at 2:00, 6:00, and 10:00 o'clock.

Figure 2-54 shows the equivalent contours for the continuous surface of configuration B.

Figure 2-55 is the slope error for configuration A. Since the hexagonal elements are flat, primary deflections result in a constant slope error over the individual surfaces. Contours all fall at the intersections of the hexagonal elements. As a result, the slope error is just printed in each hexagon. A conversion factor of 0.166 converts the slopes which are based on radian measure and unit structure radius to arc minute.

Figure 2-56 is the equivalent slope error of the continuous surface.

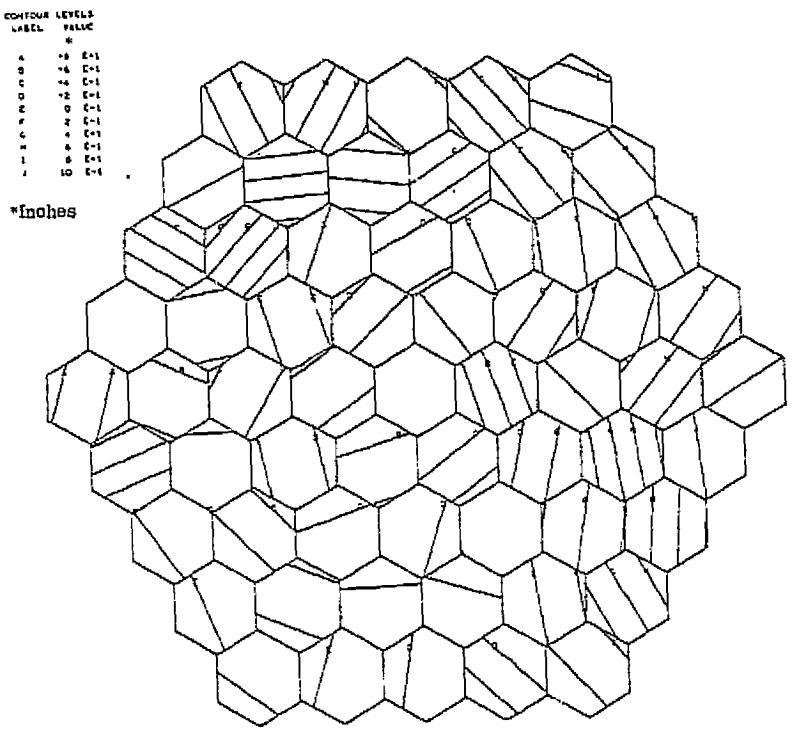

Figure 2-53. Configuration A deflections simulated manufacturing tolerance.

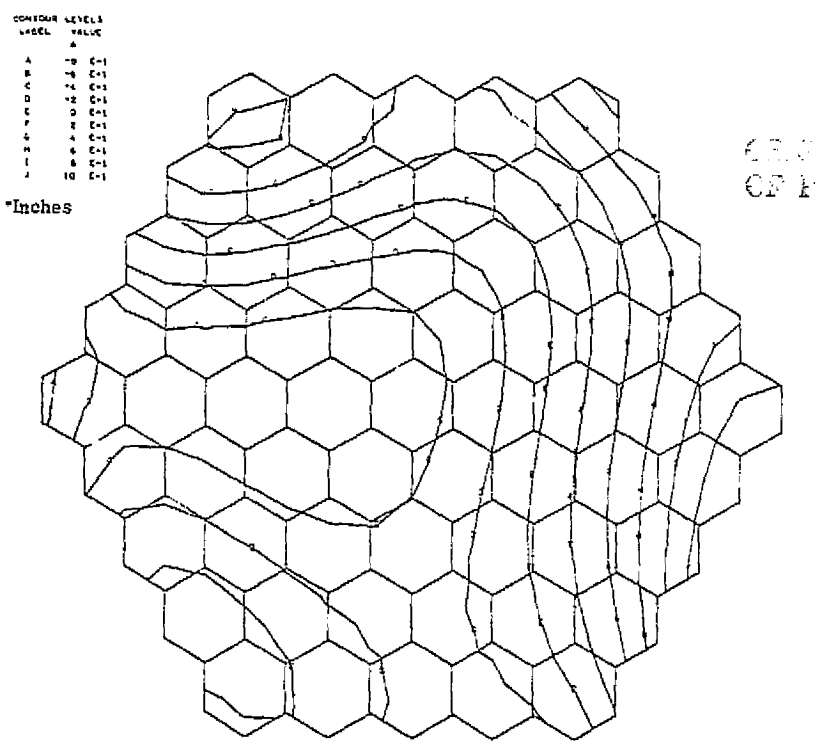

Figure 2-54. Configuration B deflections simulated manufacturing tolerances.

C-2

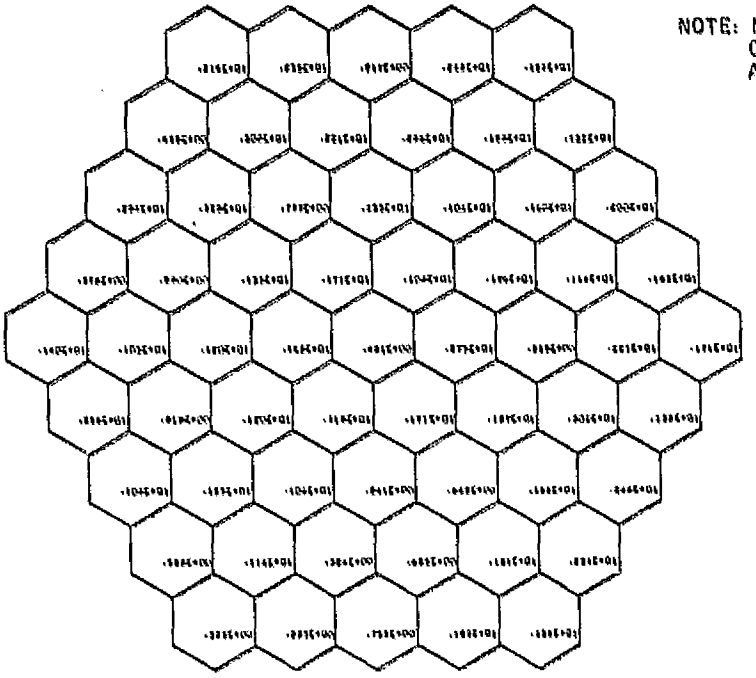

Figure 2-55. Configuration A slope error simulated manufacturing tolerance.

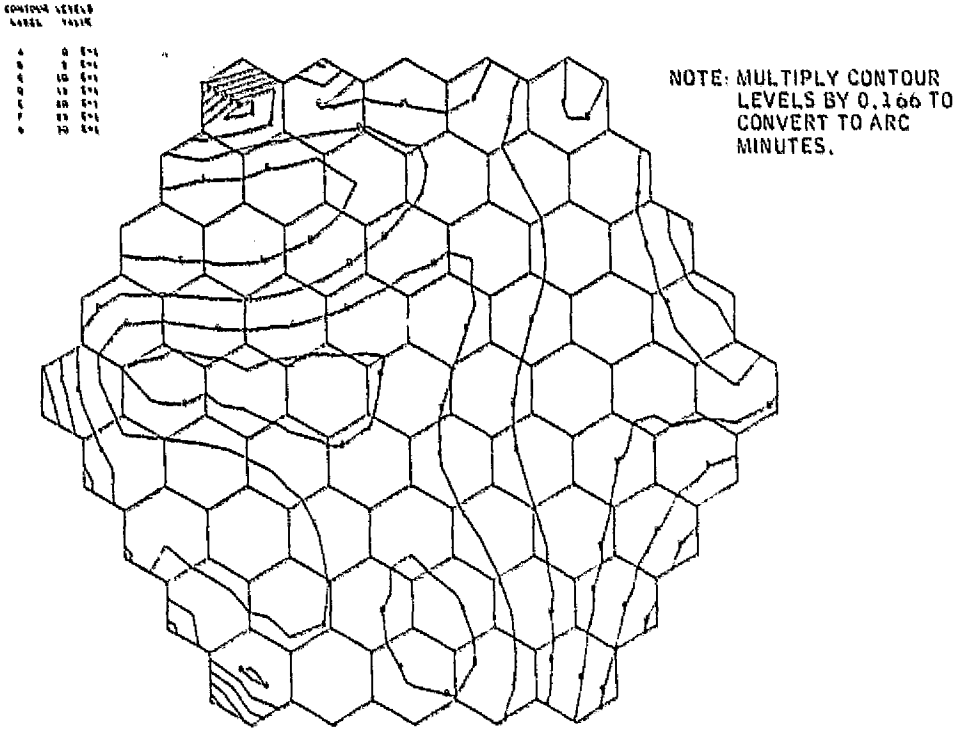

Figure 2-56. Configuration B slope error simulated manufacturing tolerance.

Report No. CASD-NAS-78-011

FINAL REPORT

ACHIEVABLE FLATNESS IN A LARGE MICROWAVE POWER ANTENNA STUDY

(DRL Item No. 2)

3. TASK 2 – OPERATIONAL ENVIRONMENT (ORBITAL) EFFECTS & FIGURE CONTROL

Prepared under
Contract No. NAS9-15423
for
National Aeronautics and Space Administration
LYNDON B. JOHNSON SPACE CENTER
Houston, Texas 77058

Prepared by
GENERAL DYNAMICS CONVAIR DIVISION
P.O. Box 80847
San Diego, California 92138

Report No. CASD-NAS-78-011

FINAL REPORT

ACHIEVABLE FLATNESS IN A LARGE MICROWAVE POWER ANTENNA STUDY

(DRL Item No. 2)

3. TASK 2 – OPERATIONAL ENVIRONMENT (ORBITAL) EFFECTS & FIGURE CONTROL

Prepared under
Contract No. NAS9-15423
for
National Aeronautics and Space Administration
LYNDON B. JOHNSON SPACE CENTER
Houston, Texas 77058

Prepared by
GENERAL DYNAMICS CONVAIR DIVISION
P.O. Box 80847
San Diego, California 92138

3

TASK 2

OPERATIONAL ENVIRONMENT (ORBITAL) EFFECTS AND FIGURE CONTROL

Forces and torques applied to the structure as a result of attitude control and miscellaneous environmental disturbances have been computed along with their effect on surface flatness. The task flow for this analysis is presented in Figure 3-1. When compared to the potential solar collector thermal transients, all other environmental forces and torques have been found to be insignificant in regard to their adverse effects on antenna flatness.

Thirty-two thermal cases have been prepared for an orbit which includes occultation. Equilibrium temperature distributions were prepared for various sun angles before and after shadowing, and transient analysis was used to determine temperatures through the shadow period. These temperatures were then used as loading conditions for the structural analysis program.

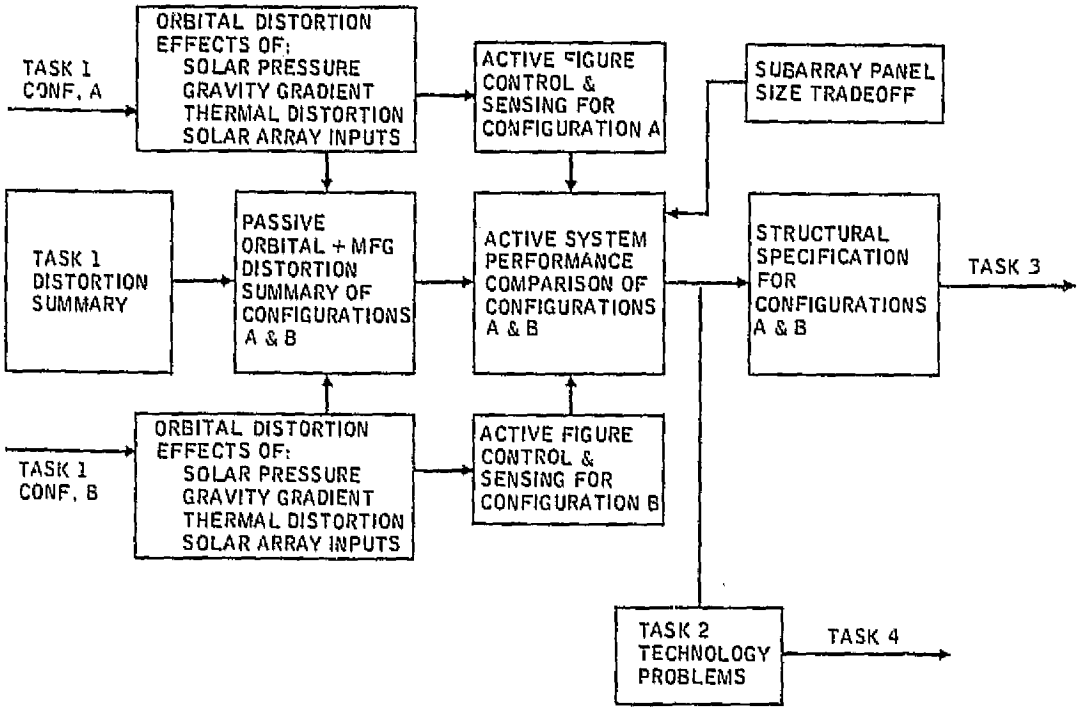

Figure 3-1. Task 2 — study flow.

PASSIVE FIGURE CONTROL CONFIGURATIONS

In all cases, the distortions and associated rms slope error are within the original slope error budget. The most critical error source is manufacturing tolerance.

ACTIVE FIGURE CONTROL CONFIGURATIONS

The primary candidate is for initial alignment to correct for manufacturing tolerance. Reduction of distortion resulting from maneuvering accelerations can readily be accomplished by increasing the depth of the structure or the elastic modulus of the material more effectively than by going to an active system. However, maneuvering distortions are small and well within budget. Fully active control would have application for correcting thermal distortion, but slope error resulting from thermal distortion appears to be negligible.

In the subarray panel size tradeoff it was concluded that, if a size change is made, it should be an increase. This results in reduction in complexity of the support structure and improvement in its accuracy.

The following sections develop the details of the study analyses and results.

3.1 OPERATIONAL ENVIRONMENT ANALYSIS

In order to determine whether figure control is required at the individual subarray level, it is necessary to define the disturbances acting on the antenna and evaluate their contributions to distortion. All of the usual space environmental effects such as gravity gradient and solar pressure will be present in addition to several rather unique configuration related disturbances.

3.1.1 SOLAR COLLECTOR THERMAL TRANSIENT — The most severe disturbance will undoubtedly be the transient which arises from the thermal distortion of the solar collector as it moves from full shadow to full sun at the equinoxes. Since a detailed evaluation of solar collector thermal properties is beyond the scope of this study, some assumptions were made in order to establish a worst case. The basic assumption was that the solar collector mass per area will be sufficiently small that the thermal lag in the structure will be negligible compared to the solar collector oscillatory bending period. Time spent in the penumbra was also assumed negligible. Thus the net effect on the antenna was modeled as a step of acceleration applied at the hub. Although the step is somewhat unrealistic, it should provide a good indication of the worst case disturbance.

The solar collector configuration assumed was Configuration 76R from the "Green Book." This configuration is 28 km long and a depth of 563 m was selected. The front to back temperature differential was estimated to be 94.4C (170F) and the temperature increase was estimated to be 220C (400F). A CTE of 9 μ/m/C (5 μ in./in./F) was selected as representative for the solar collector support structure.

The front-to-back temperature difference will cause the collector to start to curve such that the tips (top and bottom) are accelerated away from the sun as indicated on the right side of the sketch in Figure 3-2. Using the estimated data gives the distortion distance of 147.9 m (485.2 ft) relative to the center of the collector. To obtain the tip travel in an inertial frame, the center of mass shift relative to the center of the collector must also be considered. This shift is 49.3 m (161.8 ft) so the motion of the tip is actually 98.6 m (323.5 ft). Estimates of collector bending period are 15 minutes or longer. Sinusoidal motion of 98.6 m with a 15 minute period gives a maximum acceleration of 0.49×10^{-3}g for the bending transient.

The rise in temperature of 220C will cause the collector to lengthen by 27.7 m (90.9 ft) from center to tip as indicated on the left in Figure 3-2. This longitudinal motion will oscillate with a period estimated at 7.5 minutes and the maximum acceleration associated with the oscillator is 0.55×10^{-3}g.

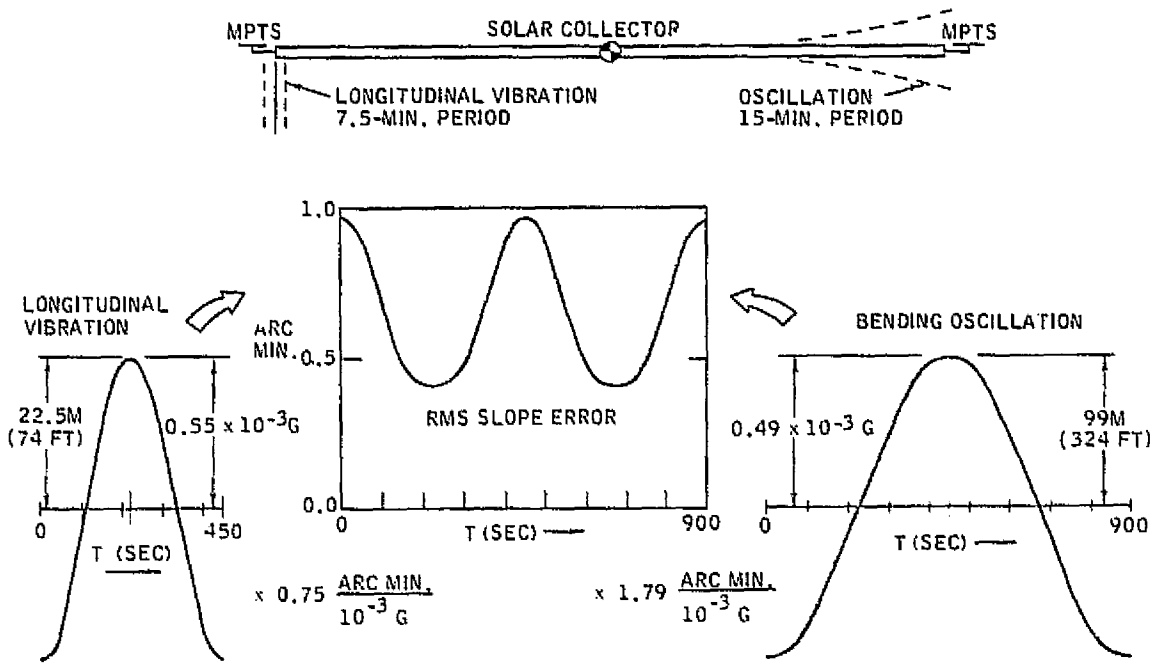

Figure 3-2. RMS slope error after occultation.

3.1.2 POINTING AND TRACKING TORQUES — If the SPS is in a perfect circular equatorial orbit, the only motion of the antenna required for perfect pointing at the earth-based rectenna is a smooth once-per-day rotation. However, since the orbit will be perturbed by earth oblateness, lunar and solar gravity, and solar pressure, the orbit will not be ideal and additional antenna motions will be required to maintain pointing. These antenna motions were calculated in general terms using small angle assumptions for inclination and eccentricity. In addition it was assumed that long term longitude drift was negligible over any one orbit.

The general expression for the pointing angles is given in Table 3-1 where AZ is azimuth (east-west motion) and EL is elevation (north-south). Table 3-2 shows the worst case pointing motions for a rectenna located along the western Canadian border (49.0 degrees North). The motion is indicated in the sketch where the beam axis must sweep out an elipse once per day.

Table 3-1. Antenna pointing relative to orbit reference frame.

POINTING ANGLE		RECTENNA LOCATION	ORBIT ECCENTRICITY	ORBIT INCLINATION
AZ (E-W)	=	$\lambda \cos\phi$	$+ 2 \cos\phi\, e \sin[\omega(t+T)]$	$+ \sin\phi\, I \sin\omega t$
		$r - \cos\phi$		
EL (N-S)	=	$\sin\phi\,(r - \cos\phi)$	$- r \sin\phi\, e \cos[\omega(t+T)]$	$-(r\cos\phi - 1)\, I \cos\omega t$
		$(r - \cos\phi)^2$		

- ϕ LATITUDE OF RECTENNA
- λ LONGITUDE DIFFERENCE BETWEEN RECTENNA & AVERAGE SPS POSITION
- e ORBITAL ECCENTRICITY
- ω SPS ORBITAL ANGULAR FREQUENCY
- t TIME FROM ASCENDING NODE
- T TIME FROM ASCENDING NODE TO PERIGEE
- I INCLINATION OF ORBIT
- r EQUIVALENT CIRCULAR ORBIT RADIUS (IN EARTH RADII)

Table 3-2. Worst case antenna pointing conditions.

ϕ = 49 DEG e = 0.04 I = 7.3 DEG T = 0

POSITION

AZ (DEG) = $0.110\lambda + 1.43 \sin\omega t$
EL (DEG) = $7.26 - 1.01 \cos\omega t$

⇒ RMS SLOPE ERROR $< 2 \times 10^{-4}$ ARC MIN

ANGULAR RATE ($\omega = 7.29 \times 10^{-5}$ RAD/SEC)

AZ (DEG/SEC) = $1.04 \times 10^{-4} \cos\omega t$
EL (DEG/SEC) = $7.36 \times 10^{-5} \sin\omega t$

⇒ RMS SLOPE ERROR $< 5 \times 10^{-7}$ ARC MIN

ANGULAR ACCELERATION

AZ (DEG/SEC^2) = $-7.85 \times 10^{-9} \sin\omega t$
EL (DEG/SEC^2) = $5.37 \times 10^{-9} \cos\omega t$

⇒ RMS SLOPE ERROR $< 2 \times 10^{-5}$ ARC MIN

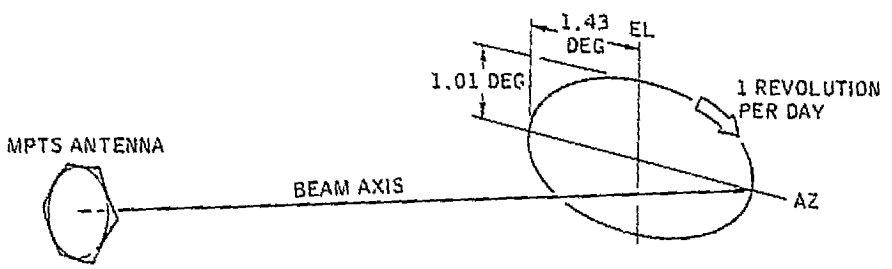

3.1.3 MISCELLANEOUS FORCES AND TORQUES — When compared to the solar collector thermal transient, all other environmental forces and torques have been found to be insignificant insofar as they impact antenna flatness. These disturbances can be insignificant insofar as flatness is concerned and still be quite significant to the pointing control system. Table 3-3 lists these disturbances along with their contribution to slope error. Forces are produced by centrifugal force as the off-axis antenna rotates once per day; by gravity gradient since the antenna is displaced far from the center of mass of the total SPS; by solar pressure; and by rf and heat radiation. Torques arise from rotating about other than a principal axis and from conventional gravity gradient.

Table 3-3. Miscellaneous forces and torques.

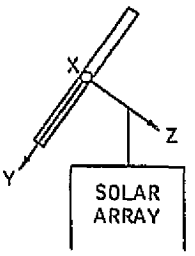

FORCES		N	LBF	RMS SLOPE ERROR (ARC MIN)
OFF AXIS ROTATION	(Fy)	1.3	0.3	
	(Fz)	10.0	2.3	
GRAVITY GRADIENT	(Fy)	582.1	130.9	
	(Fz)	43.8	9.9	
SOLAR PRESSURE	(Fz)	90.0	20.2	
RF & HEAT RADIATION	(Fz)	23.0	5.2	
TOTAL	(Fy)	583.4	131.2	⇨ 0.006
TOTAL	(Fz)	166.8	37.5	⇨ 0.004
TORQUES		**N - M**	**LBF-FT**	
DYNAMIC UNBALANCE	(Tx)	261.7	192.8	
GRAVITY GRADIENT	(Tx)	784.9	587.3	
TOTAL	(Tx)	1046.6	771.1	⇨ 0.001
			TOTAL RMS SLOPE ERROR	0.01

3.2 THERMAL ANALYSIS

The thermal model and the temperature predictions for the large microwave power antenna primary structure are presented. The boundary conditions used in the analysis including the orbit characteristics and the antenna operating conditions (radiated power distribution and waste heat assumptions) are also discussed.

Transient temperature predictions were obtained for the 660 element primary structure at 31 time points in the orbit. The predictions are based on cylindrical strut type structural elements of bare graphite/epoxy material with a solar absorptance (α_s) and thermal emittance (ϵ) of 0.91 and 0.81 respectively. The resultant orbital temperature distributions and corresponding thermal distortion calculations show a maximum slope error of about 0.19 arc-minutes at the end of the earth's shadow (a nonoperating condition). During the illuminated (operating) portions of the orbit, the maximum slope error is about 0.11 arc-minutes.

3.2.1 ORBIT AND ORIENTATION — Antenna thermal gradients, temperature levels, and associated antenna thermal distortions are influenced by the antenna's orientation with respect to the sun and the earth albedo and earth thermal heating. For this large 1 km microwave power antenna, a geosynchronous orbit (altitude ≈19,325 nmi, orbit period ≈24 hours) is specified. The antenna/solar array system orientation is such that the solar array is normal to the solar flux (maximum power generation) whereas the antenna is essentially pointing at the center of the earth (depending on receiver antenna location). For the present thermal analysis, an angle of zero degrees between the earth-sun vector and the orbit plane is employed as shown in Figure 3-3. This case yields maximum solar heating at the subsolar position and thus highest temperatures for the subarray radiator panels. It also yields the maximum earth eclipse time of about 1.16 hours. For the present analysis, a +X flight direction is assumed as shown. No attempt was made to optimize orientation for minimum distortion.

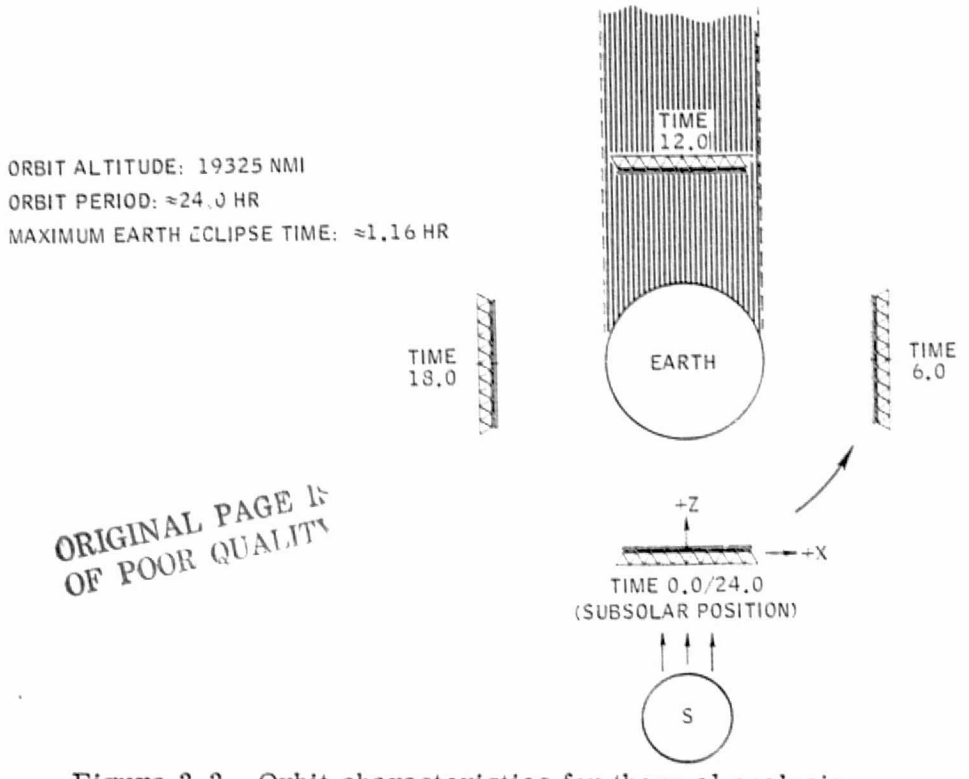

Figure 3-3. Orbit characteristics for thermal analysis.

3.2.2 ANTENNA OPERATING CONDITIONS — The subarrays attached to the antenna structure include an rf radiating surface, equipment for converting dc to rf power, and a radiator surface for disposal of waste heat. The radiators face the antenna backup structure and have a major influence on antenna structure temperatures.

The antenna radiated power distribution shown in Figure 3-4, and used in the present analysis, employs a 10-step 10-dB Gaussian taper (Reference 1, Figure IV.A.2-10). The total of 6.5×10^9 watts net radiated power for the 500 meter radius antenna excludes the power radiated but lost (not directed towards receiving antenna) due to mechanical misalignment.

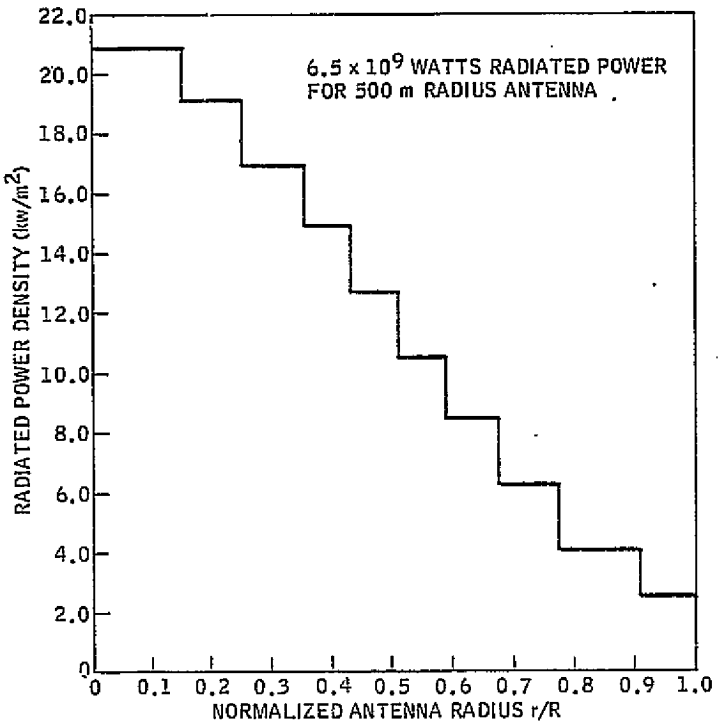

Figure 3-4. Antenna radiated power distribution.

The overall antenna efficiency and the individual component efficiencies shown in Figure 3-5 are based on the data of Reference 1, Figure IV.A.2-6. The typical waste heat calculation shown in Figure 3-5 for the center of the antenna ($r/R \leq 0.15$) shows an input of 25,500 w/m^2 required to yield the output radiated power density of 20,880 w/m^2 shown in the previous figure. The total waste heat (4194 w/m^2 shown for the antenna center) must be rejected from the subarrays. An even split of heat rejection between the rf and radiator sides of the subarrays would yield low thermal gradients across the subarrays and relatively low radiator temperatures. The rf/waveguide side of the array acts as a thermal shield, however, and the majority of the heat will be rejected by the radiator. The 90 - 10% split (suggested in Reference 1) and shown in Figure 3-5 is used in the present analysis.

Waste heat calculations at each step in the power distribution curve were used to obtain the radiator temperature distribution shown in Figure 3-6. Radiator surface thermal properties α_s and ϵ of 0.08 and 0.81 respectively are employed.

At the center of the antenna, the waste heat rejection is highest, and the addition of solar heating has very little effect on temperature. Towards the edge, solar heating is a higher percentage of the total, and daily temperature excursions (during illuminated portions of the orbit) are somewhat greater.

Reference 1. "Initial Technical Environmental Economic Evaluation of Space Solar Power Concepts," Vol. II, Aug. 31, 1976, Lyndon B. Johnson Space Center, Houston, Texas.

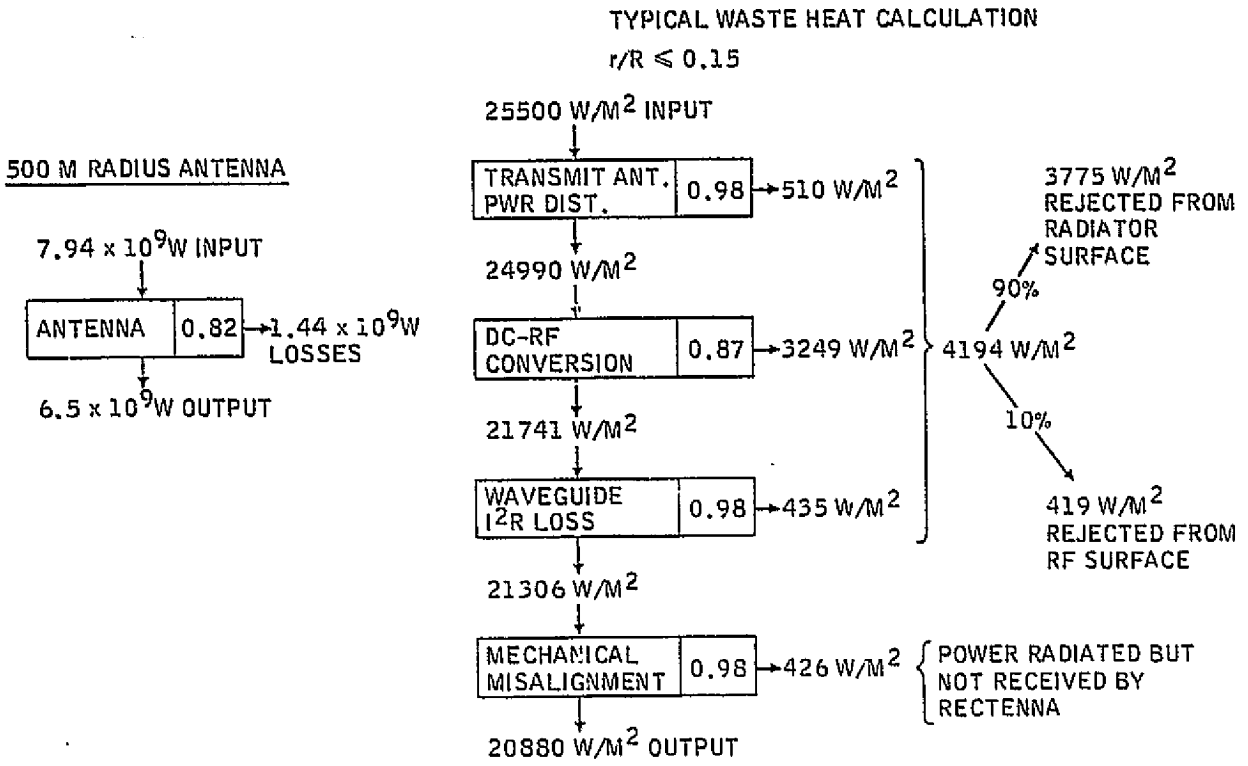

Figure 3-5. Antenna efficiency and waste heat assumptions.

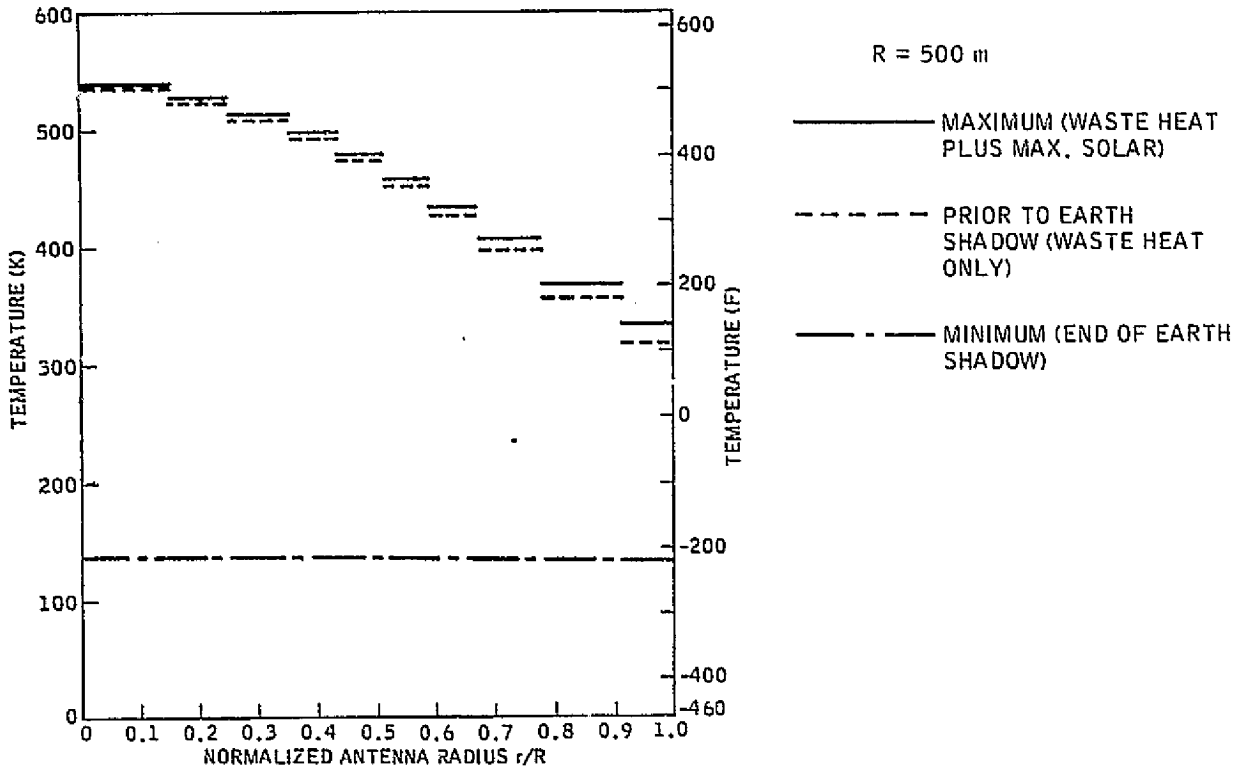

Figure 3-6. Radiator temperature distribution boundary conditions for thermal analysis.

As the antenna/solar array system enters the earth's shadow, power output from the solar array ceases, and all temperatures decrease rapidly. For the present analysis, a radiator thermal inertia is used which yields a minimum temperature of about 135K (-217F) after 1.16 hours in the earth's shadow.

The antenna backup structure temperature distribution is greatly influenced by the antenna power and waste heat distribution and thus the results discussed in the following sections are not necessarily applicable to other power distribution configurations.

3.2.3 THERMAL DESIGN — Due to the low thermal expansion coefficient of the graphite/epoxy composites used for the antenna backup structure, relatively wide temperature excursions and gradients can be tolerated and the required rf performance obtained through the use of passive thermal control methods. For the present analysis, typical surface thermal properties of the bare composite material ($\alpha_s = 0.91$, $\epsilon = 0.81$) are employed. This method yields the simplest and lowest weight system.

3.2.4 THERMAL ANALYTICAL MODEL — To provide temperature predictions for distortion analyses, orbital temperature distributions are obtained. Each of the 660 elements of the primary structure is represented by a cylindrical tube. The depth of the primary structure and its relationship to the subarray radiator surface is shown in Figure 3-7. For each element, an average view factor is obtained to each of the 10 annular areas of the subarray surface representing the steps in the power distribution curve. These view factors are used for determining heat input to the structural elements via the reflections of solar energy and the thermal radiation from the subarray radiator surfaces. The thermal nodal schematics for the symmetrical face, diagonal members, and assymetrical face of the antenna primary structure are presented in Figures 3-8 through 3-10 respectively. These figures also show the 500 m radius outline of the subarrays. Due to the long length of the structural elements, heat transfer via conduction between elements via joints at the intersections is neglected.

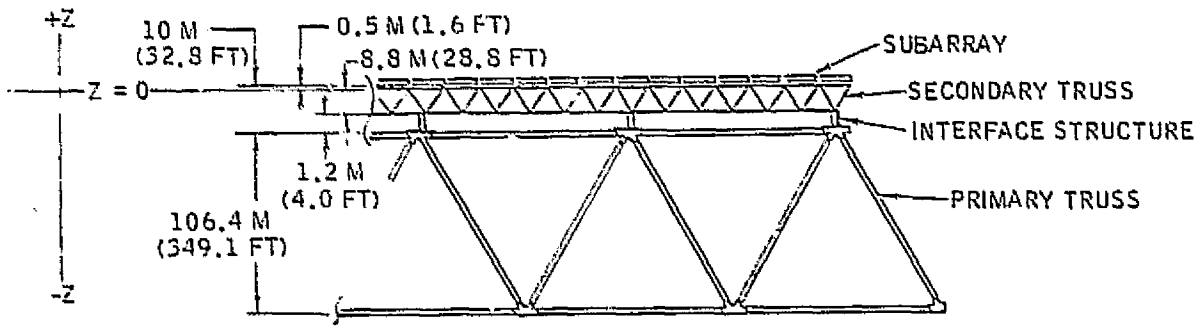

Figure 3-7. Antenna geometry for thermal analysis.

A specialized computer program is employed to determine the direct solar heating rates on the tubular elements throughout the orbit based on the nominal solar constant of 1353 w/m^2 (429 btu/hr-ft^2). For the present configuration and altitude, earth albedo and earth thermal heating rates have very little effect on temperatures and are neglected. The computer program includes the necessary logic to account for shadowing of

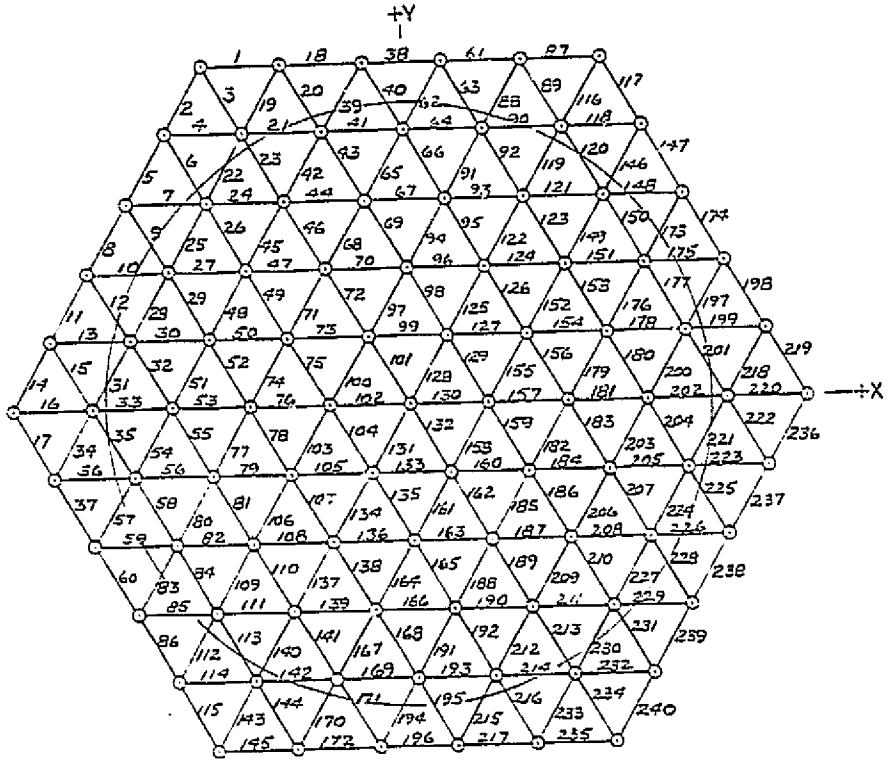

Figure 3-8. Primary structure thermal model (symmetrical face).

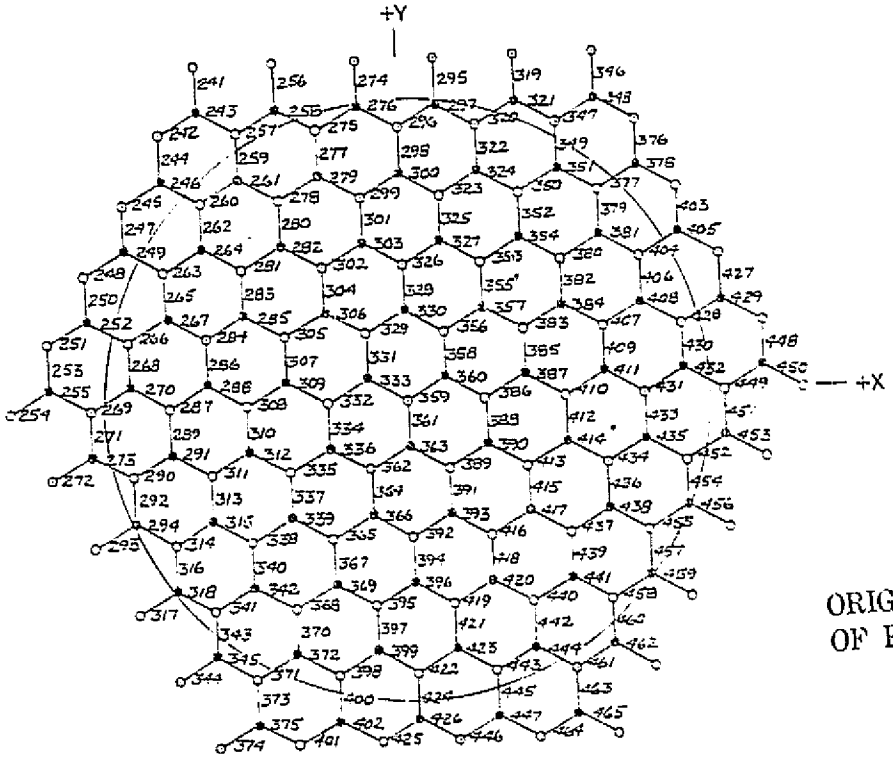

Figure 3-9. Primary structure thermal model (diagonal members).

ORIGINAL PAGE IS
OF POOR QUALITY

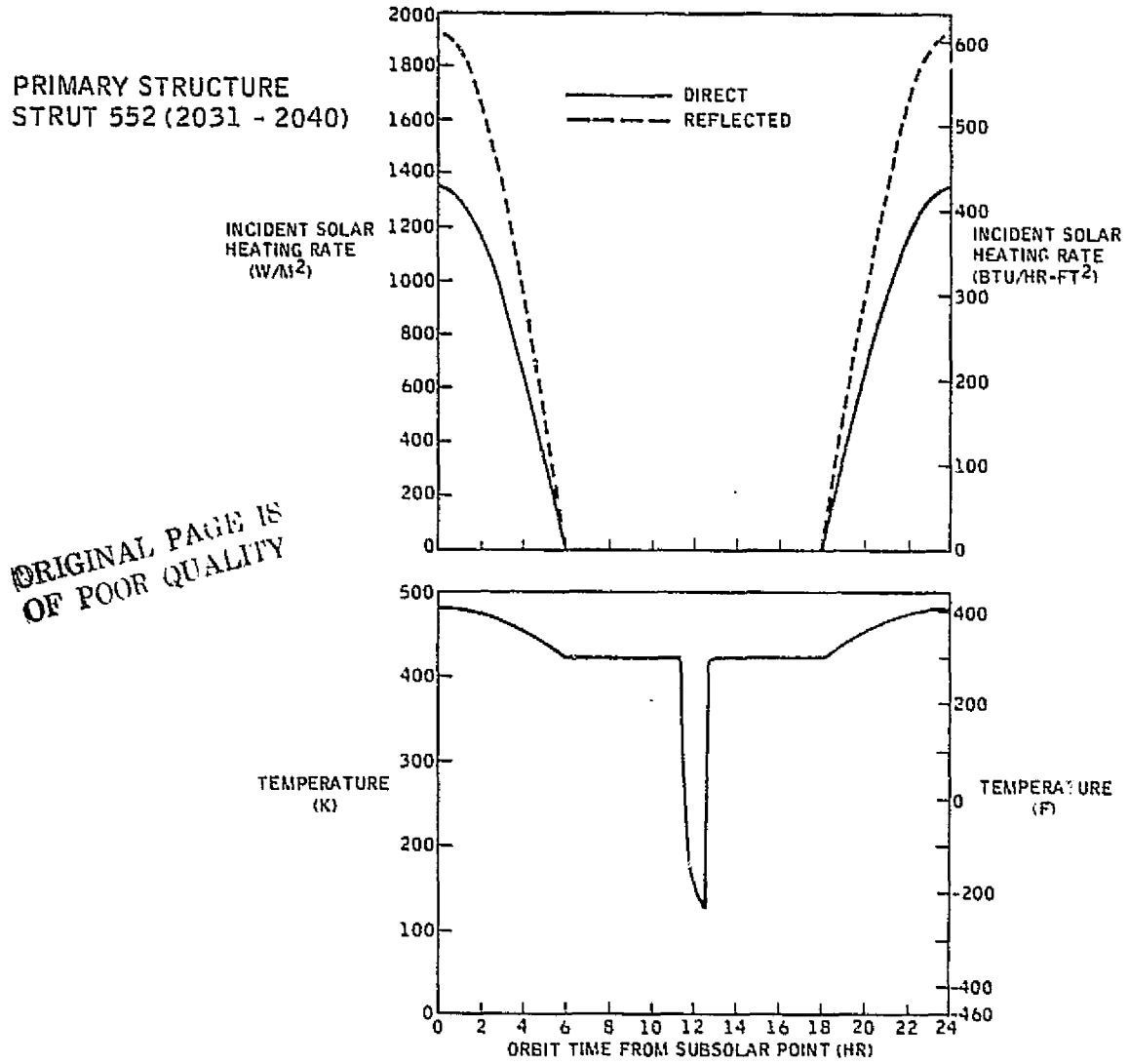

Figure 3-11. Incident solar heating rate and temperature prediction for strut 552.

of subarrays. Partial shadowing by the subarray assembly occurs between time 15.5 and 17.3 hours in the orbit but complete shadowing (by the subarray assembly) occurs for only a short period as shown.

Temperature predictions were developed for each element of the thermal model, and the resulting temperature distributions at 31 time points in the orbit as shown in Table 3-4, were employed in determining predicted orbital thermal distortion.

3.2.5 RESULTS

3.2.5.1 Orbital Thermal Distortion — The orbital thermal distortion results in terms of arc-minutes rms slope error are listed in Table 3-4 and plotted in Figure 3-13. The maximum slope error of 0.19 arc-minutes rms occurs at the end of the earth's shadow

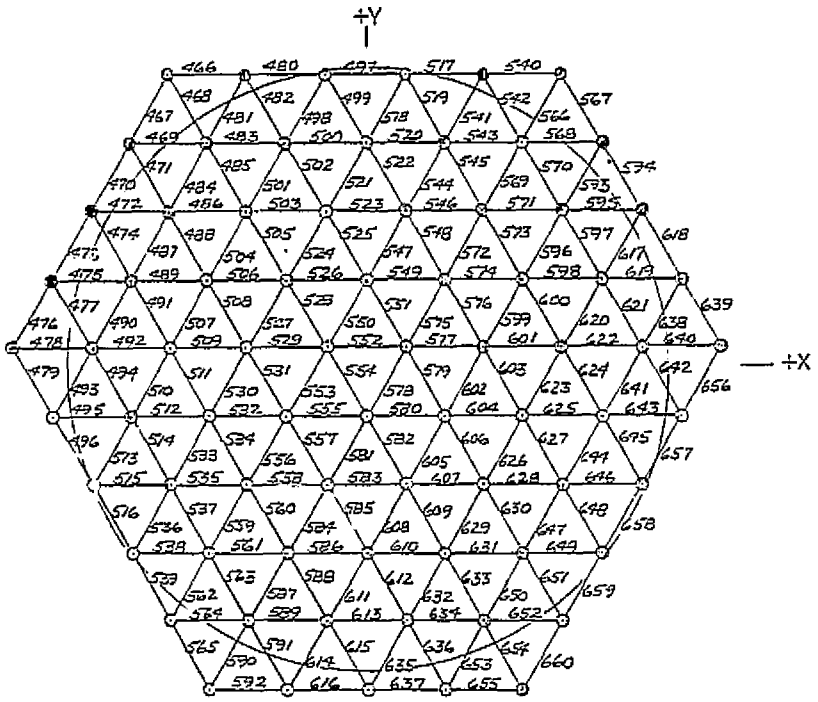

Figure 3-10. Primary structure thermal model (asymmetrical face).

solar energy by the opaque 500 m radius subarray antenna surface. Shadowing by other tubular elements was neglected, since the distance between struts to strut diameter ratio is large and resulting shadows are not well defined (penumbra effects). Logic to account for shadowing of solar energy by a parent vehicle, the solar arrays, and associated equipment is also available but was not employed during the present study. The indirect solar heating rates as a result of reflections from the radiator surface when it is illuminated by the sun are based on diffuse reflections using the view factors mentioned above. These solar heating rates (direct and reflected) and the effects of thermal heating from radiator waste heat rejection are employed to obtain temperatures for each strut throughout the daily orbit cycle.

The heating rates and the resulting transient temperature predictions obtained for two elements (struts 552 and 254) are shown in Figures 3-11 and 3-12 as examples. Strut 552 (Figure 3-11) is located near the center of the asymmetrical face. At the subsolar position (0.0/24.0 hours) this strut is normal to the solar vector, has the highest view factor to the subarray radiators, the highest reflected heating rate, and thus the highest temperature (481K (406F)). Between about 6.0 and 18.0 hours, strut 552 is completely shadowed by the subarray surface and its temperature remains constant except for the large decrease during the earth's shadow period (11.42 to 12.58 hours) as shown. Strut 254 (Figure 3-12) is a diagonal element near the -X edge of the antenna (refer to Figure 3-9). It has the lowest temperature (289K (60F)) at the subsolar position due to its relatively remote position from the edge of the 500 m radius assembly

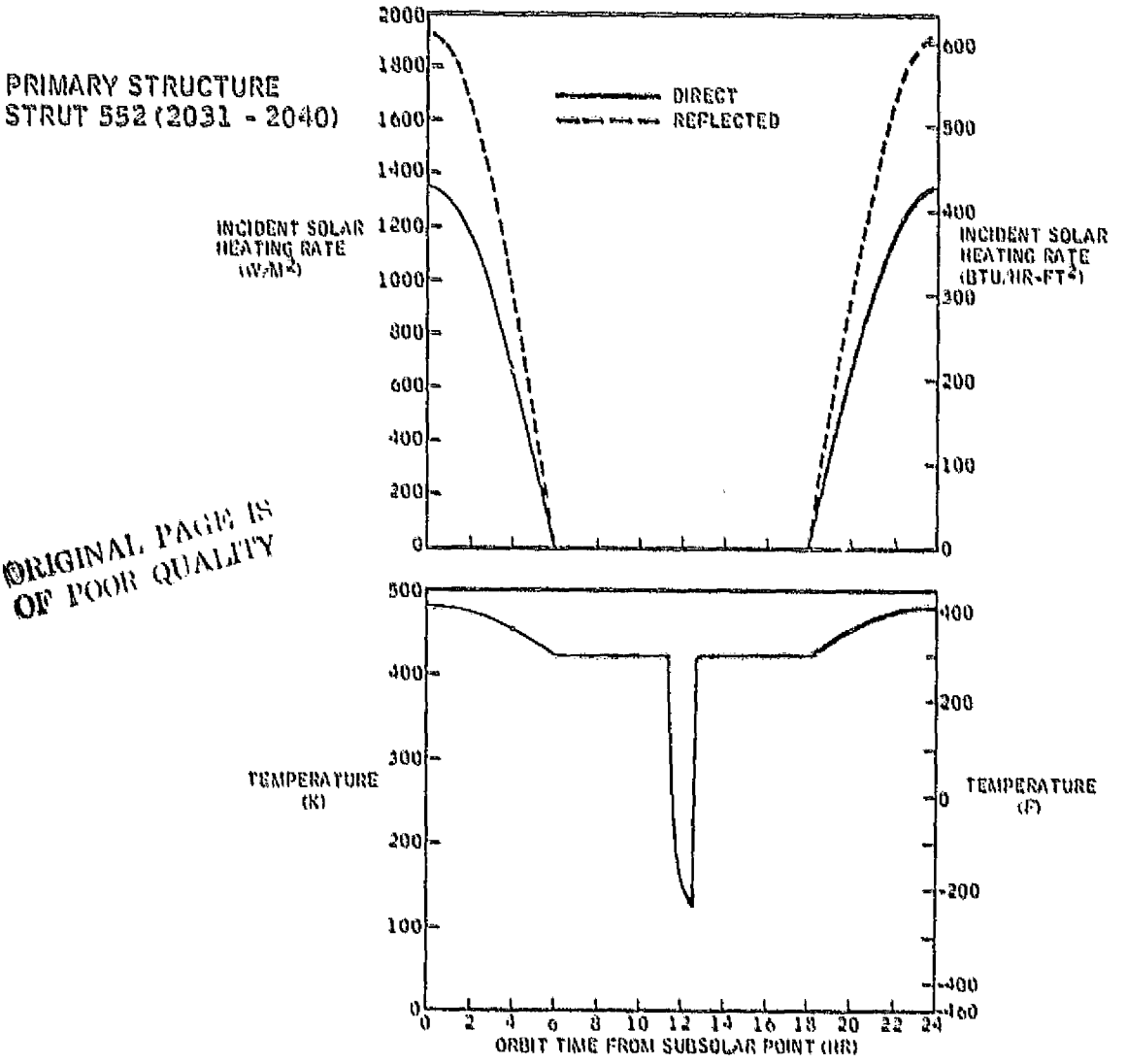

Figure 3-11. Incident solar heating rate and temperature prediction for strut 552.

of subarrays. Partial shadowing by the subarray assembly occurs between time 15.5 and 17.3 hours in the orbit but complete shadowing (by the subarray assembly) occurs for only a short period as shown.

Temperature predictions were developed for each element of the thermal model, and the resulting temperature distributions at 31 time points in the orbit as shown in Table 3-4, were employed in determining predicted orbital thermal distortion.

3.2.5 RESULTS

3.2.5.1 Orbital Thermal Distortion — The orbital thermal distortion results in terms of arc-minutes rms slope error are listed in Table 3-4 and plotted in Figure 3-13. The maximum slope error of 0.19 arc-minutes rms occurs at the end of the earth's shadow

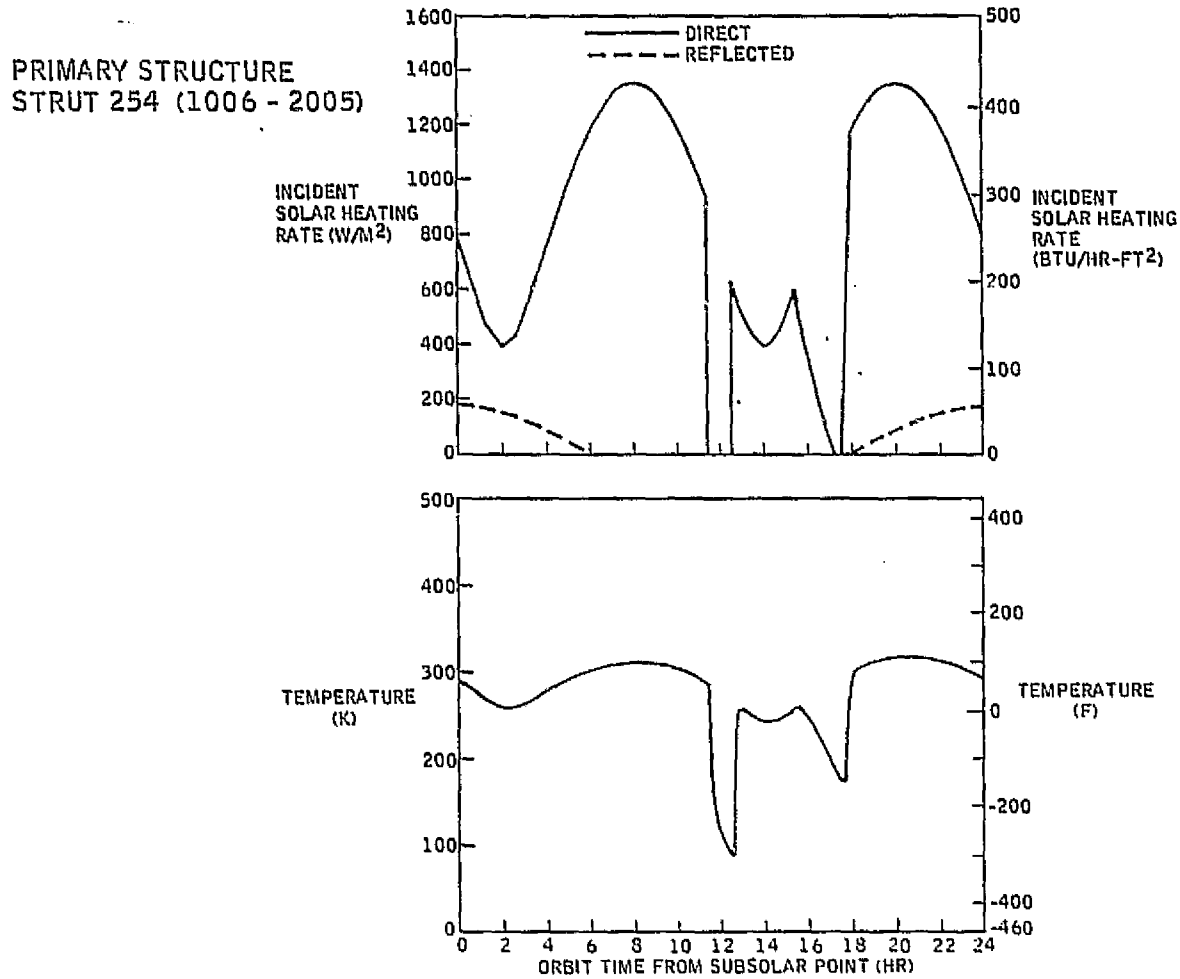

Figure 3-12. Incident solar heating rate and temperature prediction for strut 254.

where the antenna is not operating (no power output from the solar arrays) and the primary structure temperatures are low. During operational (illuminated) portions of the orbit, the maximum slope error of 0.11 arc-minutes rms occurs at the subsolar point where primary structure temperatures are highest.

Figure 3-14 shows the average temperature of the 660 primary structural members and Figure 3-15 shows the difference in temperature between the average of the 100 highest temperatures and the 100 lowest temperatures (an indication of the temperature gradient) during the orbit cycle. Except for the time during the earth's shadow, the temperature gradient parameter is relatively constant (125K to 160K). The decrease in slope error between 0.0 and about 7.0 hours in the orbit shown in Figure 3-13 correlates well with the decrease in the overall average temperature of the 660 primary members of Figure 3-14. Between about 7.0 and 11.42 hours (just prior to the earth's shadow) both slope error and average temperature remain relatively constant. Immediately after entering the earth's shadow, the slope error initially increases slowly as the average temperature passes through the reference temperatures assumed (294K(70F)).

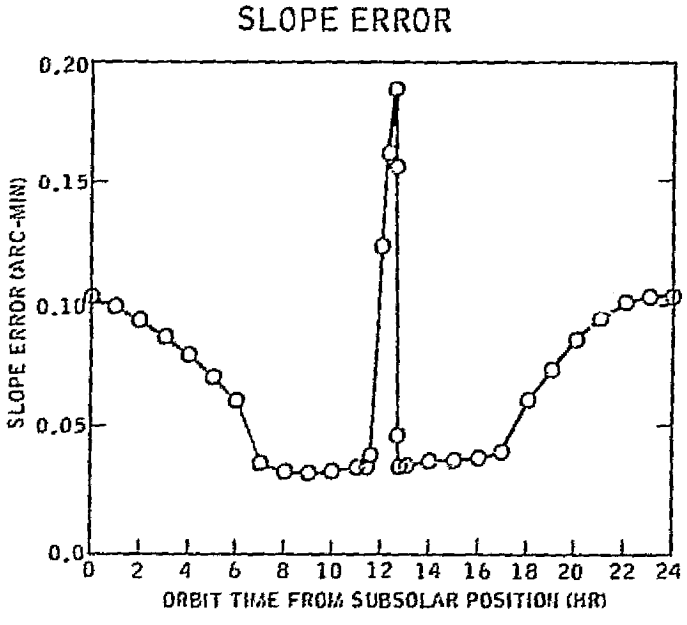

Figure 3-13. Primary structure orbital thermal distortion.

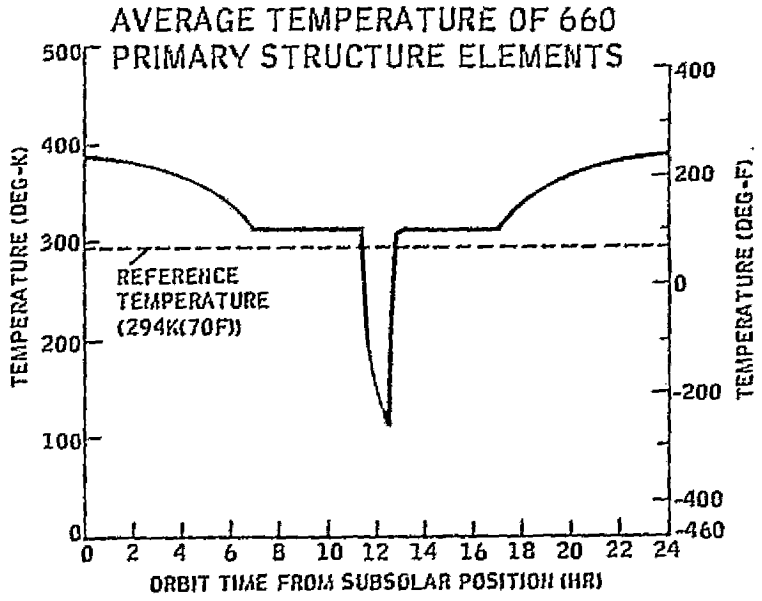

Figure 3-14. Average temperature of 660 primary structure elements.

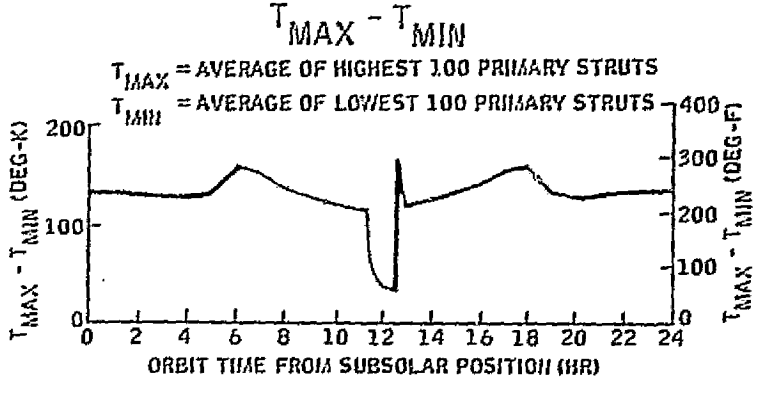

Figure 3-15. Primary structure temperature gradient parameter.

Table 3-4. Orbital thermal distortion analysis cases.

CASE NO.	ORBIT TIME (HR)	REMARKS	SLOPE ERROR (ARC-MIN)
1	0.0/24.0	SUBSOLAR POSITION	0.103
2	1.0		0.099
3	2.0		0.094
4	3.0		0.088
5	4.0		0.080
6	5.0		0.070
7	6.0		0.061
8	7.0		0.035
9	8.0		0.032
10	9.0		0.031
11	10.0		0.032
12	11.0		0.033
13	11.42	START OF EARTH SHADOW	0.033
14	11.6	EARTH SHADOW	0.038
15	12.0	" "	0.122
16	12.3	" "	0.162
17	12.58	END OF EARTH SHADOW	0.188
18	12.62		0.156
19	12.7		0.045
20	12.8		0.033
21	13.0		0.034
22	14.0		0.036
23	15.0		0.036
24	16.0		0.037
25	17.0		0.040
26	18.0		0.061
27	19.0		0.074
28	20.0		0.086
29	21.0		0.095
30	22.0		0.101
31	23.0		0.103

As temperatures continue to decrease (further removed from the reference temperature), slope error increases more rapidly and reaches a maximum when temperatures are lowest. When the antenna emerges from the earth's shadow, slope error decreases as the antenna structure warms up to operating temperature. In summary, it appears that the slope error is a function of the difference between the average temperature of the primary structure and the reference temperature for the present configuration.

The temperature distribution obtained at the subsolar position (highest operational slope error) is presented for the symmetrical face, diagonal members, and asymmetrical face in Figures 3-16 through 3-18 respectively. Maximum temperatures (481K (406F)) occur at the center of the asymmetrical face which is closest to the radiator

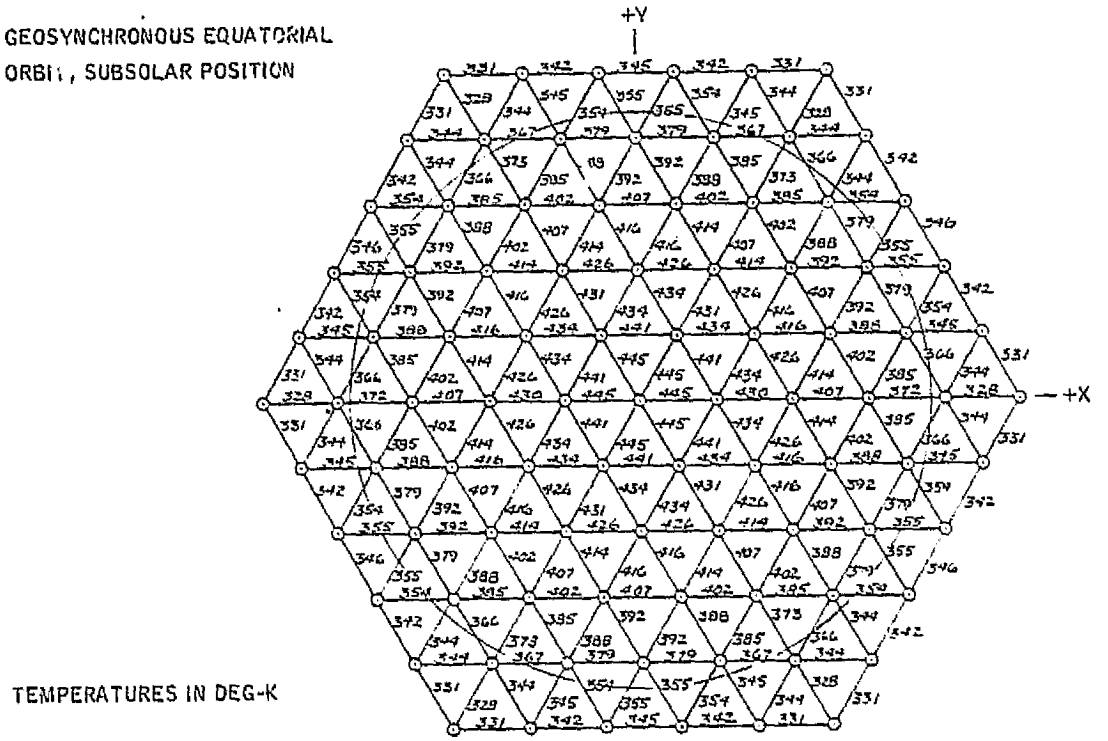

Figure 3-16. Primary structure symmetrical face temperature distribution.

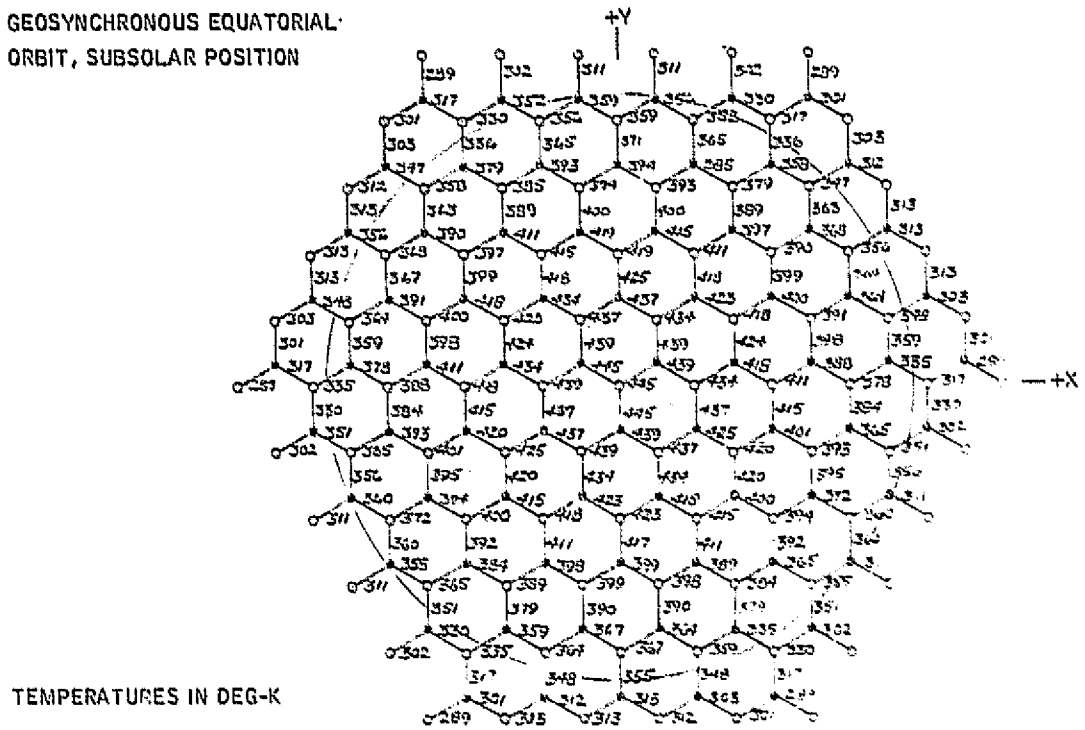

Figure 3-17. Primary structure diagonal members temperature distribution.

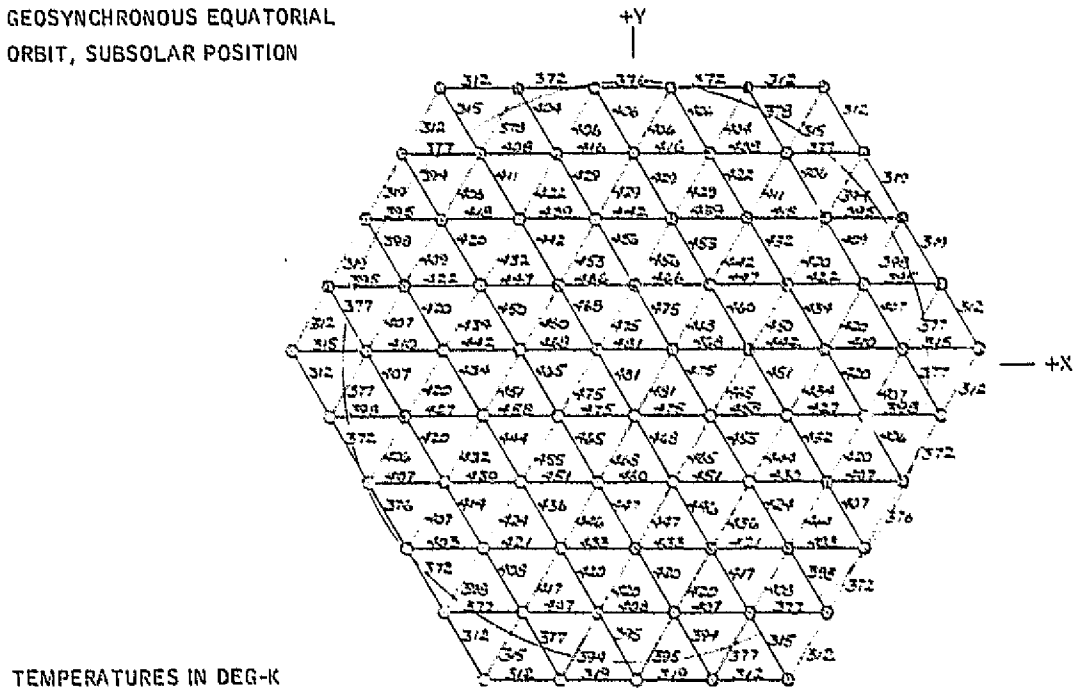

Figure 3-18. Primary structure asymmetrical face temperature distribution.

surface. The diagonal members at the six corners of the hexagonal shape experience the lowest temperatures (289K (60F)). The maximum and minimum temperatures of the three sections of the primary structure at the subsolar position are summarized below.

Subsolar Position	Maximum Temperature	Minimum Temperature
Symmetrical Face Members	445K (341F)	328K (130F)
Diagonal Members	445K (341F)	289K (60F)
Asymmetrical Face Members	481K (406F)	312K (102F)

3.2.5.2 Cylindrical Element Temperature Distribution — The slope error prediction discussed in the previous section is based on strut average temperature displacement from the reference temperature and resulting changes in strut length. The cylindrical strut elements actually have a rather severe local circumferential temperature gradient. A detailed thermal model was developed for a typical 7.62 cm (3.0 inch) diameter, 0.0508 cm (0.020 inch) thick wall isotropic composite tube near the center of the asymmetrical face (hottest location) of the primary backup structure. The multinode model includes the internal radiant heat transfer, circumferential conduction heat transfer, and external radiant heat exchange with the subarray radiator surface and deep space.

Figure 3-19 shows a sketch of the model, the surface thermal properties employed, the sun vector orientations examined, and the results. In Case I, the average temperature is highest but the thermal gradient (between locations A and B) is lowest (47K (85F)) since the tube is heated from both sides (radiator and reflected solar heating on side A and direct solar heating on side B). For Case II the solar heating is 90 degrees to the heating from the radiator and the temperature distribution is not symmetrical. The thermal gradient for this case is about 57K (103F). Although the average temperature is lowest for Case III, the thermal gradient is maximum (63K (113F)) since all heating is on the radiator side of the tube.

Although the maximum average strut temperature is about 480K (404F) as shown for Case I of Figure 3-19, the side of the strut facing the radiator actually experiences a peak temperature of about 505K (449F). Current graphite/epoxy materials have long term maximum operating temperatures of about 394K (250F) and would not tolerate the high temperatures experienced by primary structural members towards the center of the antenna. The polyimide resins can tolerate higher temperatures but further development and testing is required to characterize properties over the wide temperature range.

3.2.5.3 Radiator Configuration Effects — The primary structural element temperature predictions of Section 3.2.5.1 are based on a radiator surface with α_s and ϵ values of 0.08 and 0.81 respectively (typical of efficient radiator surface properties such as silvered teflon). This type of surface reflects solar energy primarily in a specular manner, but a diffuse analysis was assumed. Figures 3-20 and 3-21 show the effect of radiator surface properties on the temperature of struts 552 and 254 respectively at the

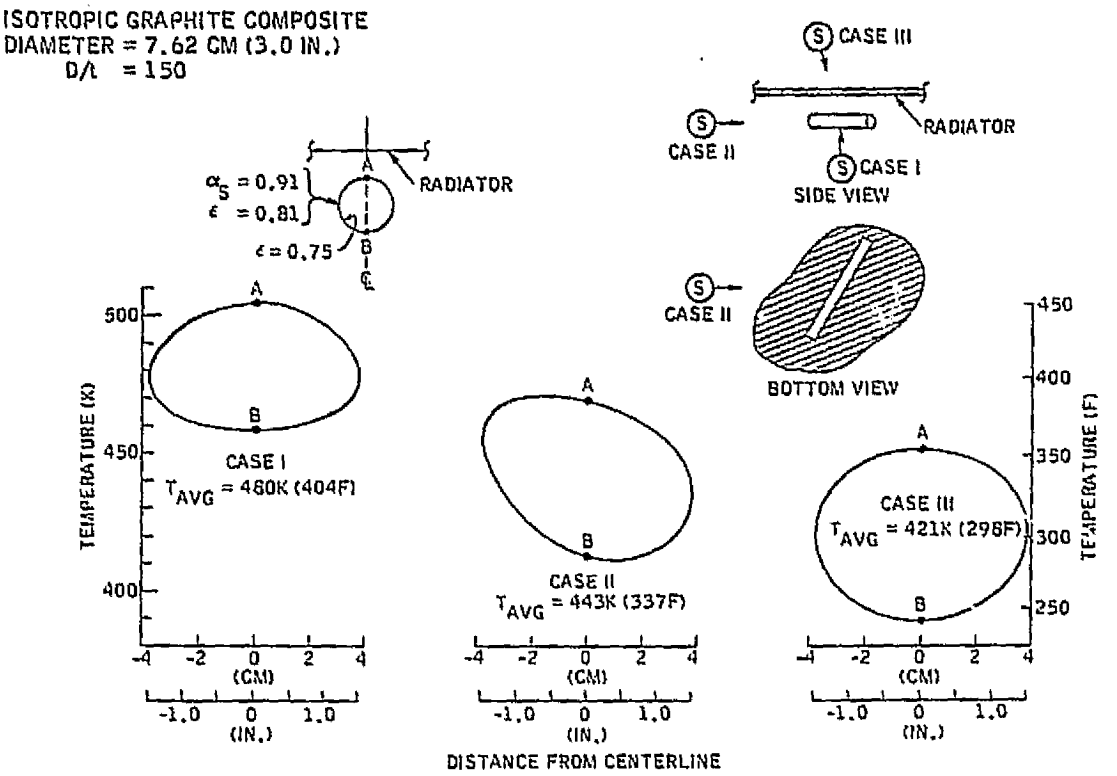

Figure 3-19. Cylindrical strut element circumferential temperature distribution.

STRUT 552 (2031-2040) AT SUBSOLAR POSITION

BARE GRAPHITE COMPOSITE CYLINDRICAL ELEMENT } α_S = 0.91, ϵ = 0.81

VIEW FACTOR TO SPACE = 0.51

VIEW FACTOR TO RADIATOR = 0.49

RADIATOR SURFACE PROPERTIES	EFFECTIVE RADIATOR TEMP. FOR STRUT 552	DIFFUSELY REFLECTING SURFACE — STRUT TEMP.	SPECULARLY REFLECTING SURFACE — STRUT TEMP.
α_S = 0.08, ϵ = 0.81	535.6K (504.1F)	480.7K (405.3F)	470.8K (387.4F)
α_S = 0.40, ϵ = 0.90	536.0K (504.8F)	479.7K (403.5F)	473.2K (391.8F)

Figure 3-20. Effect of radiator configuration on strut element 552 at subsolar position.

STRUT 254 (2006-2008) AT SUBSOLAR POSITION
BARE GRAPHITE COMPOSITE CYLINDRICAL ELEMENT $\alpha_S = 0.91$, $\epsilon = 0.81$
VIEW FACTOR TO SPACE = 0.95
VIEW FACTOR TO RADIATOR = 0.05

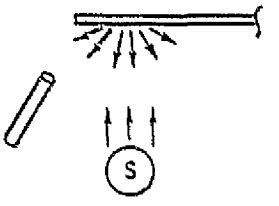

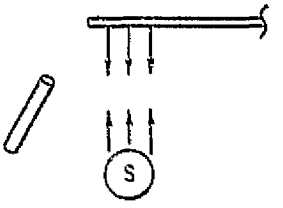

RADIATOR SURFACE PROPERTIES	EFFECTIVE RADIATOR TEMP. FOR STRUT 254	STRUT TEMP. DIFFUSELY REFLECTING SURFACE	STRUT TEMP. SPECULARLY REFLECTING SURFACE
$\alpha_S = 0.08$, $\epsilon = 0.81$	400.1K (260.1F)	289.3K (60.8F)	276.9K (38.4F)
$\alpha_S = 0.40$, $\epsilon = 0.90$	421.4K (298.5F)	288.9K (60.0F)	280.9K (45.6F)

Figure 8-21. Effect of radiator configuration on strut element 254 at subsolar position.

subarray position. A less efficient coating with an α_S of 0.40 and ϵ of 0.90 (typical of degraded white paint) which reflects solar energy primarily in a diffuse manner was also examined.

For the diffusely reflecting radiator surface case, the less efficient coating yielded strut temperature decreases of 1.0K (1.8F) or less. Although the effective radiator temperature (function of radiator array temperature distribution and view factor between strut and radiator) is higher for the less efficient radiator coating, reflected solar heating is less and the result is slightly lower strut temperatures as shown.

A comparison between the diffuse and specular cases shows lower strut temperatures for the latter. Strut 254, for example, which is at some distance from the edge of the subarray assembly, receives no reflected heating at the subsolar position for the specular case as indicated in Figure 8-21. At other orientations, however, strut 254 would receive more reflected energy for the specular case and somewhat higher temperatures would be experienced.

In general, the radiator configuration effects examined yield strut temperatures which are lower by only about 12K (22F) compared to the nominal case employed in the distortion analysis. It is believed that these temperature changes would have only a minor

effect on overall antenna thermal distortion. To fully evaluate radiator configuration effects, temperature and distortion calculations for the complete orbit would be required.

3.2.5.4 Temperature Prediction Error — Temperature predictions presented in Section 3.2.5.1 are based on a nominal solar constant and nominal strut surface thermal properties as indicated at the top of Figure 3-22. The estimated error in the solar constant, the annual variation, and the estimated variation in surface thermal properties is shown in the lower portion of the figure together with their effect on the temperature of both struts 552 and 254 at the subsolar position. The effect of variation in solar constant on radiator surface temperature and reflected heating rate is included in the calculations. The summation of the ΔTs at the bottom of Figure 3-22 shows a prediction error of about ± 10K (± 18F) or less for the two struts examined.

3.2.5.5 DC-RF Conversion Efficiency — As shown in Figure 3-5, a nominal dc-rf conversion efficiency of 0.87 is employed in waste heat and radiator temperature calculations. The comparison of results for a change in efficiency from 0.87 to 0.86 (resulting in more waste heat and higher radiator temperature) is presented in Figure 3-23. For strut 552 at the center of the antenna, the view factor to the array of radiators is high (0.49) and a strut temperature increase of +4.1K (+7.4F) is obtained.

NOMINAL CASE	STRUT #552	STRUT #254
Q_S = 1353 W/M^2 α_S = 0.91 ϵ = 0.81	T = 480.7K (405.2F)	T = 289.3K (60.8F)
VARIABLE		
SOLAR CONSTANT ERROR* Q_S = 1353 $^{+21}_{-21}$ (W/M^2)	ΔT = $^{+1.9K\ (+3.4F)}_{-1.9K\ (-3.4F)}$	ΔT = +1.1K (+2.0F) ΔT = -1.1K (-2.0F)
ANNUAL VARIATION* Q_S = 1353 $^{+46}_{-44}$ (W/M^2)	ΔT = $^{+4.0K\ (+7.3F)}_{-4.0K\ (-7.2F)}$	ΔT = +2.4K (+4.4F) ΔT = -2.3K (-4.3F)
ESTIMATED VARIATION IN α_S α_S = 0.91 $^{+0.02}_{-0.02}$	ΔT = $^{+1.0K\ (+1.8F)}_{-1.0K\ (-1.8F)}$	ΔT = +1.4K (+2.5F) ΔT = -1.4K (-2.5F)
ESTIMATED VARIATION IN ϵ ϵ = 0.81 $^{-0.05}_{+0.05}$	ΔT $^{+3.0K\ (+5.5F)}_{-2.7K\ (-4.9F)}$	ΔT = +4.0K (+7.2F) ΔT = -3.7K (-6.7F)
	$\Sigma\Delta T = ^{+9.9K\ (+18.0F)}_{-9.6K\ (-17.3F)}$	$\Sigma\Delta T = ^{+8.9K\ (+16.1F)}_{-8.5K\ (-15.5F)}$

* NASA SP-8005 (MAY 1971)
EFFECT OF VARIATION IN SOLAR CONSTANT ON SUBARRAY/RADIATOR TEMPERATURE IS INCLUDED

Figure 3-22. Temperature prediction error sources and effects.

Strut 254 at the antenna edge has a low radiator view factor (0.05) and its temperature increases by only +0.5K (+0.9F) compared to the nominal case. The net result is that for a decrease in dc-rf conversion efficiency, both the average temperature of the primary structure and the temperature gradient (between center and edge) increases and an increase in antenna distortion is anticipated.

CHANGE OF EFFICIENCY FROM 0.87 TO 0.86

SUBSOLAR POSITION

	STRUT 552 (CTR OF ANTENNA)		STRUT 254 (EDGE OF ANTENNA)	
	EFF. = 0.87 (NOMINAL)	EFF. = 0.86	EFF. = 0.87 (NOMINAL)	EFF. = 0.86
VIEW FACTOR TO SPACE	0.51		0.95	
VIEW FACTOR TO RADIATOR	0.49		0.05	
EFFECTIVE RADIATOR TEMPERATURE	535.6K(504.1F)	543.0K(517.4F)	400.1K(260.1F)	405.2K(269.3F)
STRUT TEMPERATURE	480.7K(405.3F)	484.8K(412.6F)	289.3K(60.8F)	289.8K(61.7F)
	ΔT = +4.1K (+7.4F)		ΔT = +0.5K (+0.9F)	

Figure 3-23. Effect of dc-rf conversion efficiency on primary structure temperature.

3.3 ERROR BUDGET

Slope accuracy and pointing LOS accuracy budgets were established early in the study to provide guidance in selection of materials and loading conditions, and development of control concepts. The design goal for slope accuracy is 2 arc min rms. This is apportioned to manufacturing, thermal, and maneuvering error sources. The design goal for LOS pointing accuracy is 2 arc min maximum (3σ). This is apportioned to thermal distortion, maneuvering distortion, and the control system accuracy. Manufacturing tolerance does not contribute to pointing accuracy because it is a static misalignment which is correctable by bias pointing.

A budget establishes guidelines, however, the overall goal can be met even if all individual budgeted goals are not met. If necessary, the budget can be revised when critical error sources are discovered.

Manufacturing tolerance is the most critical source in the generation of rms slope error. For material properties of GY-70/X-30, thermal distortion contribution to rms slope error is small, as is distortion resulting from environmental and control system disturbances.

The attitude control system pointing accuracy is the largest factor in LOS accuracy. For the thermal properties of GY-70/X-30, thermal pointing error is small. Actually, the control loop can be closed around the thermal distortion, so that relatively large thermal pointing errors could be offset by suitable pointing correction.

3.3.1 RMS SLOPE ACCURACY BUDGET — The initial slope accuracy budget was as follows:

	Arc Min	Percent Efficiency (Loss)
Required Slope Accuracy	3	98.0 (2.0)
RMS Slope Equivalent	3	98.0 (2.0
RMS Slope Design Goal	2	99.0 (1.0)
Manufacturing Tolerance	1.5	99.5 (0.5)
Maneuvering Accelerations	1.1	99.7 (0.3)
Thermal Distortions	0.7	99.8 (0.2)

In Section 2.3, an rms slope accuracy of 3 arc min was shown to be equivalent in energy transmission efficiency to an antenna having all array elements at 3 arc min slope error. The rms slope accuracy implies a distribution with some panels having greater than 3 arc min slope error, and the majority having less. In either case, the efficiency equivalent is 98 percent. The rms slope design goal is 2 arc min slope error, which is equivalent to 99 percent efficiency.

The major allocation is to manufacturing tolerance, with lesser goals set for maneuvering and thermal distortion effects.

Manufacturing RMS Slope Error Budget

A preliminary rms slope error budget of 1.5 arc min was assigned for combined manufacturing assembly error. From simulation and analysis we have determined the sensitivity of rms slope error to the standard deviation in critical structural dimensions.

No.	Critical Dimension	RMS Slope Error Sensitivity
1	node-to-node assembled primary strut length	0.938 arc min/cm (σ) 2.370 arc min/in. (σ)
2	primary front surface node to secondary interface	0.528 arc min/cm (σ) 1.341 arc min/in. (σ)
3	secondary rear surface node to primary interface	0.528 arc min/cm (σ) 1.341 arc min/in. (σ)
4	node-to-node assembled secondary strut length	21.16 arc min/cm (σ) 53.75 arc min/in. (σ)
5	secondary front surface node to subarray interface	6.40 arc min/cm (σ) 16.26 arc min/in. (σ)

The error budget for each of these dimensions is as follows:

No.	Standard Deviation (cm)	Standard Deviation (In.)	RMS Slope Error (arc min)
1	0.684	0.269	0.638
2	0.100	0.039	0.053
3	0.050	0.020	0.026
4	0.063	0.025	1.323
5	0.050	0.020	0.320
		RSS Total Error	1.504

Items 1 and 4 are the overall primary and secondary structural tolerance respectively. Approximately double the error allowance was made for the secondary structure because preliminary analysis showed a greater rms slope error sensitivity to dimensional error in the structure. This is primarily because the secondary structure has a larger diameter to depth ratio than the primary. With more bays in a diagonal, slope error toward the outer edge reaches higher magnitude. A square law relationship could be expected and the ratio of 14 to 10 bays would give a 2 to 1 slope error ratio for the same percentage variation in node-to-node length.

A typical distribution of slope error as a result of manufacturing tolerance for Configuration A is shown in Figure 3-24. A frequency distribution is shown in Figure 3-25.

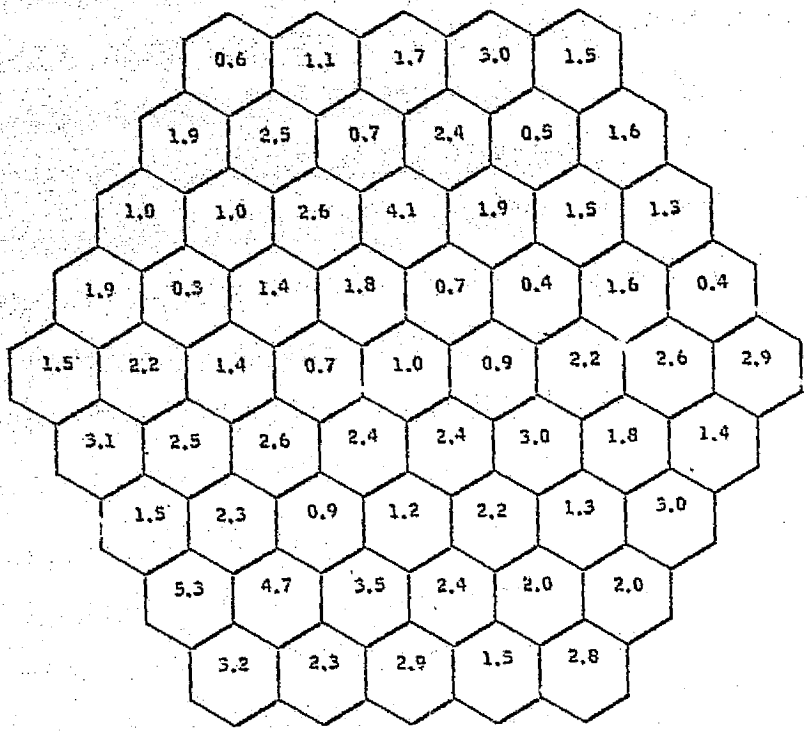

Figure 3-24. Typical manufacturing slope error distribution.

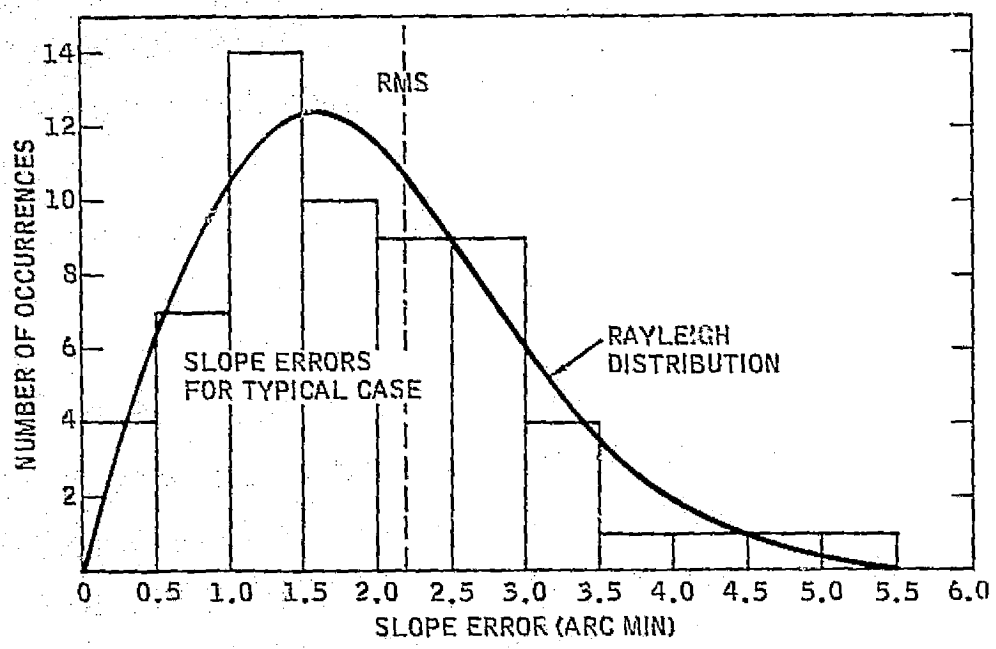

Figure 3-25. Frequency distribution of manufacturing slope error.

The agreement of the distribution of 61 slope errors grouped in 0.5 arc min steps is very good compared to the theoretical Rayleigh distribution predicted in Section 2.3. These experimental results confirm the assumptions made early in the study.

Maneuvering Accelerations Slope Error Budget

These slope errors are computed after the primary structure has been pointed correctly at the rectenna. They represent residual slope errors after a rigid body fit of the planar surface to the distorted primary surface.

The original budget for maneuvering slope error was 1.1 arc min rms. During the study, it was found that actual slope error as the result of forces and moments on the structures are very small. This 1.1 arc min allowance was allocated almost entirely to transient disturbances after shadowing. One arc min rms slope error was estimated for this disturbance. Uncorrelated minor disturbances of the environment and from attitude control corrections were budgeted at 0.5 arc min, however, none of these exceeded 0.1 arc min.

The first simulations of acceleration distortions showed that the secondary structure is more susceptible to deflection resulting from accelerations than is the primary. This results from the way each is supported; primary at three central points, and secondary elements at corners of the hexagonal structures, and because the secondary has a larger diameter to depth ratio, and finally because the secondary carries a larger proportional nonstructural mass. In the most critical direction (acceleration along the LOS), the rms slope error contribution of the primary is 0.6 arc min, while the secondary contributes 1.7 arc min rms for Configuration A, for an acceleration of 10^{-3}g.

The allocation for primary maneuvering slope error is 0.4 arc min rms, and for the secondary 0.9 arc min. The assumption of noncorrelation between primary and secondary contributions seems valid because of the differences in mounting. The errors tend to cancel so an RSS combination is realistic.

Thermal Distortion RMS Slope Error Budget

The budget for all operational thermal distortions is 0.7 arc min rms slope error. This includes all primary and secondary structural contributions that are not corrected by the attitude control. The error sources are: temperature variation, variation in CTE and also variation in E and cross-sectional areas of truss elements.

Thermal distortion of the secondary again is the more critical. The generalized slope error for 100C (180F) temperature rise and 100C (180F) additional taper across the aperture indicated a slope error of 0.12 and 0.29 arc min rms for the primary and secondary contributions respectively. These are uncorrelated, so the budget was established in that ratio: 0.3 arc min rms slope error for the primary, and 0.6 for the secondary.

3.3.2 LOS POINTING ACCURACY — Pointing accuracy is entirely a function of the distortion in the primary structure. If the primary structure interface is normal to the LOS, and represents a close approximation to a plane surface, then random and even systematic tilt of the secondary surfaces, and subarrays will not result in significant LOS pointing error.

There are two basic possibilities in the method of pointing. In the first, the control system points the primary structure central hub along the line of sight. In this case, pointing accuracy is a function of control system accuracy and structural pointing accuracy. In the second case, the control system points the beam as it is generated by the structure along the LOS. Pointing accuracy is only a function of the control system. Since subarrays will be phased individually by electronic means, the information required for control system error input is just the linear phase shift components of the phase correction being made over the aperture. The control system would continually drive the antenna to minimize the total angular phase shift required for electronic pointing.

One problem, however, is that dynamic pointing errors resulting from transient disturbances are apt to be at higher frequency than the equivalent response of the control system.

The design goal of 2 arc minute maximum mechanical LOS pointing error has been apportioned: 0.0 for manufacturing contribution, 1.0 for maneuvering distortion, 1.0 for thermal, and finally 1.4 for the attitude control system error. Again, these contributions should be uncorrelated and an RSS combination is used.

Manufacturing error does not contribute to LOS accuracy because bias corrections in attitude can be made if static beam offset from boresight is detected.

The allocations for maneuvering and thermal deflections are conservative. From a pointing control standpoint, the structure behaves essentially as a rigid body. Deflection amplitudes are small. The disturbances found in the probable environment, and the thermal distortions were such that pointing error for either source is less than 0.2 arc minutes maximum.

3.4 SENSORS AND ACTUATORS

3.4.1 SENSORS FOR MEASUREMENT OF FLATNESS — We are particularly interested in locating the positions of the 75 interface nodes between the primary and secondary structures. Displacement of these nodes relative to each other along the LOS causes beam pointing error which can be partially corrected by bias pointing of the attitude control system but ultimately must be accommodated by electronic phasing of the transmitting elements.

These 75 primary nodes will have error in position normal to the antenna reference plane as a result of residual fabrication error and distortion caused by the operational environment and attitude control accelerations.

The nodal position errors can be measured internally with respect to the coordinate system of the structural hub of the antenna. The ACS coordinate system is also related to the structural hub. In this approach, the ACS system would require an external reference to determine the correct LOS to the rectenna. Alternatively, the nodal positions can be related to an external reference such as a beacon at the rectenna. In this case, the ACS is only required to minimize the measured nodal errors.

An internally generated reference approach is attractive since it does not depend on an external source. The structure need not be oriented in a particular direction during measurement and may be oriented to the sun to achieve a uniform thermal condition. This alternative is useful during initial assembly and alignment as well as for sensing distortion for input to an active figure control system during operation.

Laser Scanning Systems

The reference can be generated by a scanning laser beam. A small low-power laser, typically helium-neon, is used to generate a pencil beam (Figure 3-26). This beam is directed through a right-angle Pentag prism scanning beam bender. The result is a reference plane which can be sensed by photodetectors. This approach is used in construction to level large ceilings and floors.

In the primary structure, one such unit could be located at the hub offset slightly from the center so that a visual path is available through the truss to each node at the primary secondary interface. A beam of 0.5 to 1 cm diameter would provide a reference to a split detector that would yield vertical positioning resolution to 1 mm without difficulty. Overall accuracy of the system would depend on stability of the reference generator unit in the hub. Primary nodes would be aligned to perhaps 3 cm (equivalent to 1 arc minute pointing of the secondary structure supported at the node). The system should be easily capable of supporting this level of alignment accuracy.

During initial assembly, the detector can be located at the node, and each node aligned to the reference plane as its structural elements are mated to the partially completed primary structure. For active control, at each node, the sensor can be coupled to a displacement actuator so that the primary structure continually maintains a flat foundation for the secondary and subarray antenna components.

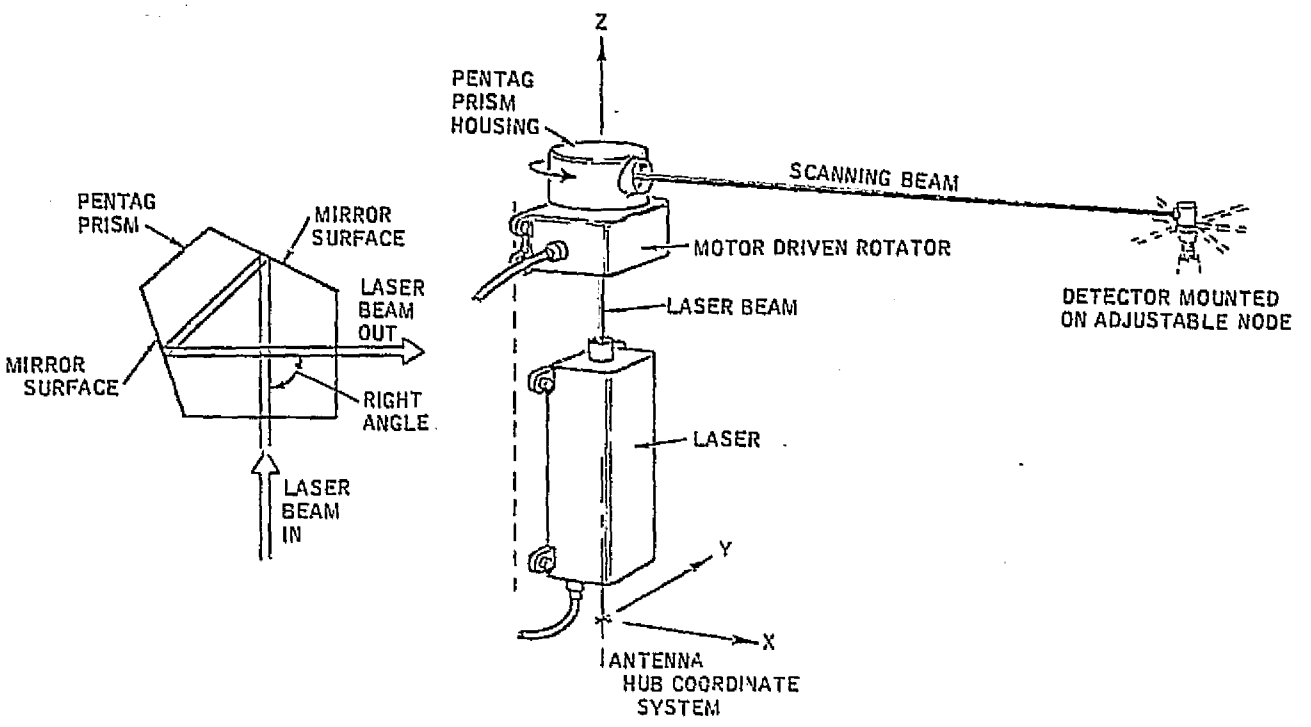

Figure 3-26. Laser reference plane generator.

Since the study has not shown a need for active control after initial assembly and alignment, another version of the laser scanner can be considered which has all the active elements located at the hub. Figure 3-27 shows this scanning laser system. In this case, the laser is used to provide a light source with illuminated small corner reflectors located at each node. The detector is an imaging system which scans the array of corner reflectors, and determines in turn, the out-of-plane displacement of the associated node.

The laser beacon and detector array scan one time per second and measure the primary figure as located by 75 individual retroreflectors. This arrangement is reasonably straightforward electronically and keeps the instrumentation relatively simple and compact. To attain the desired accuracy imposes a stringent mechanical requirement of $2 \cdot 10^{-6}$ radian wobble in the shaft which turns the assembly at one revolution per second.

The rotation rate was selected so that modal frequencies to 0.1 Hz could be measured.

A linear array of 500 elements would provide 1 mm resolution at the edge nodes. The detectors, 0.1 mm wide, form a 5 cm long linear array. Detectors of this type are currently available for use at 0.6328μ with a helium/neon laser. Rise time of these detectors is 10^{-7} to 10^{-10} seconds. At one revolution per second, the return signal has a minimum dwell of $3 \cdot 10^{-7}$ seconds as it sweeps over the array.

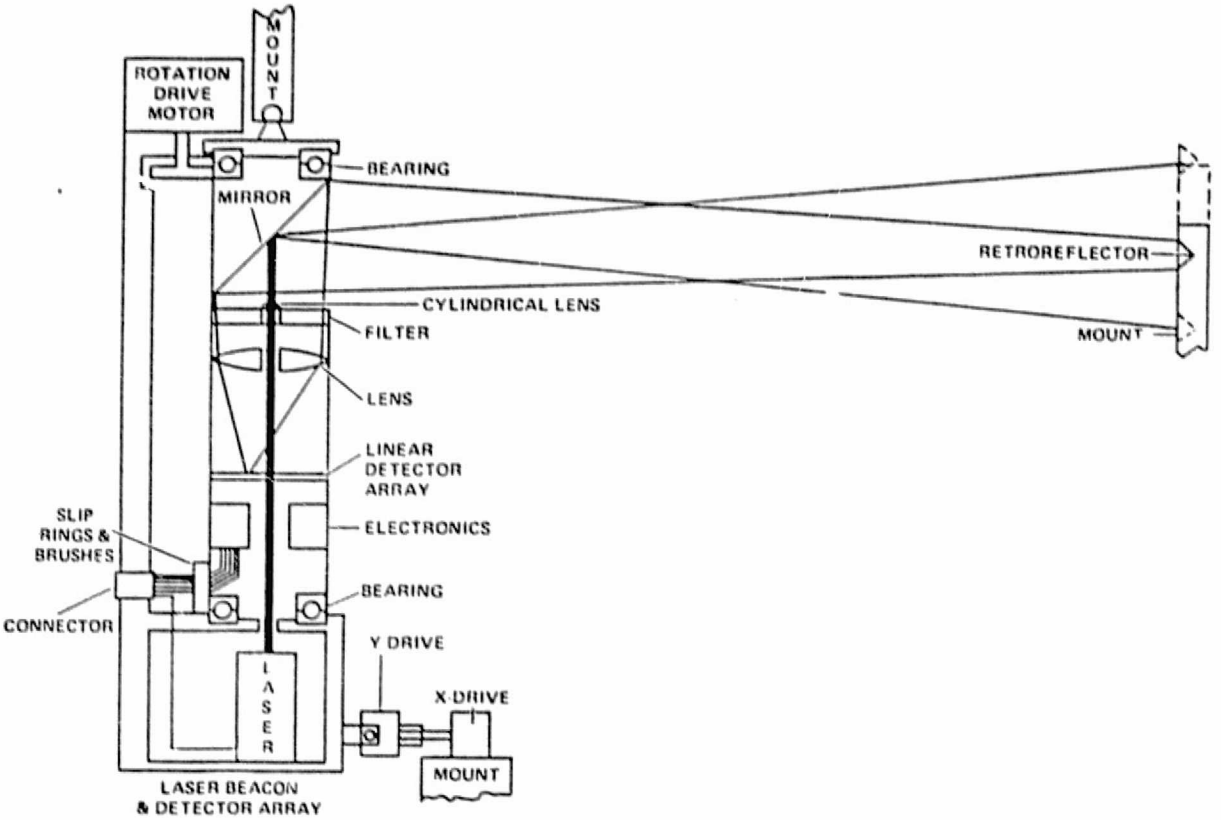

Figure 3-27. Laser beacon, detector array concept.

External Reference Approach

The external reference (for example, an rf beacon on earth) will generate a plane wave at the synchronous altitude that is curved less than ± 4 mm over the diameter of the antenna. If the curvature were a problem, an allowance could be mde for the known value.

In the case, if uncorrected, the curvature would cause the MPTS beam to focus at the rectenna rather than at infinity, so we can assume that the curved wavefront is an ideal reference.

The beacon for this purpose could operate in a number of frequency bands. If a frequency near the 2.45 GHz system frequency is used, the wavelength is about 12 cm. Simple phase comparison circuits would give accuracy to about ± 3 mm in the alignment of a node to a reference node at the hub. Some provision would be required to resolve ambiguity since the primary structure nodes could easily be more than one wavelength or 12 cm in error during the alignment process.

The ambiguity can be resolved by using a second beacon at lower frequency, e.g. 0.3 GHz. Alternatively, a pulsed laser could be used to get resolution to a few centimeters.

There is also a possibility that the phase data generated in the electronic control of the subarrays could be used for sensing of distortion in the structure. With a pilot beacon operating at 2.45 GHz, the phase measured at subarrays adjacent to primary structure nodes could be used to estimate deflection of the node. We can also guarantee that adjacent subarrays are never out of phase more than a fraction of a cycle of the pilot beacon. So it is possible to count wavelengths from one primary node to the next across the subarrays and resolve ambiguity in phase at the nodes.

Perhaps the most difficult problem in the use of a pilot beacon and wavefront sensing at each node is the comparison of the received signal to a single phase reference for the entire structure. This comparison requires communication between nodes, and precise delay information so that error in delay in the system is not interpreted as structural deflection. Since solution of this problem is inherent in the use of electronically phased subarrays, for this study the technology can be assumed to be available, and the use of an external reference is a viable alternative.

Measurement of Strut Length

Measurement during the manufacturing process is expected to make use of special measurement systems designed for that purpose only.

Measurement during fabrication may be automatic, or rely on operator assistance. In most cases, the measurement system is expected to be located at the central hub of the antenna where power, maintenance, repair, and other services are available.

The primary measurement required in the fabrication of elements of the antenna is in establishing strut length. This is most readily accomplished by comparison with master tooling.

During assembly of the structure, some measurements will probably be made between distant nodes of the truss to monitor tolerance buildup. This type of range measurement can be accomplished with laser-type surveying equipment.

A highly accurate ranging system is the Kern Mekometer ME 3000 (Figure 3-28). This unit uses a Xenon tube flashed at a rate of 100 Hz, with one microsecond flash duration. The modulation frequencies are derived from a quartz cavity resonator with elliptical polarization modulation effects by a Pockels crystal in the modulation cavity.

This system has an accuracy of $\pm$ 0.2 mm $\pm$ 10^{-6} over 3,000 m range. This is equivalent to 1.2 mm accuracy over the diameter of the antenna. Four auxiliary frequencies give unambiguous distance to 3,000 m by using the frequency difference methods. The basic unit is 46 x 16 x 22 cm, and weighs 14.5 kg. A distance measurement takes two minutes and power consumption is 18w for the conventional unit. The system appears to be adaptable to use in space and should demonstrate improved accuracy in the vacuum environment.

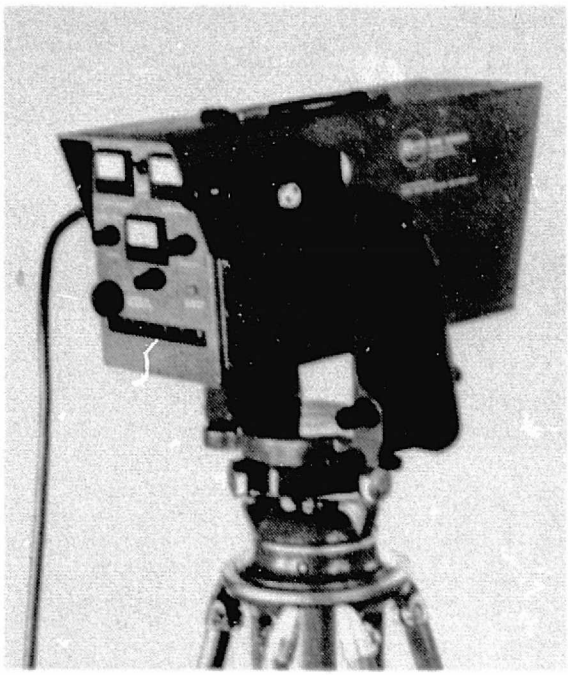

Figure 3-28. Kern mekometer ME 3000.

The mekometer measures range, and can be used to monitor variation in distance. If only variation in distance is required, e.g., to monitor distortion from an arbitrary length, then laser interferometry provides reliable, instantaneous, and extremely accurate length variation measurement.

An example of this type of system is the Hewlett-Packard 5526A Laser Measurement System. The laser is a two-frequency helium-neon unit. The two beams are orthogonally polarized so that two separate channels of measurement can be used. Polarized mirrors are used to establish a reference beam and the measurement beam for each frequency. With two independent beams, the unit can be used as a remote interferometer, to measure the variation in length between two remote points.

The laser head is 12.7 x 17.8 x 52.6 cm and weighs 7.8 kg. Accuracy is $\pm$ 0.5 ppm for the conventional unit. A major error source is variation of velocity of light due to atmospheric conditions. This accuracy would be considerably better for a space qualified unit.

These units are relatively inexpensive. For large truss structures, it could be possible to locate a laser interferometer in each primary strut. A closed-loop system would maintain the strut length in any anticipated environment. With this approach, once aligned the structure would remain dimensionally stable. One drawback to the laser interferometer is that if power is lost or the beam interrupted at any time, the length reference is lost. The length would have to be reestablished by some other method.

Another alternative in the active strut approach is to provide an internal standard such as a graphite/epoxy rod which is fabricated and calibrated to provide essentially zero thermal coefficient. This rod, protected from the environment within the primary strut would be used in a simple closed-loop system to maintain the effective length of the strut to the design value.

3.5 ACTIVE VERSUS PASSIVE FIGURE CONTROL

A primary objective of the study was to determine whether the required flatness could be achieved without resort to an active figure control system. In Task 1, it was found that maneuvering and thermal distortions are small, and the MPTS, if assembled or aligned with sufficient initial accuracy will meet the operational accuracy requirements with a passive structure. In Task 2, the thermal and acceleration environment was examined in detail and its effects on flatness were found to agree with the preliminary estimates of Task 1. Active control is not required.

Active figure control could still be a viable alternative if the resulting improvement in efficiency offset the cost and complexity of an active system. Table 3-5 lists the range of actuator options and their estimated potential for improved efficiency. The most complex system, Option 6, shows a one percent improvement in efficiency over a passive system operating at 99 percent. Since the passive systems exceed this value, the margin for improvement is even smaller.

Table 3-5. Active control options — performance improvement.

Option	RMS Slope Error (arc-min)	Link Efficiency Improvement (%)
1. Primary Shape Control 24 Actuators	0.68	0.15
2. Primary Interface Control 72 Actuators	0.85	0.18
3. Configuration A Secondary Control 122 Actuators	0.90	0.21
4. Secondary Shape Control (minimum) 732 Actuators	1.10	0.25
5. Secondary Shape Control (maximum) 2,928 Actuators	1.50	0.50
6. Subarray Interface Control 15,700 Actuators	2.00	1.00

Option 1 is for a system of actuators within the primary structure which corrects the primary only for major distortions. An 80 percent correction of rms slope error contribution from the primary structure is estimated on the basis of random distortions over the primary. Option 2 corrects the interface between the primary and secondary but not the primary distortion. Option 3 provides 2 axis tilt correction to each

secondary hexagonal element as well as correction for primary distortion. Option 4 has 12 actuators per secondary hexagonal element providing first order structural corrections. Option 5 has 48 actuators per element. Finally, Option 6 provides complete control of each subarray.

In view of the poor return suggested in Table 3-5, the more complex systems are difficult to justify. A few percent larger solar collector, and some additional subarrays on the corners of the secondary structure would give more usable energy at the rectenna (and reduce sidelobes) at less cost and better reliability than an active system.

There is still the chance that a small number of actuators operating within the primary structure could correct first order distortions. This alternative, while not improving efficiency more than a fraction of a percent, could be worthwhile in minimizing beam pointing error.

Table 3-6 lists the coefficients of the first 28 terms of an optics fit to typical distortions. The coefficients have been normalized so that relative size of the various types of distortions can be seen. The first six cases are linear and angular accelerations. The distortions are similar to those of the lowest frequency modal deformations. The quality of fit is good for all except angular acceleration about the line of sight. The structure deformed about the three support points in a distinct "3 leaf" trefoil pattern.

Figure 3-29 shows the contour plot for Z axis linear acceleration. The largest deformation is change in focal length evidenced by the circular pattern. Trefoil distortion causes the 3 way symmetry in the pattern. Figure 3-30 shows the angular acceleration about the Z axis. Now only trefoil distortion can be seen in the pattern. For comparison, Figure 3-31 shows the 11th case, a random strut length distortion.

Cases 7 through 12 are random distortions generated by using a normally distributed temperature for each strut and constant E and CTE. The result simulates random strut length in manufacture. The optics fit is not particularly good, an average of about 80 percent. Almost all terms have significance, not like in accelerations where only a few terms of the polynomial describe the surface. The last case was generated by a gaussian distribution of temperature over the aperture. It resulted in almost pure defocus and spherical aberration.

A detailed placement of actuators in the primary structure was not attempted. From the optics fit analysis we can project that 24 actuators, at best, would correct as well as indicated by the optics fit. This would result in perhaps a 90 percent correction of acceleration and 80 percent correction of random deformations in the primary.

In the long run, it would probably be easier to let the primary deform, and simply correct the interface. This is Option 2. It would require 72 actuators. Actually 75 actuators would probably be used with three failures allowed before system degradation would begin.

Table 3-6. Polynomial fit to typical distortions.

POLYNOMIAL TERMS	CONDITION	LINEAR ACCELERATION			ANG.ACCEL.ABOUT			RANDOM STRUT LENGTH						GAUSSIAN T. DIST.	TYPES OF DISTORTION
		X	Y	Z	X	Y	Z								
	CASE	1	2	3	4	5	6	7	8	9	10	11	12	13	
1	1			0.07				0.33	-0.41	-0.32	-0.30	-0.25	-0.39	-0.30	GROUP PHASE SHIFT
$\rho\cos\theta$	2	0.37	-	-	-	0.38	-	-	0.59	-0.11	-0.04	0.06	0.27	-	TILT, LINEAR PHASE SHIFT
$\rho\sin\theta$	3	-	0.37	-	0.38	-	-	0.15	-0.07	-0.28	0.21	-0.12	-0.18	-	
ρ^2	4	-	-	1.00	-	-	-	0.78	1.00	1.00	0.89	0.91	0.80	1.00	DEFOCUS
$\rho^2\cos\theta$	5	-	0.66	-	0.63	-	-	0.02	0.09	-0.14	-0.11	-0.24	-0.54	-	ASTIGMATISM, ANTICLASTIC BENDING
$\rho^2\sin\theta$	6	0.66	-	-	-	-0.63	-	-0.58	-0.25	-0.46	-0.11	-0.07	0.21	-	
$\rho^3\cos\theta$	7	0.99	-	-	-	-1.00	-	-0.96	-0.62	-0.18	-0.20	0.28	-	-	COMA
$\rho^3\sin\theta$	8	-	0.99	-	1.00	-	-	0.46	0.62	0.26	0.21	0.12	1.00	-	
$\rho^3\cos3\theta$	9	-	-	-	-	-	1.00	0.01	0.65	0.02	0.03	-0.04	0.06	-	TREFOIL DISTORTION
$\rho^3\sin3\theta$	10	-	-	0.42	-	-	-	0.07	-0.27	-0.32	0.01	-0.07	-0.32	-0.16	
ρ^4	11	-	-	-0.16	-	-	-	-0.39	-0.10	-0.54	-1.00	-1.00	-0.49	-0.90	SPHERICAL ABERRATION
$\rho^4\cos2\theta$	12	-	-1.00	-	-0.89	-	-	-0.19	-0.07	0.36	0.39	0.19	0.33	-	HIGHER ORDER ASTIGMATISM
$\rho^4\sin2\theta$	13	-1.00	-	-	-	0.89	-	1.00	0.46	0.97	0.52	0.03	-0.11	-	
$\rho^4\cos4\theta$	14	-	0.04	-	-	-	-	-0.16	-0.21	0.08	0.12	0.19	-0.10	-	
$\rho^4\sin4\theta$	15	-0.04	-	-	-	-	-	0.29	0.18	0.16	0.16	-0.11	0.24	-	
$\rho^5\cos\theta$	16	-0.48	-	-	-	0.48	-	0.53	0.49	0.17	0.29	-0.14	0.01	-	HIGHER ORDER COMA
$\rho^5\sin\theta$	17	-	-0.48	-	-0.48	-	-	0.27	-0.35	-0.26	0.10	-0.10	-0.67	-	
$\rho^5\cos3\theta$	18	-	-	-	-	-	-0.68	0.11	-0.40	0.04	-0.03	0.03	-0.13	-	HIGHER ORDER TREFOIL DISTORTION
$\rho^5\sin3\theta$	19	-	-	-0.33	-	-	-	-0.11	0.13	0.24	0.10	-	0.15	0.08	
$\rho\cos5\theta$	20	0.02	-	-	-	-0.02	-	-	-0.01	-	-0.02	0.02	-	-	
$\rho\sin5\theta$	21	-	-0.02	-	-0.02	-	-	-0.03	-0.08	-0.01	0.06	0.02	0.03	-	
ρ^6	22	-	-	-0.07	-	-	-	0.10	0.25	0.10	0.43	0.44	-	0.32	HIGHER ORDER SPHERICAL ABERRATION
$\rho^6\cos2\theta$	23	-	0.51	-	0.44	-	-	0.05	0.05	0.31	0.13	-0.09	-0.08	-	HIGHER ORDER ASTIGMATISM
$\rho^6\sin2\theta$	24	0.51	-	-	-	0.44	-	-0.61	-0.26	-0.49	0.34	0.04	-0.15	-	
$\rho^6\cos4\theta$	25	-	0.05	-	-0.01	-	-	0.20	0.07	-0.11	-0.15	-0.14	0.17	-	
$\rho^6\sin4\theta$	26	0.05	-	-	-	-0.01	-	0.26	-0.24	-0.14	-0.16	0.12	-0.23	-	
$\rho^6\cos6\theta$	27	-	-	0.01	-	-	-	-	-	0.04	-0.03	-0.02	0.04	-0.01	
$\rho^6\sin6\theta$	28	-	-	-	-	-	-	-0.04	0.01	0.02	0.02	-0.01	0.05	-	
QUALITY OF FIT (%)		97.1	97.1	95.7	97.2	97.2	69.2	83.0	76.9	80.9	81.7	78.1	68.4	93.5	

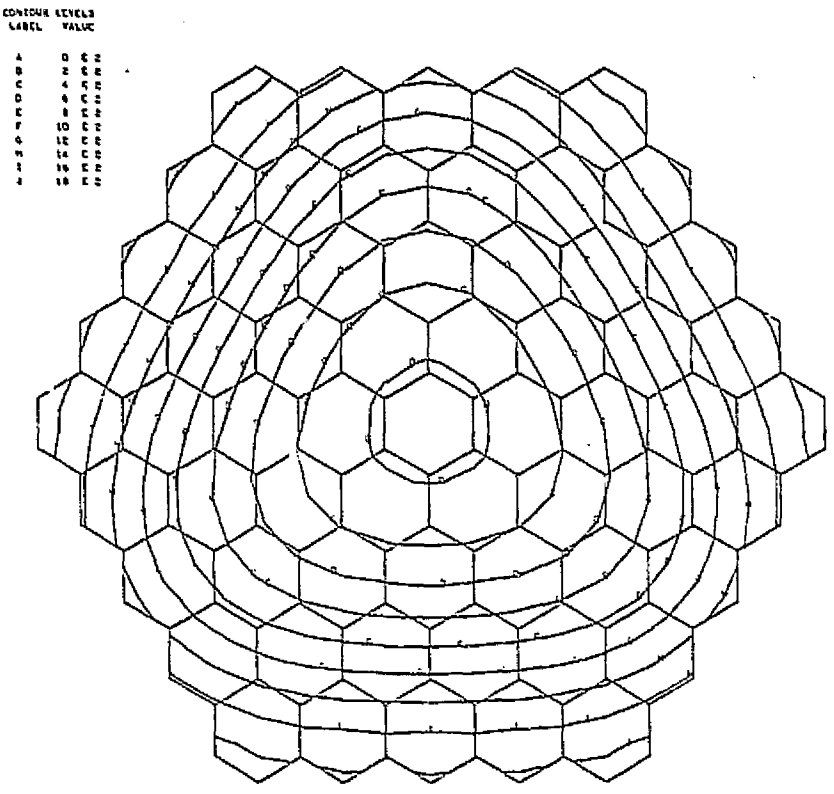

Figure 3-29. Z-axis acceleration distortion.

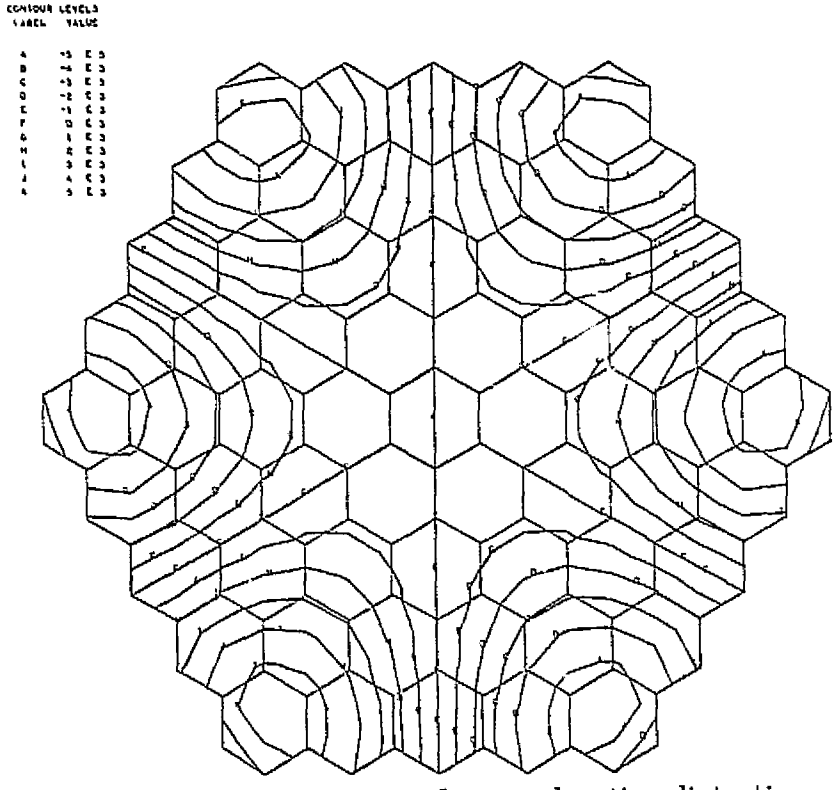

Figure 3-30. Z-axis angular acceleration distortion.

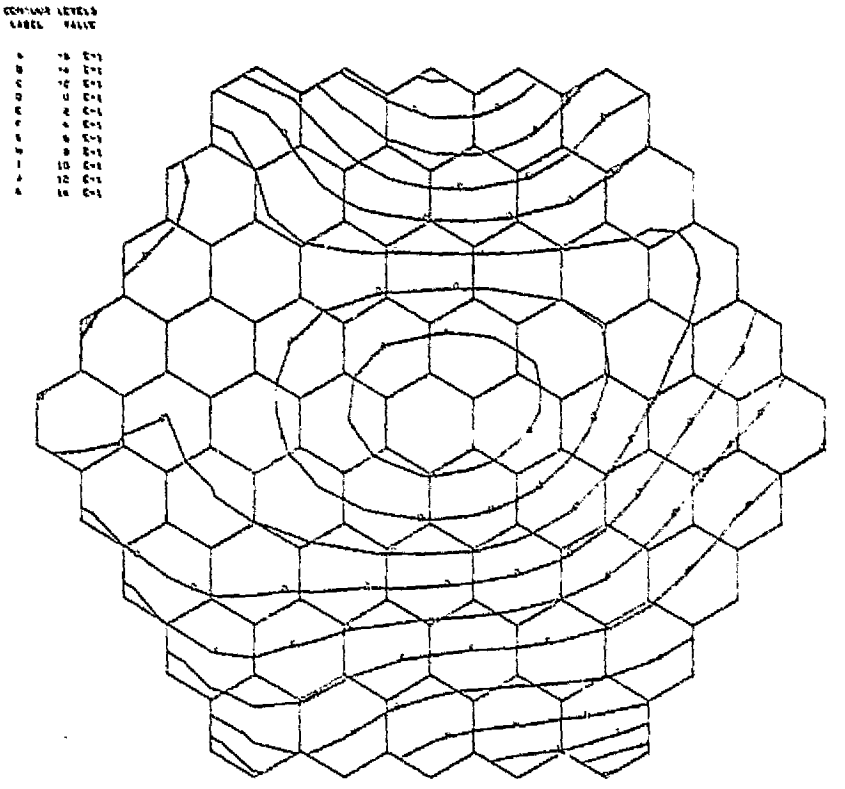

Figure 3-31. Random strut length distortion.

3.6 STRUCTURAL SPECIFICATION (BASELINE DESIGN)

It was determined that it would be helpful to define the major elements of a structural specification for the MPTS antenna. This specification is found in Appendix A.

The mission of the MPTS antenna structure is to provide a stable platform for mounting klystron/waveguide/thermal radiator units (subarrays). For each subarray a slope error of less than three arc minutes is a primary requirement.

Interface control drawings will be prepared to describe the antenna assembly, its datum references, volume available for support structure, mechanical references, and structural interfaces.

The structure is to be capable of withstanding both space and earth environments without degradation in functional performance or operation below the requirements set forth in the structural specification.

Materials for the MPTS antenna will be chosen on the basis of adequate strength allowables for the expected loading conditions, and environment.

When designing the structure, consideration will be given to the items listed below:

a. Dimensional stability
b. Manufacturability
c. Overall structural stiffness
d. Mission life
e. Stress margin
f. Serviceability

Active mechanical alignment mechanisms are not a preferred method to achieve the required flatness, but if used, they would be required to fulfill the requirements as set forth in Specification MIL-A-83577 dated 15 June 1975 for moving mechanical assemblies for space vehicles.

3.7 SUBARRAY SIZE TRADES

Variation in subarray size can have significant effect on slope error of the surface. A larger subarray results in an apparent improvement in rms slope accuracy of the supporting structure, but the gain is offset by larger slope error in the subarray itself or by increased subarray structure weight.

All other analyses in this study are based on a 10-bay primary and 61 14-bay secondary structures (the latter supported separately in configuration A, or joined to form a continuous structure in configuration B). Truss angles are derived from use of a regular tetrahedron as the basic 3-dimensional truss building block.

In this analysis, the basic geometry is unchanged, but the number of bays in the primary and secondary structures are varied to effect discrete changes in subarray size. In addition to the 10-bay primary, 8 and 12-bay configurations are considered. Similarly 12 and 16-bay secondary structures bracket the baseline 14-bay configuration. These combinations provide an additional 8 configurations. The number of secondary bays across the diameter of the reflector surface is:

		Number of Secondary Bays		
		12	14	16
Number of	8	96	112	128
Primary	10	120	140	160
Bays	12	144	168	192

The variation in number of subarrays across the diameter is 96 to 192, corresponding to a subarray size ratio of 2:1. The baseline 10 x 14 bay baseline has subarray panel size of 10.75 x 9.31 m (35.27 x 30.54 ft).

The options are ordered according to subarray size in the following listing:

Option No.	Primary Bays	Secondary Bays	Subarray Size (m)	Subarray Size (ft)
1	8	12	15.68 x 13.58	51.43 x 44.54
2	8	14	18.44 x 11.64	44.09 x 38.18
3	10	12	12.54 x 10.86	41.15 x 35.64
4	8	16	11.76 x 10.18	38.58 x 33.41
5*	10	14	10.75 x 9.31	35.27 x 30.54
6	12	12	10.45 x 9.05	34.29 x 29.70
7	10	16	9.41 x 8.15	30.86 x 26.78
8	12	14	8.96 x 7.76	29.39 x 25.45
9	12	16	7.84 x 6.79	25.72 x 22.27

*Baseline

We have a set of nine subarray sizes, with an overall area ratio of 4:1 which represents the probable range of practical subarray size for the MPTS.

Experience has shown that surface deflections are inversely proportional to depth squared for these truss structures. A parametric study with modeling and computer simulation of configurations with varying bay numbers is beyond the scope of this study. However, the existing data can be interpreted to get evidence to support the depth-square approximation. RMS normal error to the surface was computed for the secondary structure, first for all nodes, then for all surface nodes except those on the outer ring, to simulate a 2-bay reduction, and finally, all nodes except those on the outer 2 rings to simulate a 4-bay reduction in configuration. Case 4 random temperatures were used to generate typical deflections. The results are as follows:

No.of Bays	RMS Error	Scaled To Full Diameter	Actual Ratio	Predicted Ratio
14	0.132	0.132	-	-
12	0.086	0.100	0.76	0.78
10	0.056	0.078	0.59	0.51

As seen above, with constant diameter, the rms surface error is proportional to the square of the number of bays, hence inversely proportional to the square of the depth of the truss.

Slope error is dimensionless. It is proportional to normal error, and inversely proportional to bay size. From this relationship, it follows that slope error is proportional to the number of bays cubed.

The cube rule is used to estimate the gain/loss in slope error for the various bay options relative to the baseline:

Option Number	Primary Bays	Bay Factor	Secondary Bays	Bay Factor	Total Slope Error
1	8	0.512	12	0.630	0.607
2	8	0.512	14	1.000	0.916
3	10	1.000	12	0.630	0.729
4	8	0.512	16	1.493	1.341
5*	10	1.000	14	1.000	1.000
6	12	1.728	12	0.630	0.986
7	10	1.000	16	1.493	1.401
8	12	1.728	14	1.000	1.201
9	12	1.728	16	1.493	1.550

*Baseline

In the last column, a total slope error is estimated relative to the baseline 10 x 14 configuration. In combining the factors for the secondary and primary, a ratio of 1.87:1 was used as typical for the rms slope error of the secondary relative to that of the primary.

The conclusions drawn from above are that for LOS accuracy where secondary slope error is not significant, a reduction of primary bays from 10 to 8 would halve the pointing error. For rms slope error, the secondary error predominates, and the most improvement is made by reducing the number of bays in a secondary structure segment.

Before a trade in subarray size can be made, the probable loss in subarray slope accuracy must be considered. If surface accuracy is maintained to a fixed fraction of diameter of the subarray, and the individual radiating element spacing in the subarray remains unchanged, then the slope error would effectively increase with subarray diameter. Practically, with about the same complexity and weight per unit area of subarray, the slope error would increase with the square of dimension. Most of the gain in the structural flatness accuracy would be lost in increased subarray error. Total structural slope error is adjusted as follows:

Option	Effective Subarray Dimensions		Structural Slope Error	Subarray Factor	Overall Slope Error
	Meters	Feet			
1	14.59	47.87	0.607	2.129	1.292
2	12.51	41.04	0.916	1.565	1.434
3	11.67	38.29	0.729	1.362	0.993
4	10.94	35.90	1.341	1.197	1.605
5*	10.00	32.82	1.000	1.000	1.000
6	9.72	31.91	0.986	0.972	0.958
7	8.76	28.73	1.401	0.876	1.227
8	8.34	27.36	1.201	0.834	1.002
9	7.30	23.94	1.550	0.730	1.132

*Baseline

In the above listing, the assumption is made that as size increases, effective slope error increases for the subarray according to a square law. To be conservative, with reduction in size, a linear relationship in improvement is used.

The results show that an increase in size in the subarray can lead to a small improvement in slope error. This is illustrated by Option 3 where the secondary is reduced to 12 bays. The only other improvement that is indicated is going to a more symmetric 12 x 12 bay configuration. With some loss of LOS accuracy, a small improvement can be made in rms slope error. The additional complexity of having 6 percent more subarrays must be considered.

The final conclusion is that if a subarray size change is made, it should be an increase. This results in reduction in complexity of the support structure, and improvement in its accuracy. One discrete step size to an effective dimension of 11.67 m (38.29 ft) shows most promise of improved performance. Larger panels can also be effective, but increased difficulty in maintaining the subarray panel within tolerance must be considered. This change would result in a 26 percent decrease in the number of subarrays, and equivalent reduction in the number of supporting truss elements.

Report No. CASD-NAS-78-011

FINAL REPORT

ACHIEVABLE FLATNESS IN A LARGE MICROWAVE POWER ANTENNA STUDY

(DRL Item No. 2)

4. TASK 3 – FIGURE & POINTING CONTROL MATRIX

Prepared under
Contract No. NAS9-15423
for
National Aeronautics and Space Administration
LYNDON B. JOHNSON SPACE CENTER
Houston, Texas 77058

Prepared by
GENERAL DYNAMICS CONVAIR DIVISION
P.O. Box 80847
San Diego, California 92138

4

TASK 3

FIGURE AND POINTING CONTROL MATRIX

The effects of the control system on the structure were evaluated for different control techniques. Of the techniques examined, mechanical actuators and mechanical cable systems offer the most promise. Cable dynamic problems remain to be resolved before making a firm commitment to this concept. Magnetic and counterweight concepts are penalized by gross size and resulting configuration impacts.

Figure 4-1 summarizes Task 3 study activities and flow.

Detail task considerations are given in the following sections.

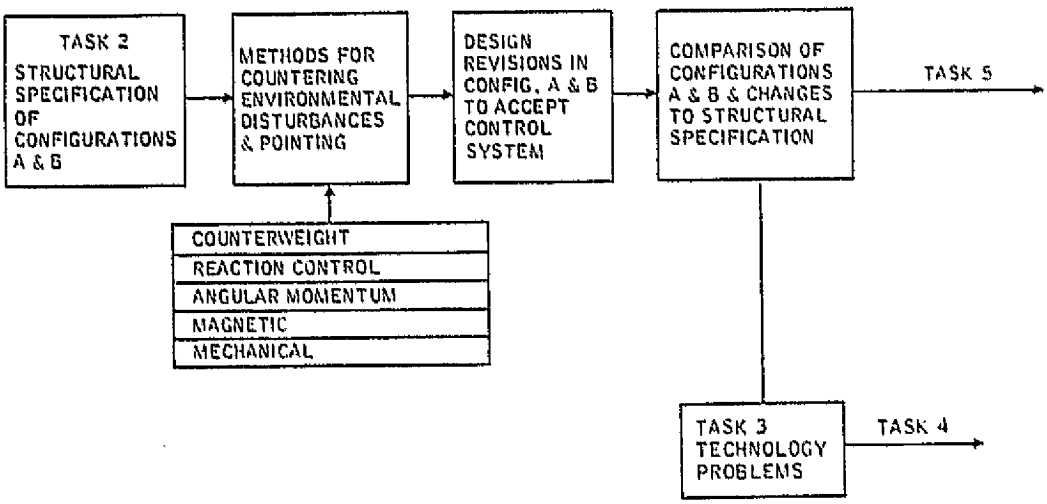

Figure 4-1. Task 3 flow.

4.1 CONTROL REQUIREMENTS

The exact requirement for the allowable angular error between the antenna normal and the line-of-sight to the rectenna is still evolving, but a final value of one or two arc minutes appears most probable at this time. A budgetary allocation of 1.4 arc minutes is used in this study. The power beam is controlled by phasing techniques to greater accuracy than is the rigid body of the antenna and the tolerable error for the rigid body is set by the tracking range of the phasing technique. Power beam phasing uses a pilot or reference beam from the rectenna which is also used for sensing rigid body pointing errors in azimuth and elevation (Section IV-C-5 of the Green Book). This error sensing

technique is expected to be accurate to 0.1 arc minute with a range of ± 0.7 degree before ambiguities occur. Thus an acquisition sensing system is required, in addition to the phase sensing, to bring the antenna within ± 0.7 degree so the tracking system can take over.

The tracking motions vary with inclination, eccentricity, and longitudinal drifts that result from earth oblateness, lunar and solar gravity, and solar pressure. A worst case actuation is shown in Table 3-2 where the antenna line-of-sight describes an ellipse once a day. The ellipse has a major axis of 2.86 degrees and a minor axis of 2.02 degrees. The table also shows a fixed elevation angle of 7.3 degrees for pointing to the U.S.-Canadian border at 49 degrees North latitude. Thus relative to an orbital reference frame the required motion capability in elevation would be 8.3 degrees (7.3 fixed and 1.01 from half the minor axis of the ellipse). Some additional motion capability in elevation will be required since the solar collector will probably not remain in precise alignment with its desired reference frame. Although the solar collector attitude hold requirements are not known at this time, gravity gradient dictates that off-nominal attitude errors be quite small. This is because the SPS is in an orientation where gravity gradient acts as a negative spring: at zero error little or no torque is needed to hold attitude, but any error results in torques which cause the error to grow which results in the need for more control torque to stop the drift and more work to return to zero error. Thus the collector motions have been assumed small and the required maximum elevation capability has been selected to be 10 degrees.

There are two different cases for the minimum required elevation. If it assumed that the same end of the SPS is always oriented in a northerly direction, a northerly elevation of 4.7 degrees will cover the southern tip of Florida. Allowing for the tracking ellipse and solar collector motion gives a minimum northerly elevation of 2.0 degrees. Thus for this case, the elevation pointing capability would be from 2 to 10 degrees or a nominal angle of 6 degrees with plus and minus 4 degrees of motion. However, one of the candidates for providing maximum SPS output at the peak load seasons (mid-summer and mid-winter) while still maintaining the perpendicular-to-orbit plane orientation would be to point the individual collector elements about 23 degrees away from the structure and invert the entire SPS every spring and fall. This turnover approach requires 20 degrees of elevation capability, plus and minus 10 degrees about zero. In either case, the antenna requires unlimited continuous freedom to rotate in azimuth.

The requirement that pointing be maintained in the presence of environmental disturbances is usually implied rather than stated explicitly. However, the potential severe impact of a rather unique gravity gradient problem on the pointing system deserves more attention here than is usually given gravity gradient. The usual gravity gradient torque arises from differences in principal moments of inertia: the problem here is the gravity gradient force which acts on unbalanced masses. This force acting on the lever arm from the support point to the unbalanced mass can cause torques which are orders of magnitude greater than those from moment of inertia differences. Figure 4-2 shows the torque parametrically. One conclusion from the figure might be that an elongated, narrow solar collector is undesirable and that reducing the torque on the antenna by use of a shape that placed the antenna closer to the total center of mass is

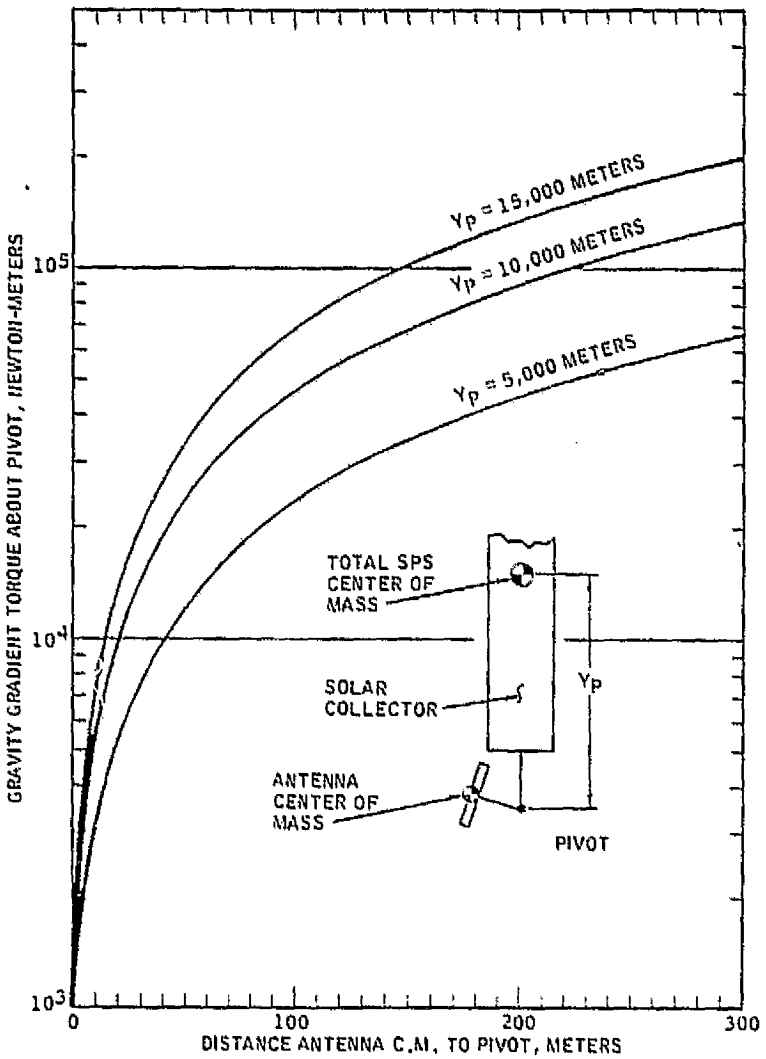

Figure 4-2. Torque from gravity gradient and unbalanced mass.

a practical solution. However, geometries which would ease the antenna control problem would impart severe penalties to the solar collector control because its gravity gradient problem would be more severe.

4.2 TECHNIQUES FOR COUNTERING GRAVITY GRADIENT

The gravity gradient torque from the orbital force acting on an unbalanced mass which is far from the system center of mass must be accounted for before seriously considering any pointing technique. As various gravity gradient countering techniques are presented for consideration, it should be kept in mind that these techniques are candidates for comparison and not all of them will be reasonable solutions.

4.2.1 COUNTERWEIGHT — The time-honored method for designing small gravity gradient satellites is to use long thin rods with tip weights to control the principal moments of inertia. Thus it is reasonable to consider a counterweight on a long boom for the first technique.

Pointing the antenna at the continental United States from equatorial orbit prevents the principal axes of the antenna from ever being aligned with a local vertical reference frame. Therefore, the antenna as currently envisioned cannot achieve zero gravity gradient torque unless all three moments of inertia are equal. To eliminate the gravity gradient force and the resultant torque, the antenna's center of mass must coincide with the pivot point. When using a single counterweight there are an infinite number of arm-weight combinations which will provide either static balance or equal moments of inertia. However, given a specific antenna mounting, there is only one arm length and one counterweight mass which can meet the dual requirement of balance and equal inertia. Simultaneous solution of the two conditions gives the counterweight characteristics shown in Figure 4-3. Several items of interest may be determined from the figure. First is that for pivot-to-center-of-mass distances of 70 m or greater, the mass of the counterweight starts to exceed the weight of the antenna itself. Second, the counterweight arm becomes very long (greater than a kilometer) as the pivot point and center of mass are brought together. There is a mathematical peculiarity as the pivot point approaches the center of mass: the arm length is squared in the moment of inertia calculation and a small mass value times the long arm length squared is able to compensate moments of inertia although the mass times the arm to the first power makes little change in the combined center of mass.

4.2.2 REACTION CONTROL — Although the 30 year life of the SPS would tend to make mass expulsion or reaction control a poor candidate for overcoming steady torques, the unusually long arm (500 m) available to reaction control might tend to make it an attractive candidate. Two reaction control systems were selected for evaluation: O_2/H_2 using electrolysis represents a relatively conventional approach, and the MPD-arc jet was used for an advanced approach. As a "first cut" the 30 year propellant requirements were calculated for the two different systems. A specific impulse of 3900 m/s (400 lbf-sec/lbm) was used for O_2/H_2 and 9800 m/s (10000 sec) for the MPD-arc jet. It must be emphasized that propellant weight is only part of the story: thruster life, thruster weight, weight penalty for power, etc. have not been included in this first cut calculation. The propellant weight is shown parametrically in Figure 4-4 along with the counterweight mass from Figure 4-2. Inspection of the figure shows that O_2/H_2 is an order of magnitude heavier than the counterweight and that the counterweight is lighter than the MPD-arc jet except for very adverse configurations.

4.2.3 ANGULAR MOMENTUM COMPENSATION — Proper selection of an internal angular momentum to the antenna will result in the gravity gradient torque providing the useful function of pulling the antenna around at the desired rate. The relationship of interest is

$$T = \omega_o \times H \times \sin\theta$$

where

- T is the external torque,
- ω_o is the desired angular rate (orbital rate),
- H is the internal angular momentum, and
- θ is the angle between the torque vector and the angular momentum vector.

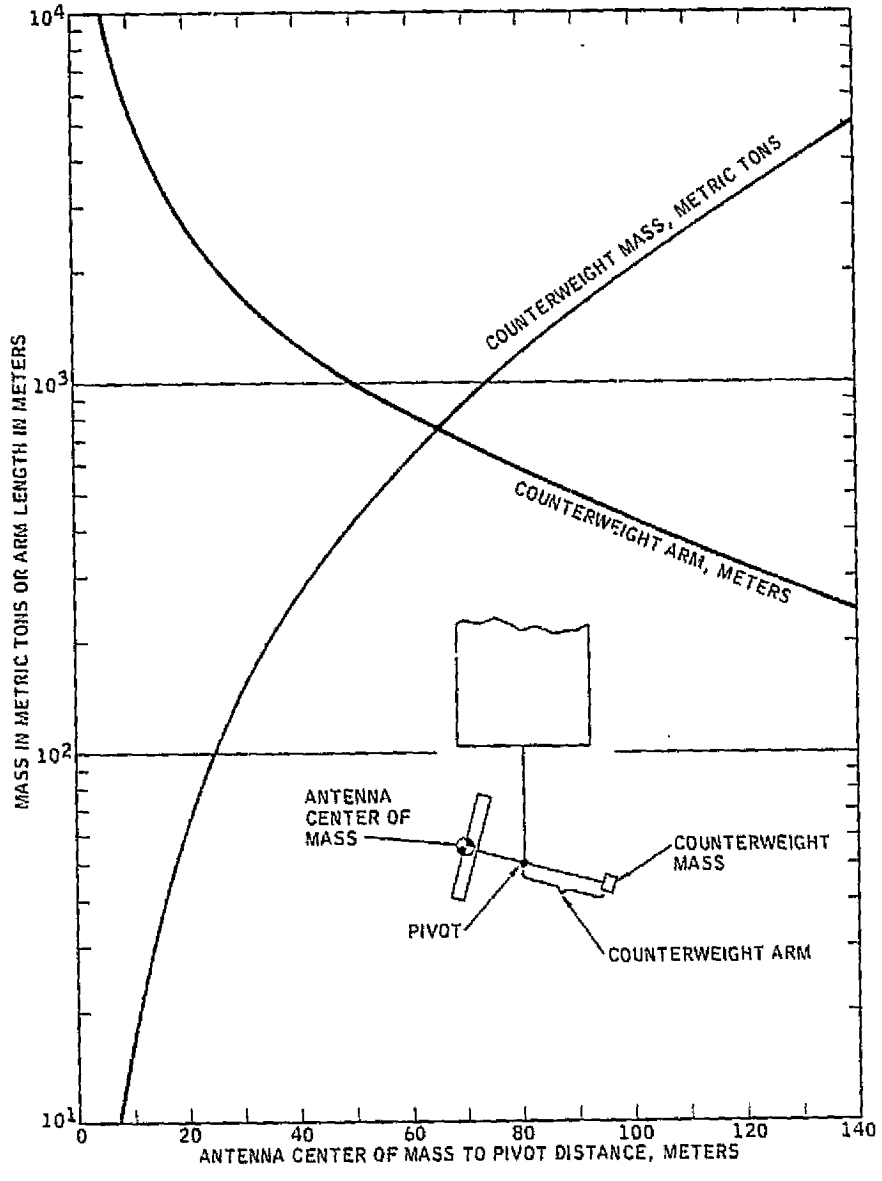

Figure 4-3., Counterweight characteristics for complete elimination of gravity gradient torque.

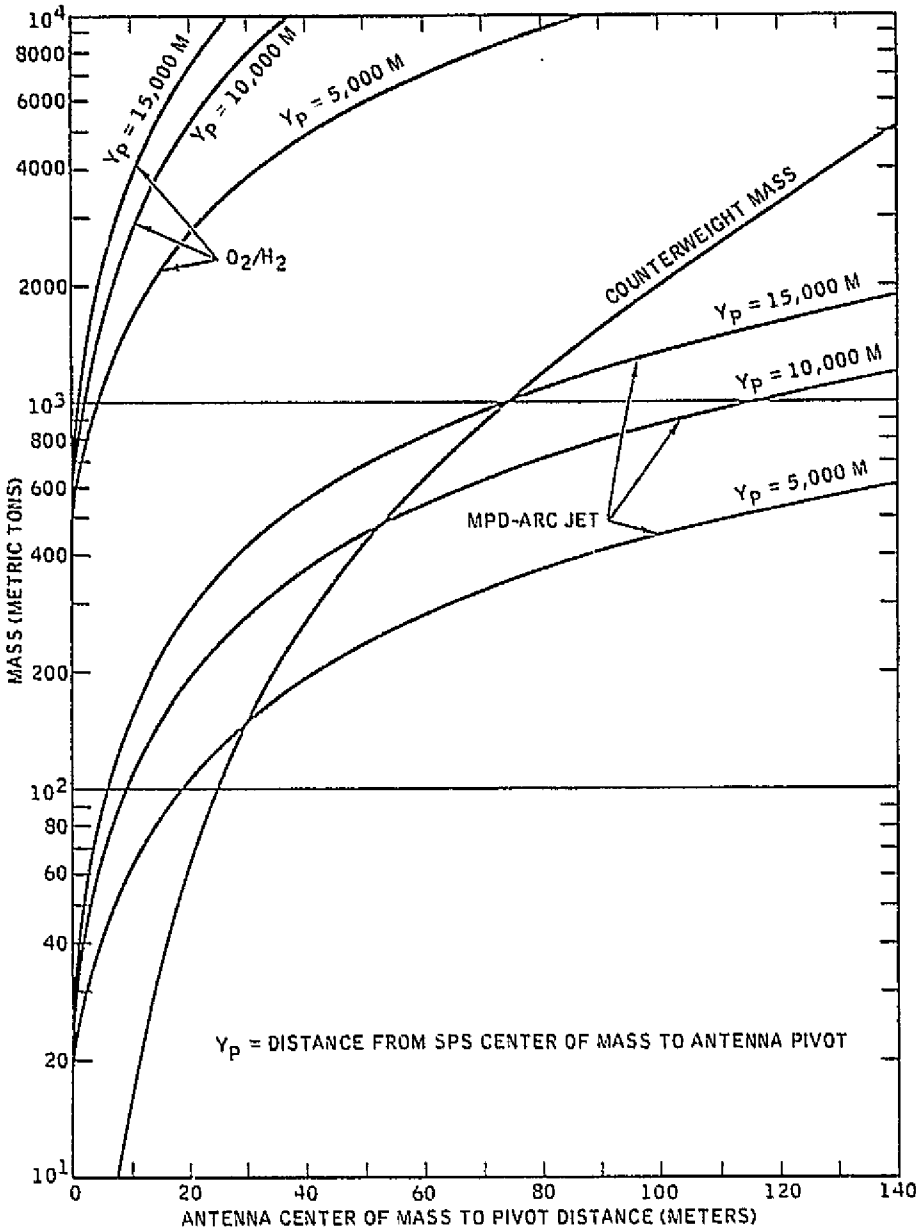

Figure 4-4. Propellant required to overcome gravity gradient.

The angle between the torque and the angular momentum vector is placed at 90 degrees by installing the angular momentum devices so the vector is parallel to the line-of-sight of the antenna. Then, if T/H equals 7.29×10^{-5}, the antenna will be driven so as to rotate once per day.

The weight of past angular momentum devices is such that such a scheme could not compete with counterweights or reaction control but the annular momentum control

device (AMCD) discussed in Reference 4-1 shows promise of dramatically increasing the angular momentum per mass. The reference shows that given the same shape factor, working stress, and rim density, angular momentum per mass is proportional to rim radius. Using data from the existing experimental AMCD, a conservative estimate for the characteristic of interest is

$$H/m = 60r_0 \text{ Newton Meter Sec per Kg}$$

where r_0 is the radius in meters.

The required AMCD mass based on the above relation has been listed for two antenna pivot distances in Table 4-1 along with the mass for a counterweight and MPD-arc jet propellant. A radius of 0.8 meter (the present experimental AMCD) is appreciably heavier than the other two approaches. Using a radius of 10 meters gives a device which is of about the same mass as the other approaches and using the full 500 meter

Table 4-1. Comparison of AMCD weights estimated to counter gravity gradient.

ANTENNA CENTER OF MASS TO PIVOT DISTANCE (METERS)	GRAVITY GRADIENT TORQUE (NEWTON - METERS)	REQUIRED ANGULAR MOMENTUM (NEWTON - METER - SEC)	AMCD MASS IN M.T. FOR 0.8 METER RADIUS	AMCD MASS IN M.T. FOR 10 METER RADIUS	AMCD MASS IN M.T. FOR 500 METER RADIUS	COUNTERWEIGHT MASS (METRIC TONS)	MPD-ARC JET PROPELLANT, M.T.
25	1.75×10^4	2.4×10^8	5×10^3	4×10^2	8.0	10^2	3.5×10^2
100	7×10^4	9.6×10^8	4×10^4	1.6×10^3	32.0	2×10^3	1.3×10^3

radius of the antenna give the AMCD a clear edge insofar as weight is concerned. Although the comparative weights are attractive, the problems associated with fabricating a 500 meter radius rim in space have not been studied and the possibility of fabricating so as to be able to operate a large rim at the same stress as a small rim is sufficiently questionable that the large rim is not considered a prime candidate.

4.2.4 MAGNETIC CONTROL — The earth's magnetic field is nominally perpendicular to the orbital plane for an equatorial orbit which is the correct orientation to interact with a current loop around the outside perimeter of the antenna so as to act against the

Reference 4-1. Anderson, W.W.; and Groom, N.J.; The Annular Momentum Control Device (AMCD) and Potential Applications, NASA TN-D-7866, March 1975.

gravity gradient torque. However, there are several problems with magnetic control, the first of which is the extreme weakness of the earth's field at synchronous orbit. If the antenna were statically balanced so that only moment of inertia differences produced torque, the current loop would require 50,000 amp tons. Assuming copper and a current density of 3 amps per square millimeter gives a coil weight of 460 metric tons and a resistive loss of about 10 megawatts. Referring to Figure 4-4, this mass of 460 M.T. places magnetic control in about the same class as the O_2/H_2 reaction control which was not even competitive with a counterweight. A second limitation of magnetic control is that either large energy storage or an alternate system would be required to prevent total loss of control and possible structural damage during occultation.

4.2.5 MECHANICAL SUPPORT — The techniques considered thus far have the desirable feature of not reacting the gravity gradient torque into the support structure. Although we have not, as part of this study, evaluated antenna support towers, it would appear that the additional strength in the tower is a more reasonable solution than the large masses required for the foregoing techniques.

Four possible arrangements for direct support against gravity gradient are shown in Figure 4-5. Candidate A retains an essentially free-floating characteristic by using force servos and cables to counter sustained torques and forces. Any standard spacecraft attitude control technique such as angular momentum exchange or reaction control could be used for the fine pointing. The force servos would be follow-up devices which would change force level slowly when logic indicated that pointing control was encountering bias torques. An actuator with unlimited freedom about the long axis has been used in all of the configurations shown. This actuator is required since the torque which must be reacted is judged to be greater than could be handled by a ball joint alone. This single degree of freedom actuator would include brushes for power transmission and be driven essentially as a clock at a constant rate such that brush stiction breakout is never seen by the antenna. Power transmission across other limited freedom elements would be by flex leads.

Using position actuators instead of force servos as shown in Figure 4-5B, is another possibility. In the B configuration, one of the actuators must serve as a rigid beam to support the antenna. This support might be better supplied by a beam as shown in C. The basic trade between B and C would be the requirement for three actuators in B, one of which must take lateral loads, versus two actuators with longer strokes as required by C. Both B and C will have relatively appreciable torques at the tower/solar collector interface that can be eliminated by use of the dog leg shape for the tower such that the nominal center of mass of the antenna/tower combinations is directly above the solar collector attach point.

4.3 POINTING TECHNIQUES

All of the pointing techniques considered are strongly influenced by the particular method of countering gravity gradient which is employed: pointing and gravity gradient countering must generally be considered in combination.

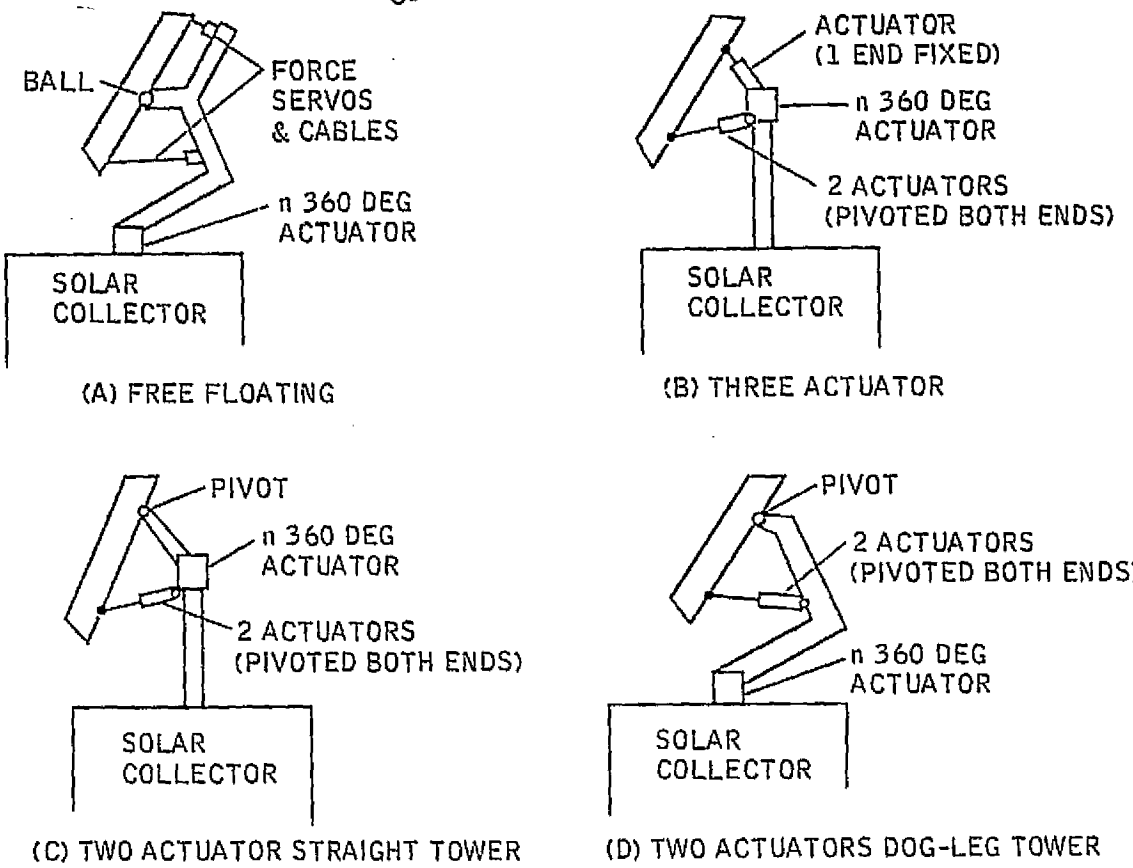

Figure 4-5. Direct support candidates.

4.3.1 ACQUISITION — The first step in pointing is to acquire the rectenna within the ± 0.7 degree range of the phase sensing system used for pointing error determination. Since the antenna does not have sufficient rotational freedom to acquire from any arbitrary solar collector orientation, it is assumed that the solar collector is in its proper attitude. Since the solar collector thus provides a reference, an earth sensor and some logic are the only additional items needed for acquisition. The azimuth drive can be used to rotate the antenna until the earth sensor acquires earth. An alternate approach would be to let the orbital motion bring earth into the view of a nonrotating antenna. With the earth sensor providing error signals based on ground-supplied data for azimuth and elevation for that particular SPS at that time of day, the pointing system will be operated to null the error signals. An earth sensor at synchronous altitudes typically has an accuracy potential of 0.05 degree so that even with some installation misalignment and tracking error, the phase sensing system should be well within its nonambiguous range. At this point the normal tracking mode can be engaged and normal pointing operation achieved.

4.3.2 STABILITY — In a dynamic system such as the antenna where the sensors and the actuators are separated by flexible structure, stability should always be a concern. However, based on such data as is available, there appears to be no unusual stability problem. The lowest oscillatory mode of the antenna has been calculated to be about

0.53 radians per second (12 second period) whereas the first oscillatory mode of the solar collector has been estimated to be 0.007 radian per second (900 second period) or slower. Getting the control crossover frequency at the geometric mean of the two gives a "control frequency" of 0.06 radian per second. This is a factor of 8.7 below the antenna's first mode which is favorable for stability since a factor of 5 is commonly considered adequate. At the same time solar collector bending disturbances are countered by the open loop gain being up at least a factor of 8.7 which will provide good apparent stiffness. The crossover of 0.06 radian corresponds to a 16 second time constant which coupled with a maximum tracking rate of 1.04×10^{-4} degree/sec gives a dynamic tracking error of only 0.1 arc minute even if integral compensation is not employed. In short, the frequency separation between the structural characteristics of the antenna and the solar collector shows the capability for good stability and good tracking performance. However, no data is available on the antenna/tower combination and the above conclusion should be reviewed when antenna/tower dynamics have been investigated.

4.3.3 DIRECT DRIVE — For the antenna/tower arrangements shown in B, C, and D of Figure 4-5, the pointing system is essentially brute force positioning of the actuators. Assuming that the actuator attach points are 500 meters apart, positioning the antenna to 0.1 arc minute corresponds to positioning the actuator to within 1.5 centimeters. It is not expected that actuator positioning accuracy will be a problem even with large actuators.

The cable arrangement of Figure 4-5A can also be used for direct drive if the upper extension of the tower is made into the upper two arms of a "Y". This is probably the simplest of the direct drive approaches since the long actuators with pivots at both ends are not required. The cable drive could be either with force servos and rate feedback for stabilization or with position servos with force sensing for follow-up operation to prevent the cables from pulling against each other to an excessive amount. Experience has shown that cable systems such as this can be tricky and a detailed evaluation including tower stiffness and dynamics should be conducted before seriously considering them for a baseline.

4.3.4 ANGULAR MOMENTUM EXCHANGE — If the essentially free floating arrangement of Figure 4-5A can be pointed by angular momentum exchange, this would provide smooth operation without any resupply requirements. Using the maximum rates shown in Table 3-2 and allowing 150 meters for the pivot to center of mass offset (moment of inertia increase) gives a requirement of 1.18×10^6 Newton-meter-seconds in azimuth and 0.84×10^6 n-m-sec in elevation for a total capacity of 2.02×10^6. This much angular momentum in AMCDs sized as the current 0.8 m radius unit would require about 42 metric tons. However, 10 m radius units mounted with their spin axes parallel to the plane of the antenna would have a mass of 3.4 metric tons.

4.3.5 REACTION CONTROL — Again using the arrangement of Figure 4-5A, pointing could be provided by reaction control thrusters mounted on the outside edges of the primary structure so as to provide maximum moment arm. The angular accelerations of Table 3-2 were used to estimate the 30 year impulse requirement to be 1.8×10^8

Newton-meter-seconds. The 30 year propellant requirement would be 46.3 metric tons for an O_2/H_2 system and 1.8 metric tons for a MPD-arc jet system.

4.3.6 NUTATION CONTROL — Using the angular momentum compensation of Section 4.2.3 for countering gravity gradient introduces a tendency of the antenna to nutate as a spinning body with a frequency of the net angular momentum divided by the moment of inertia. For a mounting which is unbalanced by 25 meters, the nutation period is 4.7 hours and a configuration with a 100 m offset would have a period of about 1.2 hours. This oscillation is of sufficiently long period that it can be readily controlled by the particular pointing technique selected.

4.3.7 MODAL DAMPING — One of the concerns with large space structures has been the possibility of large structural oscillations which could exist for long periods of time because of poor inherent damping. In order to evaluate the potential severity of structural oscillation problems, the first three oscillatory modes of the antenna were simulated along with an active damping system. The simulated structure was disturbed by a step force of 44,500 Newtons (10,000 lb) applied to the center of the antenna. A total of seven runs were made with different damping systems and time histories from one of the runs are shown in Figure 4-6. There are four actuators (or groups of actuators): X and Y actuators at nodes 1006 and 1086. The slope time histories at the top of the figure show the maximum deformation at node 1006 to be about 0.007 degree (0.4 arc minute) about the Y axis. The lower traces show the X and Y actuator torques.

It was found that with actuators mounted at the corner points of the hexagon structure, all runs could be matched very well by:

$$\text{Torque per Actuator} = \frac{33 \times 10^6}{N\, T_{\frac{1}{2}}} \text{ Newton-Meters}$$

where: N is the total number of actuators.
$T_{\frac{1}{2}}$ is the time in seconds for the transient to damp to half amplitude.

The above relation assumes the problem to be linear (no actuator saturation) so the corresponding torque requirements for different sizes of disturbance can be readily proportioned. Using Figure 4-6 as an example, the time to half amplitude is about 8 seconds. With $T_{\frac{1}{2}} = 8$ and $N = 4$, the torque expression gives a torque per actuator of about 10^6 Newton-meters (8.8×10^6 pound-inches) which compares reasonably well with the peak value of about 8×10^6 pound-inches exhibited by the Y actuator. It is again noted that this need not be all from one piece of hardware but could be the summed capability of any number of actuators acting about the Y axis at the specified locations.

In view of the result that a large step of force only produced 0.4 arc minute in surface deformation, active modal damping does not appear to be required. However, this conclusion should be re-examined if vibration sources such as rotating machinery are present.

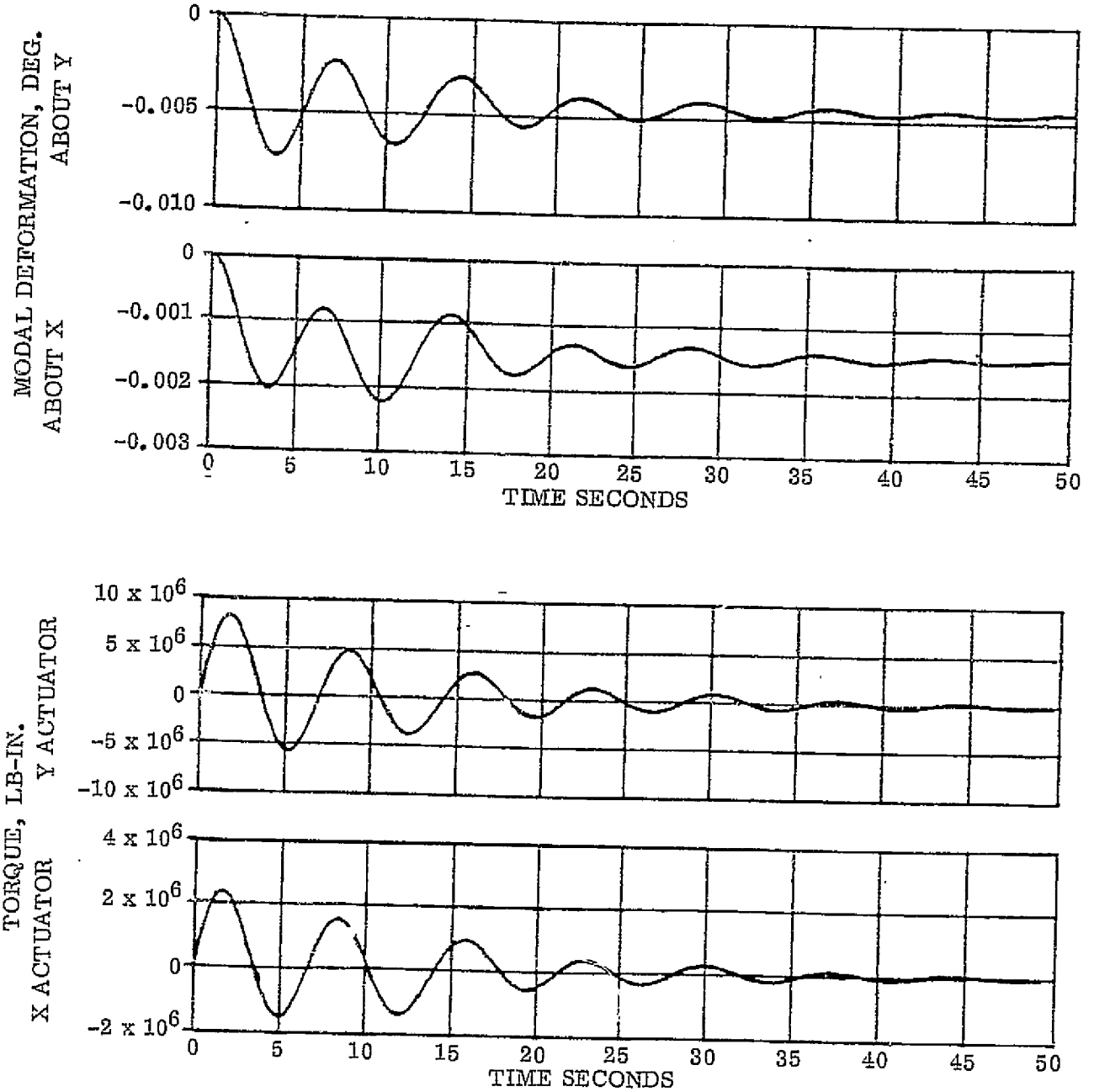

Figure 4-6. Modal damping system time histories for node 1006.

4.4 CONTROL SYSTEM STRUCTURAL MODIFICATIONS

Present concepts for the MPTS antenna require it to rotate about one or more axes with respect to the main structure. Rotation is necessary to allow the solar collectors to be directed toward the sun while the transmitting antenna remains pointed to a fixed ground rectenna (see Figure 4-7). The joints must provide structural stability and mechanisms to provide the proper antenna orientations as well as a means to transfer power.

Preliminary analysis by NASA has indicated that the use of slip rings and brushes for transferring power across a 360-degree continuously rotating joint will be more efficient and have less mass than other concepts. Structural and thermal considerations will most likely determine the joint dimensions. Flexible cables are prime candidates for use across joints that have limited freedom.

There are many options possible for the rotating joint configuration. An extensive trade study and design effort is required to optimize the system from the standpoints of transportation, assembly, complexity, and pointing performance, all of which is outside the scope of this study. This study has assumed a rigid interface where the antenna attaches to the joint, i.e., it accounts for all tolerance buildups between the antenna structure rotating joint interface to the antenna structure subarray interface.

A potential rotating joint and support structure at the MPTS antenna/SPS interface might look like Figure 4-8.

Besides the ability to rotate 360-degrees to track the sun, the ability to point the MPTS antenna at various locations on the earth can be accomplished by linear adjustment devices (like screw jacks) at either the support tripod to primary space polygon (node) interface or by making the upper and lower members in the support boom adjustable to allow tilting the rotating pivot joint (see Figure 4-8).

The support structure that attaches the MPTS antenna to the SPS is very similar to the type of construction used to build the MPTS primary structure. Triangular struts could be used for the support tripod. They would be attached to the primary structure at three of the six hard points on the lower surface of the common space polygon. Where these triangular support beams join together at the rotating joint, they form a hexagonal shape with unequal length sides similar to the joint discussed in Section 2.2 for the primary structures diagonal struts (see Figure 4-9).

Pointing control may be accomplished by a variety of methods as has been shown in the preceeding sections. The MPTS antenna baseline design can accommodate most of them very easily. The primary structures space polygon, where all the struts attach, is a "hard point." It lends itself to mounting attitude control thrusters, etc., then to distribute the load throughout the stiff geodetic structure. Likewise an annular momentum control device (AMCD) such as the one developed for NASA Langley Research Center by Ball Brothers Research Corp., and later modified by Sperry Flight Systems (see Figure 4-10) would fit nicely inside the primary space polygons. The

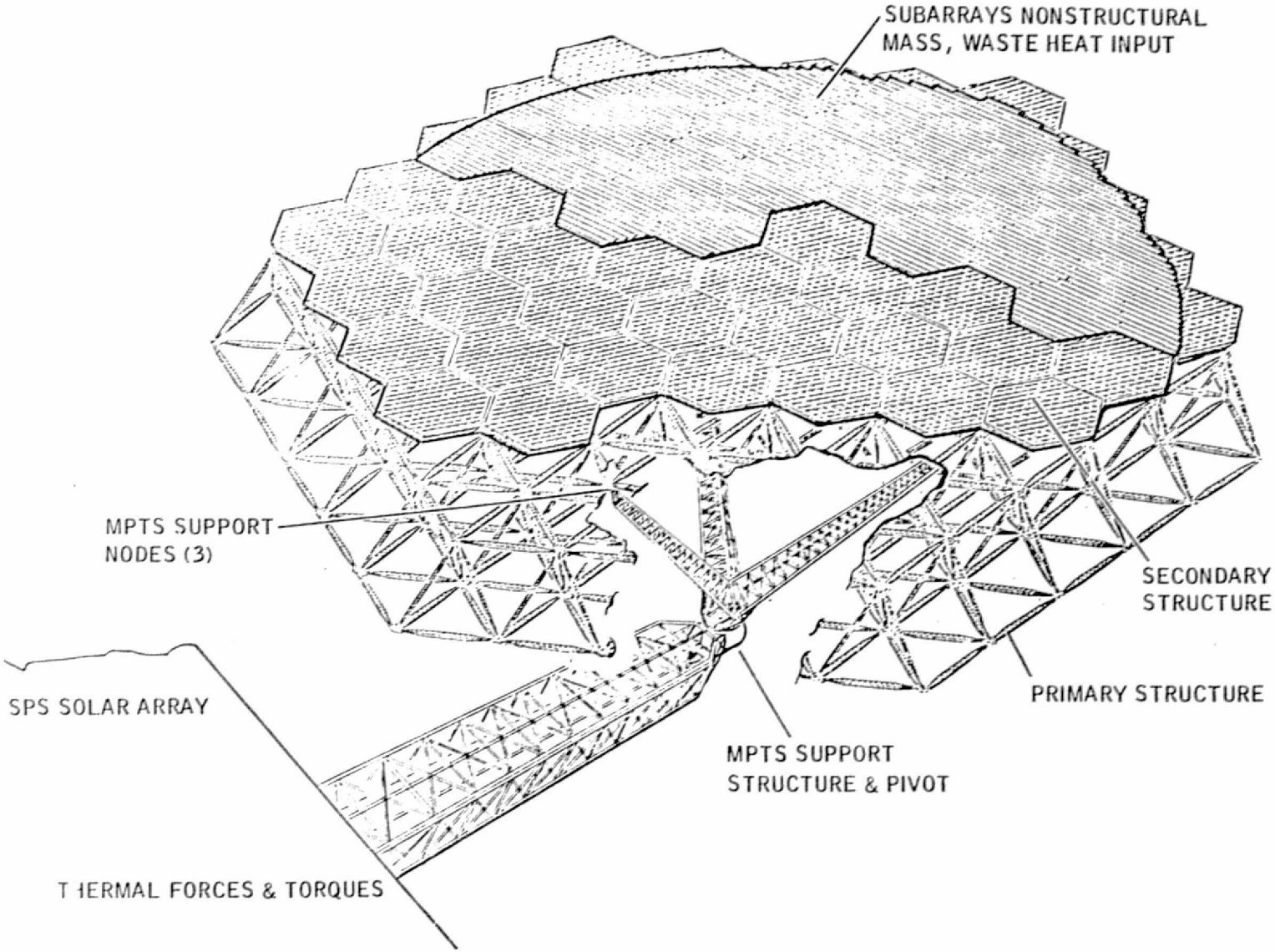

Figure 4-7. SPS to MPTS antenna interface considerations.

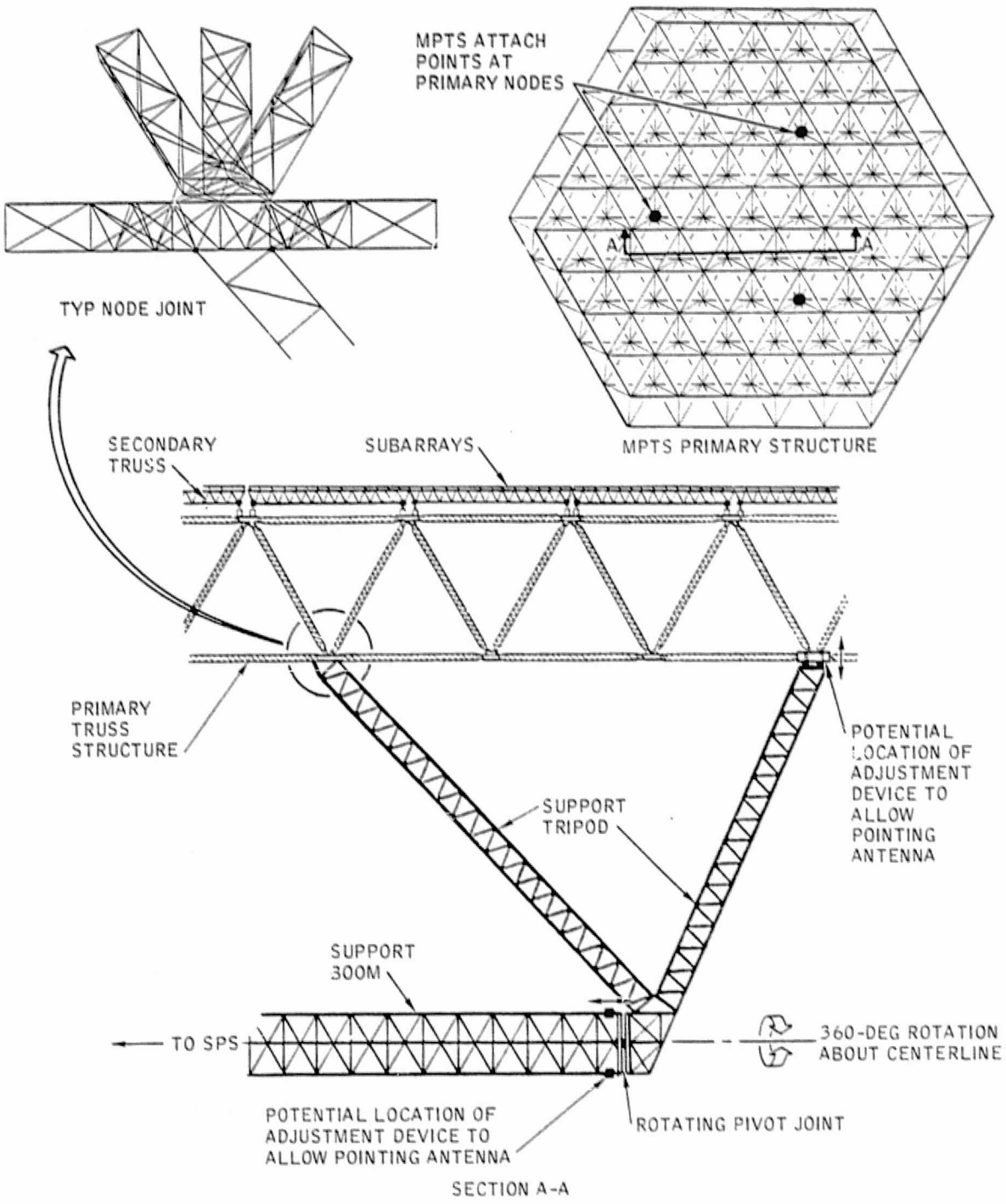

Figure 4-8. Primary to support structure interface.

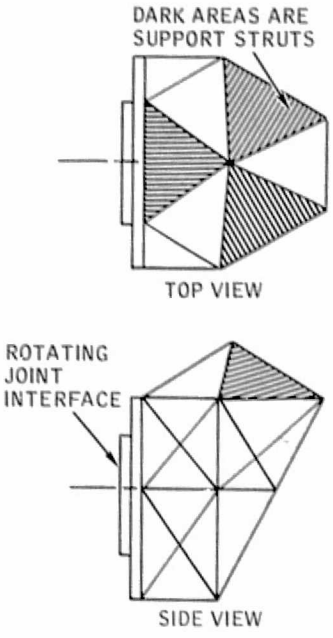

Figure 4-9. Support struts to rotating joint interface.

shape of the polygon structure being hexagonal provides six hard points to attach the magnetic suspension system.

4.5 CONTROL TECHNIQUES MATRIX

Having considered countering gravity gradient and pointing as somewhat separable problems, this section will address appropriate combinations of the two. A summary of the combinations is shown in Table 4-2.

The counterweight technique can be combined with direct drive, angular momentum exchange, or reaction control. The large mass of the counterweight is a disadvantage and more control power will be needed because of the resulting larger moment of inertia. Although counterweight techniques are not ruled out, they are not considered prime candidates.

Reaction control for countering the environment is actually more massive than the counterweight when the integrated 30 year propellant is considered but may be somewhat more practical since all of the propellant

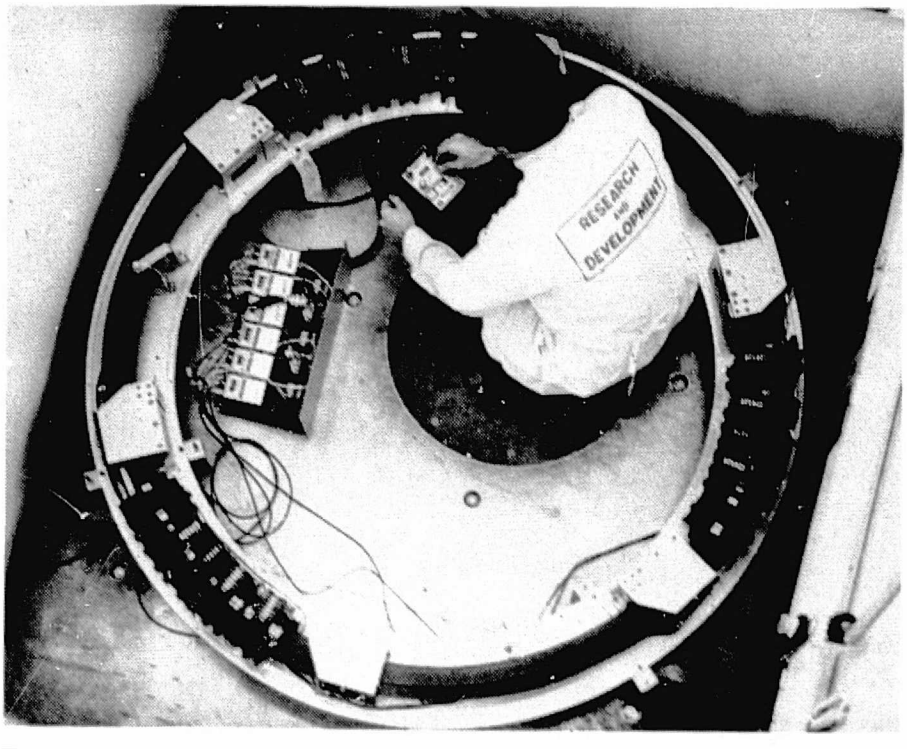

Figure 4-10. Annular momentum control device being tested at Sperry Flight Systems following modifications.

Table 4-2. Control techniques matrix.

GRAVITY GRADIENT COUNTERING TECHNIQUE	POINTING TECHNIQUE		
	DIRECT DRIVE	ANGULAR MOMENTUM EXCHANGE	REACTION CONTROL
COUNTER WEIGHT	GOOD PERFORMANCE POTENTIAL BUT MASSIVE		
REACTION CONTROL	NOT COMPATIBLE	GOOD PERFORMANCE — MASSIVE 30 YR PROPELLANT REQUIREMENT	
LARGE AMCD	NOT COMPATIBLE	GOOD PERFORMANCE BUT HAS RIM FABRICATION QUESTION	
MECHANICAL ACTUATOR	GOOD PERFORMANCE UNRESOLVED HARDWARE & TOWER QUESTIONS	NOT COMPATIBLE	
MECHANICAL CABLE		NO DEFINABLE BENEFIT OVER DIRECT DRIVE	
MAGNETIC	MASSIVE & HAS OCCULTATION PROBLEM — RECOMMEND NO FURTHER CONSIDERATION		

need not be in place before operation of the SPS begins. If resupply is practical, reaction control may be a better candidate than the counterweight. Direct drive pointing is incompatible with this approach, but either angular momentum exchange or reaction control pointing should perform quite well. Angular momentum would provide the smoother system, but the propellant for reaction control pointing would probably be noise level compared to the amount needed to counter gravity gradient.

A large AMCD sized to interact with environmental torques so as to precess at the rate required for the daily rotation will perform very well with either momentum exchange pointing or reaction control pointing. However, this is a questionable candidate because of possible problems of fabricating a 1.0 Km diameter rim in orbit which is balanced and which can take the required spin loads.

The mechanical actuators for both environmental torques and pointing appear to be one of two most promising approaches. Questions remain, however, about interaction

and interface with the tower and about suitable large actuators for 30 years of space operation.

Using mechanical cable for environmental torques and pointing is the other very promising approach. Again, tower interactions and interfaces need further study. Cable dynamics have caused problems in some past closed loop systems and especially careful study should be given the dynamics of cable, antenna, and tower interaction before selecting the cable technique as a baseline system. However, if the dynamics problems can be resolved, this approach offers the payoff of maximum simplicity and minimum weight.

4.6 SPECIFICATION FOR STRUCTURAL MODIFICATIONS

The specification controlling the structure used to attach the various control devices and the MPTS support tripod beams will be the same as for the basic MPTS structure (reference Appendix).

The sizes of the structural elements will of course vary significantly. But in an effort to simplify the in-orbit construction task, it would be logical to use the same beam building method, construction techniques, joints, materials, etc. as are used in the construction of the MPTS structure.

Report No. CASD-NAS-78-011

FINAL REPORT

ACHIEVABLE FLATNESS IN A LARGE MICROWAVE POWER ANTENNA STUDY

(DRL Item No. 2)

5. TASK 5 — MATERIAL PROPERTIES

Prepared under
Contract No. NAS9-15423
for
National Aeronautics and Space Administration
LYNDON B. JOHNSON SPACE CENTER
Houston, Texas 77058

Prepared by
GENERAL DYNAMICS CONVAIR DIVISION
P.O. Box 80847
San Diego, California 92138

5

TASK 5
MATERIAL PROPERTIES

5.1 COEFFICIENT OF THERMAL EXPANSION

Use of composite materials with near-zero coefficient of thermal expansion is critical to the construction of thermally stable structures. Laminates can be tailored to get a theoretical CTE of zero at one temperature by use of mixtures of fibers, crossplies, and varying fiber content. Although the mean value of a series of composite parts may be near zero, the individual parts have CTEs which are distributed about the mean. The effects of the statistical distribution of CTE have been found to be more significant than those of the average value in the achievable flatness for the MPTS. The more different materials used in the composite, and the reliance on critical fiber content or crossply angles to achieve zero CTE may actually increase the variation in CTE of individual specimens about the mean.

Pseudoisotropic GY-70/X-30 is an example of a graphite/epoxy material with inherently low coefficient, typically -0.04 μ/m/C (-0.02 μin./in./F). For the SPS structures, it can be assumed that a materials development program will yield a more efficient composite than GY-70/X-30. It would have higher E, lower CTE, lower cost, and less dispersion in composite properties. Since it cannot be used at the anticipated operational temperatures of the MPTS, it is not recommended. However, it is being used in similar dimensionally stable space structures, and statistical CTE data is available for this composite. Its material properties provide a convenient baseline for this study.

Table 5-1 lists the measured CTE for 45 samples of GY-70/X-30. This data was accumulated for 10 batches of prepreg fiber. To be more specific, each value should be associated with a temperature, or be said to represent the average CTE for a particular temperature range.

In general, the values shown are for moderate temperatures. Actually CTE for graphite/epoxy is relatively independent of temperature, so lumping the values in the table is reasonably valid. On the basis of these measurements, the predicted CTE for pseudoisotropic GY-70/X-30 is -0.038 μ/m/C (-0.021 μin./in./F) with a standard deviation of 0.072 (0.040).

As stated above, CTE for graphite/epoxy is usually relatively constant with temperature. We calculated the temperature dependency of CTE for GY-70/X-30 pseudoisotropic material. The temperature dependent CTE function is:

$$CTE(T) = A(T - 70) + B$$

where: A is a random variable with mean μ_a = -2.30E-6 and standard deviation σ_a = -2.52E-4

B is a random variable with mean μ_b = -2.29E-2 and standard deviation σ_b = 2.71E-2

T is in degrees Fahrenheit, and CTE has units of μin./in./F

Table 5-1. Pseudoisotropic GY-70/X-30 average coefficient of thermal expansion.

Lot No.	μ/m/C*	(μin./in./F)	Lot. No.	μ/m/C*	(μin./in./F)
6B-90	-0.103	-0.057	6B-90	-0.059	-0.033
	-0.077	-0.043		-0.040	-0.022
	-0.061	-0.034		-0.027	-0.015
	-0.049	-0.027		-0.000	0.000
	0.036	0.020	6C-37	-0.018	0.010
	-0.094	-0.052	5D-2	-0.049	-0.027
	0.009	0.005	4B-98	-0.077	-0.043
	-0.045	-0.025	5C-48	-0.099	-0.055
	-0.005	-0.003	4C-66	-0.144	-0.080
	0.018	0.010		-0.108	-0.060
	-0.067	-0.037		-0.092	-0.051
	-0.121	-0.067		-0.133	-0.074
	-0.104	-0.058		-0.083	-0.046
	-0.167	-0.093	4C-79	0.041	0.023
	0.004	0.002		0.036	0.020
	-0.108	-0.060		0.068	0.038
	-0.027	-0.015		0.029	0.016
	-0.077	-0.043	HEAO	0.173	0.096
	0.013	0.007		0.148	0.082
	-0.099	-0.055		-0.034	-0.019
	-0.050	-0.028		0.050	0.028
	-0.040	-0.022	4D-17/18	-0.126	-0.070
	-0.005	-0.003			

*Measurement Accuracy is ± 0.02 (± 0.01)

This model adjusts the CTE for temperature, and also incorporates the predicted distribution as a function of temperature. The variation of mean value of CTE is very small with temperature, but the distribution broadens as the temperature moves away from the reference 70F. A 100F temperature change doubles the effective standard deviation in CTE. This analysis was conducted in English units to be compatible with the test data. The final result is interpreted in metric units.

The coefficients A and B were computed from 29 CTE measurements of batch 6B-90 GY-70/X-30 composite for which microstrain vs. temperature data was available. Figure 5-1 shows straight line segments connecting the data points. The starting microstrain value is arbitrary since only the slope of the curve has significance. In Figure 5-2, a best fit (least squares) parabola:

$$a\,(T-70)^2 + b\,(T-70) + C$$

was fit to each specimen's data points. In Figure 5-3, only a $(T-70)^2 + b\,(T-70)$ was plotted. This normalizes all the curves to 0 microstrain at 70F. The mean and

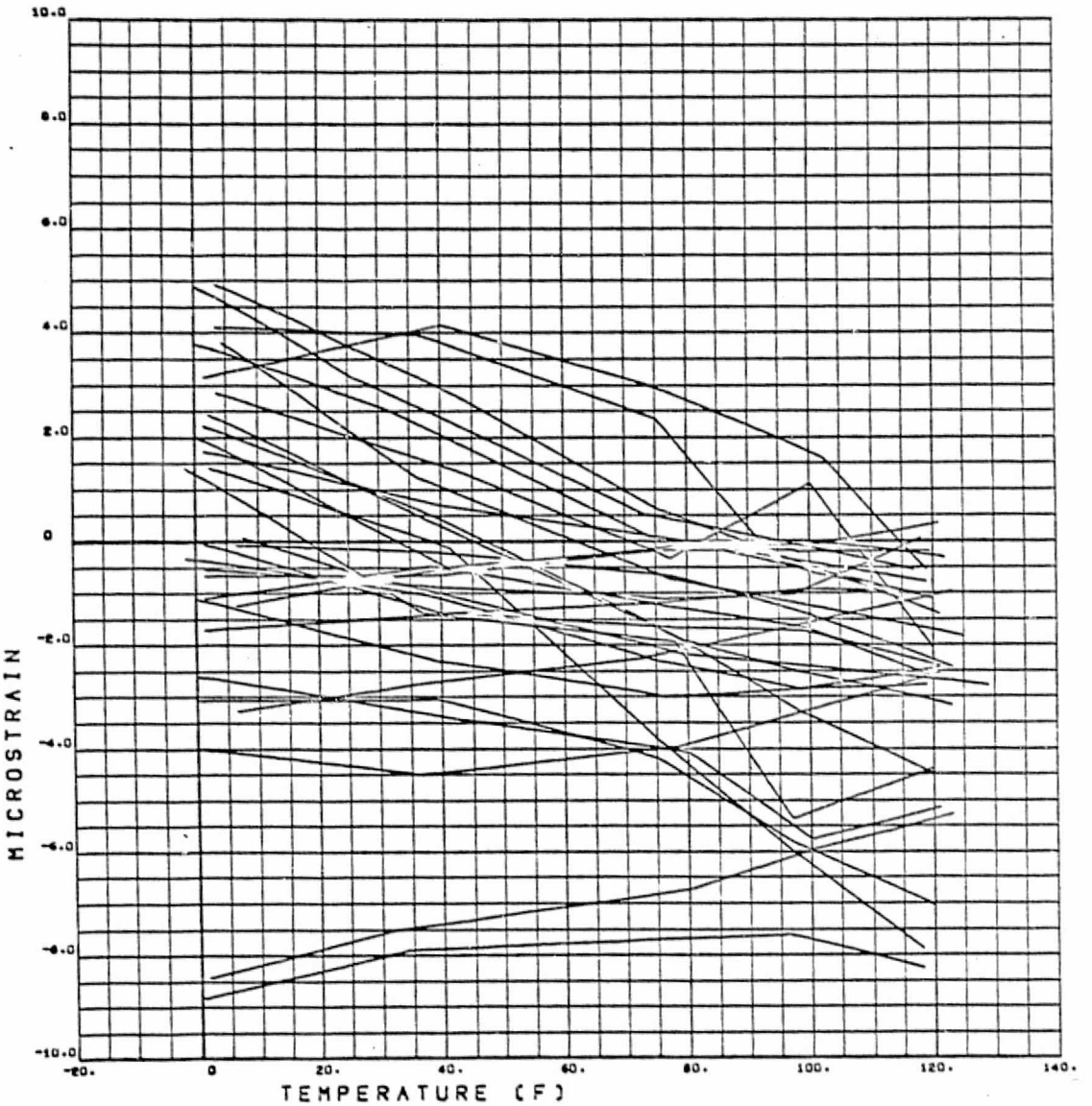

Figure 5-1. Original test data — 29 specimens ($\Delta L/L$ versus temperature for GY-70/X-30).

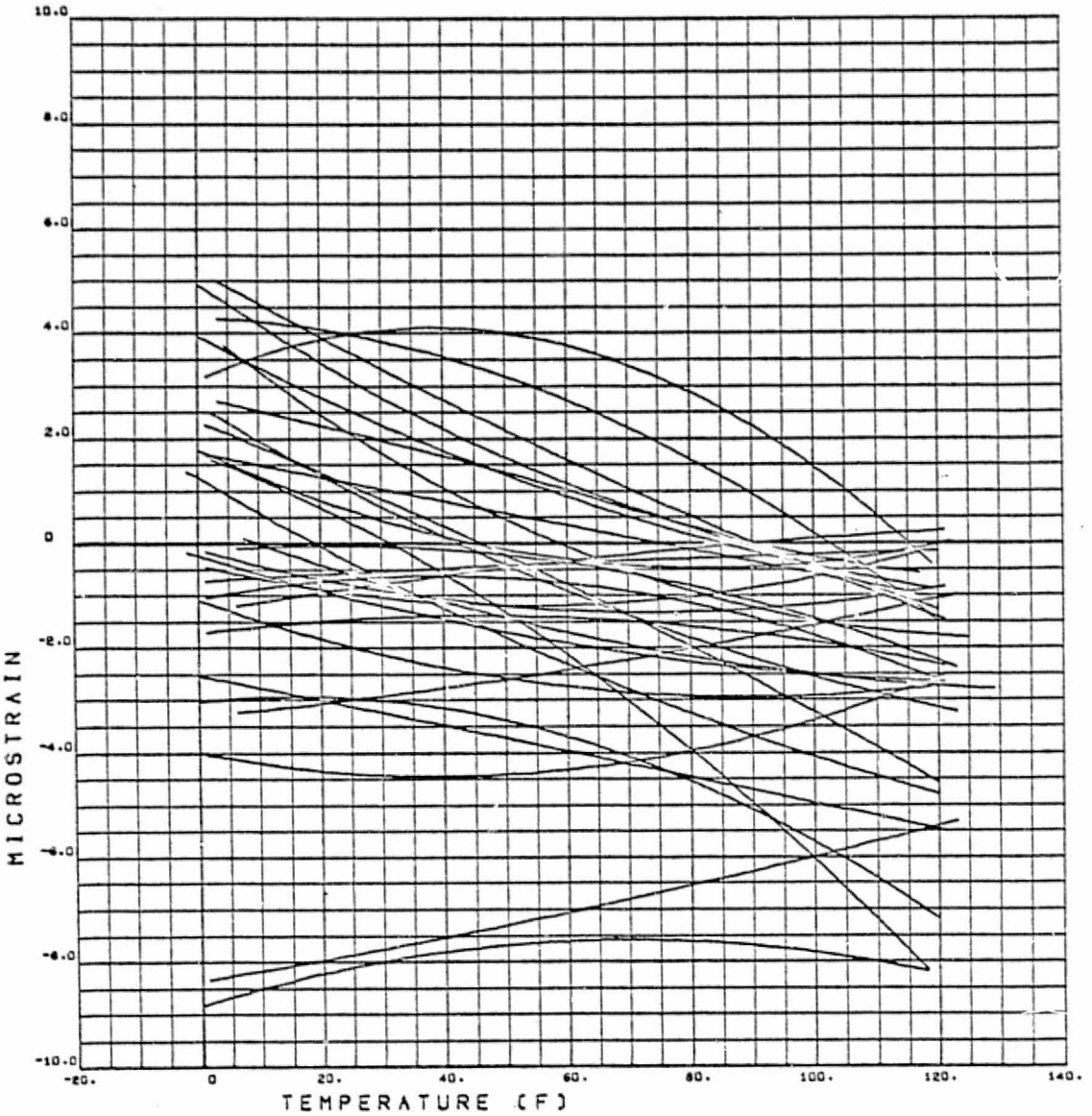

Figure 5-2. Smoothed original data makes use of best fit quadratics.

standard deviation of a and b were than determined. In Figure 5-4, $\mu_a (T-70)^2 + \mu_b (T-70)$ was plotted. This shows the stability of CTE over a moderate temperature range since the slope is essentially constant. In Figure 5-5, $A(T-70)^2 + B(T-70)$ was plotted where A and B were determined by use of μ_a, σ_a, μ_b, σ_b and a random number generator. Twenty-nine cases of random A and B were generated to simulate the distribution of experimental CTE in Figure 5-3. We believe that use of this model gives the most accurate estimate of the types and magnitudes of thermally induced distortion for the MPTS in the operational environment.

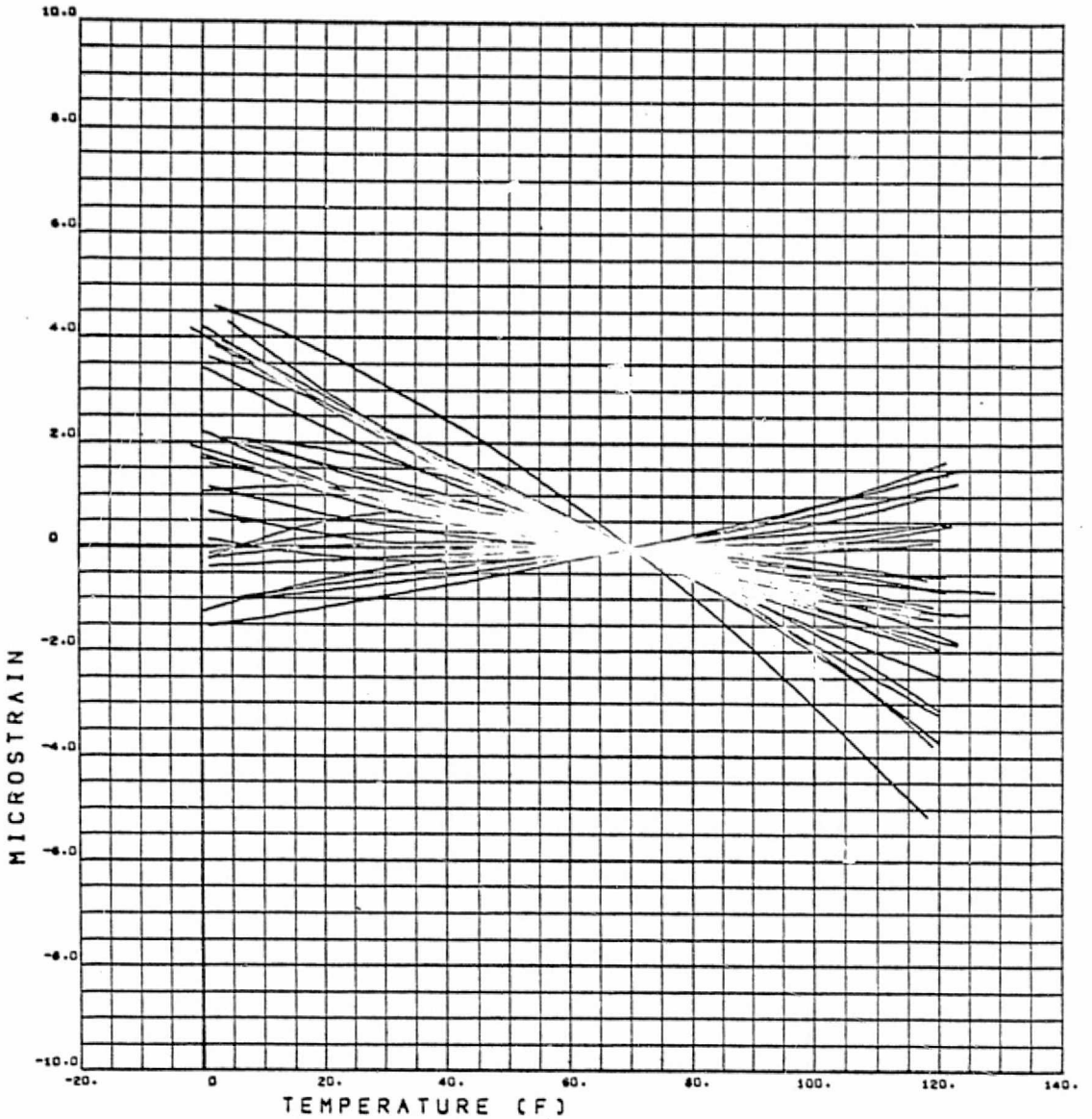

Figure 5-3. The smoothed data is then normalized to 70F.

The coefficient of thermal expansion is then the temperature derivative of the microstrain curves. The mean value of CTE, and the anticipated range of values anticipated for a large sample at any temperature is illustrated in Figure 5-6.

The microstrain measured in the determination of CTE is small, typically less than 10. The measurement requires the use of a laser interferometer or comparison of specimen length to the length of a calibrated standard. In the latter approach, a laser beam is deflected by a mirror balanced across the specimen and reference. The former method is very accurate, but difficult to use in routine CTE measurement. The latter method has been used to measure the specimens analyzed in this section. There is considerable scatter in the data due to the measurement procedure. The true distribution of

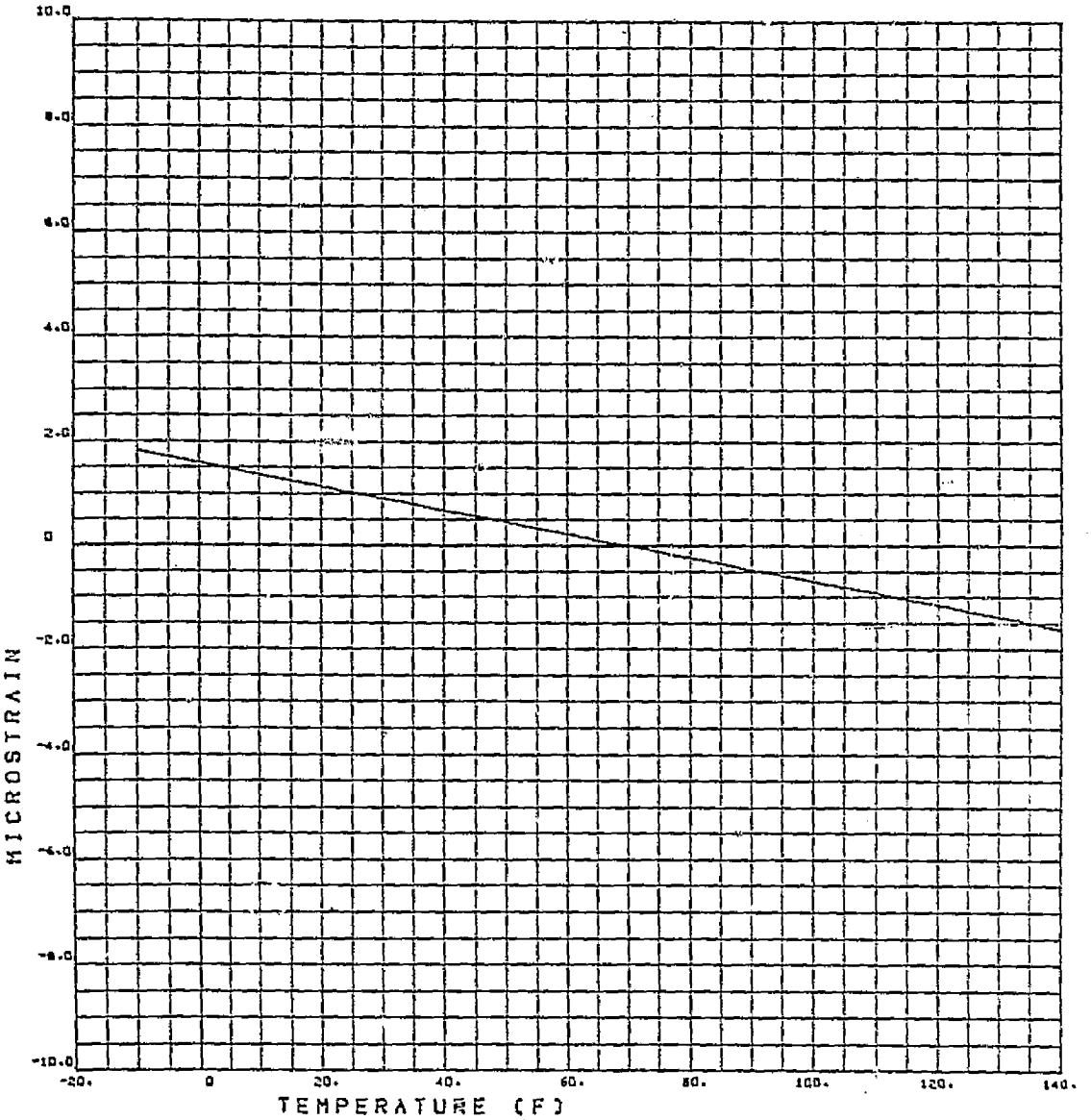

Figure 5-4. Best fit quadratic for 29 specimens.

CTE can be expected to be less than the measured distribution. This approach, which was developed to determine average CTE and not necessarily distribution is accurate for that purpose. Use of a laser interferometer to measure the distribution of a large sample would be the more accurate method.

There are other considerations, however, which must be taken into account before a material is considered to be fully characterized as to thermal stability for use in the SPS structures. These include changes in CTE with time, under load, after thermal cycling, after thermal shock, and if applicable after exposure to moisture and drying cycles. All of these effects are being investigated.

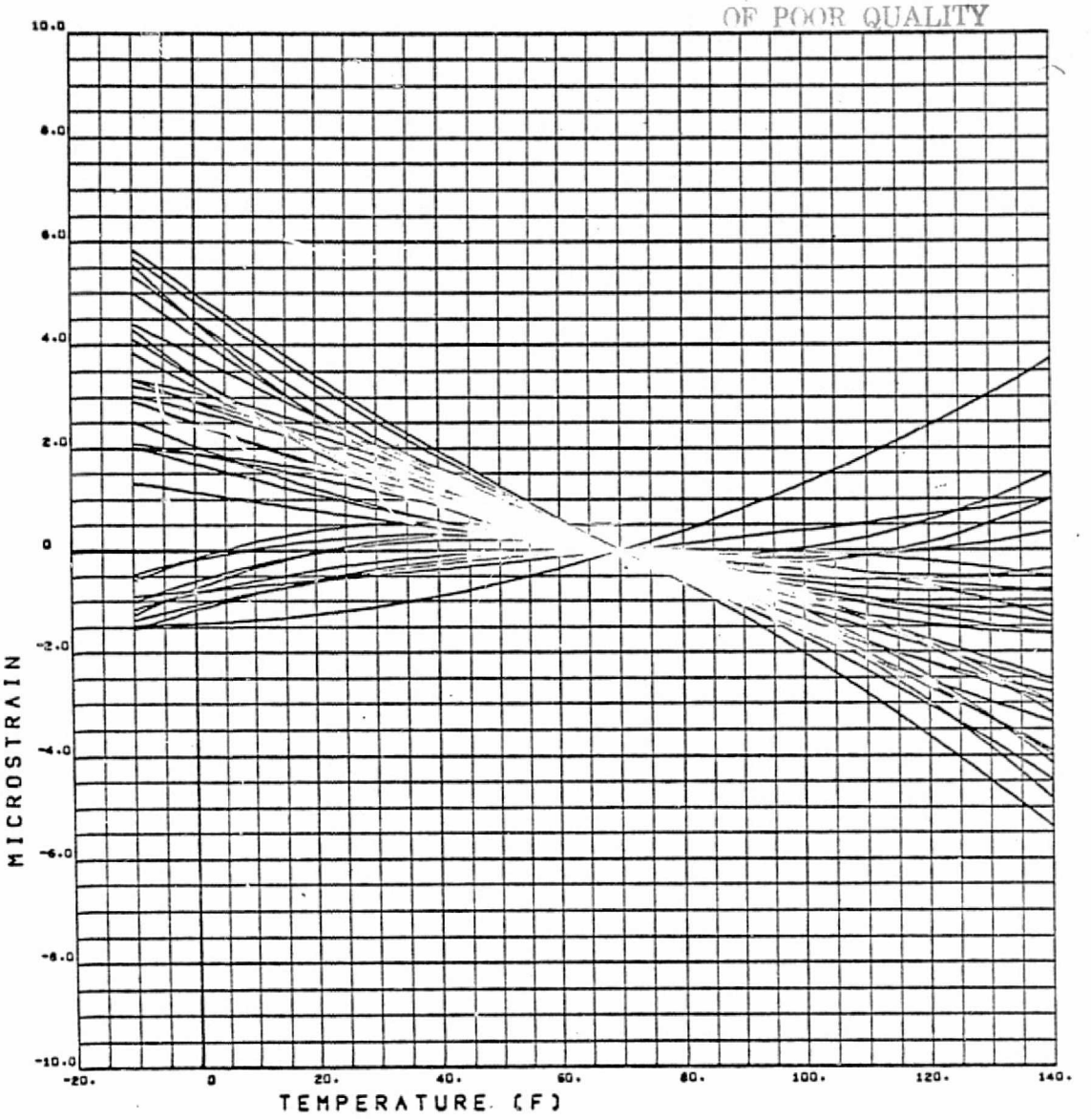

Figure 5-5. Example of random microstrain predicted for 29 additional samples.

5.2 STRENGTH AND MODULUS

A relatively large sample of GY-70/X-30 specimens, both unidirectional and pseudo-isotropic, is available for analysis. The objective of the analysis is to determine the statistical distribution in tensile and compressive strength of the composites and the elastic modulus. MIL-HDBK-5 specifications are then applied to determine "B Allowable" values for these composites. In this study, the material properties of GY-70/X-30 are used as typical of the G/E which will probably be available for use in SPS fabrication. The fiber itself would be suitable for the MPTS application — except for cost. The resin system does not meet maximum operational temperature

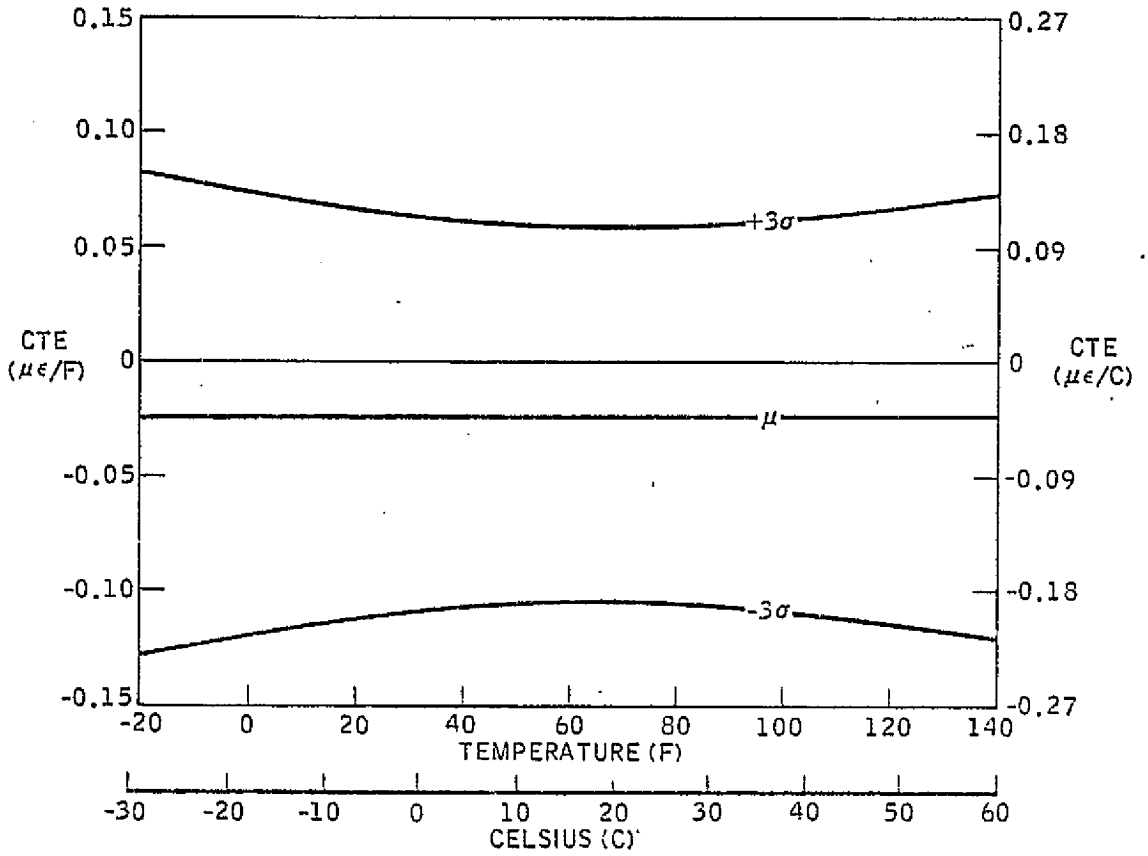

CTE = f (C) =

-4.12×10^{-8}

$+4.88 \times 10^{-8}$ G

-7.45×10^{-12} (C - 21.2)

$+8.16 \times 10^{-12}$ (C - 21.1) G

CTE = f (T) =

-2.29×10^{-8}

$+2.71 \times 10^{-8}$ G

-2.30×10^{-12} (T - 70)

$+2.52 \times 10^{-10}$ (T - 70) G

Where G is a random gaussian variable with zero mean and unity standard deviation.

Figure 5-6. Random, temperature dependent model of CTE for pseudoisotropic GY-70/X-30.

requirements. Lower cost fibers (e.g. pitch fibers) are becoming available, and high temperature resin systems are also in use. The statistical properties of these advanced composites are not expected to be very different from the GY-70/X-30 baseline composite.

The accumulated strength and modulus data for GY-70/X-30 is listed in Table 5-2. In Table 5-3 the mean of the sample, $\bar{x}$, the sample standard deviation, s, and the number of specimens in the sample, m, are reported.

In order to establish design allowables it is necessary to have data adequate to represent the current process capability of a material. Normally, a minimum of 100 individual measurements are required. These data should contain measurements from at least 10 production batches or lots from each of a majority of the major producers of the material. For materials on which there is little background information or the scatter in properties is great, more data is required. If possible, data from more than one test facility should be used.

These test requirements are difficult to meet for graphite/epoxy materials. For GY-70/X-30, the fiber GY-70 is made by one manufacturer, the resin X-30 by another, and there presently are no alternative sources. The prepreg is made by a third organization, then the layup and cure by a fourth. Variation in procedure at any point in the manufacturing process can cause a significant change in the material properties.

For the manufacture of SPS graphite/epoxy components, many manufacturers will be involved but also uniform process specifications will be used, and the statistical distribution of properties will probably be better than that reflected by the data in Table 5-2.

In the design of aerospace components, the "B Allowable" is a mechanical-property value above which at least 90 percent of the entire population of values is expected to fall with a confidence of 95 percent. That is, the confidence is 95 percent that at least 90 percent of the entire population would exceed the "B" values; determined by $x - ks$. The coefficient "k" is the one-sided tolerance factor for a normal distribution. Values for k are computed from noncentral t-distribution for n-1 degrees of freedom.

A table of k(P, 0.95, n) is given in MIL-HDBK-5, pages 9-76 to 9-81, 1 September 1971. Using this table, for P = 0.90 ("B" Allowable), the values of k are determined for Table 5-3. The B allowable, $x - ks$ is then shown for strength and modulus.

Since this method requires that the distribution of the variable is normal, an alternative method of computing B allowable is given in MIL-HDBK-5, page 9-82, which is valid for any distribution. The data is repeated here in Table 5-4.

The measured values are ordered from low to high. The table is entered at the largest value of n equal to or less than the sample size. The value of the 'r'th specimen counting from the lowest value is the best estimate for B allowable. The

Table 5-2. . Strength and modulus of GY-70/X-30.

07/31/78 STRENGTH AND MODULUS OF GY-70/X-30 PAGE 1

-------LOT NO.-------	----------UNIDIRECTIONAL----------						----------ISOTROPIC----------					
	FTU	ET	UT	FCU	EC	UC	FTU	ET	UT	FCU	EC	UC
6B-90	93.4	46.7	.310	64.9	41.1	.270	35.1	15.6	.350	36.8	14.2	.320
6B-90	94.8	47.8	.300	83.3	45.1	.340	26.9	14.3	.320	33.5	13.7	.270
6B-90	81.7	46.5	.300	81.8	41.2	.230	33.3	14.7	.300	37.6	14.0	.270
6B-90	83.8	47.3	.310	88.6	43.0	----	----	----	----	----	----	----
6B-90	99.9	46.0	.330	65.1	41.6	.330	----	----	----	----	----	----
6B-90 TAG ENDS	----	----	----	----	----	----	32.1	14.1	.320	----	----	----
6B-90 TAG ENDS	----	----	----	----	----	----	31.0	15.5	.305	----	----	----
6B-90 TAG ENDS	----	----	----	----	----	----	28.6	15.9	.320	----	----	----
6B-90 TAG ENDS	----	----	----	----	----	----	37.1	15.5	.330	----	----	----
6B-90 TAG ENDS	----	----	----	----	----	----	41.8	16.2	.315	----	----	----
6B-90 TAG ENDS	----	----	----	----	----	----	32.5	15.5	.320	----	----	----
6B-90 TAG ENDS	----	----	----	----	----	----	35.2	15.3	.320	----	----	----
6B-90 TAG ENDS	----	----	----	----	----	----	36.7	15.1	.300	----	----	----
6B-90 TAG ENDS	----	----	----	----	----	----	34.8	14.8	.315	----	----	----
6B-90 TAG ENDS	----	----	----	----	----	----	34.8	15.0	.320	----	----	----
6B-90 TAG ENDS	----	----	----	----	----	----	37.3	16.0	.300	----	----	----
6B-90 TAG ENDS	----	----	----	----	----	----	37.8	15.5	.330	----	----	----
6C-37	96.8	45.8	----	----	----	----	32.0	13.8	----	----	----	----
6C-37	113.2	46.1	----	----	----	----	32.8	14.1	----	----	----	----
6C-37	84.0	47.0	----	----	----	----	36.1	15.1	----	----	----	----
5D-2	119.1	46.3	----	----	----	----	37.8	16.1	----	----	----	----
5D-2	120.7	47.9	----	----	----	----	37.0	15.6	----	----	----	----
5D-2	114.1	46.5	----	----	----	----	37.4	16.4	----	----	----	----
4B-98 SHIPMENT 4	146.9	46.7	----	----	----	----	32.3	15.7	----	----	----	----
4B-98 SHIPMENT 4	147.7	45.1	----	----	----	----	33.8	15.6	----	----	----	----
4B-98 SHIPMENT 4	143.5	46.0	----	----	----	----	----	----	----	----	----	----
4B-98 SHIPMENT 2	141.5	48.2	----	----	----	----	50.6	15.8	----	----	----	----
4B-98 SHIPMENT 2	133.3	47.2	----	----	----	----	43.2	15.9	----	----	----	----
4B-98 SHIPMENT 2	97.3	48.2	----	----	----	----	----	----	----	----	----	----
4B-98 SHIPMENT 1	87.5	47.4	.330	105.6	----	----	43.4	16.8	----	----	----	----
4B-98 SHIPMENT 1	----	----	----	114.7	----	----	----	----	----	----	----	----

Table 5-2. Strength and modulus of GY-70/X-30. (Cont'd)

07/31/78 STRENGTH AND MODULUS OF GY-70/X-30 PAGE 2

-------LOT NO.-------	UNIDIRECTIONAL						ISOTROPIC					
	FTU	ET	UT	FCU	EC	UC	FTU	ET	UT	FCU	EC	UC
4B-98 SHIPMENT 1	----	----	----	95.1	----	----	----	----	----	----	----	----
4B-98 SHIPMENT 1	119.7	52.1	.340	107.9	----	----	49.9	16.3	----	----	----	----
4B-98 SHIPMENT 1	103.2	48.6	.310	110.5	----	----	----	----	----	----	----	----
3B-88	96.8	45.0	----	----	----	----	28.4	13.0	.330	----	----	----
3B-88	127.8	43.8	----	----	----	----	30.8	14.3	.290	----	----	----
3B-88	131.0	45.0	----	----	----	----	33.1	14.1	.320	----	----	----
4A-13	----	----	----	----	----	----	44.2	16.3	----	----	----	----
4A-13	----	----	----	----	----	----	38.7	15.8	----	----	----	----
4A-37	83.3	47.0	----	----	----	----	30.6	13.6	----	----	----	----
4A-37	97.4	45.9	----	----	----	----	31.2	14.4	----	----	----	----
4A-37	70.6	46.9	----	----	----	----	----	----	----	----	----	----
4A-48	86.0	47.6	----	----	----	----	27.6	14.5	----	----	----	----
4A-48	88.5	46.7	----	----	----	----	33.8	15.6	----	----	----	----
4A-48	82.2	48.0	----	----	----	----	----	----	----	----	----	----
4A-61	88.4	48.8	----	----	----	----	35.3	16.9	----	----	----	----
4A-61	103.5	48.4	----	----	----	----	33.6	15.9	----	----	----	----
4A-61	101.7	50.0	----	----	----	----	----	----	----	----	----	----
4A-65	103.9	45.8	----	----	----	----	43.4	16.2	----	----	----	----
4A-65	109.6	46.0	----	----	----	----	----	----	----	----	----	----
4A-65	121.0	45.2	----	----	----	----	----	----	----	----	----	----
4A-82	129.5	44.8	----	----	----	----	31.2	14.9	----	----	----	----
4A-82	131.8	44.4	----	----	----	----	34.1	15.2	----	----	----	----
4A-82	108.4	46.6	----	----	----	----	----	----	----	----	----	----
4A-87	135.4	48.7	----	----	----	----	40.4	15.6	----	----	----	----
4A-87	91.4	48.2	----	----	----	----	41.0	14.8	----	----	----	----
4A-87	116.1	49.4	----	----	----	----	----	----	----	----	----	----
4B-12	159.6	47.1	----	----	----	----	36.2	13.8	----	----	----	----
4B-12	130.6	47.7	----	----	----	----	39.3	15.2	----	----	----	----
4B-12	140.9	47.3	----	----	----	----	----	----	----	----	----	----
4A-99	119.4	44.8	----	----	----	----	42.5	17.2	----	----	----	----
4A-99	110.0	45.4	----	----	----	----	41.7	17.0	----	----	----	----

Table 5-2. Strength and modulus of GY-70/X-30. (Cont'd)

07/31/78 STRENGTH AND MODULUS OF GY-70/X-30 PAGE 3

LOT NO.	UNIDIRECTIONAL						ISOTROPIC					
	FTU	ET	UT	FCU	EC	UC	FTU	ET	UT	FCU	EC	UC
4A-99	100.0	48.7	----	----	----	----	----	----	----	----	----	----
QC PANELS	----	----	----	----	----	----	39.8	16.1	----	----	----	----
QC PANELS	----	----	----	----	----	----	42.0	16.2	----	----	----	----
QC PANELS	----	----	----	----	----	----	33.7	15.0	----	----	----	----
QC PANELS	----	----	----	----	----	----	31.9	15.7	----	----	----	----
QC PANELS	----	----	----	----	----	----	36.6	16.3	----	----	----	----
QC PANELS	----	----	----	----	----	----	38.7	15.2	----	----	----	----
6A-76	129.4	51.1	.240	----	----	----	----	----	----	----	----	----
6A-76	103.7	53.7	.295	----	----	----	----	----	----	----	----	----
6A-76	113.0	51.4	.270	----	----	----	----	----	----	----	----	----
5C-48	155.1	50.5	----	----	----	----	42.6	17.0	----	----	----	----
5C-48	145.3	52.9	----	----	----	----	48.1	17.1	----	----	----	----
5C-48	156.1	50.2	----	----	----	----	----	----	----	----	----	----
5B-63	----	----	----	----	----	----	38.5	16.2	.320	----	----	----
5B-63	----	----	----	----	----	----	38.0	14.3	.370	----	----	----
5B-63	----	----	----	----	----	----	40.8	16.3	.350	----	----	----
5B-63	----	----	----	----	----	----	38.7	17.2	.370	----	----	----
5B-63	----	----	----	----	----	----	40.8	14.8	.275	----	----	----
5B-63	----	----	----	----	----	----	36.4	15.4	.300	----	----	----
PANEL M-4	113.1	51.5	.270	----	----	----	----	----	----	----	----	----
PANEL M-4	105.4	45.2	.210	----	----	----	----	----	----	----	----	----
PANEL M-4	112.6	51.1	----	----	----	----	----	----	----	----	----	----
2D-51	131.0	45.0	.280	----	----	----	----	----	----	----	----	----
2D-51	127.8	45.0	.250	----	----	----	----	----	----	----	----	----
2D-51	96.8	43.8	.310	----	----	----	----	----	----	----	----	----
4C-66	----	----	----	106.5	45.0	----	----	----	----	36.3	15.0	----
4C-66	----	----	----	104.4	46.5	----	----	----	----	35.6	14.9	----
4C-66	----	----	----	105.0	48.0	----	----	----	----	34.1	14.7	----
4C-66	----	----	----	87.5	49.0	----	----	----	----	38.8	16.0	----
4C-66	----	----	----	95.8	46.5	----	----	----	----	34.4	13.8	----
4C-66	----	----	----	97.2	46.7	----	----	----	----	34.2	13.7	----

Table 5-2. Strength and modulus of GY-70/X-30. (Cont'd)

07/31/78 STRENGTH AND MODULUS OF GY-70/X-30 PAGE 4

LOT NO.	UNIDIRECTIONAL						ISOTROPIC					
	FTU	ET	UT	FCU	EC	UC	FTU	ET	UT	FCU	EC	UC
4C-66	----	----	----	102.3	----	----	----	----	----	33.5	13.5	----
4C-66	----	----	----	97.9	----	----	----	----	----	34.5	----	----
4C-66	----	----	----	101.6	----	----	----	----	----	35.1	14.6	----
4C-66	----	----	----	104.0	----	----	----	----	----	34.3	14.0	----
4C-66	----	----	----	96.1	----	----	----	----	----	33.2	14.8	----
4C-66	----	----	----	87.6	----	----	----	----	----	34.3	14.0	----
4C-79	----	----	----	----	42.0	----	----	----	----	31.0	12.0	----
4C-79	----	----	----	90.9	44.0	----	----	----	----	39.0	14.0	----
4C-79	----	----	----	109.9	41.5	----	----	----	----	30.9	12.5	----
4C-79	----	----	----	104.8	43.5	----	----	----	----	38.4	13.0	----
4C-79	----	----	----	108.0	42.0	----	----	----	----	37.8	13.6	----
4C-79	----	----	----	108.4	42.0	----	----	----	----	34.7	13.7	----
4D-18	----	----	----	----	----	----	41.4	15.6	----	34.8	14.0	----
4D-18	----	----	----	----	----	----	41.5	16.2	----	----	----	----
4D-18	----	----	----	----	----	----	42.6	15.1	----	----	----	----
4D-40	----	----	----	----	----	----	46.9	17.0	----	32.3	14.0	----
4D-40	----	----	----	----	----	----	47.6	15.6	----	----	----	----
4D-40	----	----	----	----	----	----	44.8	16.0	----	----	----	----
4D-18/19/40	----	----	----	----	----	----	33.5	16.4	----	35.0	13.0	----
4D-18/19/40	----	----	----	----	----	----	40.7	17.0	----	----	----	----
4D-18/19/40	----	----	----	----	----	----	40.0	16.0	----	----	----	----
4D-36/37	----	----	----	----	----	----	47.3	16.7	----	36.6	13.6	----
4D-36/37	----	----	----	----	----	----	42.2	15.3	----	----	----	----
4D-36/37	----	----	----	----	----	----	47.5	15.7	----	----	----	----
4D-38/39	----	----	----	----	----	----	46.7	15.4	----	32.5	13.4	----
4D-38/39	----	----	----	----	----	----	43.4	15.5	----	----	----	----
4D-38/39	----	----	----	----	----	----	47.6	16.8	----	----	----	----
4D-36 TO -39	----	----	----	----	----	----	47.1	17.7	----	40.7	13.7	----
4D-36 TO -39	----	----	----	----	----	----	37.7	14.3	----	----	----	----
4D-36 TO -39	----	----	----	----	----	----	45.7	16.2	----	----	----	----
4D-41/42/43	----	----	----	----	----	----	43.8	15.0	----	33.5	14.9	----

Table 5-2. Strength and modulus of GY-70/X-30. (Cont'd)

07/31/78 STRENGTH AND MODULUS OF GY-70/X-30 PAGE 5

LOT NO.	UNIDIRECTIONAL						ISOTROPIC					
	FTU	ET	UT	FCU	EC	UC	FTU	ET	UT	FCU	EC	UC
40-41/42/43	----	----	----	----	----	----	40.7	16.2	----	----	----	----
40-41/42/43	----	----	----	----	----	----	46.8	16.2	----	----	----	----
40-44/45	----	----	----	----	----	----	42.7	16.1	----	36.4	14.8	----
40-44/45	----	----	----	----	----	----	38.9	17.4	----	----	----	----
40-44/45	----	----	----	----	----	----	45.1	16.6	----	----	----	----
40-41 TO 45	----	----	----	----	----	----	41.0	16.6	----	36.2	15.9	----
40-41 TO 45	----	----	----	----	----	----	44.2	16.6	----	----	----	----
40-41 TO 45	----	----	----	----	----	----	47.4	17.1	----	----	----	----
4C-94	----	----	----	----	----	----	22.8	14.4	----	----	----	----
4C-94	----	----	----	----	----	----	29.1	15.6	----	----	----	----
4C-94	----	----	----	----	----	----	29.9	15.2	----	----	----	----
5D-9140-91	----	----	----	----	----	----	38.8	16.4	----	----	----	----
5D-9140-91	----	----	----	----	----	----	39.7	14.8	----	----	----	----
5D-9140-91	----	----	----	----	----	----	39.7	15.4	----	----	----	----
4E-17	----	----	----	----	----	----	36.2	15.1	----	----	----	----
4E-17	----	----	----	----	----	----	43.0	15.3	----	----	----	----
4E-17	----	----	----	----	----	----	42.2	15.9	----	----	----	----
4C-94/4D-91/4E-17	----	----	----	----	----	----	30.5	15.9	----	----	----	----
4C-94/4D-91/4E-17	----	----	----	----	----	----	29.2	----	----	----	----	----
4C-94/4D-91/4E-17	----	----	----	----	----	----	27.8	----	----	----	----	----
TAG END SPEC.	----	----	----	----	----	----	41.9	----	----	----	----	----
TAG END SPEC.	----	----	----	----	----	----	41.3	----	----	----	----	----
TAG END SPEC.	----	----	----	----	----	----	37.2	----	----	----	----	----
TAG END SPEC.	----	----	----	----	----	----	41.4	16.4	----	----	----	----
TAG END SPEC.	----	----	----	----	----	----	42.1	16.9	----	----	----	----
TAG END SPEC.	----	----	----	----	----	----	39.1	16.0	----	----	----	----
5A-73	----	----	----	----	----	----	36.0	14.1	----	----	----	----
5A-73	----	----	----	----	----	----	31.2	14.8	----	----	----	----
5A-73	----	----	----	----	----	----	36.2	17.5	----	----	----	----
5A-73	----	----	----	----	----	----	38.5	15.7	----	----	----	----
5A-73	----	----	----	----	----	----	36.0	15.5	----	----	----	----

Table 5-2. Strength and modulus of GY-70/X-30. (Concl'd)

07/31/78 STRENGTH AND MODULUS OF GY-70/X-30 PAGE 6

-------LOT NO.------	----------UNIDIRECTIONAL----------						----------ISOTROPIC----------					
	FTU	ET	UT	FCU	EC	UC	FTU	ET	UT	FCU	EC	UC
5A-73	----	----	----	----	----	----	33.6	13.3	----	----	----	----
5A-16	----	----	----	----	----	----	35.1	----	----	----	----	----
5A-16	----	----	----	----	----	----	28.8	----	----	----	----	----
5A-16	----	----	----	----	----	----	34.2	----	----	----	----	----
4E-46	----	----	----	----	----	----	29.9	----	----	----	----	----
4E-46	----	----	----	----	----	----	37.7	----	----	----	----	----
4E-46	----	----	----	----	----	----	29.9	----	----	----	----	----
TAG ENDS HEAD	----	----	----	----	----	----	26.0	17.5	----	----	----	----
TAG ENDS HEAD	----	----	----	----	----	----	30.5	17.0	----	----	----	----
TAG ENDS HEAD	----	----	----	----	----	----	24.8	16.5	----	----	----	----
TAG ENDS HEAD	----	----	----	----	----	----	42.1	16.8	----	----	----	----
TAG ENDS HEAD	----	----	----	----	----	----	40.1	17.2	----	----	----	----
TAG ENDS HEAD	----	----	----	----	----	----	41.6	17.0	----	----	----	----
4D-17/18	107.2	49.8	----	----	----	----	36.1	15.3	----	----	----	----
4D-17/18	111.9	50.6	----	----	----	----	38.8	16.0	----	----	----	----
4D-17/18	109.1	50.2	----	----	----	----	----	----	----	----	----	----
4D-88	136.4	48.0	----	----	----	----	38.8	14.8	----	----	----	----
4D-88	130.2	48.8	----	----	----	----	40.7	15.1	----	----	----	----
4D-88	143.1	48.5	----	----	----	----	----	----	----	----	----	----
C8-416	71.2	47.7	----	----	----	----	----	----	----	----	----	----
C8-416	87.7	47.3	----	----	----	----	----	----	----	----	----	----
C8-416	81.5	44.9	----	----	----	----	----	----	----	----	----	----
C8-362	91.6	44.8	----	----	----	----	----	----	----	----	----	----
C8-362	87.3	45.2	----	----	----	----	----	----	----	----	----	----
C8-362	87.9	45.4	----	----	----	----	----	----	----	----	----	----
C8-427	83.4	44.0	----	----	----	----	----	----	----	----	----	----
C8-427	79.8	41.2	----	----	----	----	----	----	----	----	----	----
C8-427	77.9	43.5	----	----	----	----	----	----	----	----	----	----

Table 5-3. Statistical properties of strength and modulus of GY-70/X-30.

-------LOT NO.-------	----------UNIDIRECTIONAL----------						----------ISOTROPIC----------					
	FTU	ET	UT	FCU	EC	UC	FTU	ET	UT	FCU	EC	UC
AVERAGE VALUE, $\bar{x}$	110.3	47.3	.291	97.2	44.0	.293	37.8	15.7	.320	35.2	14.0	.287
STANDARD DEVIATION, s	22.53	2.39	.036	12.76	2.56	.052	5.85	.98	.023	2.34	.89	.029
NUMBER OF SAMPLES, n	74	74	16	27	17	4	128	117	24	30	29	3
TOLERANCE FACTOR, k	1.572	1.572		1.811	2.002		1.496	1.506		1.777	1.788	
B ALLOWABLE [1]	74.9	43.5		74.1	38.9		29.0	14.2		31.0	12.4	
B ALLOWABLE [2]	77.9	43.8		N/A	N/A		28.4	14.1		30.9	12.0	

1. NORMAL DISTRIBUTION, $\bar{x} - ks$
2. DISTRIBUTION UNKNOWN, RANK METHOD

Table 5-4. Ranks, r, of observations, n, for an unknown distribution having the probability and confidence of A and B values.

B Basis		B Basis		B Basis	
n	r	n	r	n	r
29	1	321	24	1269	110
46	2	345	26	1376	120
61	3	368	28	1483	130
76	4	391	30	1590	140
89	5	413	32	1696	150
103	6	436	34	1803	160
116	7	459	36	1909	170
129	8	481	38	2015	180
142	9	504	40	2120	190
154	10	560	45	2230	200
167	11	615	50	2330	210
179	12	671	55	2430	220
191	13	726	60	2530	230
203	14	781	65	2630	240
215	15	836	70	2730	250
227	16	890	75	2830	260
239	17	945	80	2930	270
251	18	999	85	3000	277
263	19	1053	90		
275	20	1107	95		
298	22	1161	100		

agreement is reasonably good between the two approaches. The latter approach is probably more valid because the sample sizes have not been large enough to get good approximation to a normal distribution.

5.3 SHORT TERM DIMENSIONAL STABILITY (UNDER TRANSIENT THERMAL CONDITIONS)

As part of on-going programs for the shuttle Remote Maneuvering System (RMS) arms and the Thematic Mapper, Convair has recommended optical/laser interferometric measurement techniques for evaluating dimensional stability of components. These same techniques, with only minor adaptation for size and, perhaps, remote operation, are applicable to this study.

5.3.1 RMS ARMS — Thermal expansion tests are performed to determine the coefficient of thermal expansion along the length of the test specimens. Both Arm Boom Test Composite assemblies that completed thermal vacuum tests are subjected to Thermal Expansion tests as follows:

1. The Lower Arm Boom Test composite is fitted with 3/8 inch aluminum adapter flanges with provisions for mounting mirrors to each flange. Both optical mirrors are spring loaded to the respective aluminum end flanges. The front mirror has two 3/8 inch diameter holes through which the laser beams pass to reach the rear mirror. The distance between the mirrors is monitored by the built-in sensor of the Hewlett-Packard Model 5526A Laser Dilatometer system capable of measuring changes in the test specimen length within $\pm$ 1 x 10^6 inches.

2. The test specimen assembly is installed in a test setup similar to that shown in Figure 5-7 with the test specimen suspended inside the environmental chamber by means of a vibration isolating suspension system.

3. The pressure of the vacuum chamber is reduced to 1 x 10^{-6} torr and maintained during thermal expansion testing.

4. The test specimen is cycled through a sequence of:

   — 1 hour @ 75F
   — Increase to +232F; stabilize 1 hour
   — Decrease to -240F; stabilize 1 hour
   — Return to 75F; stabilize 1 hour.

   At each temperature level measure and record the length of the test specimen.

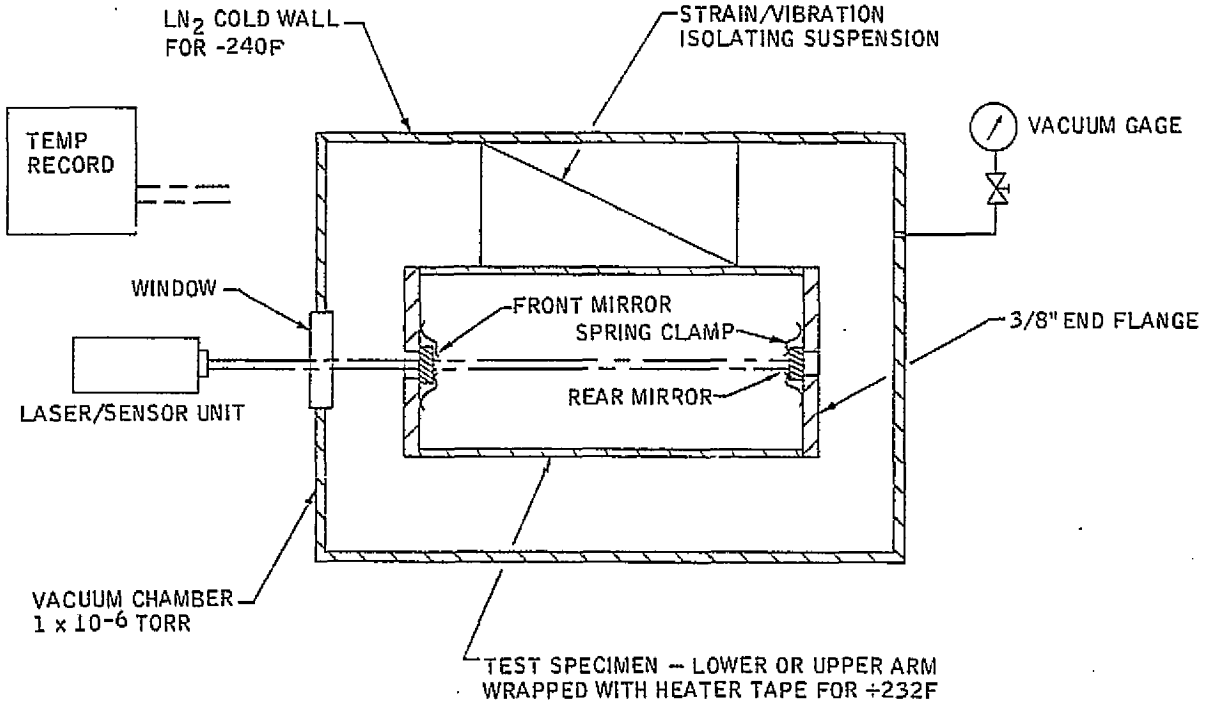

Figure 5-7. RMS; typical thermal expansion test setup.

5. Calculate and record the change in the length of the test specimen from its length at +75F and the specimen length at the three temperatures of +232F, -100F, and -240F. This ΔL data is used to calculate the coefficient of thermal expansion. The following formula is used to determine the coefficient of thermal expansion:

$$\text{Coefficient of Thermal Expansion} = \frac{\Delta L}{L \Delta T} \text{ in./in./F}$$

L = Length of test specimen at 75F (inches).

ΔL = Change in length of specimen at +232F, -100F and -240F.

ΔT = Change in test specimen temperature from 75F.

5.3.2 THEMATIC MAPPER — A similar procedure, with a test setup adapted to the different configuration of the mapper, is used, as follows:

1. Install two mirrors on the test specimen at points A and B, as shown in Figures 5-8 and 5-9, by use of spring clamps. The mirrors are used to measure longitudinal thermal expansion of the test specimen. The distance between the mirrors is monitored by the built-in sensor of a Hewlett-Packard Model 5526A laser dilatometer.

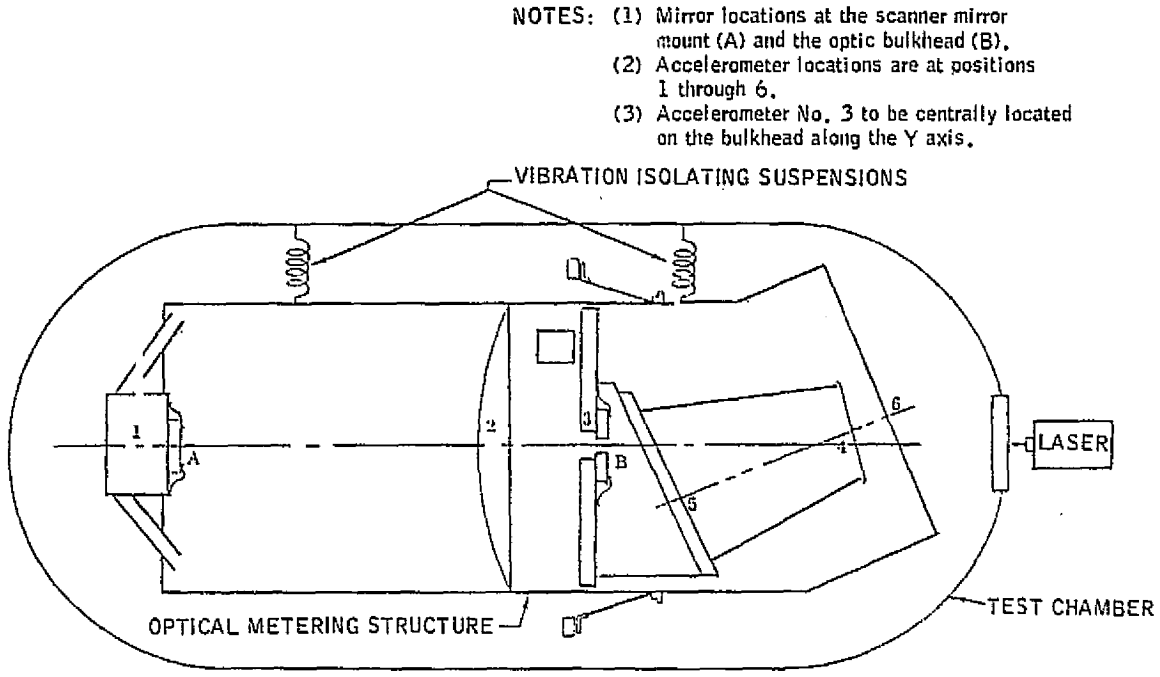

Figure 5-8. Thematic Mapper; thermal expansion test setup.

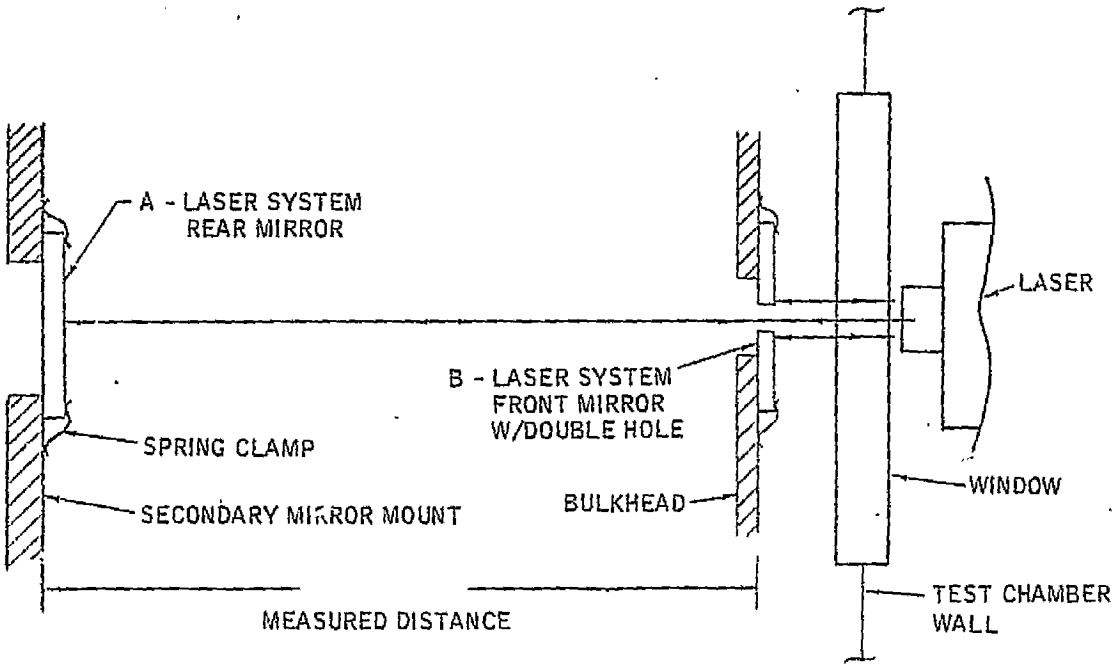

Figure 5-9. Laser measurement of thermal expansion.

2. The test specimen is installed in a test setup similar to that shown in Figure 5-8. The test specimen is suspended in a temperature-vacuum chamber by means of vibration isolating suspensions. An aluminum ring is attached to the forward end of the support cone to simulate the thermal expansion constraint of the mounting ring.

3. Cycle the test specimen temperature ten times in the following sequence. This temperature cycling is to stabilize the thermal expansion of the test specimen:

   a. Room ambient
   b. +165F
   c. +5F
   d. Room ambient

4. Decrease the chamber pressure to 10 microtorr and maintain it during thermal expansion testing.

5. Perform the daily schedule of temperature cycling and measurement as specified in Figure 5-10. After each temperature change, allow the test specimen to temperature stabilize for two hours before each measurement. Measure the test specimen with the dilatometer as shown in Figure 5-8. Record the results.

6. After the completion of the temperature test of step (4), allow the chamber pressure and temperature to return to room ambient conditions.

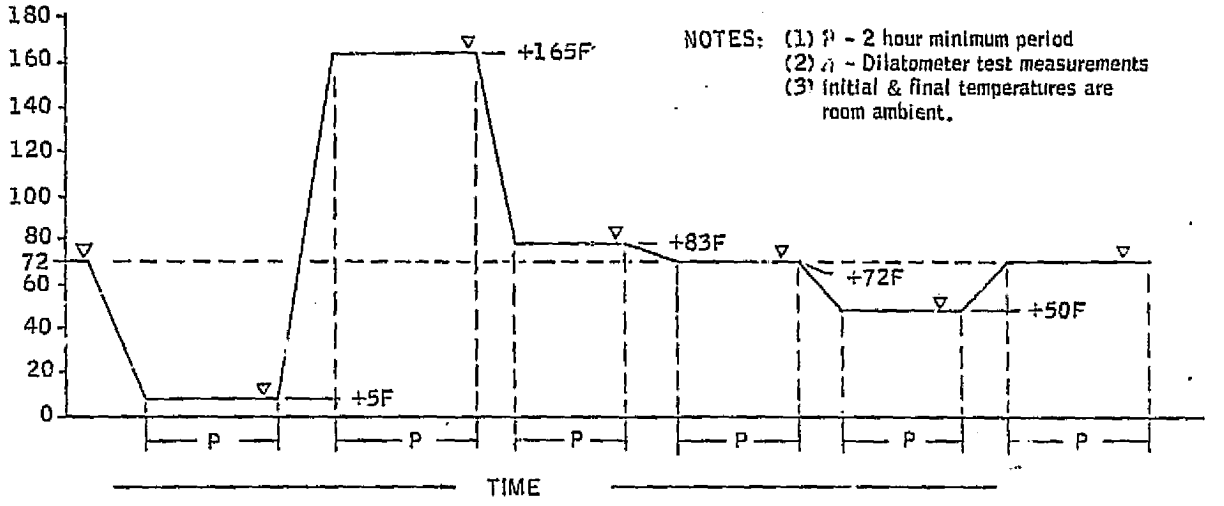

Figure 5-10. Temperature cycling schedule.

5.4 LONG TERM DIMENSIONAL STABILITY (UNDER STEADY LOAD CONDITIONS)

Experiments are currently underway at General Dynamics/Convair to measure the long term dimensional stability of graphite/epoxy laminates under tension loading. Long specimens (60 inches) of 8-ply GY-70/X-30 pseudoisotropic laminates are being loaded at about 25 and 50% of ultimate tension load. Measurements of the relative motion of two points, 36 inches apart, in a uniform stress field is obtained using dial gages. A spacer of ultra low expansion (ULE) glass provides a means of obtaining these measurements. These tests are being conducted under controlled conditions of temperature and humidity, so that these factors have no influence of the behavior of the test specimens. Unloaded control specimens serve to identify any environmentally-induced behavior that might occur.

The purpose of these tests is to determine long term creep characteristics over a period of several months, limits of such creep behavior, permanent set, if any, and time required to stabilize after removal of load.

Additional creep tests that are indicated include compression, bending and shear load conditions to evaluate the influence of stress state on the long term dimensional stability of graphite/epoxy material.

Report No. CASD-NAS-78-011

FINAL REPORT

ACHIEVABLE FLATNESS IN A LARGE MICROWAVE POWER ANTENNA STUDY

(DRL Item No. 2)

6. TASK 4 – TECHNOLOGY PLAN

Prepared under
Contract No. NAS9-15423
for
National Aeronautics and Space Administration
LYNDON B. JOHNSON SPACE CENTER
Houston, Texas 77058

Prepared by
GENERAL DYNAMICS CONVAIR DIVISION
P.O. Box 80847
San Diego, California 92138

6

TASK 4

TECHNOLOGY PLAN

This study has indicated several areas in which technology developments are required in order to support a 1987 new start commitment for the SPS. A 3- to 4-year program is indicated (see Figure 6-1). As a follow-on to these developments, or, at least after some basics have been established, a further set of areas relating to on-orbit operations can be projected. Typically, these include (Figure 6-1):

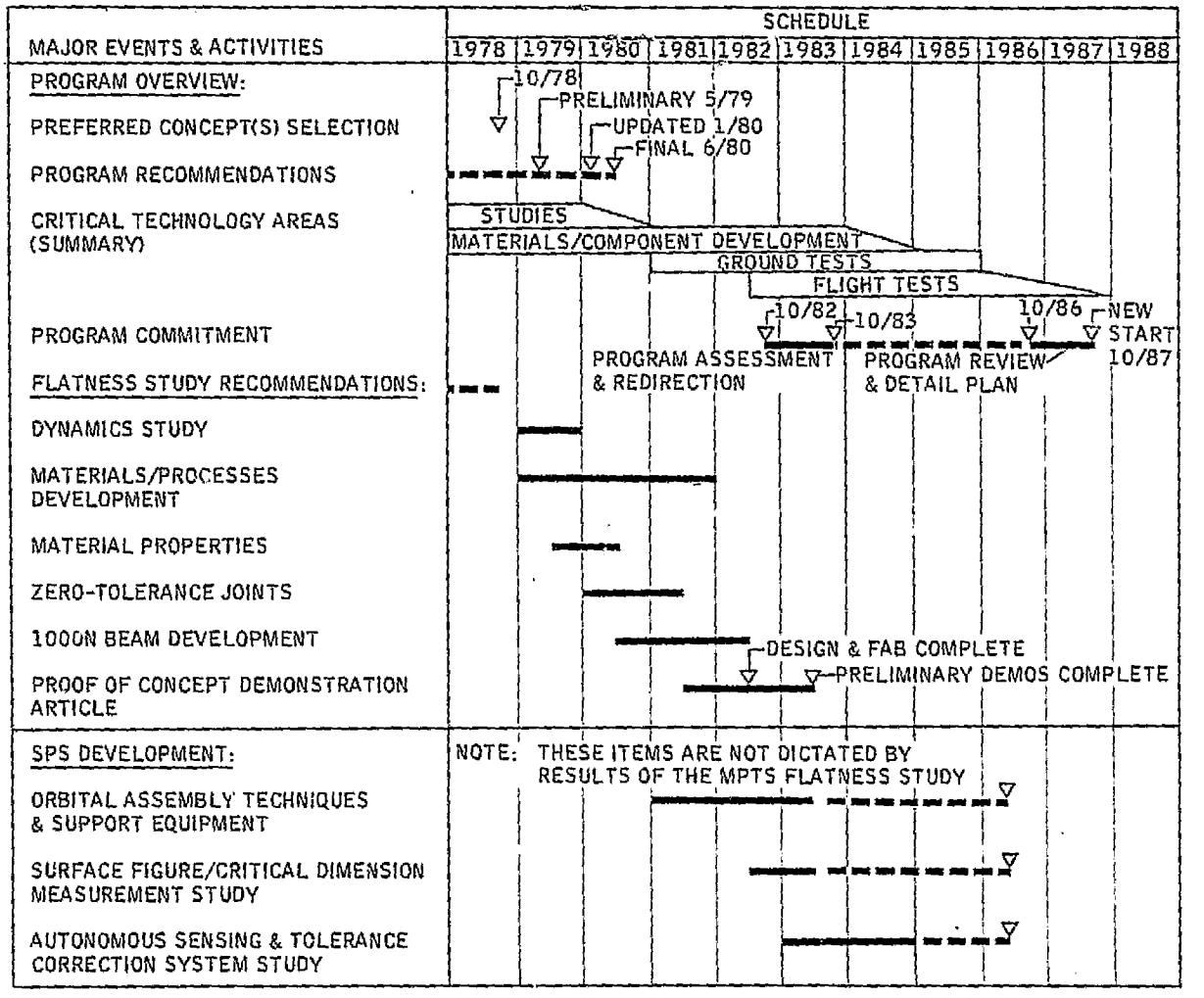

Figure 6-1. Overall technology development schedule.

- Orbital assembly techniques and support equipment.
- Surface figure/critical dimension measurement.
- Autonomous sensing and tolerance correction.

These are not considered to be within the scope of the present discussion.

6.1 TECHNOLOGY AREAS

6.1.1 DYNAMICS/CONTROL TECHNIQUES — The influence of gravity gradient on antenna control has been found to be unexpectedly severe because of the great distance from the antenna to the SPS center of mass. As a result, the control problem changed from that of a conventional space attitude control system for a freely floating body to one where gravity gradient accommodation was the principal concern. Since the techniques other than direct support carry severe mass penalties, direct support should be evaluated in more detail. Whereas this study concentrated on the antenna itself, an early study is required which considers the mounting of the antenna and the tower as a single problem. Lower dynamics large actuators, cable systems, and combined geometry need to be considered in greater detail to assure that direct support of gravity gradient forces and direct drive for pointing are indeed low-risk solutions.

6.1.2 MATERIALS — Material development to achieve a near zero coefficient of thermal expansion with a very high modulus of elasticity (E). While Convair has achieved CTE in the 0.04×10^{-6} cm/cm/C range with isotropic GY-70/X-30, the E is only 11.2×10^9 N/m^2. Techniques to achieve the same low CTE with an E of 21 to 28 x 10^9 N/m^2 should be investigated.

6.1.3 STRUCTURES TECHNOLOGY — Although the MPTS antenna structure could be manufactured using current technology, additional technology developments should be directed to improved efficiencies in both the construction and operation of the system.

The MPTS antenna structure will require additional studies and further advancements in space manufacturing of large beams, thermal coatings that maintain their stability over 30 years, assembly and service techniques for the overall structure, and improved ground analytical techniques and methods for simulating static and dynamic properties of large structures in space.

Specific items requiring attention are:

- Zero-Tolerance Joints
- 1000 Newton (Low Force) Beams

6.1.4 PROOF OF CONCEPT (POC) DEMONSTRATION MODEL — A POC model is required to combine technology developments and SPS/MPTS structural concepts. It then serves as a test bed and demonstration article for dynamic response,

environmental testing, materials, fabrication process proofing, and member installation and handling.

6.2 DETAILED TECHNOLOGY PLANS

6.2.1 DYNAMICS/CONTROL TECHNIQUES — This study has found that gravity gradient acting on the MPTS antenna creates an environmental torque which requires massive techniques for countering unless direct mechanical support is used for the antenna. By designing the antenna and support structure such that the center of mass of the combination is on the principal long axis of the solar collector, the gravity gradient torque is taken up in the mechanical support and not transmitted to the solar collector. The first bending frequencies of the antenna and the solar collector are sufficiently separated frequencywise that no unusual bending/control system interaction problems should exist if the antenna support structure is considered to be rigid. However, the support will not be infinitely rigid and it is unknown what constitutes sufficient rigidity or whether any unreasonable penalties arise from achieving that rigidity. The support stiffness requirements cannot be based on linear considerations entirely since the excitation of bending modes by breakout friction is a potentially major problem in achieving sufficiently accurate pointing.

Three candidate direct support/direct drive configurations are defined as follows (see Figure 6-2):

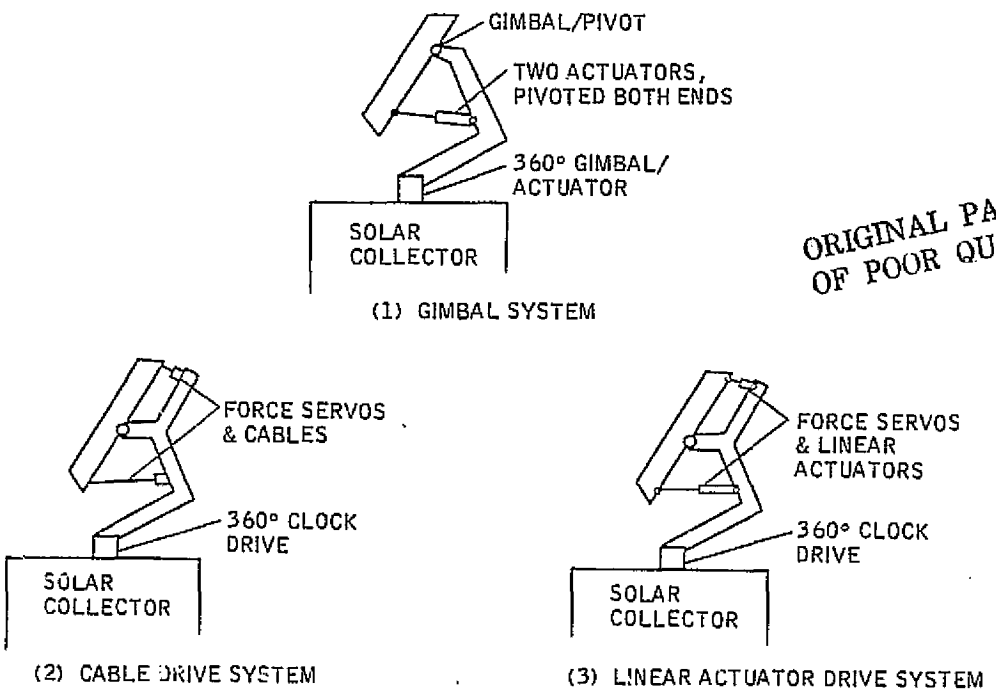

Figure 6-2. Candidate systems for direct support/ direct drive.

1. Gimbaled — a conventional gimbal arrangement with the antenna supported along the x-axis with limited freedom of rotation. The half-ring gimbal is supported at the base by an unlimited Y rotation actuator. All actuators are of the rotary type with flex leads transmitting the power across the elevation actuator bearings and brushes or slip rings for the azimuth drive.

2. Cable Drive — The antenna is pivoted on a single central ball with three cables for positioning the antenna in two limited degrees of freedom. The support is a single dog-legged tower with a clock drive at the base. Power is transmitted across the ball via flex leads. Brushes or slip rings are used in the clock drive.

3. Linear Actuator — the antenna is pivoted on a single central ball with two linear actuators used for positioning the antenna in two limited degrees of freedom. The dog leg tower and the clock drive at the base are the same as for the cable drive concept.

The basic objective of the effort is to determine the feasibility of constructing MPTS antenna support structures which could provide a suitable base for direct mechanical pointing of the antenna to 1.4 arc minutes with non-idealized actuators.

Task 1: Parametric Stiffness Analysis

Perform design studies to identify design techniques and weight penalties for achieving varying degrees of stiffness in each of the three candidate antenna support configurations. The studies will include two or more techniques of tying the antenna support into the solar collector and the corresponding stiffness and weight characteristics.

Task 2: Parametric Pointing Analysis

Perform dynamic studies to identify the relative merits of the three candidate pointing techniques as to their pointing potential. Factors to be considered include estimated friction differences, actuator to antenna stiffness, actuator attachment local stiffness and solar collector stiffness.

Task 3: Pointing Simulation

Based on the results of Tasks 1 and 2, select and refine a point design for more detailed evaluation. Perform computer simulation to establish pointing accuracy potential at various levels of pivot and actuator frictions. Simulation will include as a minimum support structural dynamics, estimated solar collector structural dynamics, actuator dynamics, and all identifiable friction sources.

Task 4: Requirements Definition

Establish required minimum allowable friction levels to achieve 1.4 arc minutes pointing of the antenna as a rigid body. Conduct studies and surveys to establish

the feasibility of achieving the required friction levels. Establish antenna support structure stiffness requirements and the attendant weight penalties, if any.

The feasibility, or lack thereof, of accurately pointing the MPTS antenna by simple direct drive techniques should be established during Calendar 1979 (Figure 6-3). Should additional resolution of the issue be required, there will then be time prior to 1987 to consider alternate approaches such as active damping of the support structure.

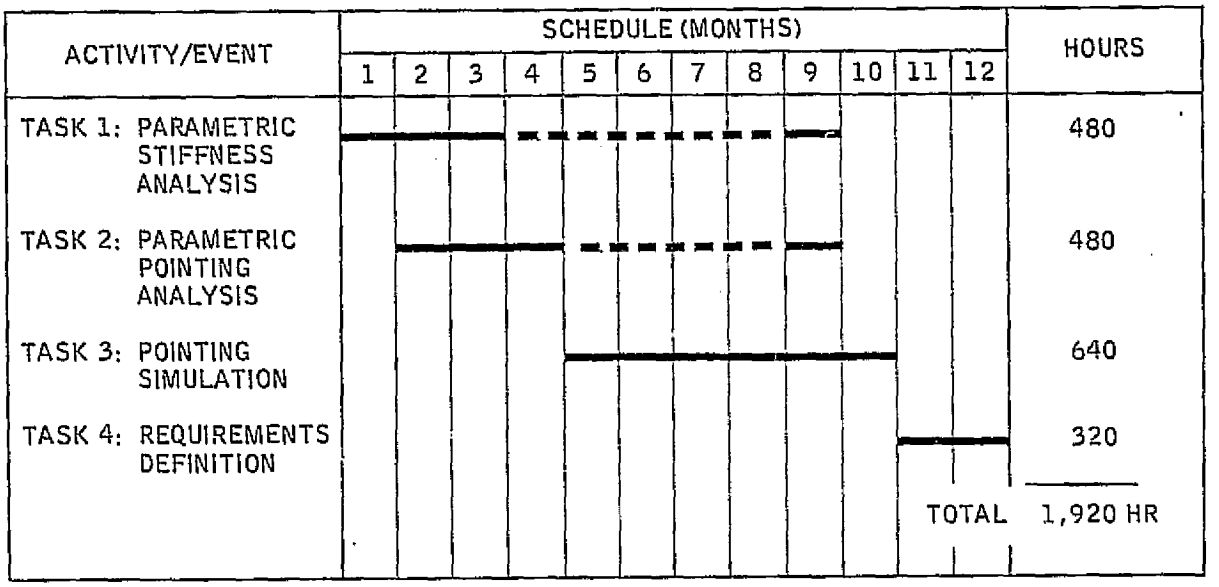

Figure 6-3. Dynamics study summary schedule.

6.2.2 MATERIAL AND PROCESS SELECTION — Large quantities of high-temperature graphite composites are required for the fabrication of MPTS structures. We know the operational environment, and required service life. The building of large structural elements will occur probably in LEO, and handling loads are predictable for the transport and assembly into the completed structure at GEO. Pitch fiber/polyimide composites, either thermoplastic or thermosetting, are prime candidates for this application, however, there are many options within these general categories as well as replacement matrices which could be developed to better meet the MPTS requirements.

The selection of the process is inseparable from the formulation of the fiber/matrix composite. For a semi- to fully-automated process for manufacture of structural elements in space, process control should ensure that material properties of the completed parts are within tolerance. Combination of fiber and matrix, if accomplished in orbit, should not result in unusable by-products. The cure and/or forming operations should not generate waste, either as a by-product or in unsatisfactory structural elements. Automated process control is required to monitor the production, detect out-of-tolerance conditions and take corrective action without astronaut participation.

Figure 6-4 summarizes the approach to materials/process/fabrication analysis.

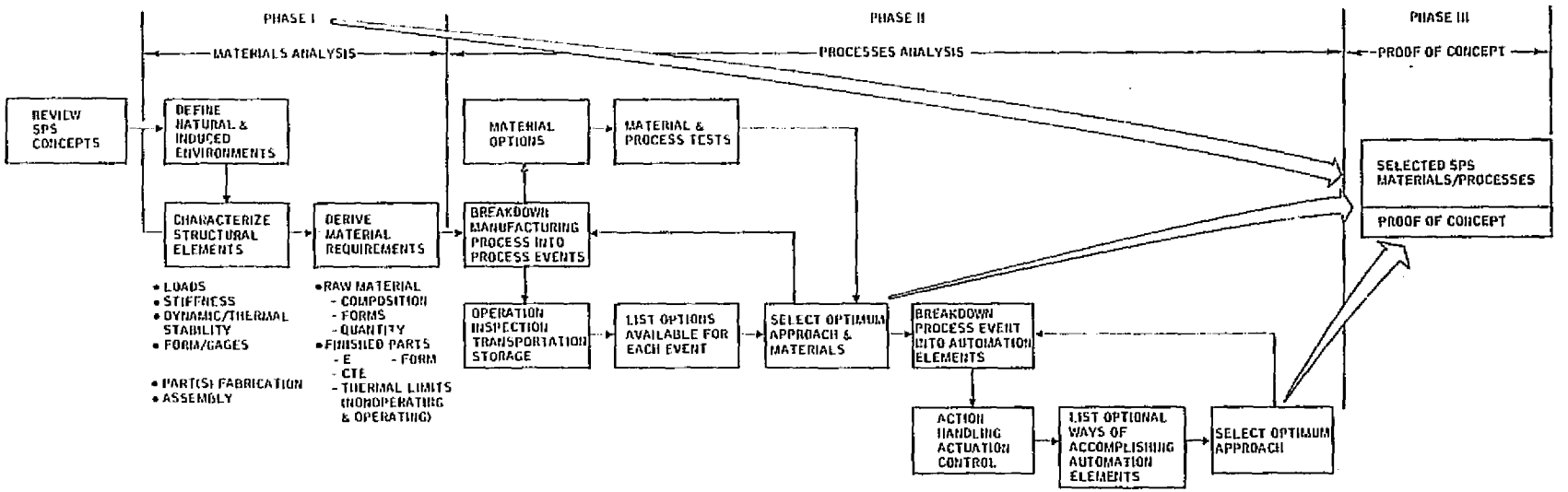

Figure 6-4. Material and process analysis study flow.

The objectives of the first phase of this program are to determine the options of processes and materials that can be applied to the MPTS structure fabrication, the general performance of each option in terms of cost, energy requirement, availability, material properties, etc., and then selection of the best candidate systems for a detailed comparison study.

The second phase is a laboratory program of development and testing of processes and material options with the objective of selecting the prime candidate system. This program will include planning of proof-of-concept shuttle experiments.

The final phase will include pilot-plant production of materials, and simulated and in-space fabrication of major components of the MPTS structure.

Program schedule is shown in Figure 6-5.

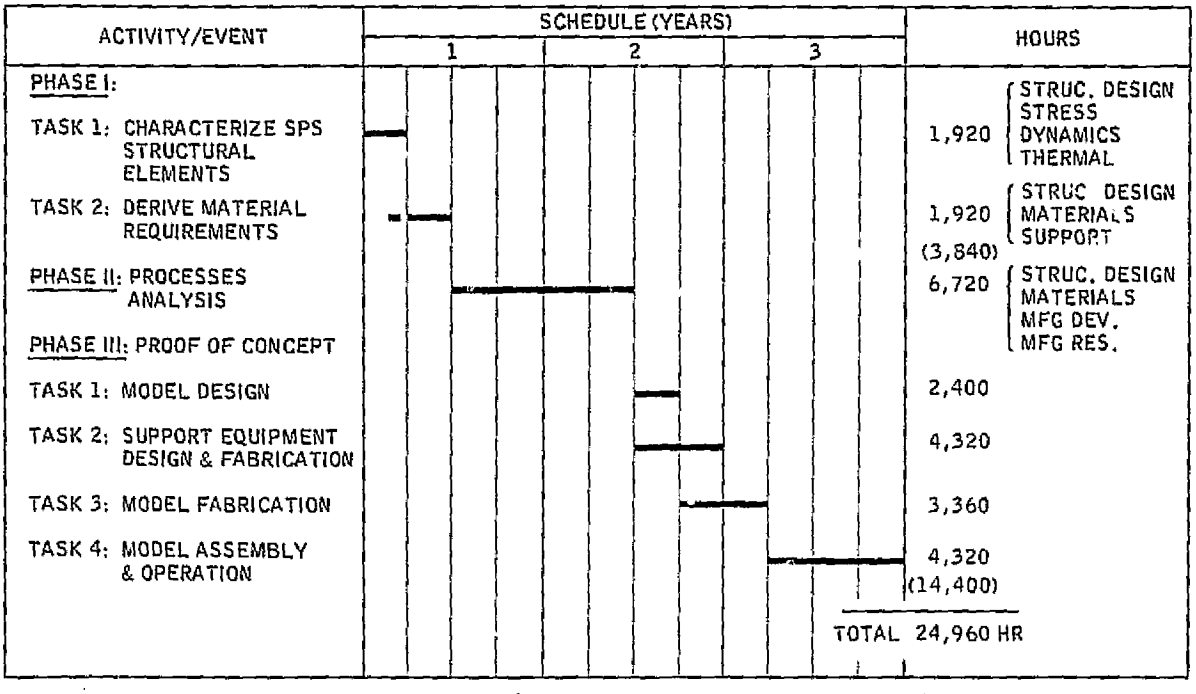

Figure 6-5. Materials/processes development schedule.

6.2.3 MATERIAL PROPERTIES — Pitch fiber is a good candidate for SPS structure fabrication because of its potential savings in cost and energy over conventional polyacrylonitrile (PAN) fiber. Currently it lacks availability and quality has not been consistent. It should be available in larger quantities and with more uniform properties within a year.

Polyimide matrix systems are usually recommended for applications requiring elevated operating temperatures. Polyimides may alleviate the high temperature problems, but introduce others. Graphite/polyimide composites require special care in fabrication to get repeatable composite properties. They are susceptible to voids and delamination, and uncertainty in their thermal stability.

Very little material property data is available for this fiber/resin system. The objective of this task is to characterize a representative pitch fiber/polyimide composite for potential application to the MPTS support structures.

A test flow diagram is shown in Figure 6-6. Prepreg material is assumed to be available from one or more suppliers. Prepreg material is evaluated for percent resin solids, resin flow, percent volatiles and hardness time/temperature. An infrared scan is made of one extracted matrix sample from each batch to ensure that no chemical change has been made in the resin system. Visual inspection of quality, such as fiber strightness, gaps, lamina thickness and irregularities is made.

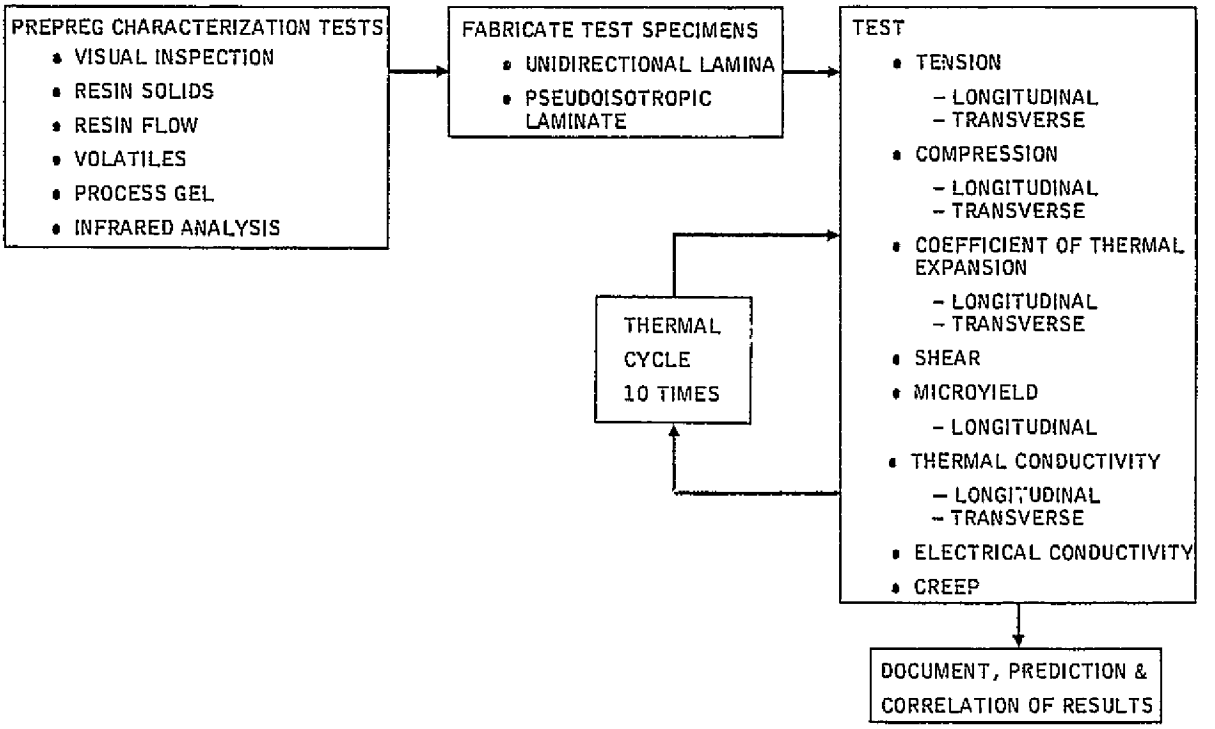

Figure 6-6. Test flow diagram.

For the destructive F_{TU} and F_{CU} tests, a minimum of 6 specimens is recommended for each test condition and for each batch of material tested. Measurement of CTE would benefit from a larger sample, e.g. 12 specimens for each test condition. A group of samples could be used to determine the CTE over the operational range, 100 - 200C (212 - 392F), then the average CTE to shadow (liquid nitrogen) temperature. After a number of cycles from full-sun operational temperature to dormant shadow temperature, the CTE measurements would be repeated to detect nonreversible structural changes.

Other samples would be thermally cycled over the orbital extremes, then F_{TU} and F_{CU} determined. Since E_T and E_C are important to flatness, these could be

determined before and after thermal cycling. CTE specimens could be used to determine strength and modulus after CTE tests are completed.

Thermal capacity and conductivity are included because of their importance in simulation of the temperatures of the MPTS structure.

A period of 2 to 3 months would be required at the beginning of the program for material specifications, ordering and procurement. Formalization of the test plan would also be accomplished in this time.

All of the tests considered here except creep could be accomplished in a short time, perhaps six months. CTE measurement would be the pacing item since limited numbers of laser dilatometers are available. Convair has developed a 4-specimen dilatometer that will expedite measurement of larger sample sizes.

An important consideration, and one not easily satisfied, is the measurement of long term microstrain. The composite is required to maintain dimensional stability under load, and at elevated temperatures. Some test specimens should be prepared and placed under stress in an arrangement where microstrain can be monitored.

A summary schedule is presented in Figure 6-7.

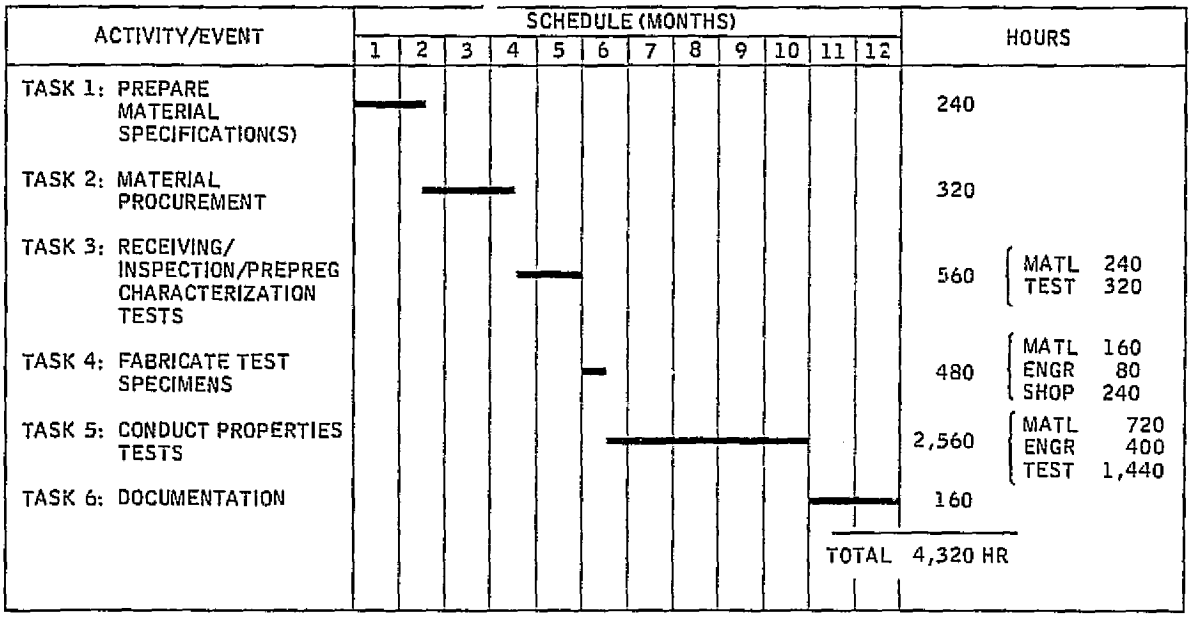

Figure 6-7. Material properties summary schedule.

6.2.4 ZERO TOLERANCE JOINTS — Multi-jointed tetrahedral truss structures are subject to potential surface distortions caused by manufacturing tolerance buildups at individual truss member intersections. Structures with free-play or slack in their joints do not respond to thermal, static or dynamic loads in a linear manner. In some cases joint free-play may completely alter load paths and hence structural response.

Early in the assembly of a tetrahedral truss, a stable configuration is reached. After this point, if additional struts are not of perfect length they must be stretch or shortened to fit the available space and thus induce fabrication loads and deforı tions into the structure. Such loads can be quite high, greatly exceeding the strer ability of an EVA crew member, and will necessitate the use of a jack-like tool to apply the required installation force.

To alleviate these design deficiencies some form of zero tolerance joint will be required to attach adjacent struts at their common intersection points.

Figure 6-8 summarizes the study activities and task flow required to arrive at a rational joint design which will address these problem areas.

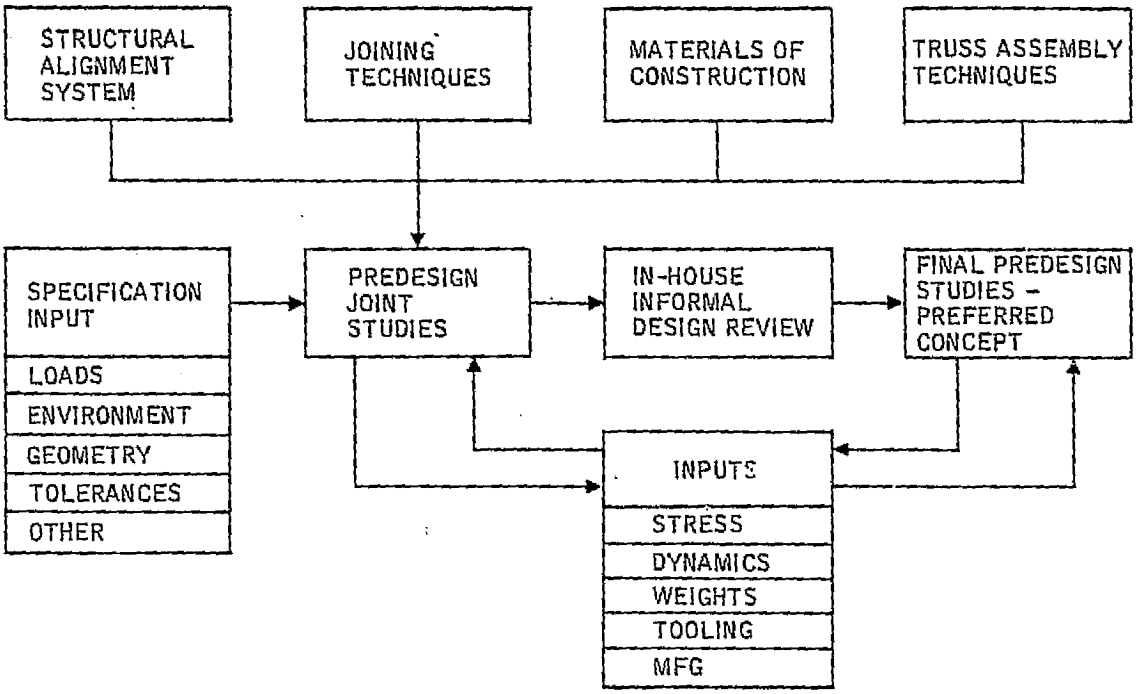

Figure 6-8. Joint study flow diagram.

Task 1: Requirements Review

Review member configurations, materials and alignment systems to define generic types of joints and requirements for each type. Assembly techniques and associated tools and support equipment will also be considered in this review.

Task 2: Joining Techniques Evaluation

Review typical joining techniques:

— Solid State Welding
  - Cold Welding
  - Diffusion Welding
  - Ultrasonic Welding

— Electronic Beam Welding

— Resistance Welding

— Laser Welding

— Brazing

— Adhesive Bonding

— Mechanical Fasteners

Evaluate techniques for parameters and characteristics such as outgassing, residual stress/distortion, loose materials (fasteners, debris), weld quality, joint quality, power requirements, operations (EVA, tools, support equipment).

Task 3: Material Selection Trade

Review member materials and evaluate joint materials for compatibility, workability and net contribution to dimensional stability.

Task 4: Joint Predesign Study

Develop joint predesigns for various member configurations, loads and tolerance requirements.

Task 5: Joint Trade Study

Evaluate the joints designed in Task 4 for feasibility, complexity, support requirements, and on-orbit fabrication/assembly. Select one or two candidates for further development.

Task 6: Technical Support

Provide stress, weights, dynamics, thermal, tooling and manufacturing support for Tasks 1 through 5.

Task 7: Design Full-Scale Joints

Conduct detail designs of candidate joints and attaching structural members; level to be of sufficient detail for production operations.

Task 8: Fabricate Development Parts and Subassemblies

Fabricate a sufficient quantity of detail parts and subassemblies to conduct production process proofing tests (approximately 6 of each type of joint).

Task 9: Develop Assembly Processes

Assemble joints with a range of variation in processes (e.g., practical limits of weld schedules) and conduct simple structural tests to select optimum process. Define tooling required for assembly operations.

Note: Such tools would then become the subject of a separate development program.

Task 10: Fabricate Parts and Subassemblies

Fabricate a set of parts and subassemblies for each type of joint to be qualified. Design refinements, derived in other tasks, would be incorporated.

Task 11: Assemble Qualification Test Model(s)

Using the processes developed in Task 9, assemble joints of each type for use in the qualification test program.

Task 12: Conduct Joint Qualification Tests

Perform typical qualification tests of the selected joints under load, as follows:

- Tension
- Compression
- Bending/Buckling
- Thermal Cycling
- Thermal Expansion

A summary schedule for joint development is shown in Figure 6-9.

6.2.2 1000 NEWTON BEAMS —The possibility exists to design a structure that will not experience the large thermal loads when the antenna is in the all-cold condition. Assuming this design is selected, the structural beams could be reduced from their present size to possibly as little as a beam designed to carry only 1000 Newtons. The "1000 Newton Beam" follow-on program would investigate candidate materials, sizing of beam, manufacturing and handling of beam in space, and joining methods including the possibility of having a spring-loaded detent joint that allows load relief at say 950 Newtons to prevent catastrophic failure of the beam.

The task flow for this study is shown in Figure 6-10.

A potential joint design may incorporate a spring-loaded detent that would be designed to move if the load on the beam exceeds a set amount. One such joint design is shown in Figure 6-11. This consists of a strut end with slopes in two directions to a center detent groove. Balls are inserted and held in place by a spring-loaded collar. If an excessive load is applied the balls roll out of the detent and expand the outer spring. When the load is reduced the spring forces the balls back into the detent.

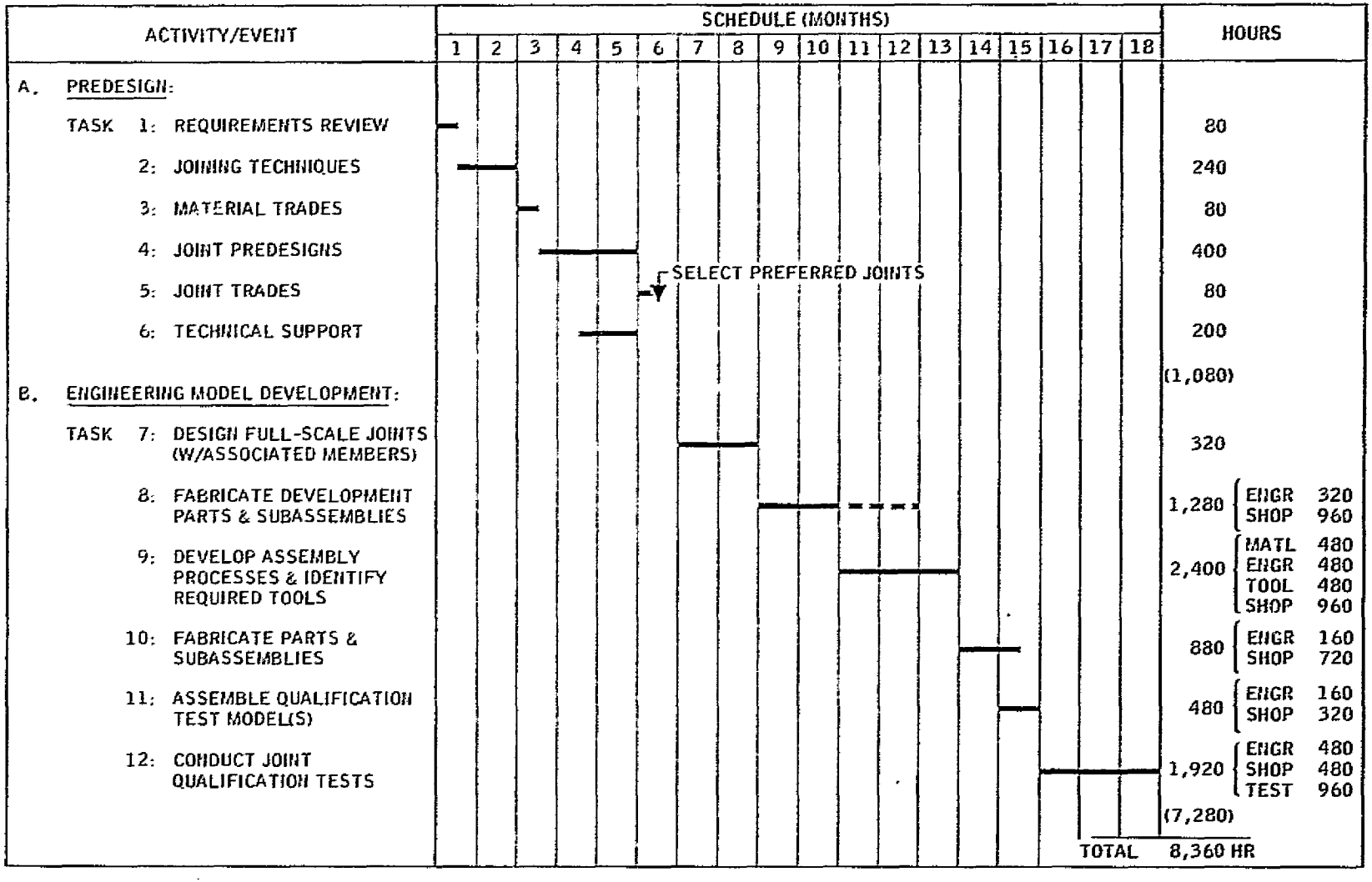

Figure 6-9. Zero-tolerance joint development schedule.

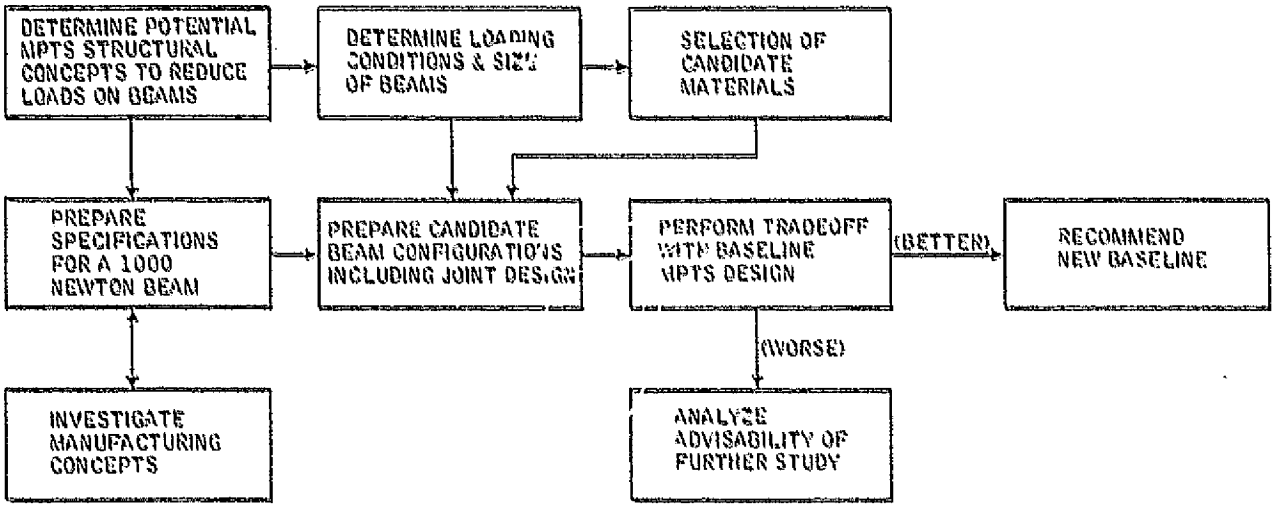

Figure 6-10. 1000N beam study task flow.

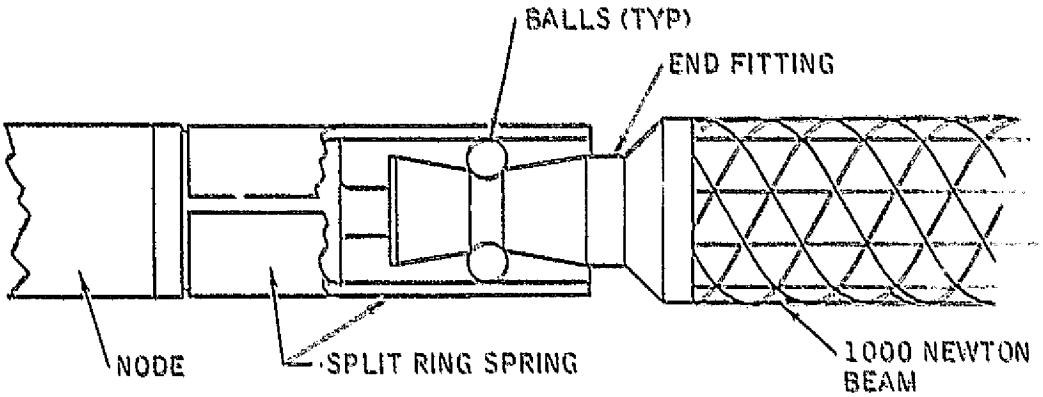

Figure 6-11. Overload safety device for 1000 Newton beams.

Another form of protection for the 1000N truss member uses tension only elements to preload the tetratress when under operating thermal loads. Figure 6-12 shows a plan view of the 660 struts of the primary structure. In this example, a CTE of -0.038 €/C (-0.021 €/F) was used for all struts except the 30 edge struts that form the perimeter. These were set at CTE of -1.08 €/C (-0.60 €/F). A uniform temperature rise of 111C (200F) was used to apply a thermal load. The edge members simulated unidirectional cables. Members in tension are illustrated as continuous lines, and the members in compression by interrupted lines.

In the study, an optimum pattern of preload cable members could be determined so that at operating temperatures the structure would be a fully redundant tetratruss. At temperatures below minimum operating conditions, the tension cables would slacken. The remaining struts would be the minimum number to maintain configuration. The structure would deform, but be essentially stress-free in the cold state.

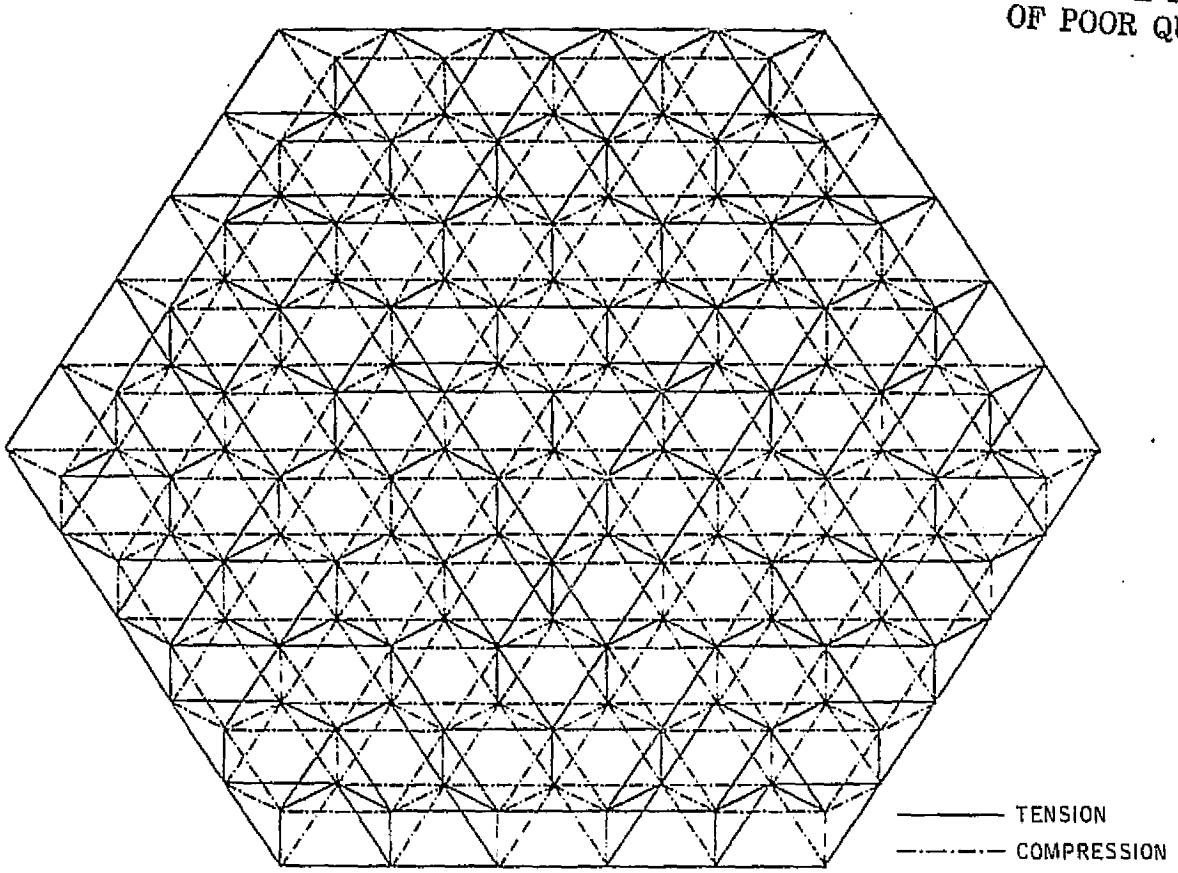

Figure 6-12. Stress reversal distribution under hoop tension loading.

Substitution of cables for redundant struts would facilitate assembly at nonoperational temperatures in a relatively stress-free condition.

6.2.6 PROOF OF CONCEPT DEMONSTRATION MODEL — A Proof Of Concept (POC) model is proposed to demonstrate the MPTS antenna elements. As shown in Figure 6-13, a combination of bays from both primary and secondary structures is recommended. This will demonstrate, at a subscale level, typical bays and their constituent structural elements, joints, connections and materials. It will also demonstrate installation and interface controls between primary and secondary structural elements.

A summary plan for development of the model is shown in Figure 6-14. The corresponding preliminary schedule is presented in Figure 6-15.

Task 1: POC Model Design

Prepare drawings for:

- constant length primary structure surface struts and diagonal members for 3-bay structural assembly.
- constant length secondary structure surface struts and diagonals for two 14-bay structural assemblies.

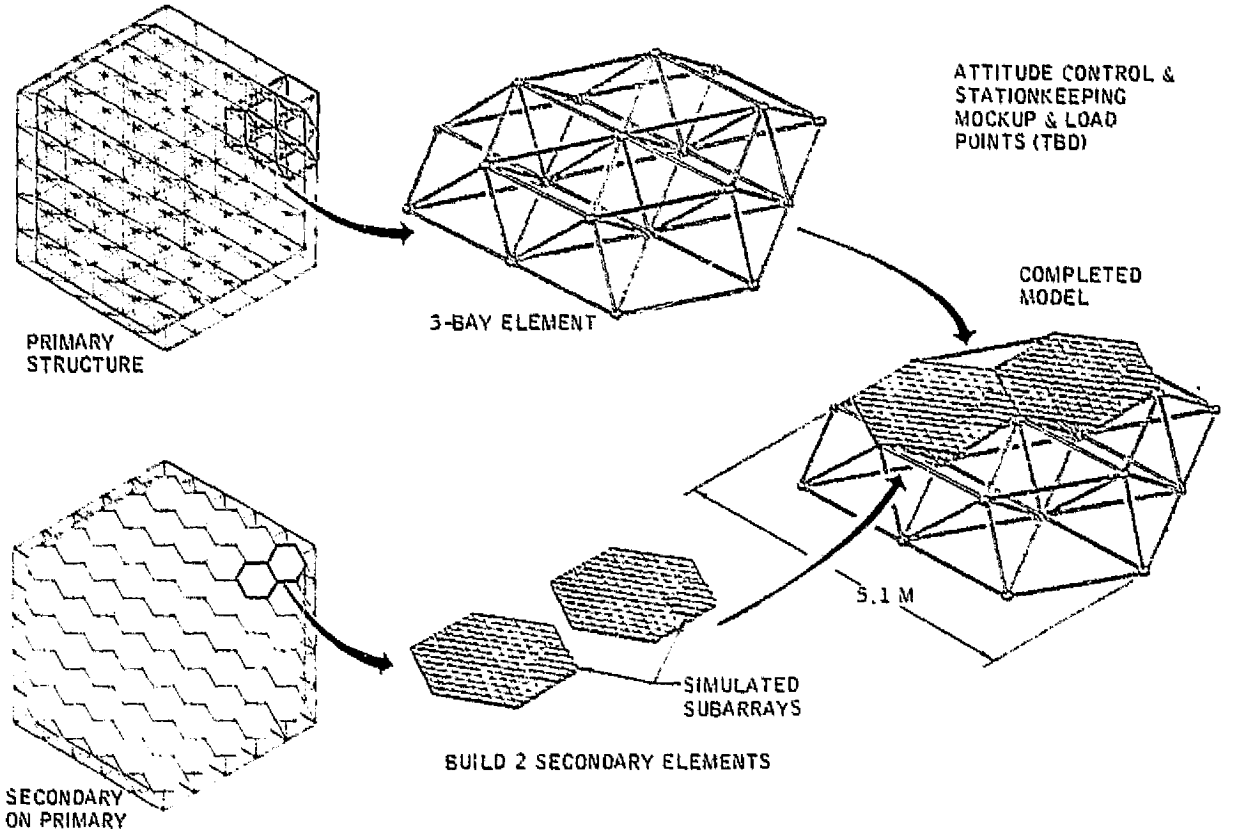

Figure 6-13. Proposed POC demonstration model.

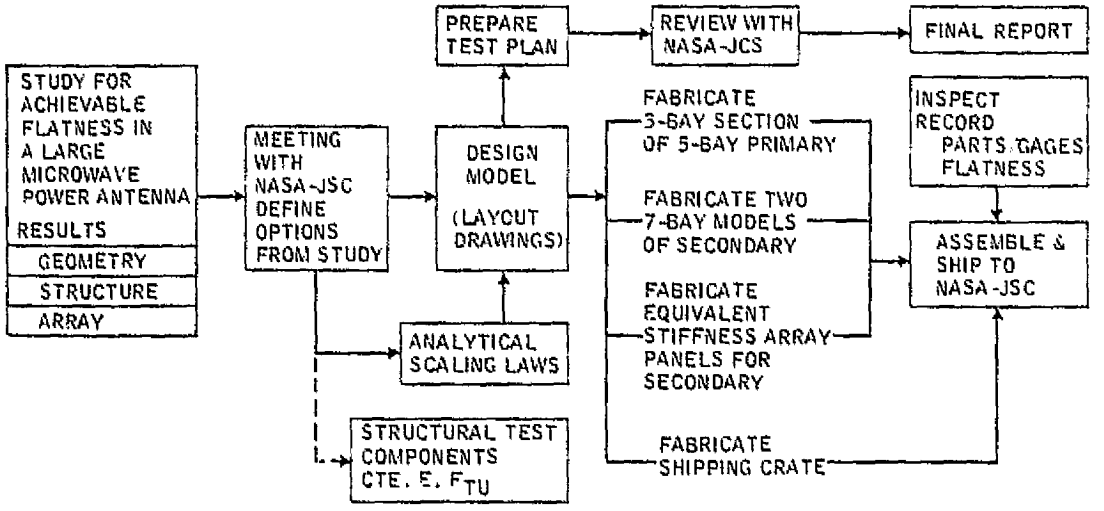

Figure 6-14. POC demonstration model plan.

— 3-bay primary structure spider assemblies, including both front and back of spiders.

— 14-bay secondary structure spider assemblies.

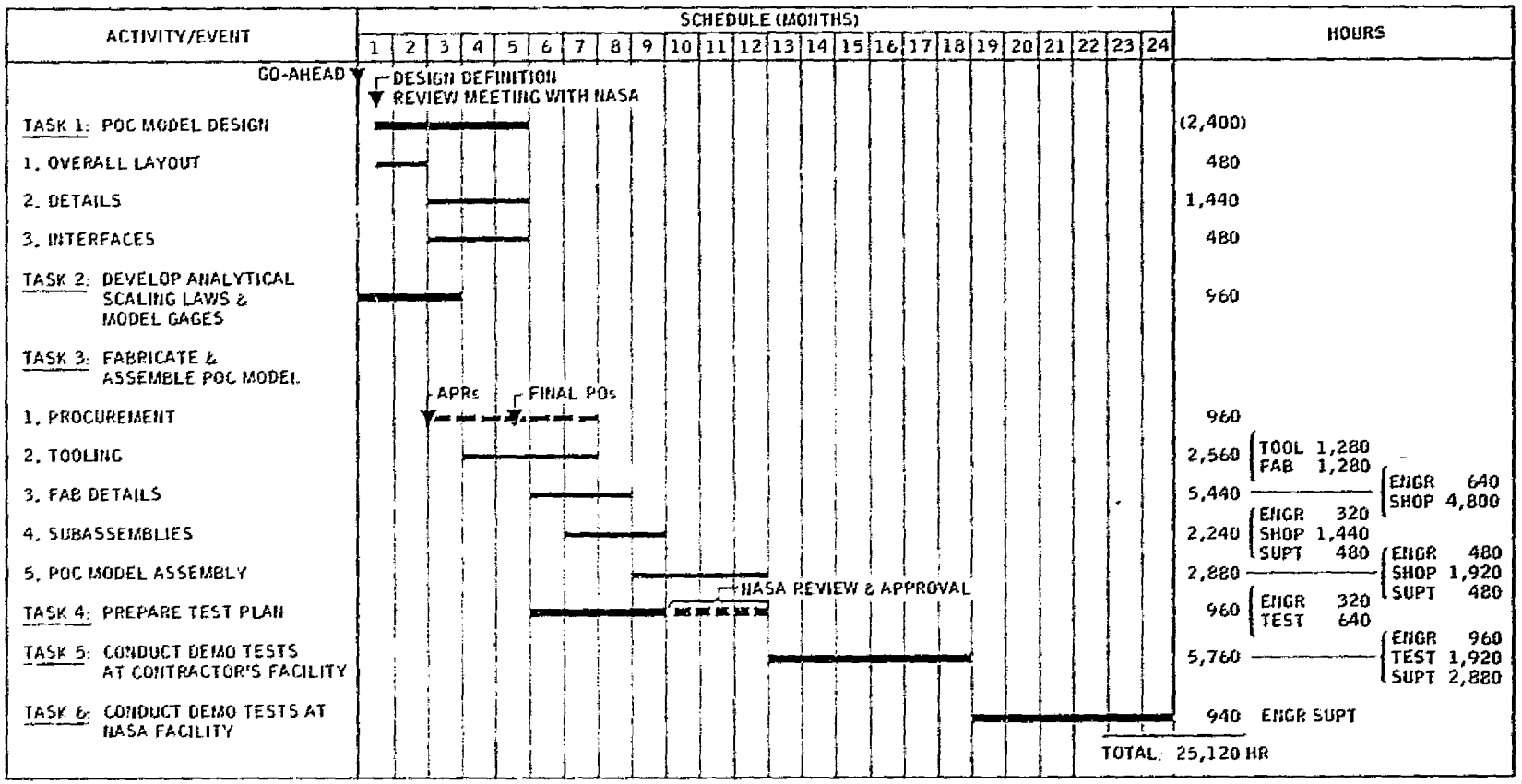

Figure 6-15. POC demonstration model development schedule.

— structural assembly of 3-bay primary structural assembly and 14-bay secondary structural assembly.

— modulus to simulate subarray panels, including installation on secondary structural assembly.

— demonstration model assembly.

Task 2: Model Scaling and Gages

Perform dimensional analysis and scaling of the tetrahedral truss elements for the demonstration model.

Task 3: Fabricate and Assemble POC Model

- PROCUREMENT — Provide procurement assist to engineering in procuring raw material/purchased parts and subcontracted hardware items.

- TOOLING — Provide tool design and tool manufacturing support during model component fabrication and assembly. Prepare tool orders and planning documents.

- MANUFACTURE — Fabricate 3-bay primary structural members (struts and diagonals) from graphite/epoxy material.
  - Utilizing mandrels, lay up graphite/epoxy materials in accordance with engineering design. Vacuum bag laid up part, cure in autoclave, debag and trim.
  - Fabricate simulated subarray panel modules in accordance with engineering design. Perform subassembly of modules.
  - Fabricate attitude control mockup and load point pads.

- ASSEMBLY — Assemble 3-bay primary and 14-bay secondary structural assemblies utilizing shop aid assembly fixture and procure parts (spiders, pins, etc.) and raw material (tubes). Assemble MPTS demonstration model, including installation of simulated subarray panels. Attach attitude control and load pads.

- QUALITY CONTROL — Provide receiving-inspection services to engineering during material/purchase parts procurement cycle. Provide inspection support during fabrication of tools and MPTS model detail parts fabrication and assembly.

Task 4: Test Plan

Prepare a detail MPTS demonstration model test plan which will include test environments, conditions, etc. to prove the concepts which the model is intended to demonstrate. These include simulation of structural and attitude control systems. The

plan covers testing to be performed at the contractor's facility, as well as those to be conducted by NASA in conjunction with other SPS/MPTS demonstrations.

Task 5: Contractor Test Program

Typical tests include attitude control responses, natural frequency modal survey, static and dynamic loads, deployment, assembly, and utility of support tools and equipment, and environmental tests.

Task 6: NASA Test Program

Contractor will provide support, as required, for NASA test program.

Report No. CASD-NAS-78-011

FINAL REPORT

ACHIEVABLE FLATNESS IN A LARGE MICROWAVE POWER ANTENNA STUDY

(DRL Item No. 2)

APPENDIX A
MPTS ANTENNA STRUCTURAL SPECIFICATION

Prepared under
Contract No. NAS9-15423
for
National Aeronautics and Space Administration
LYNDON B. JOHNSON SPACE CENTER
Houston, Texas 77058

Prepared by
GENERAL DYNAMICS CONVAIR DIVISION
P.O. Box 80847
San Diego, California 92138

GENERAL DYNAMICS
Convair Division
CODE IDENT NO.
14170

SPECIFICATION NO.	REV
N/A	
DATE: 31 July 1978	PAGE: 1 OF 19
CONTRACT NO.: NAS9-15423	

MICROWAVE POWER TRANSMISSION SYSTEM
(MPTS)
ANTENNA,
STRUCTURAL SPECIFICATION

PREPARED BY _____
J. J. Smith

APPROVED BY _____

CHECKED BY _____

SPECIFICATION CHANGE NOTICES—INCORPORATED IN SPEC REVISIONS

SCN NO(S)	INCORP BY	CHECK BY	APPROVED BY	DATE	SPEC REV	REVISION PACKAGE NO.	RELEASE

INITIAL PACKAGE NO.	RELEASE	DOC TYPE	DISTR CODE

1.0 SCOPE

This specification defines the performance criteria, environmental, manufacturing, test, handling, and shipping requirements for the microwave power antenna structure.

2.0 APPLICABLE DOCUMENTS

The following documents form a part of this specification to the extent specified herein. In the event of conflict between the documents referenced herein and the contents of this specification, the contents of this specification shall be considered the superseding requirement.

Specifications

MIL-A-83577 75 Jun 15	Assemblies, Mechanical for Space Vehicles, Design and Testing Requirements, General Specification for
FED-STD-209B 73 Apr 24	Clean Room and Work Station Requirements Controlled Environment
MIL-STD-1538 73 Apr 11	Spare Parts and Maintenance Support of Space and Missile Systems Undergoing RDT&E
MIL-STD-810B 78 Jul 31 Chg 4, 70 Sep 21	Environmental Test Methods
JSC-07700 Vol. 14	Space Shuttle Specs — System Payload Accommodation
MIL-STD-889B 76 Jul 07	Dissimilar Metals
S-32-061, GSFC Oct. 69 (Updated)	General Environmental Test for Geosynchronous Spacecraft
S-320-G-1 Oct. 69	General Environmental Test Spec for Spacecraft and Components
X-325-67-70	GSFC Magnetic Field Restraints for Spacecraft Systems and Subsystems
X-325-71-488	Supplements — Subsystems

Other Publications

NASA-SP-R-0022A	Vacuum Stability Requirements of Polymeric Material for Spacecraft Application
MIL-HDBK-5	Metallic Materials and Elements for Aerospace Vehicle Structures

Other Documents

Drawing No.

xx-xxxx	Spec Control Drawings
xx-xxxx	Interface Control Drawings

3.0 REQUIREMENTS

3.1 PHYSICAL REQUIREMENTS

It shall be the mission of the microwave power antenna structure to provide a stable platform for mounting klystron/waveguide/thermal radiator units (subarrays). Slope error of less than 3 arc minutes for each subarray is a primary requirement.

In addition the antenna must be capable of stationkeeping, and have figure and pointing control.

3.1.1 INTERFACES — An interface control drawing (ICD) (Drawing No. xx-xxxx) shall be prepared to describe the antenna assembly, its datum references, and volume available for support structure, mechanical references, and the structural attachment interface requirements for the primary structure to gimbal and secondary structure to subarray attachment. The ICD shall show the physical relationships between the antenna assemblies and the adjacent spacecraft structure and other components.

3.2 DESIGN REQUIREMENTS

3.2.1 DESIGN ATTRIBUTES — Throughout the various stages of design, consideration shall be given to the items listed below.

a. Dimensional stability
b. Manufacturability
c. Overall structural stiffness
d. Mission life
e. Stress margin
f. Serviceability

3.2.2 STRUCTURAL REQUIREMENTS — The primary and secondary structure, subarray supports, and the antenna assembly supporting structure shall be shown by analyses to be capable of withstanding, or shall be protected against degradation in

functional performance or operation, the environments noted in this section. Factors for design purposes shall be introduced commensurate with the objectives of safety, reliability, and producibility.

Selected deliverable structure (hardware) shall be proof-tested, using a load which will be determined from stress analysis.

3.2.2.1 Mass Properties — The total antenna assembly weight, including the primary and secondary structure, interconnecting hardware, and the subarray kinematic links, but not the subarray panels or their loose hardware, shall have a design target of 1.3M kilograms.

3.2.2.2 Center of Gravity — The center of gravity (cg) of the reflector assembly shall be computed (predicted) during the design phase. Selected components shall be weighed and their cg determined prior to assembly to verify the analyses. The location of the cg shall be referenced to the datums defined on ICD No. xx-xxxx.

3.2.2.3 Moments of Inertia (MOI) — The MOI of the reflector assembly shall be computed about 3 orthogonal axes through the cg. The MOI calculations shall be accurate within 5 percent.

3.2.2.4 Interchangeability — All parts, subassemblies, and assemblies having the same part number shall be interchangeable with respect to form, fit, and function.

3.2.3 IDENTIFICATION AND MARKING — Each deliverable unit and each shipping container at the time of delivery shall be permanently identified to the extent listed on ICD No. xx-xxxx.

3.2.4 SURFACE PROFILE — To achieve the primary goal of the antenna structure to maintain a pointing accuracy of within 3 arc minutes for the subarrays, the manufacturing/assembly tolerances, maneuvering accelerations, and thermal distortions all need to be controlled.

A total slope accuracy budget of 2 arc minutes is to be used as a design goal. The allocation of the above mentioned three major error categories are as follows:

		Arc Minute Budget
Manufacturing Tolerance		1.5
Maneuvering Accelerations		1.1
Thermal Distortions		0.7
RSS Total	=	1.99 arc min.

Sufficient information shall be submitted to ascertain that the antenna design meets the above requirements.

3.2.5 ACTIVE MECHANICAL ALIGNMENT PROVISIONS — It is preferred that the structure be constructed so as to meet the less than 3 arc minute error requirement without active controls. Their use as an alternative to the close-tolerance manufacturing of antenna truss elements can be considered in addition to baseline design using only "passive" adjustments to meet the requirements of this specification. (A passive adjustment is one that is required to be done only during the assembly/manufacturing phase.)

3.2.5.1 Subarray Adjustment and Mechanical Reference — The subarray support system shall incorporate provisions for an optimum position passive adjustment (one time only adjustment) of the location of the subarrays, and shall incorporate a method that will define this physical location for reference purposes after adjustments are completed. The adjustment mechanism shall permit removal and reinstallation of a subarray to the original 3 arc minute pointing accuracy.

A system shall be provided for replacing an adjustment mechanism without losing the subarray's adjustment.

3.2.5.2 Surface Tolerance, Worst Case in Orbit — Considering manufacturing deviations and the worst case thermal distortion in orbit, it shall be shown by analysis and component tests that the requirements stated in this section will be met.

3.2.6 ANTENNA GEOMETRY — The baseline geometry is shown in Figures 1 and 2. It is a two-tier structure consisting of one large 10-bay primary and 61 smaller 14-bay secondary tetrahedral truss structures. The primary truss structure is made from equal length truss struts joined at 60 degree surface angles at each node to form a flat surface. A passive alignment system may be used between the primary and secondary structures to compensate for loss of surface flatness due to manufacturing tolerance buildup, etc. A kinematic attachment method is assumed necessary to accommodate thermal expansion differences between the primary and secondary structures.

A modification of the above attachment method may also be used for the subarray support system.

Reference ICD No. xx-xxxx for complete details of the antenna structure.

3.2.7 ANTENNA MANUFACTURING/ASSEMBLY TOLERANCES — Manufacturing and assembly tolerances are the largest contributor to the rms slope error of the subarrays.

The allowable budget amounts are shown in Table 1. These values assume a passive configuration, i.e., no active adjustment control.

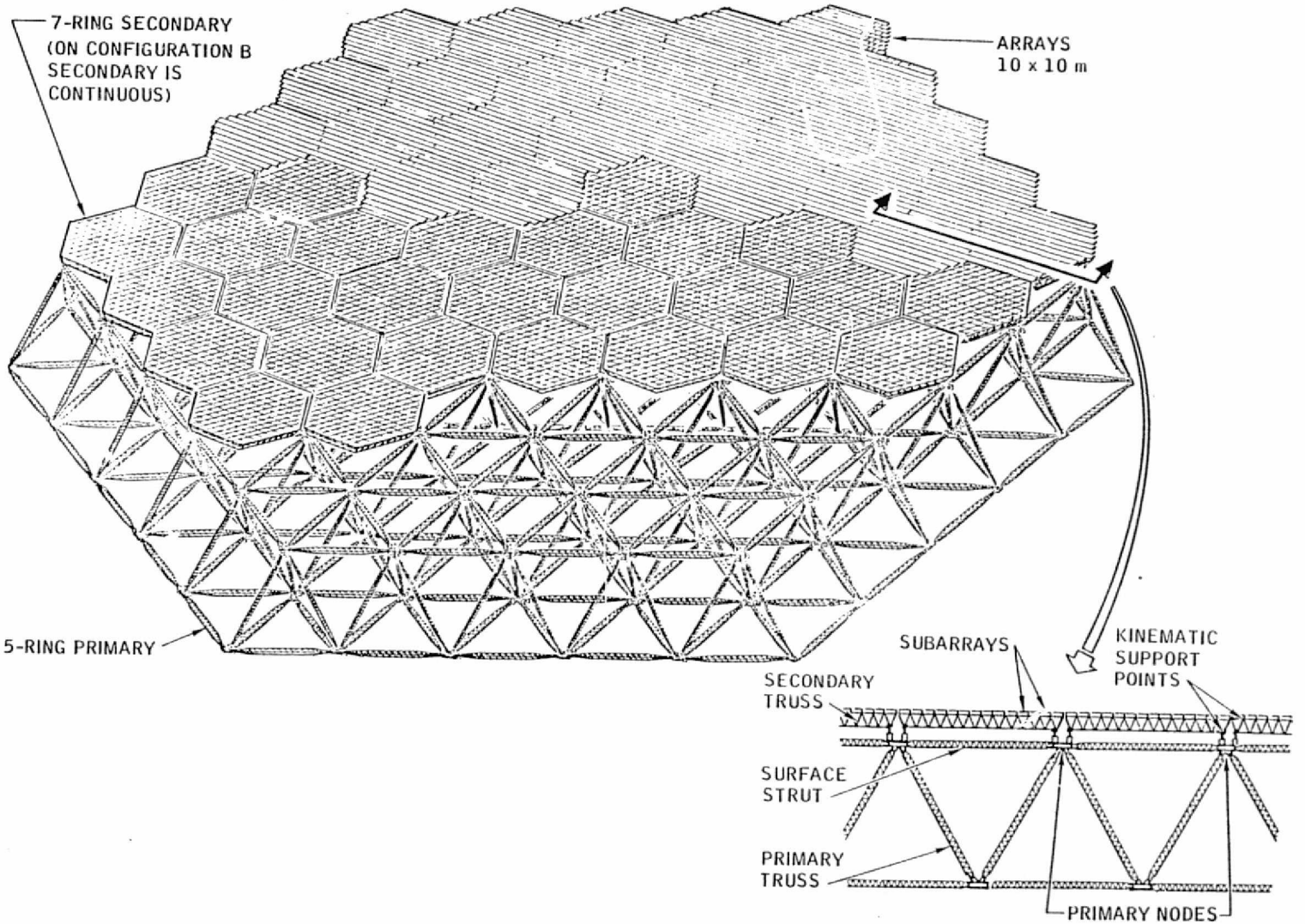

Figure 1. Basic configuration.

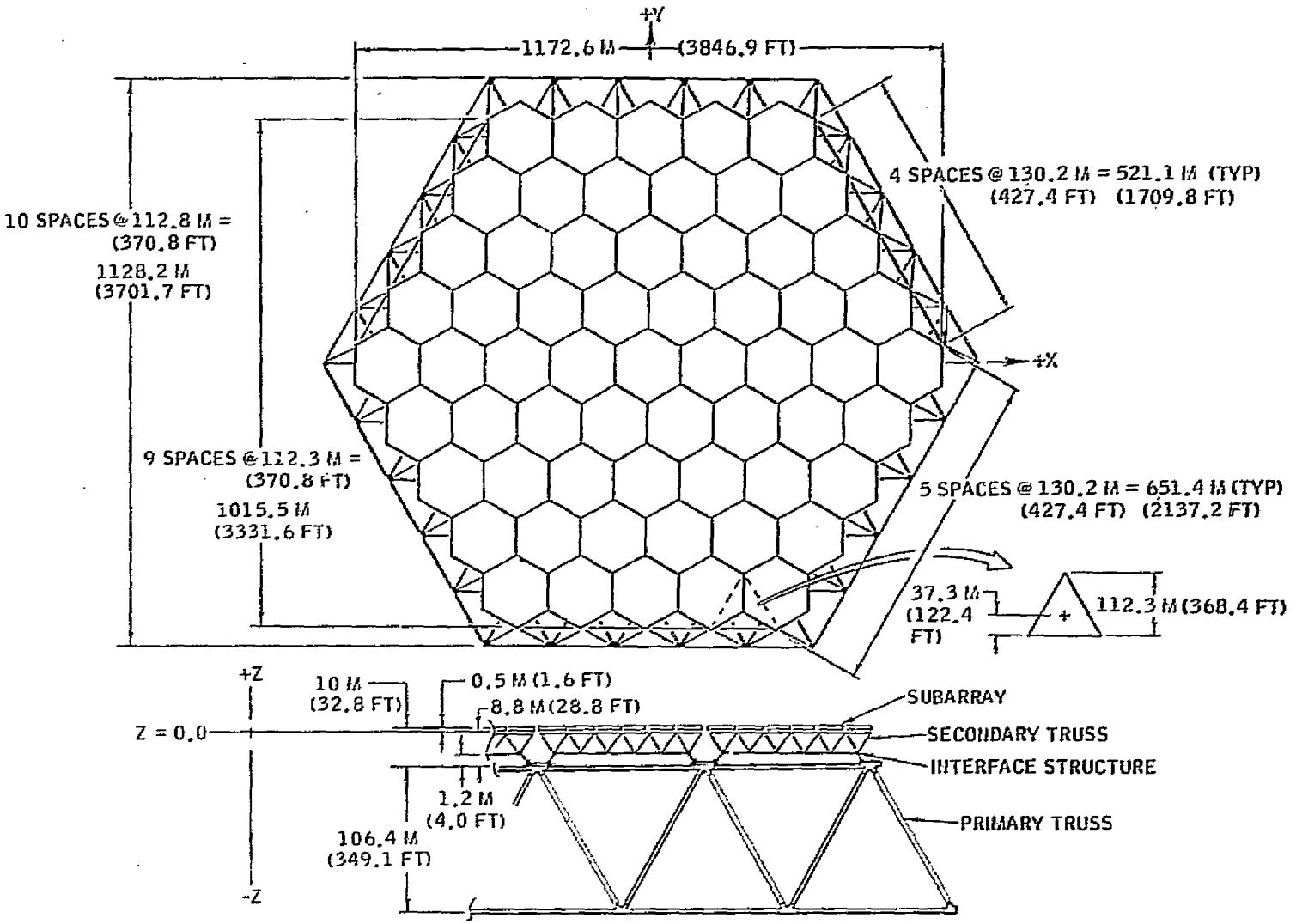

Figure 2. Baseline structural geometry.

Table 1. Tolerance budgets

Function	Primary	Secondary	Subarray
Spider Fabrication	± 0.030	± 0.010	N/A
Strut Length	± 0.150	± 0.020	N/A
Alignment (Straightness)	± 0.030	± 0.010	± 0.010
Strut Joint Slop	0	0	0
Actuator Joint Slop	± 0.001	± 0.001	N/A
Measurement Tolerance	0	0	0
Miscellaneous (Assembly Tolerance)	± 0.050	± 0.010	± 0.010
RSS Subtotals	0.164	0.028	0.014

RSS Total = 0.166 in.

Arc Min. Equivalent = 1.49

(Design Goal = ≤ 1.5 arc min.)

3.2.8 MATERIAL PROPERTIES AND ALLOWABLES

3.2.8.1 Sources — Material strengths and other mechanical and physical properties shall be from Seller's test data or other verified engineering development test values when appropriate. Strength allowables and other mechanical properties used shall be appropriate to the loading conditions, design environments, and stress states for each structural member.

3.2.8.2 Values — Allowable material strengths used in designs shall consider all of the effects of temperature and time associated with the design environments. Allowable yield and ultimate properties are as follows:

1. For Metals
   a. For single load path structures, the minimum guaranteed values (A values in MIL-HDBK-5) are to be used.
   b. For multiple load path structures, the 90 percent probability values (B values in MIL-HDBK-5) are to be used.
2. For Graphite
   a. For single load path structures, the minimum guaranteed (2 sigma) values are to be used for tension and compression strength based on test results, 16 samples each.
   b. For multiple load path structures, the typical (average) values are to be used.

Load Factors	Limit Load	Ultimate Load
Flight loads	1.0	1.25
Nonflight loads	1.0	1.5

3.3 ENVIRONMENTAL REQUIREMENTS

3.3.1 SHIPPING, HANDLING AND STORAGE ENVIRONMENTS

3.3.1.1 Antenna Hardware in Shipping/Storage Containers — The deliverable antenna hardware, when packaged in accord with MIL-B-26195, shall be capable of warehouse storage for 5 years without degradation.

The requirements of MIL-P-116E shall be incorporated for long term storage.

3.3.1.2 Antenna Hardware Out of Shipping/Storage Container — The degradation of the hardware projected through 5 years of storage and 7.5 years in orbit based on the measurable degradation at the end of three years storage outside of the shipping/storage container under the following environmental conditions, shall not degrade the performance of the antenna hardware below the specification requirements.

1. Temperature: from +25 to +150F
2. Humidity: less than 60 percent
3. Sand, dust, fungus, salt, and corrosive atmospheres: the unprotected reflector assembly will not be exposed to sand or dust, nor intentionally to fungus, salt, or corrosive atmospheres.
4. Handling shocks: accelerations and impacts applied to the antenna assembly through the handling equipment are not to exceed 1.1 g.
5. Vibration: not applicable.

3.3.1.3 Handling Equipment for Deliverable Hardware — All equipment used to handle the deliverable hardware shall conform to MIL-S-8512B.

3.3.1.4 Support Equipment — All equipment used to support the deliverable hardware shall conform to MIL-S-8512B.

3.3.1.5 Handling Provisions — Strong points shall be provided as suitable to allow transporting, assembling, supporting, hoisting, or otherwise handling the deliverable hardware.

All completed hardware shall be protected against contamination and packaged in handling/storage containers.

3.3.1.6 Handling Load Factor — For general handling purposes during manufacture, assembly, test, hoisting, and erection, a resultant load factor of 2.0 shall be considered to act in any one direction. This load factor is equivalent steady-state value, inclusive of dynamic effects, to be applied to all structural elements simultaneously.

3.3.2 PRELAUNCH ENVIRONMENTS AT THE LAUNCH SITE

3.3.2.1 Temperature and Humidity — Air conditioned temperatures range from +25 to +100F; relative humidity will be less than 60 percent until liftoff. Prior to air conditioning, the temperature range is from +25 to +150F. Prevention of condensation to protect thermal control surfaces shall be provided.

3.3.3 BOOST AND ORBIT — The antenna hardware shall withstand the following specified boost and orbit environmental conditions without damage or degradation of performance (reference Table 2 for environmental condition tolerances).

3.3.3.1 Flight Profile — Figure 3 describes the expected flight profile for design purposes. Assume the space shuttle as a launch vehicle.

The orbital parameters are also shown in Figure 3.

Table 2. Tolerances on environmental conditions.

Temperature	± 5F degrees
Humidity (relative)	± 5 percent
Acceleration	± 5 percent
Barometric pressure	± 20 percent
Sound pressure level (1/3 octave band)	± 3 dB
Sound pressure level (OSL)	± 1 dB
Acoustic spectrum (1/3 octave band center frequencies)	± 10 percent
Natural frequency	± 1 percent
These test condition tolerances shall not apply on undefined ambient conditions.	

3.3.3.2 STS Temperatures During Launch and Orbit — The STS Orbiter is designed for attitude hold capabilities. During the 3-hour thermal conditioning periods, the vehicle holds at approximately five revolutions per hour (barbecue mode) about the X-axis with the orientation of the X-axis perpendicular to the Earth-Sun line within ± 20 degrees, or it can be oriented at preferred thermal attitudes. On-orbit thermal conditioning lasting as long as 12 hours (before the deorbit maneuver) is allocated for missions on which the thermal protection subsystem temperatures exceed the design limits associated with a single-orbit mission.

Cargo temperatures for a typical flight are shown in Figure 4.

3.3.3.3 Orbital Temperature Cycling — The antenna assembly shall be exposed to temperature cycles in orbit for 7.5 years minimum considering a maximum of 3600 eclipses of approximately 60 minutes duration.

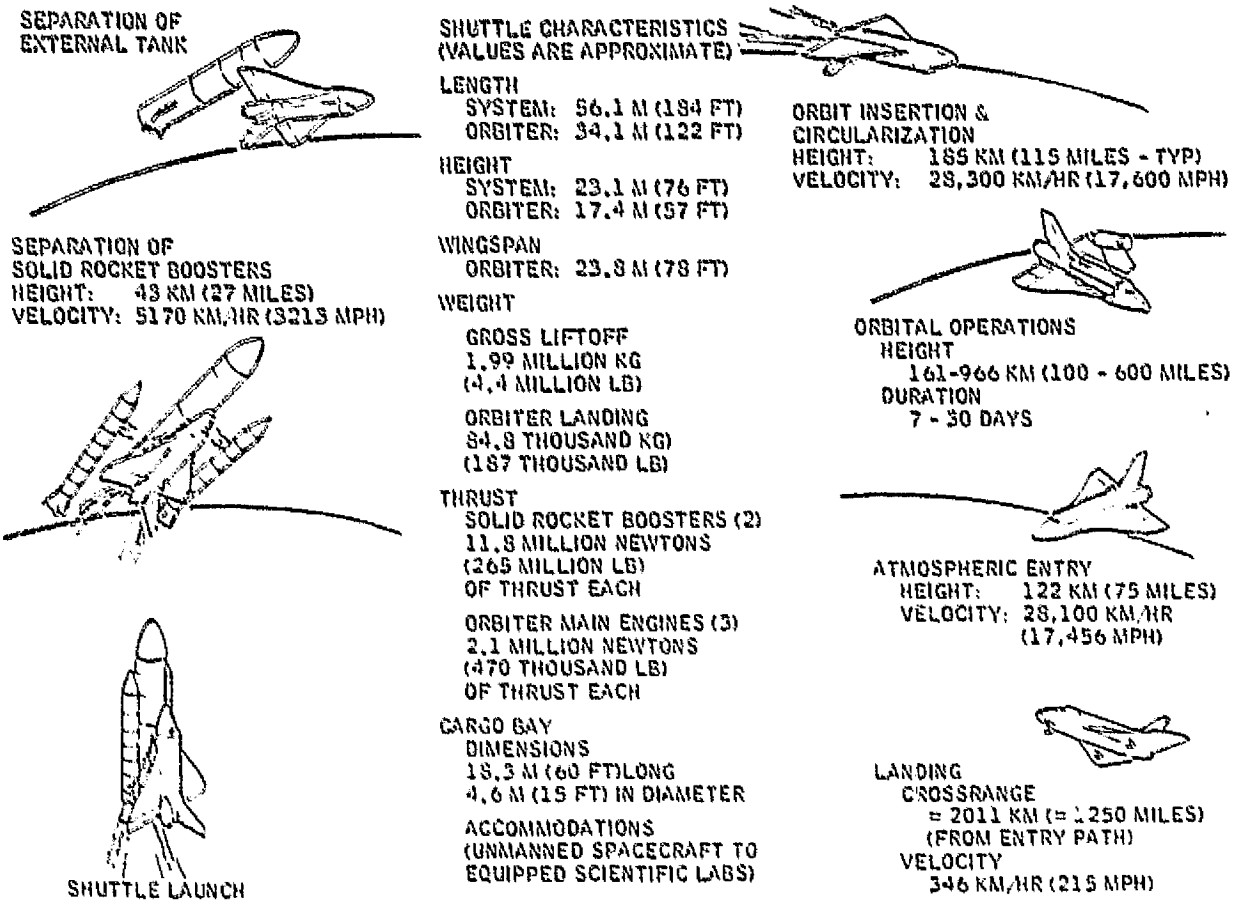

Figure 3. Typical launch and ascent profile.

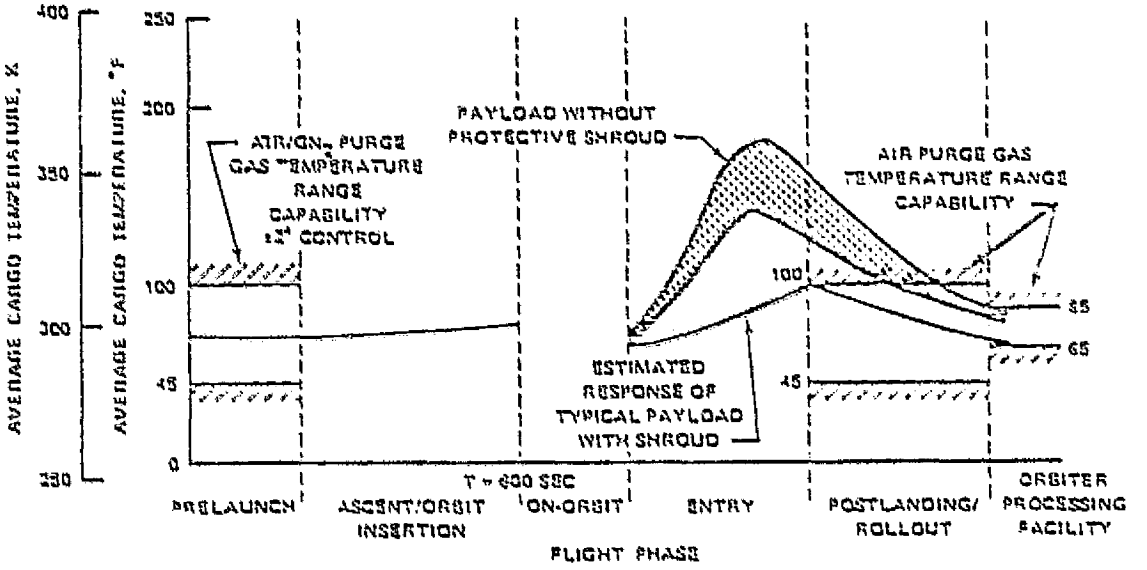

Figure 4. Cargo bay thermal environment during the phases of a typical flight.

3.3.3.4 STS Vibration — The estimated random vibration and appropriate exposure durations for the cabin and midfuselage to payload interfaces caused by the fluctuating pressure loads are shown in Figure 5. The levels shown are typical of liftoff, transonic flight, and performance at maximum aerodynamic pressure. The midfuselage/payload interface vibration environment is based on the response of unloaded interface structure and should be considered the upper limit. The vibration inputs at the interface will be reduced by addition of the payload and support structures between the interface and payload component.

Vibration resulting from acoustic spectra is generated in the cargo bay by the engine exhaust and by aerodynamic noise during atmospheric flight. These predicted maximums are illustrated in Figure 6. The data presented are based on an empty cargo bay and may be modified by the addition of payloads, depending on their characteristics. Aerodynamic noise during entry is significantly less than on ascent.

3.3.3.5 Thermal — A geosynchronous orbit with an altitude of 19,325 nmi and an orbit period of about 24 hours is specified for the large 1 km microwave power antenna. The antenna/solar array system orientation is such that the solar array is normal to the solar flux (maximum power generation) whereas the antenna is essentially pointing at the center of the earth (depending on receiver antenna location). For the thermal analysis, an angle of zero degrees between the earth-sun vector and the orbit plane is to be employed. This case yields maximum solar heating and thus highest temperatures for the subarray radiator panels. It also yields the maximum earth shadow time of about 1.16 hours. Reference ICD No. xx-xxxx for thermal load information.

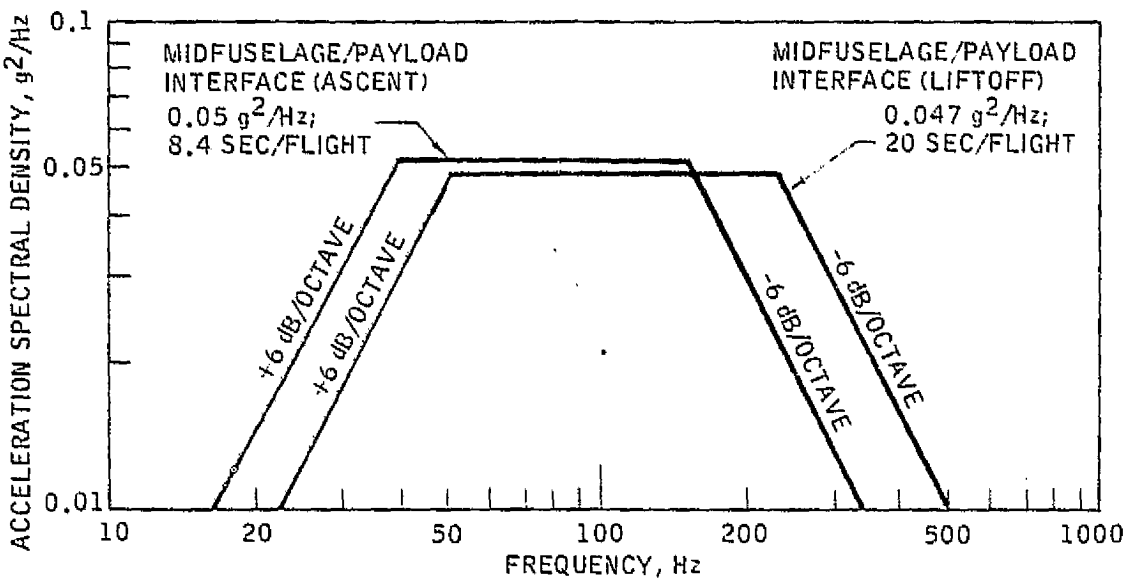

Figure 5. Random vibration at midfuselage main longeron payload attachment points interface and in the cabin.

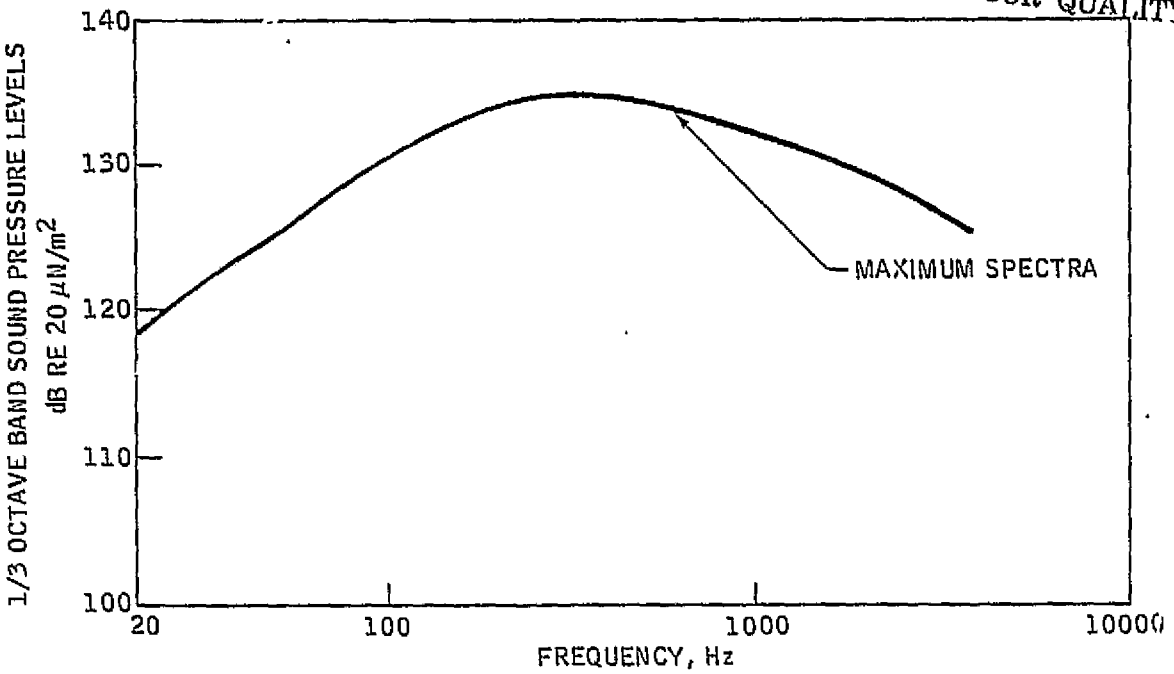

Figure 6. Analytical prediction of maximum Orbiter cargo bay acoustic spectra.

3.3.3.6 Steady State Solar Illumination — The antenna system design shall be capable of meeting performance specifications when subjected to direct illumination for steady state thermal conditions with the sun incident on the antenna from any direction including shadowing by the adjacent structure and other elements (see ICD No. xx-xxxx).

3.3.3.7 Generated Environments — No liquid or gas which is corrosive, erosive, explosive or noxious shall be exhausted from the hardware. All materials shall be compatible with an absolute pressure of 10^{-6} torr for the test and 10^{-13} torr for operational life. All materials shall be selected in accordance with report GSFC X-735-69-471.

3.3.3.8 Pressure and Venting — With the vents open, the STS cargo bay pressure closely follows the flight atmospheric pressures. The payload vent sequencing is as follows:

Prelaunch	Closed (vent no. 6 in purge position)	Entry (high heat zone)	All closed
Liftoff (T = 0)	Closed	Atmospheric (75,000 ±5,000 ft (23 ± 1.5 kilometers)) to landing	All open
T + 10 seconds	All Open	Postlanding purge	Closed (vent no. 6 in purge position)
Orbit insertion	All open		
On orbit	All open		
Preentry preparation	All closed		

During the orbital phase, the cargo bay operates unpressurized. Pressures for other flight phases are shown in Figure 7.

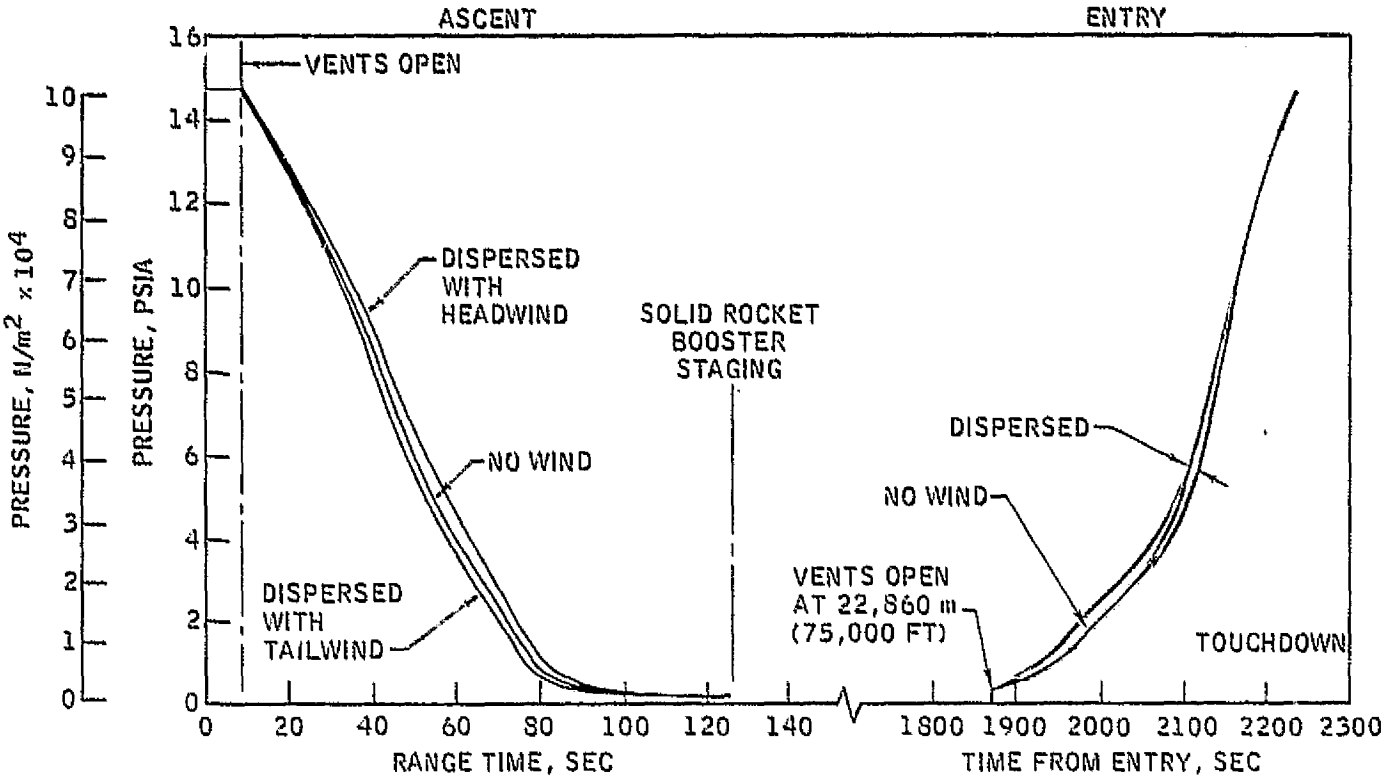

Figure 7. STS cargo bay internal pressure.

3.3.4 NATURAL RADIATION ENVIRONMENT — The antenna assembly shall be designed to withstand the following radiation environment and duration without damage, deterioration, or degradation of performance.

Solar and trapped particle radiation for a minimum of 7.5 years. The daily fluxes of trapped electrons and protons are given in Tables 3 and 4. The integrated solar proton fluence shall be as in Figure 8.

Table 3. Trapped electrons.

The time-averaged daily integral flux spectrum for trapped electrons is:

Energy (E) MEV	Flux with energies greater than E Electons/cm^2 - day
0.1	0.439E12
0.5	0.316E12
1.0	0.728E10
2.0	0.157E10
3.0	0.458E9
4.0	0.149E9
5.0	0.509E8
6.0	0.180E8

Figure 4. Trapped protons

The time-averaged daily integral flux spectrum for trapped protons is:

Energy (E) MEV	Flux with energies greater than E Protons/cm^2 - day
0.4	0.616E12
1.0	0.115E12
4.0	0.110E11
15.0	0.294E9
30.0	0.501E8
50.0	0.111E8
100.0	0.572E7
300.0	0.587E6

4.0 QUALITY ASSURANCE PROVISIONS

4.1 GENERAL

Dimensions, design features, material suitability, and functional requirements specified in this section shall be formally verified to establish the acceptability of the product. All testing shall conform to requirements of MIL-C-45662 and MIL-STD-831.

4.2 INSPECTION

Items not conforming to the criteria specified herein are to be submitted to Material Review, individual evaluation, and dispositioning by designated representatives.

4.2.1 TOLERANCES — Compliance of the antenna assembly with every tolerance specified in this document or on ICD No. xx-xxxx shall be adequately demonstrated by Quality Control records. This proof of compliance may involve physical measurement of the manufactured items or, where appropriate, proof that the tooling will guarantee compliance.

4.2.2 SPACE ENVELOPE — Fit check tooling shall be used to show that the antenna is within the limits of the space envelope, as defined on ICD No. xx-xxxx. Compliance with this paragraph shall be documented in Quality Control records.

4.2.3 SOURCE INSPECTION — A resident source inspector may be provided for the duration of product manufacturing and testing.

4.3 QUALITY PROGRAM

A formal Quality Assurance Program shall be implemented.

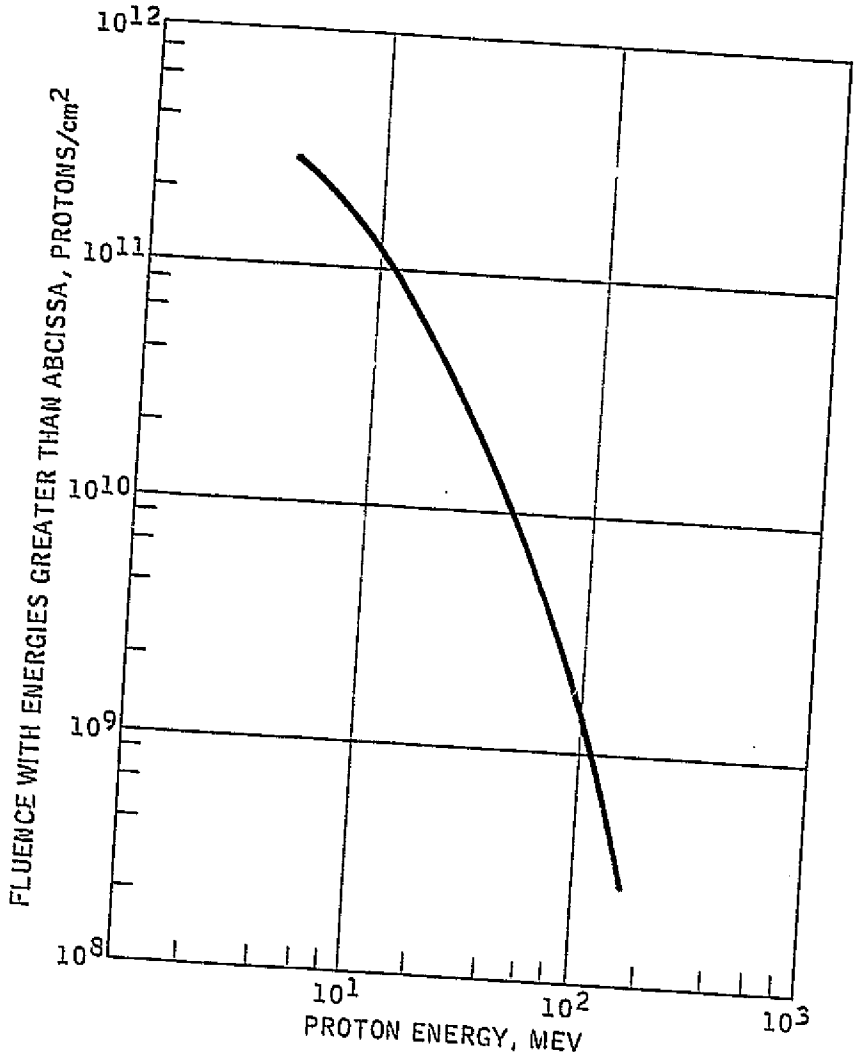

Figure 8. Integrated solar proton fluence.

4.3.1 CALIBRATION — Records of the calibration of all test and measuring equipment used shall be generated and documented, in accordance with document xx-xxxx.

4.3.2 INSPECTION AND TEST PROCEDURES — Verification, acceptance inspection, and acceptance test procedures for the antenna hardware shall be prepared and documented by the subcontractor in accordance with document xx-xxxx.

4.4 PHYSICAL QUALIFICATION

4.4.1 WEIGHT DETERMINATION — The weight of each deliverable component shall be measured with an accuracy of 5 percent.

4.4.2 CENTER OF GRAVITY DETERMINATION — The location of the total cg shall be calculated and shall meet the requirements of paragraph 3.2.2.2.

4.4.3 TESTING — STRUCTURAL

4.4.3.1 Acoustic Vibration — A qualification test unit will be required to withstand, without damage, the acoustic levels shown in Figure 9.

4.4.3.2 Environmental Test — It shall be demonstrated that the equipment will meet all functional requirements when subjected to an environment which simulates the effects of exposure for 7.5 years in the space environment given in paragraph 3.3.2. If no data exists on substantially the same materials, samples of the actual materials shall be tested in UV and in electron and proton beams to establish conformance with this section.

Environmental testing shall be accomplished in accordance with MIL-STD-810B.

4.4.3.3 Loads Verification — Verification of the load-carrying capabilities of the deliverable hardware will be via a static load test. This load test will be performed on a representative deliverable package, and on a representative STS payload package if different than above.

4.4.3.4 Factors-of-Safety

Condition	Yield	Ultimate
a. Ground Handling and Transportation		
1. Involving personnel safety.	1.15	1.50
2. Where personnel safety is not involved.	1.00	1.25
b. STS Flight Operations		
1. Involving crew safety.	1.00	1.40
2. Where crew safety is not involved.	1.00	1.25
c. Emergency Landing	—	1.00

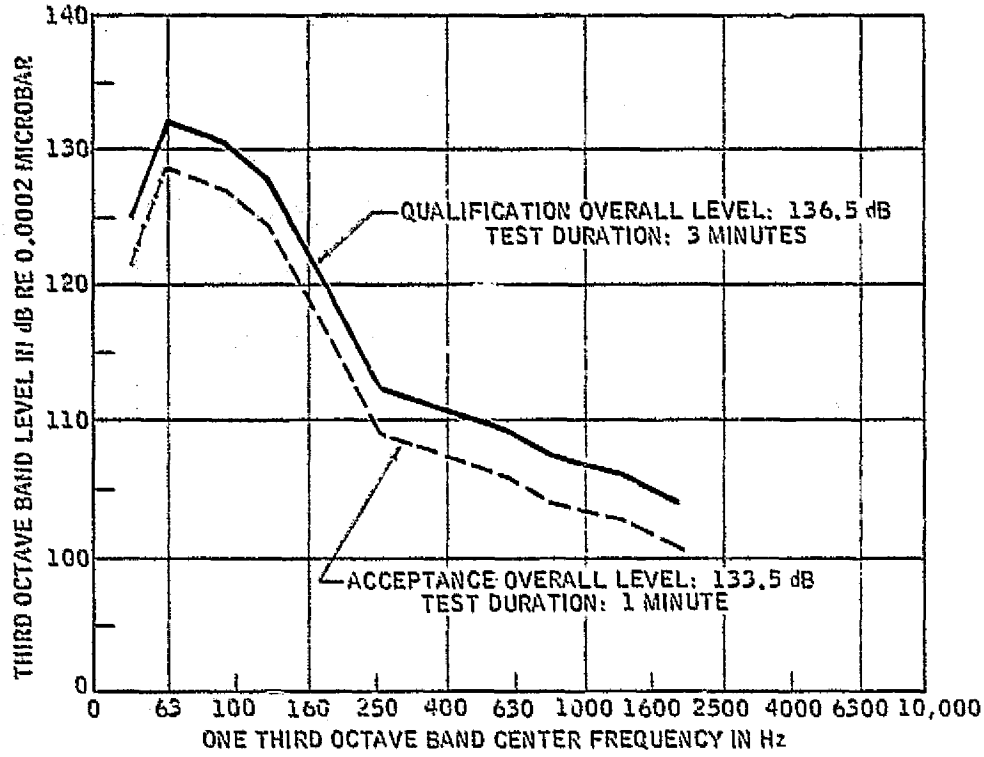

ONE THIRD OCTAVE CENTER FREQUENCY (Hz)	ACCEPTANCE	QUALIFICATION
50	122.0	125.0
63	128.5	131.5
80	128.0	131.0
100	127.0	130.0
125	123.5	126.5
160	119.0	122.0
200	114.0	117.0
250	109.5	112.5
315	108.5	111.5

ONE THIRD OCTAVE CENTER FREQUENCY (Hz)	ACCEPTANCE	QUALIFICATION
400	107.5	110.5
500	107.0	110.0
630	106.0	109.0
800	104.5	107.5
1000	103.5	106.5
1250	102.5	105.5
1600	102.0	105.0
2000	101.0	104.0

Figure 9. Acoustic spectrum (STS configuration).

The guiding safety requirement for STS operations shall be that a failure of any component does not endanger the orbiter vehicle and its flight crew. The loading conditions which could cause crew safety hazards are listed in Table 5.

Table 5. Applicability of 1.4 factor-of-safety. (Emergency landing events)

Phase	Potential Hazard	Loading Condition
Ascent	Puncture of orbiter doors or fuel tanks below cargo-bay liner	$\pm$X, $\pm$Y
	Where failure on ascent could result in puncture of crew-cabin bulkhead at orbiter station 582 during landing for about-once-around condition.	-Z
Landing	Puncture of orbiter fuel tanks below cargo-bay liner.	-X
	Puncture of crew-cabin bulkhead at orbiter station 582.	$\pm$Z

5.0 PREPARATION FOR DELIVERY

Packing and packaging arrangements shall provide adequate protection for the antenna component parts to withstand the environmental conditions incident to transportation, handling, and storage.

Each deliverable unit shall be cleaned, and labeled prior to shipment.

6.0 NOTES